

Advanced Test Reactor Core Modeling Update Project

Annual Report for Fiscal Year 2011

David W. Nigg
Kevin A. Steuhm

September 2011



The INL is a U.S. Department of Energy National Laboratory
operated by Battelle Energy Alliance

Advanced Test Reactor Core Modeling Update Project Annual Report for Fiscal Year 2011

**David W. Nigg
Kevin A. Steuhm**

September 2011

**Idaho National Laboratory
Nuclear Science and Technology Directorate
Idaho Falls, Idaho 83415**

<http://www.inl.gov>

**Prepared for the
U.S. Department of Energy
Office of Nuclear Energy
Under DOE Idaho Operations Office
Contract DE-AC07-05ID14517**

DISCLAIMER

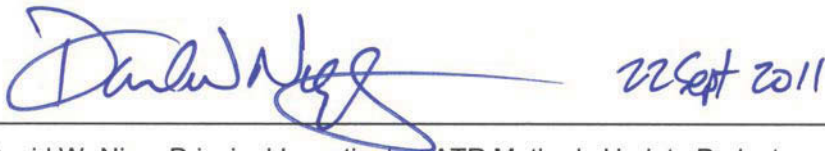
This information was prepared as an account of work sponsored by an agency of the U.S. Government. Neither the U.S. Government nor any agency thereof, nor any of their employees, makes any warranty, expressed or implied, or assumes any legal liability or responsibility for the accuracy, completeness, or usefulness, of any information, apparatus, product, or process disclosed, or represents that its use would not infringe privately owned rights. References herein to any specific commercial product, process, or service by trade name, trade mark, manufacturer, or otherwise, does not necessarily constitute or imply its endorsement, recommendation, or favoring by the U.S. Government or any agency thereof. The views and opinions of authors expressed herein do not necessarily state or reflect those of the U.S. Government or any agency thereof.

Nuclear Science and Technology Directorate

**Advanced Test Reactor Core Modeling Update Project
Annual Report for Fiscal Year 2011**

**INL/EXT-11-23348 (R1)
September 2011**

Approval:

A handwritten signature in blue ink, which appears to read "David W. Nigg", is written over a horizontal line. To the right of the signature, the date "22 Sept 2011" is handwritten in the same ink.

David W. Nigg, Principal Investigator, ATR Methods Update Project

EXECUTIVE SUMMARY

Legacy computational reactor physics software tools and protocols currently used for support of Advanced Test Reactor (ATR) core fuel management and safety assurance, and to some extent, experiment management, are inconsistent with the state of modern nuclear engineering practice, and are becoming increasingly difficult to properly verify and validate (V&V) according to modern standards. Furthermore, the legacy staff knowledge required for application of these tools and protocols from the 1960s and 1970s is rapidly being lost due to staff turnover and retirements. In late 2009, the Idaho National Laboratory (INL) initiated a focused effort, the ATR Core Modeling Update Project, to address this situation through the introduction of modern high-fidelity computational software and protocols. This aggressive computational and experimental campaign will have a broad strategic impact on the operation of the ATR, both in terms of improved computational efficiency and accuracy for support of ongoing DOE programs as well as in terms of national and international recognition of the ATR National Scientific User Facility (NSUF).

The ATR Core Modeling Update Project, targeted for full implementation in phase with the next anticipated ATR Core Internals Changeout (CIC) in the 2014 time frame, began during the last quarter of Fiscal Year 2009, and has just completed its second full year. Key accomplishments so far have encompassed both computational as well as experimental work. A new suite of stochastic and deterministic transport theory based reactor physics codes and their supporting nuclear data libraries (HELIOS, KENO6/SCALE, NEWT/SCALE, ATTLA, and an extended implementation of MCNP5) has been installed at the INL under various licensing arrangements. Corresponding models of the ATR and ATRC are now operational with all five codes, demonstrating the basic feasibility of the new code packages for their intended purpose. Of particular importance, a set of as-run core depletion HELIOS calculations for all ATR cycles since August 2009 was successfully completed during 2011. This major effort supported a decision late in the year to proceed with the phased incorporation of the HELIOS methodology into the ATR Core Safety Analysis Package (CSAP) preparation process, in parallel with the established PDQ-based methodology, beginning in Fiscal Year 2012. Finally, a capability for rigorous sensitivity analysis and uncertainty quantification based on the TSUNAMI system is being implemented and initial computational results have been obtained. This capability will have many applications as a tool for understanding the margins of uncertainty in the new models as well as for validation experiment design and interpretation.

On the experimental side of the project, new hardware was fabricated, measurement protocols were approved, and the first four of six planned application-specific physics code validation measurements based on neutron activation spectrometry were conducted at the ATRC facility. These measurements will continue through 2013 and will include the introduction of additional new experimental hardware to broaden the scope of the validation protocols. Further opportunities to collaborate with various other ongoing experimental campaigns in the ATRC and ATR will be identified as the Core Modeling Update Project proceeds, with a particular emphasis on collaboration with U-Mo fuel qualification experiments being conducted in connection with the DOE Reduced Enrichment for Research and Training Reactors (RERTR) Program. Such opportunities are expected to include RERTR-related experiments in the ATRC and possibly a “depressurized” low-power run of the ATR itself during 2012.

A second component of the experimental validation campaign involves the possible construction of a system for non-invasive measurement of the burnup of ATR fuel elements *in-situ* in the ATR canal. Post-irradiation ATR fuel burnup measurements will serve as a key fuel depletion model validation tool and also as an aid in improved fuel management. Initial in-canal feasibility measurements to identify appropriate engineering parameters and radiation measurement instrumentation for such a system were conducted during 2010 with significant additional progress in 2011, including the preparation and

transmittal, to the Department of Energy, of a proposal for construction of a permanent system for non-invasive *in-situ* fuel element burnup measurements in the ATR canal.

It is also important to recognize that the ATR Core Modeling Update Project represents not only an investment in new technology. It also represents a key investment in the new generation of INL scientific and engineering staff who will, by demographic necessity, assume leadership roles in the overall ATR enterprise over the next several years. Accordingly, several students and early-career INL Scientific and Engineering staff members are being proactively integrated into the effort and this will accelerate in 2012 and beyond.

Finally we note that although full implementation of the new computational models and protocols will extend over a period of a few years, interim applications in the much nearer term have already been demonstrated. For example, these demonstrations included an analysis that was useful for understanding the cause of some ATR operational issues in December 2009 that were triggered by a larger than acceptable discrepancy between the measured excess core reactivity and a calculated value that was based on the legacy computational methods. As the Core Modeling Update Project proceeds, we anticipate further such interim, informal applications in parallel with formal qualification of the system under applicable INL and external Quality Assurance procedures and standards.

CONTENTS

EXECUTIVE SUMMARY	v
ACRONYMS	viii
1.0 INTRODUCTION	1
2.0 HELIOS MODEL DEVELOPMENT FOR ATR CSAP AND FUEL MANAGEMENT APPLICATIONS	10
3.0 HIGH-FIDELITY MODELS TO SUPPORT VALIDATION EXPERIMENTS IN THE ATRC	45
4.0 VALIDATION EXPERIMENTS IN THE ATRC	89
5.0 FEASIBILITY TESTING FOR ATR FUEL BURNUP MEASUREMENT SYSTEM ...	113
6.0 REFERENCES.....	136
APPENDIX A - SAMPLE HELIOS INPUT FOR MERGED STRUCTURES.....	140
APPENDIX B – METHOD USED FOR LEAST-SQUARES ADJUSTMENT OF NEUTRON SPECTRA USING ACTIVATION DATA.....	166

ACRONYMS

AGR	Advanced Gas Reactor
ATR	Advanced Test Reactor
ATRC	Advanced Test Reactor Critical Facility
CFD	Computational Fluid Dynamics
CIC	Core Internals Changeout
CSAP	Core Safety Assurance Package
ENDF	Evaluated Nuclear Data File
NST	Nuclear Science and Technology
NSUF	National Scientific User Facility
RERTR	Reduced Enrichment for Research and Test Reactors
V&V	Verification and Validation
DHA	Detector Housing Assembly
DPA	Down Pipe Assembly
FBUMS	Fuel Burnup Measurement System
FEC	Fuel Element Carriage
HPGe	High Purity Germanium
HPXe	High Pressure Xenon
INL	Idaho National Laboratory
LaBr ₃	Lanthanum Bromide
LST	Lead Screw Trolley
XSC	X Scan Carriage
OSCC	Outer Shim Control Cylinder
ESAP	Experiment Safety Analysis Package
IRPhE	OECD International Reactor physics Experiment Evaluation (Program)
OECD	Organization for Economic Cooperation and Development
QA	Quality Assurance
LEP	(ATR) Life Extension Program
ICSBE	OECD International Criticality Safety benchmark Experiment Evaluation (Program)
DOE	(US) Department of Energy

1.0 INTRODUCTION

David W. Nigg (INL)

This Annual Report documents the accomplishments of the ATR Core Modeling Update Project during Fiscal Year 2011. A brief overview of the background, rationale, organizational structure, and a basic summary of progress to-date for the project is provided below. Later sections cover additional detail on specific technical accomplishments during the year.

1.1 Description of the Advanced Test Reactor

The Advanced Test Reactor (ATR), located at the Idaho National Laboratory (INL), is one of only a few high-power research reactors of its type in the world, with a variety of missions involving accelerated testing of nuclear fuel and other materials in a very high neutron flux environment, medical and industrial isotope production, and other applications. Along with its companion critical mockup (ATRC), the ATR is one of the key nuclear engineering research and testing facilities within the US Department of Energy (DOE) National Laboratory Complex. The ATR and ATRC also serve as the centerpieces of the recently-formed ATR National Scientific User Facility (NSUF), whose purpose is to facilitate the current trend toward broadening the applications of the ATR beyond its traditional base.

The ATR (Figures 1.1 and 1.2) is a highly-heterogeneous light-water and beryllium moderated, beryllium reflected, light-water cooled system with highly-enriched (93% ^{235}U) plate-type fuel elements arranged in a serpentine pattern. Gross reactivity and power distribution control during operation is achieved through the use of eight pairs of rotating control drums with hafnium neutron absorber plates on one side as can be seen in Figure 1.1. There are several design features incorporated into the ATR and ATRC (Figures 1.3 and 1.4) to optimize experimental capabilities. These features include: a) the use of flux traps to provide high thermal neutron fluxes for irradiation or experiments in nine regions, b) incorporation of special control shim design to retain axial flux symmetry throughout an ATR fuel cycle; and c) regional power control to provide capability for power shifting between core lobes to optimize the neutron flux distribution for a wide range of simultaneous experiments. The ATR can be operated at powers as high as 250 MW although most routine applications do not require the maximum power. Typical thermal neutron fluxes in the flux traps can be as high as 5.0×10^{14} n/cm²-s. Typical operating cycle lengths are in the range of 45–60 days. The core fuel configuration and the experiment loadings are usually rearranged between cycles and each fuel element is typically burned for two or three cycles during its useful lifetime.

The ATRC is an open-pool nuclear mock-up of the ATR that typically operates at approximately 600 W and produces a thermal neutron flux in the traps that is in the range of 1.0×10^9 n/cm²-s. As is the case for the ATR, the core consists of a 4-ft-high (122 cm), uniform-width, vertical 40-element fuel annulus shaped in a serpentine fashion between and around nine flux-trap areas located in a three-by-three square array. The cruciform fixture inside the serpentine is called the neck shim housing. The reactivity of the core is controlled by: (a) five vertically withdrawn safety rods that use cadmium as the poison material; (b) 24 vertically withdrawn hafnium neck shim rods; and (c) eight pairs of rotating outer shim control cylinders (OSCCs) that use hafnium poison plates.

ATRC criticality can normally be stably attained at a power as low as 0.25 mW and the maximum rated power is 5 kW. The ATRC facility is typically used with prototype experiments to characterize in advance, with precision and accuracy, the expected changes in core reactivity to be expected for the same experiments in the ATR. Useful physics data can also be obtained for evaluating the worth and calibration of control elements as well as thermal and fast neutron distributions.

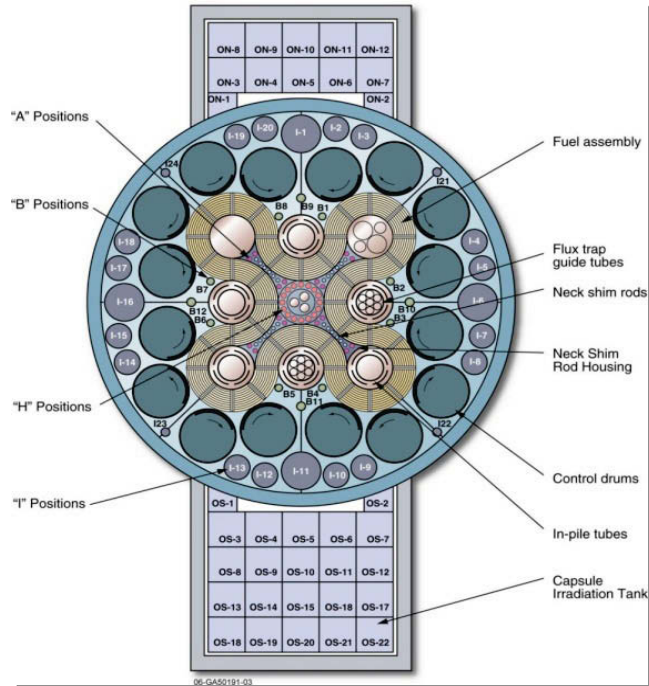


Figure 1.1. Core and reflector geometry of the Advanced Test Reactor.

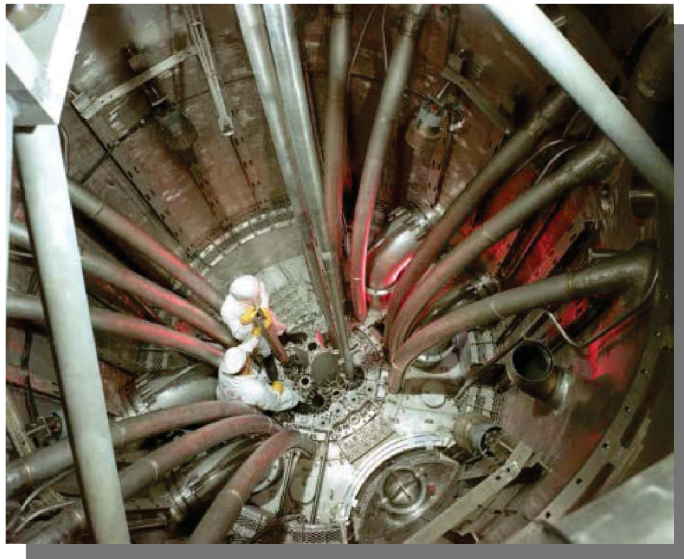


Figure 1.2. View into the ATR pressure vessel.



Figure 1.3. The Advanced Test Reactor Critical Facility.

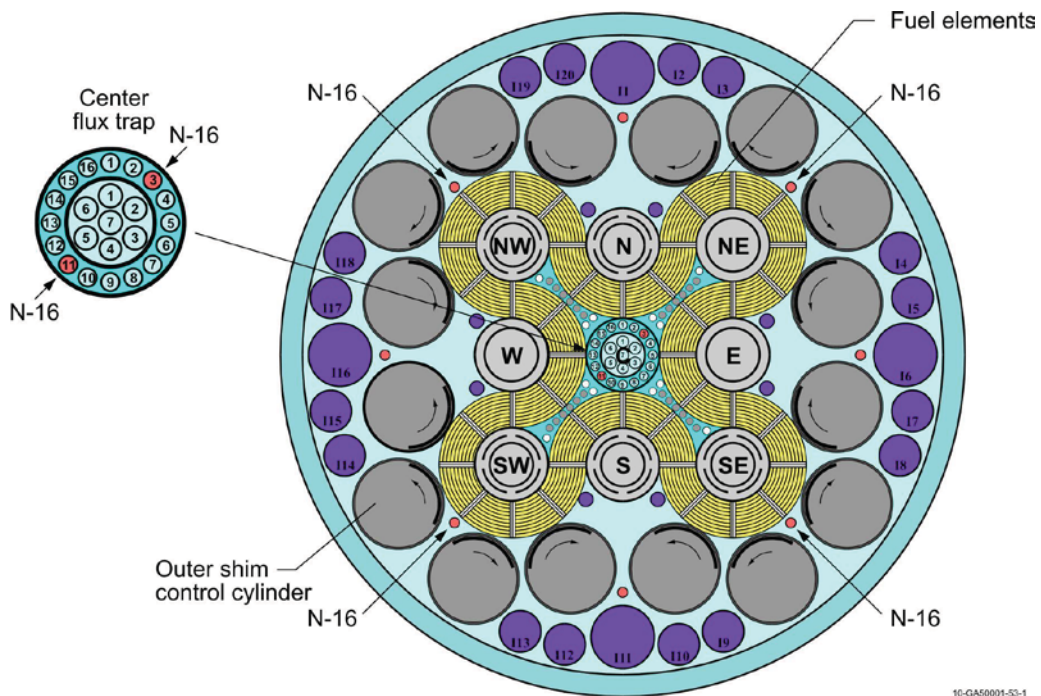


Figure 1.4. ATRC Configuration, showing the NW LIPT Flux Trap and six N-16 positions.

1.2 Rationale for the ATR Core Modeling Update Project

Computational reactor physics modeling is used extensively to support ATR experiment design, operations and fuel cycle management, core and experiment safety analysis, and many other applications. Experiment design and analysis for the ATR is generally supported by very detailed and sophisticated three-dimensional Monte Carlo analysis, typically using the internationally recognized continuous-energy MCNP5 code (Goorley et al., 2004) coupled to extensive fuel isotope buildup and depletion analysis where appropriate. On the other hand, the computational reactor physics software tools and protocols currently used for ATR core fuel cycle analysis and operational support are largely based on four-group diffusion theory in Cartesian geometry (Pfeifer et al., 1971) with heavy reliance on “tuned” nuclear parameter input data. These methods are obsolete and have been superseded in the general reactor physics community by high-fidelity multidimensional transport-theory-based methods. As a result, the historical approach to ATR reactor physics operational support is inconsistent with the state of modern nuclear engineering practice and nearly impossible to properly verify and validate (V&V) according to modern standards. Furthermore, some aspects of the analysis process are highly empirical in nature, with many “correction factors” and approximations that require very specialized experience to apply. The legacy staff knowledge from the 1960s and 1970s that is essential for the successful application of these various approximations and old computational processes is rapidly being lost due to staff turnover and retirements. Finally, future clients of the ATR NSUF are anticipated to be experienced in the use of modern computational methods available for nuclear systems modeling and are likely to expect corresponding computational support services within the NSUF infrastructure.

Figure 1.5 illustrates one of the challenges experienced recently with the legacy physics computational methods used for ATR operational support. A fueled experiment associated with the DOE Next Generation Nuclear Plant Advanced Gas Reactor development program was scheduled for irradiation in the south flux trap of the ATR as shown. However, uncertainties in the supporting computations were such that it was not possible to determine the neutronics effects of this experiment on neighboring flux traps to sufficient accuracy, and the operational margins of conservatism that were required caused the experiment to be delayed until a later ATR cycle at significant expense. In a second example of the impact of uncertainty in the current computational methods, some operational issues arose in December 2009 that were triggered by a larger than acceptable discrepancy between the calculated and measured excess core reactivity. These issues were resolved via standard procedures, but schedules were adversely impacted and the root cause was largely traced to problems with the legacy computational model of an experiment in the central flux trap.

Continued successful operation of the ATR is dependent, in part, on the proactive introduction of modern high-fidelity computational software and protocols, with appropriate V&V, within the next 3-4 years via the ATR Core Modeling Update Project described in this report. This aggressive computational and experimental campaign will have a broad strategic impact on the operation of the ATR, both in terms of improved computational efficiency and accuracy for support of ongoing DOE programs as well as national and international recognition of the ATR NSUF. The new computational and V&V protocols will be broadly applicable across all programs that use the ATR and ATRC. The developmental effort is in fact already leveraged with several other INL projects including the ATR Life Extension Program (LEP), the DOE Reduced Enrichment for Research and Test Reactor (RERTR) initiative, and an INL collaboration with Idaho State University (ISU), the Atomic Energy Commission of France (CEA), and the National Atomic Energy Commission of Argentina (CNEA) to evaluate various options for in-core ATR and ATRC instrumentation upgrades under the auspices of the NSUF (Rempe et al., 2010).

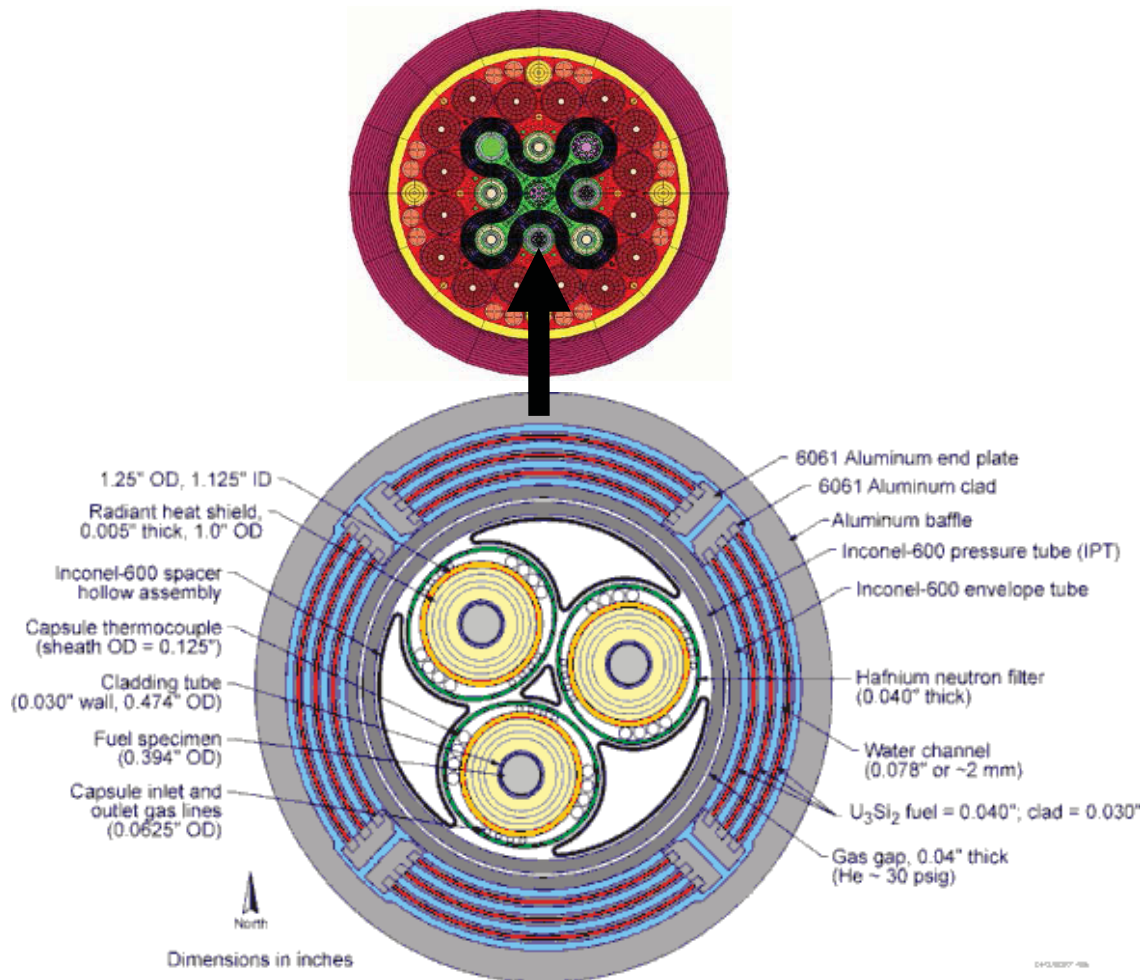


Figure 1.5. Gas Test Loop experiment designed for placement in the ATR south flux trap.

1.3 Technical Objectives of the Core Modeling Update Project

Prior to the initiation of the Core Modeling Update Project in late 2009, the INL was already making a few efforts to modernize ATR reactor physics analysis capabilities using current standard software. Those efforts have produced some important progress, especially for experiment design and analysis as noted earlier. However, this has largely been on an *ad-hoc* basis, and several key tasks remain. These tasks include:

- Implementation of complementary, self-consistent multidimensional stochastic and deterministic neutron transport models of the ATR and ATRC cores using well-established and recognized science-based software packages consistent with current practice
- Standardized computational procedures and training, more easily transferred to new staff members
- Additional Verification & Validation, with development of standard apparatus and protocols for detailed neutron flux distribution and spectrum validation measurements in the core and selected

flux traps that can be adapted as needed for changing experimental conditions and repeated on a regular basis. This also offers an opportunity to make much more effective use of ATRC both within the INL and as a key component of the National Scientific User Facility

Figure 1.6 shows the suite of new tools that will be available and how they generally relate to one another. This illustration is however not a computational flow chart or procedure *per se*. Specific computational protocols using the tools shown in Figure 1.6 for routine ATR support applications will be specified in approved procedures. These procedures will prescribe the geometric modeling input files, nuclear data files, and other aspects of each specific computational protocol. For example there will be a procedure for performance of core-follow calculations for a particular ATR operational cycle using the new tools.

The most recent release of the Evaluated Nuclear Data Files (ENDF/B Version 7) will be used to provide the basic cross section data and other nuclear parameters required for all of the modeling codes. The ENDF physical nuclear data files are processed into computationally-useful formats using the standard publically-available NJOY or AMPX (Radiation Safety Information Computational Center, 2010) codes as applicable to a particular module as shown at the top of the Figure.

As noted earlier, the MCNP5 three-dimensional stochastic simulation code is already used extensively for ATR experiment design and analysis and, to some limited extent, core analysis. Under the Core Modeling Update Project, we are also introducing the KENO stochastic simulation code (Hollenbach et al., 1996), primarily for detailed core analysis in connection with ongoing ATR and ATRC operations as well as for support of the possible conversion of the ATR (and presumably ATRC) to low-enrichment fuel (LEU) under the DOE RERTR Program. The KENO code is useful both as a stand-alone analysis and verification tool as well as in conjunction with the TSUNAMI (Broadhead et al., 2004, Williams et al., 2008) sensitivity-uncertainty analysis system available with the SCALE nuclear system analysis package (Bowman et al., 2009). During Fiscal year 2012, we will also investigate the possibility of incorporating the extremely sophisticated MC21 stochastic simulation and depletion code (Sutton et al., 2007) into the new suite.

The right-hand side of Figure 1.6 shows the new high-fidelity deterministic transport computational tools that are being integrated into the system. HELIOS (Studsvik Scandpower, 2008) and ATTILA (McGhee et al., 2006) are commercial grade software products now in place at the INL under permanent sitewide licenses. NEWT (DeHart, 2006) together with its SCALE-based support infrastructure is a well-established and verified software tool developed within the DOE National Laboratory system. All three code packages have various strengths and weaknesses, but taken together they will provide the necessary high-fidelity neutron and gamma transport capability that is required for various aspects of ATR and ATRC core modeling as summarized in Figure 1.6. These aspects are described in much more detail in Sections 2 and 3 of this report.

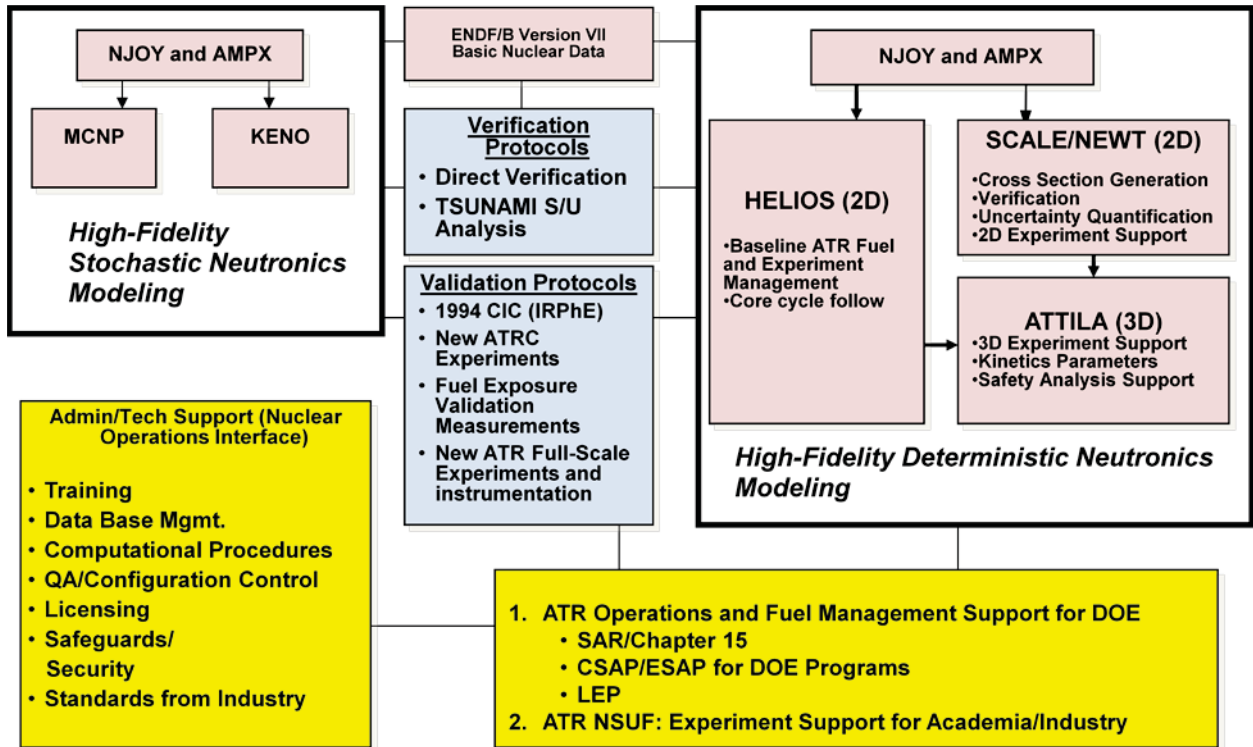


Figure 1.6. Advanced computational tool suite for the ATR and ATRC, with supporting verification, validation and administrative infrastructure.

As always, theory and experiment must be consistent in any scientific or engineering enterprise. The Core Modeling Update Project also includes several activities designed to incorporate historical validation data from earlier ATR and ATRC experiments as well as to develop new validation data specific to the new computational models and protocols. In particular, much of the initial model development has been based on a very well documented critical experiment conducted as part of the 1994 ATR Core Internals Changeout (CIC) activity (Kim and Schnitzler, 2008), which will be described in detail later. New core flux measurements in both ATRC and ATR are also underway. Section 4 of this report describes plans and accomplishments in this area during FY-2011. In addition, the Core Modeling Update Project includes a task described in Section 5 to develop non-invasive methods for post-irradiation measurement of exposure (or “burnup”) in ATR fuel elements, both as an aid in characterizing the existing inventory of used elements as well as to provide additional validation data for the new ATR core follow and fuel cycle design models.

1.4 Project Structure and Technical Team

The ATR Core Modeling Update project includes 5 technical tasks. It is largely organized and funded as a part of the larger ATR Life Extension Program (LEP). The five tasks, which also provide the framework for the structure of this Annual Report, are as follows:

Task 1: Project Management: Includes sponsor/Collaborator interface maintenance, project documentation and planning, software licensing, travel, and university interfaces including student support.

Task 2: ATR Model Development and V&V: Includes development, verification, and validation of baseline KENO, HELIOS, NEWT and ATTILA models for current ATR reactor applications and to support the possible conversion of the ATR to LEU under the RERTR program. This includes fuel cycle

management and neutronics support to core safety analysis, and limited development of capabilities for experiment analysis to the extent that experiment neutronics impacts the operation of the reactor overall. (Detailed ATR experiment design and analysis is ordinarily handled separately, as part of the workscope for each individual experiment series, and is not considered to be a part of the Core Modeling Update Project). Details of FY-11 activities and accomplishments in connection with this task are reported in Section 2 of this Annual Report. In FY-2011, these activities were almost exclusively focused on demonstrating feasibility of the HELIOS system as a new primary reactor physics tool to support core design and fuel cycle analysis tasks that are required for preparation of Core Safety Analysis Packages for each ATR cycle.

Task 3: ATRC Model Development and V&V: Includes development and application of baseline KENO, HELIOS, NEWT, and ATTILA models for support of ATRC validation experiments pertinent to the Core Modeling Update Project. This task also largely includes the development and application of new capabilities for rigorous sensitivity studies pertinent to uncertainty quantification in the new computational models. Details of FY-11 activities and accomplishments in connection with this task are reported in Section 3 of this Annual Report.

Task 4: Neutronics Validation Experiments: This task includes the performance and reporting of new validation experiments in ATRC and ATR (as feasible) that are pertinent to quality assurance of the new computational models. It supports development of apparatus and protocols for a standard set of neutron activation spectrometry measurements that can be used on a more routine basis in the future for code validation as dictated by evolving ATR applications. This task also includes collaboration with various other DOE and NSUF projects where there is mutual benefit in terms of new physics validation data. Currently these include a project funded under the NSUF to investigate the feasibility of various techniques for online neutron flux measurements in the experiment positions as well as a near-term experiment involvement involving the testing of a prototype LEU ATR fuel element in the ATRC. Details of FY-11 activities and accomplishments in connection with this task are reported in Section 4 of this Annual Report.

Task 5: In-Canal ATR Fuel Exposure Validation Measurements: This task is focused on development of a non-invasive method and apparatus for measurement of the isotopic composition of used ATR fuel elements to infer the burnup. The current workscope includes a series of scoping measurements conducted in FY-10, with ongoing data analysis through FY-11 and the first part of FY-12. It also includes the specification of a conceptual design for a permanent measurement system that can be installed in the fuel storage canal. Final design, construction and qualification of a permanent system will then be formally proposed for inclusion in the long-term scope of the Core Modeling Update Project. Details of FY-11 activities and accomplishments in connection with this task are reported in Section 5 of this Annual Report.

The leadership team for the ATR Core Modeling Update Project consists of a Principal Investigator, a Project Manager, and several senior co-investigators who are responsible for various key aspects of each task listed above. It is important to recognize that the ATR Core Modeling Update Project represents not only an investment in new technology. It also represents a key investment in the new generation of INL scientific and engineering staff who will, by demographic necessity, assume leadership roles in the overall ATR enterprise over the next several years. Accordingly, several students and early-career INL Scientific and Engineering staff members are also being proactively integrated into the effort, and this will accelerate in 2011 and beyond. The students supported by the project in 2011 included two from the University of Utah and one from the University of Texas. In the latter case the student earned his PhD degree in connection with the Modeling Update project during FY-11.

1.5 Overview of FY-2011 Accomplishments

The Core Modeling Update Project is expected to require 48-50 months to complete, and is targeted for full implementation in phase with the anticipated ATR Core Internals Changeout (CIC) in the 2014 time

frame. The project began during the last quarter of Fiscal Year 2009, and has just completed its second full year. Some key accomplishments in the first 26 months are briefly summarized below, along with a description of planned next steps in several areas during FY-2012 and beyond. Additional technical details are provided in the remainder of this Annual Report.

- Baseline HELIOS, NEWT, ATTLA, KENO, and MCNP models of ATR and ATRC are operational, demonstrating the basic feasibility of these code packages for their intended purpose.
- The initial demonstration-level HELIOS model of the ATR includes the capability to simulate fuel depletion and replacement. Informal cycle follow calculations beginning with Cycle 145A (August 2009 startup) were completed through the current (September 2011) cycle. These calculations will be continued and refined in 2012 with the objective of bringing the model current to the cycle being run in the third quarter of that year. The HELIOS methodology will run in parallel with the standard PDQ-based CSAP methodology thereafter. This will provide the basis for more formal acceptance testing and qualification of the core fuel cycle computational models and protocols in 2013 and beyond, with the goal of full conversion to the new fuel cycle model in time to support reactor startup after the CIC that is anticipated in the 2014 time frame.
- New experimental hardware was fabricated and measurement protocols were approved for the first planned set of flux validation measurements in the ATRC. The first four irradiations of this series were then completed in collaboration with the NSUF Instrumentation Evaluation project mentioned earlier. These measurements will continue through much of 2012 and 2013, with additional new experimental hardware being fabricated and introduced into the protocols along the way. Additional opportunities to collaborate with various planned experimental campaigns in the ATRC and ATR will be identified as the Core Modeling Update Project proceeds. Such opportunities are expected to include additional RERTR-related experiments in the ATRC and possibly a “depressurized” low-power run of the ATR itself.
- In-canal feasibility measurements for construction of a permanent fuel burnup validation system continued throughout the year. Results indicate that construction of a permanent measurement system is feasible. Data analysis for these measurements will continue through the first part of 2012. Conceptual design of a permanent system for burnup measurements was also completed in early 2011 and a proposal for construction of such a permanent system was prepared.
- Students and early-career INL Scientific and Engineering staff are being integrated into the effort as noted in the previous section. This will accelerate in 2012 and beyond for the reasons already noted.
- In-Canal ATR experimental fuel element burnup measurement feasibility studies completed in FY-10 and FY-11 have already produced some original scientific results, and have served as a very useful model for how the INL R&D organization and the INL Nuclear Operations Organization can positively and proactively work safely and effectively together to accomplish the larger goals of the INL as a whole.
- The adoption of the Studsvik Scandpower HELIOS code for ATR fuel cycle physics and fuel cycle analysis has significantly advanced the goals of the BEA Center for Nuclear Systems Design and Analysis, a formal collaboration between Studsvik and INL that was established in 2005 under the then-new INL Management and Operations Contract between Battelle Energy Alliance and the US Department of Energy.

2.0 HELIOS MODEL DEVELOPMENT FOR ATR CSAP AND FUEL MANAGEMENT APPLICATIONS

2.1 Evolution of the ATR HELIOS Model

Sam Bays (INL)

The ATR HELIOS model has undergone significant evolution since the first demonstration model was generated in connection with an unrelated project in September 2005 and subsequently incorporated into the ATR Methods Update Project at its inception in August 2009. Since then, multiple developers have made concerted efforts to modify and verify this root model in a manner that will make it suitable for performing ATR core fuel cycle analysis to support the preparation of Core Safety Analysis Packages (CSAP). During Fiscal Year 2011, these modeling efforts were consolidated to establish a common base model, Version 1. The original base model is considered to be Version 0. Figure 2.1 shows the hierarchy of model evolution from Version 0 to the consolidated Version 1.0 model and the current Version 1.1 beta model under development.

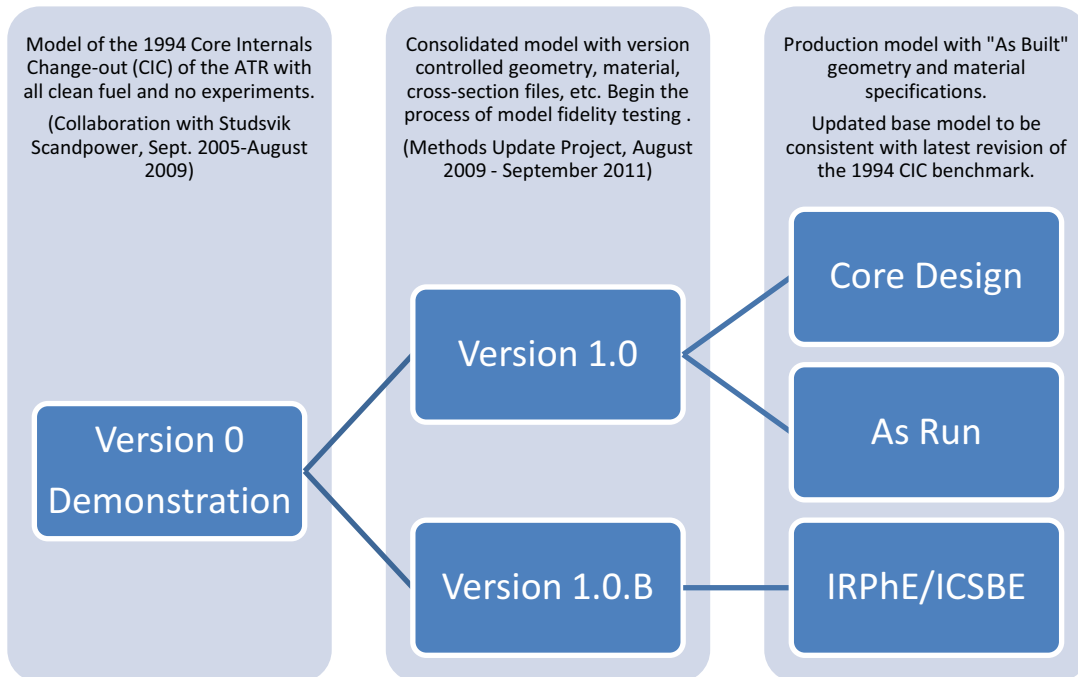


Figure 2.1. Evolutionary history of the ATR HELIOS model.

To move from demonstration to a production model with a software quality assurance pedigree, certain elements of software life cycle design have been adopted. As a starting point for discussion, we mention the waterfall model for sequential design implementation. Though we do not rigorously follow the waterfall design process, we have borrowed certain aspects of it to guide a graduated process to evolve the model from Version 0 to Version 1.1. In the waterfall model, an idea progresses towards a product following sequential completion of the following steps.

Requirements: We performed a rigorous review of ATR technical and regulatory design (CSAP) requirements and current best practices used by ATR Engineering as discussed in Section 2.2.

Design: HELIOS supports the parsing of model input into a short input and a “SET” or expert input. The intent of the SET input is to not expose the user to components of the model considered to be *set* and not subject to regular changes. The SET input file can be further parsed into hierarchies and catalogues of expert input that can be organized into a file directory system. We have taken this approach to morph Version 0 to Version 1. This allows for incremental upgrades to the base model contained in the SET Version 1 directory system in a way that seamlessly carries over to testing going on else-where in the project where the only changes necessary are with the short input. An example of this would be a change to the beryllium reflector geometry definition in the SET files by one developer. The developers performing core follow “As-Run” and benchmark calculations only need to provide the directory call to the reflector’s SET file in the same area of the short input where the cross-section file is called. Ongoing activities in the design process include:

- Develop safety analysis calculations for supporting ATR core design and safety assurance (i.e. CSAP).
- Mesh/angle/energy refinement and convergence studies.
- Generation of SET files describing experiments.
- Parsing the model into an As-Built model meeting current core specifications apart from a validation model that is current with the latest publication of the International Handbook of Evaluated Reactor Physics Benchmark Experiments (IRPhE) and International Handbook of Evaluated Criticality Safety Benchmark Experiments (ISCBE)^a.
- Geometry update of the reflector geometry description such that certain features do not lie on a current coupling interface between quadrants, currently a carryover of the Version 0 model.

Implementation: Currently, the Version 1 model has been established for the purpose of demonstrating experiment-independent core-follow capability for cycles 145A through 149B. Also, model adaptations are under active development for core design.

Verification (and Validation): The Version 1 model has also been preliminarily tested in accordance to the IRPhE ATR 1994 CIC.

Maintenance: All work currently being conducted with the ATR HELIOS model is currently stored on a version controlled central repository server. All production calculations are performed on a self-maintained computer system.

This approach to the production of a model satisfactory to ATR Engineering needs support the basis for the decision in late 2011 to adopt HELIOS as the ATR core design software of choice for ultimate replacement of the legacy software, PDQ, currently used for CSAP physics support.

2.2 CSAP Requirements vs. HELIOS Capabilities

Emily Swain (INL)

Several different types of physics analyses are performed to satisfy the ATR Updated Final Safety Analysis Report (UFSAR) requirements for each operational cycle. The analyses pertaining to the ATR core as a whole and specifically to the driver fuel are reported in the Core Safety Assurance Package (CSAP). Analyses pertaining to experiments are reported in corresponding documentation created for

^a All modeling work to date assumes that the core specifications are consistent with the IRPhE revision 0 record for the 1994 Core Internals Change-out (CIC). The IRPhE ATR 1994 CIC benchmark is now up to Rev 4.

each experiment. Taken together, this documentation provides DOE with assurance that the UFSAR requirements are being met for each cycle.

A major component of the CSAP documentation consists of physics data produced by the existing suite of codes associated with the diffusion code PDQ. The current effort being undertaken is designed to replace the PDQ physics analysis methodology with an improved methodology capable of calculating and analyzing data that is ultimately reported in the CSAP documentation. Experience gained in the first two years of the Methods Update project now supports a decision that the methodology associated with the HELIOS code will be a suitable replacement for the PDQ methodology presently in place.

In order to completely replace the PDQ physics analysis methodology, the HELIOS code system will need to be capable of representing the neutronics of each ATR cycle. Specifically, the new methodology must be able to track and deplete the driver fuel elements, control surfaces, and beryllium reflector. Also, the total power of the ATR can vary over the course of a cycle, and this must be accommodated in the computations. Reactor physics data such as neutron flux and local fission power must also be available to compare against component design criteria and predict component lifetimes that are dependent upon neutronic damage. From a practical perspective, the computer time requirements for all calculations defined in the CSAP protocol must also be compatible with the established time schedule for analyses required for a given cycle.

2.2.1 Lobe Power Prediction

Due to the design and operational features of the ATR, an extensive set of performance objectives arises from the basic CSAP requirements. The design of the ATR core allows for direct control of four corner lobes whose powers are very loosely coupled, essentially independent as a practical matter. These lobe powers are controlled through the placement of control surfaces and through the fuel distribution in the core. Thus, the methodology must be able to identify the lobe powers achieved when the total core power, fuel, and control surface positions are specified. This information is then used to iteratively predict the necessary control surface positions at various points in the cycle. Given the predicted control surface positions, the methodology must also be capable of accurately forecasting the lobe power associated with the center of the core over the length of the cycle. Due to the capability of a large variation in power distribution, predicted lobe powers at reactor startup also must be supplied so that the Log-N chambers can be properly positioned to provide appropriate instrumentation coverage during the approach to criticality.

2.2.2 Excess Reactivity Prediction

The physics analysis methodology must also predict the excess reactivity available in the core. This prediction ensures that sufficient fuel has been loaded into the core to reach the desired cycle length as well as that control positions are able to maintain a critical state while producing the required lobe powers for the cycle. The methodology must also provide a prediction of the critical shim positions at initial startup so that a comparison against the actual critical shim positions can be made. This comparison ensures that the core has been loaded as expected, that the fuel elements have been properly seated, and that a safety rod has not become stuck in the core. Sufficient excess reactivity must also be shown to be available to restart the operation of the core in the event of an unplanned shutdown.

2.2.3 Influence of In-Pile Experiments

A unique aspect of the ATR reactor is that it contains experimental positions located throughout the core which can affect the driver elements and other core components. Thus, the methodology must support experiment changes within the core models. Requirements associated with experiments include a

methodology to deal with a variety of complex geometries and materials. Experiments impose an additional asymmetric reactivity influence upon the ATR's already asymmetric clover-leaf power shape. The level of detail in a given experiment may far supersede what is necessary to capture the reactivity pull on the fuel elements. Therefore, it is current practice to perform some level of local smearing of verbose experiment features. Experiments often have axial variations, so the methodology must be able to approximately represent the effects of a three-dimensional experiment on the driver fuel, whether through a two-dimensional model that utilizes homogenization, through an explicit three-dimensional model, etc. Note that there are also capabilities that allow experimental movement through the center of the reactor core during operation, such as the hydraulic shuttle system and the motor-driven positioners. The model must also be able to appropriately represent the effects of these moveable experiments on the driver fuel.

The cycle being modeled must meet the requirements of the various customers that sponsor the experiments associated with each cycle. Thus, the requirements of the lobe powers, cycle length, and outage length specified in the Integrated Strategic Operational Plan (ISOP) must be met when performing ATR physics analyses. Experiment analysts have also requested operational restraints in the past, such as limits on the acceptable positions of the control surfaces. These requirements and constraints necessitate that the methodology allow the discretion of the user when selecting time step lengths and control surface positions.

2.2.4 Fuel Burnup Prediction

The methodology must be capable of a prediction of the burnup experienced by the driver fuel. Driver fuel isotopic data must be provided to the experimenters so that experimental results can be properly modeled. The methodology must also be able to store the isotopic data in support of fuel shuffling, experiment movement (e.g. use of the hydrolytic shuttle system) and control surface movement (e.g. insertion of a neck shim) experienced during the operation of an ATR cycle. The methodology must also support the rotational movement of the Outer Shim Control Cylinders (OSCCs).

2.2.5 Safety Coefficient and Scenario Calculations

The methodology must also support changes in the thermodynamic state of materials in the core. For instance, the ATR reactor is capable of performing both pressurized and depressurized operations, so both of these states must be capable of being modeled. Also, analyses must be able to perform branching calculations for determination of temperature coefficients (e.g. determine moderator, fuel, and void temperature coefficients) so that this information can be transferred to the tools used to analyze transient accidents.

To ensure the safety of the personnel, requirements that are designed to alert operators to unsafe conditions are in place. Comparisons between the lobe power indications, quadrant power indications, and temperature changes between the coolant inlet and quadrant outlets are used to verify proper instrumentation function^b. The criteria for acceptance of these comparisons are set based upon element power predictions determined through the use of several different scenarios. These scenarios utilize a variety of control surface positions and lobe power assumptions. In addition, the safe handling of fuel after a cycle is ensured through the use of a specified delay time before core unloading. This minimum delay time is established by the maximum element power giving the maximum fission product concentration and associated radiation field and decay heat that workers must contend with during an outage. Thus, the methodology must be able to predict element powers under a variety of core conditions.

^b Temperature measurements for these four outlet flow paths can be used to back-calculate the enthalpy rise (i.e., fission energy imparted to the reactor coolant) in each quadrant of the core, one lobe per quadrant.

2.2.6 Information Management

Although the fuel selection, control surface positions, and time steps are ultimately at the discretion of the user, it is important that the physics methodology provide the user with informative data that can aid in his/her decisions. Therefore, the methodology must maintain element records that provide sufficient data on the history of an element so that fuel element selection and shuffling can be supported. The historical data should include previous cycles, positions, powers, exposures, fuel content, manufacturing restrictions, and cumulative fission densities obtained during the lifetime of each element. Additionally, a database of new and recycled elements available for use in coming cycles must be available.

2.2.7 Peak Power Information

Additional requirements are specifically requested by the UFSAR. Most of these requirements are designed to protect the fuel elements from blistering or bowing during a transient by analyzing the enthalpy rise presented to the coolant over the axially-oriented hot stripe of an element. Limitations to specifications known as Effective Plate Powers (EPP) and Effective Point Powers (EPP) have been put in place to provide engineering margin to blistering and bowing accidents. These limits are based upon the maximum specifications identified in the core during the cycle at steady state conditions and the worst-case azimuthal power density gradient along a fuel plate.

The UFSAR explicitly defines many of the specification terms. It defines EPP as the EPP multiplied by the average axial peaking factor. It defines EPP as the total core power multiplied by the point-to-core average power density ratio at a point. The average axial peaking factor is defined as the average value of the normalized axial peak-to-average power density ratio over a fuel plate. These values are determined from a prediction that places each of the lobe powers at the maximum value allowed during the cycle. The traditional interpretation of these specifications has been presented in the equations below. These equations also introduce the use of an instrument error term that is specified by lobe and a plate restrictions term that is specified by plate.

$$\text{Power Ratio lobe} = (\text{Total Power}) (\text{Maximum Lobe Power} / \text{Nominal Lobe Power})$$
$$\text{EPP plate, time step} = (\text{Point-to-Core Power Density Ratio plate, time step}) (\text{Power Ratio lobe}) / (\text{Instrument Error lobe}) / \text{Plate Restrictions, plate}$$
$$\text{EPP plate, time step} = (\text{EPP plate, time step}) (\text{Axial Peaking Factor element, time step})$$

To comply with these EPP requirements, the replacement methodology must be able to calculate the azimuthal power density trend along a plate, which is highly sensitive to OSCC position, and calculate the axial peak-to-average power density ratio over a fuel plate. Traditionally, the axial power density distribution has been calculated through the use of empirical equations. The replacement methodology can utilize these empirical equations to provide a three-dimensional answer or substitute the equations with a different calculation, if appropriate.

2.2.8 Peak Exposure Information

UFSAR limitations have also been placed on the maximum fission density experienced in an element, so the methodology must be able to track the cumulative fission density experienced by an element and predict the fission density of each element at the end of the cycle. A restriction upon cycle length is then put in place that utilizes both reactivity and element fission density data. The fission density calculations also enable burnup rate calculations by element position in the core, which is useful during the element selection and placement process. A prediction of the recyclable elements available after the completion

of a cycle is also possible. Typically, surveillances must be performed on the actual center lobe powers experienced during startup and the initial xenon peak to ensure that a fission density limit will not be violated at the end of the cycle. This is due to the large uncertainty present in the current methodology when predicting center lobe power.

The current methodology utilizes several modeling assumptions that require adjustments to the results produced directly from PDQ. These adjustments account for the historical biases and uncertainties in the model, the three-dimensional effects that have not been included in the two-dimensional model, and the modeling bias introduced by the use of discrete OSCC positions to represent the continuous adjustment of the actual positions used to control the ATR. Biases similar to these are expected in the replacement methodology to at least some extent, although smaller. Thus, the methodology must account for these effects, incorporate necessary adjustments into the methodology, and allow for updates obtained from comparisons to operational data, such as reactivity worth measurements.

2.2.9 HELIOS Capabilities

The 2-D neutronics code that serves as the backbone of the proposed methodology change is the HELIOS code system. This lattice code, which utilizes transport theory, has a proven record of accurately modeling the depletion of commercial reactors, has an up-to-date isotopic library that has been adjusted specifically for use with the ATR reactor, and has active commercial support from the supplier. The code is able to analyze the entire core without the use of reflective boundaries, and can be run on a modern computer in a very reasonable amount of time.

The HELIOS code exhibits many important characteristics necessary for proper modeling of the ATR core. The geometry construction within the code is very flexible, so it is able to model the driver fuel elements and complex experiments in great detail. It utilizes a hierarchical system of embedded geometry structures (enables experiment swapping and fuel shuffling) and subsystems (for grouping structures into neutronically unique regions and then coupling among these regions) which allows for model modularity, configuration control and user friendliness superior to other relevant physics simulation software. The HELIOS code also utilizes material definitions, temperatures, and densities that can be easily overlaid on a complex geometry. The adaptable nature of the overlays provides a simple method of modeling experiment movement, control surface movement, and kinetic effects. It has been shown that discrete OSCC movement can be easily represented through the use of material overlays. It is also possible to rotate the entire OSCC component to a precise position, although this does increase the computational resources needed.

The user interface allows for variation in material, temperature, density, power, and time step length for each time step modeled. These features allow simple manipulations of the control surfaces and power levels. Straightforward isotope tracking and storage allows for fuel shuffling, depletable neck shims and safety rods, and even experimental position changes from cycle to cycle. The set of isotopes used by HELIOS presents a more complete picture of the make-up of materials, unlike PDQ which must use a mock lumped fission product isotope to properly account for all of the neutronic effects experienced by the ATR core.

Although most of the depletion characteristics can be easily modeled by HELIOS, the poisoning of the beryllium reflector may be the exception. Currently, HELIOS does not support beryllium depletion. Due to the large volume of beryllium and the complex geometry of the reflector blocks, the computational resources needed by HELIOS to deplete the reflector may become prohibitive. However, the major effect of the beryllium depletion is a cumulative effect from the buildup of helium and hydrogen trapped within the blocks. Since the buildup during a single cycle is minor, a tool independent of HELIOS can be used to update the material specifications, as needed. The solution to this problem will become apparent as

options are explored, code capabilities are evolved, and computational resources naturally increase with the passage of time. In any event, a methodology can be developed to properly deplete the reflector.

A potential challenge for the HELIOS code is the axial variations present in experiment test trains. The same issue exists with the use of the 2-D PDQ code to perform cycle analyses. An approach similar to that used with PDQ could also be used in the HELIOS-based methodology. A model of the RZ plane was created to represent a single lobe of the ATR core. The use of an RZ model could allow the user to create a homogenized experiment representation that could be incorporated into the model of the XY plane. Another solution to this problem may be through the use of an experiment model in the MCNP or ATTILA codes. Note that MCNP is already in use for neutronic analyses performed for the experiment. Although the methodology has not been established, it is anticipated that an approximation of the experimental effects can be developed that will fulfill the UFSAR requirements.

The output provided by the HELIOS code includes all of the data necessary to calculate the specifications required by the UFSAR. The post-processor associated with HELIOS enables data collection from each time point as well as time-averaged data. The areas over which data is averaged and/or totaled can be explicitly defined by the user. It can provide eigenvalue measurements, flux measurements, power measurements, and isotopic make-up for each defined area. HELIOS will output the volumes and initial heavy metal mass of these areas as well. Since HELIOS is a lattice code, microscopic and macroscopic cross sections for the defined areas can be retrieved from the output. The post-processor also allows the user to create formulae that can be used to calculate the various specifications described in the UFSAR. Given the appropriate geometric definitions, it is expected that the output from HELIOS can provide all of the physics data needed for the CSAP documentation.

Although the foundation for a replacement methodology based on the HELIOS system has now been laid, there are some details that remain to be thoroughly investigated. It can be expected that additional areas of concern will be discovered. However, the HELIOS code has been able to fulfill requirements where other codes have failed and it is expected that HELIOS will be able to fully replace the current physics analysis methodology. In addition, it is reasonable to expect that the data quality of a HELIOS-based methodology will surpass that of the current methodology. Improved accuracy in predictions could greatly increase the utility of the ATR reactor by reducing the use of conservative assumptions and decreasing the inaccuracy of fluence predictions on the experiments.

2.3 Description of the ATR HELIOS Model

Sam Bays (INL)

2.3.1 Model Modularity

The Version 0 ATR HELIOS model contained a 388 line short input and a 4268 line SET file making work with the model unwieldy. This file has since been parsed out into a directory structure enabling a modular, almost object oriented, structure and functionality. This is a significant improvement for training as well as enabling in-parallel model development efforts by different developers.

HELIOS enables division of the problem into geometric regions called structures. These structures can be lumped into sub-systems of shared neutronic importance within the model (e.g., an ATR lobe) to make the complete system. In this way, the ATR model geometry is essentially a large jig-saw puzzle of connected polygonal structures to comprise the entire system. The sub-system approach allows for current coupling between structures. No sub-systems are currently used partly due to the fact that the structures themselves are sufficiently large to be considered a neutronically unique region.

The sub-system approach also allows for repetitive geometry without requiring a fixed mesh, e.g., triangular or square pitch is not mandated for repetitive geometry. This modularity allows for relatively simple swap-in/out of one structure for another. An example of this could be swapping in one experiment for another within a given flux trap. Another example could be replacing any given fuel element (19 plates/element) with a new element design that has 21 plates/element.

Two requirements must be respected. One, the outer connecting nodes (i.e., intersection of two line-segments of a structures polygonal shape) of the new structure must be identical to the original structure. In other words, the outer shape of the flux-trap cannot be changed or it would not fit into the jig-saw puzzle that is the entire system. However, the internal nodes can be changed to construct an experimental geometry. Two, the structure (or sub-system) must be neutronically unique such that the angular quadrature of the current coupling to adjacent puzzle pieces is still valid.

2.3.2 Material Overlays

HELIOS enables hierarchical overlaying of material (composition, temperature, density) definitions from the system-level down to the individual flat-source-region. This allows for simulation of shuffling and control material insertion/removal at a mesh-by-mesh fidelity. For example, previously, the OSCC's were rotated using a geometry option that rotates the OSCC mesh within the greater core mesh. HELIOS does not allow for multiple core meshes during a given depletion calculation. Therefore, the previous OSCC rotation method required a new HELIOS calculation for every new core state, such as OSCC rotation or neck-shim removal. The new method keeps the mesh scheme fixed but with much greater azimuthal discretization of the mesh to accommodate up to 3.75° of rotation^c. Rotation is then accomplished by overlaying the absorber material, Hafnium, into the appropriate meshes for each new core state with a unique OSCC rotation. The Hf overlay method has also been implemented in the model to move each of the 24 neck shim and regulating rods independently. The drawback of this method is the potential need for high spatial mesh to accommodate very small drum rotations. However, it was found that a significant difference in the critical eigenvalue results from the change in drum meshing. These results will be discussed in Section 2.4. Figure 2.2 shows the change in OSCC definition from Version 0 to Version 1.

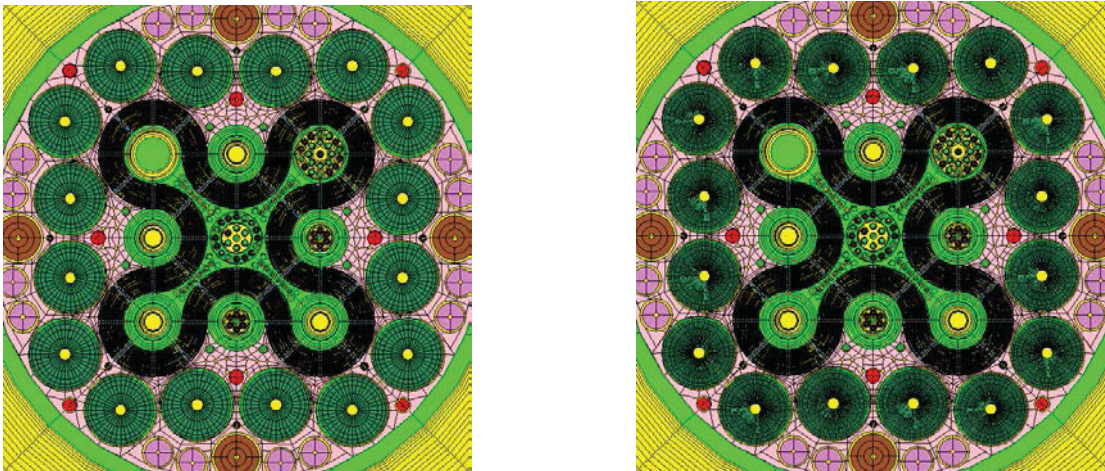


Figure 2.2. The Version 0 and Version 1 models (Left and Right, respectively) configured to represent the IRPhE ATR 1994 CIC.

^c The Version 0 drums had 36 azimuthal angles of discretization.

2.3.2 HELIOS Database Feature

The fuel shuffling and isotopic tracking methodology has been updated to better meet the needs of performing “As-Run” calculations, i.e., core-follow. Instead of using an i/o interface to transfer and store isotopic information to the ATR model, the data corresponding to each fuel-element are stored in a Hermes data-base file. The file handle given to this Hermes file contains the location along the ATR fuel serpentine, fuel element serial number, core cycle number and beginning-of-cycle (or end-of-cycle) state. This file system is then used to track the entire life-cycle of a fuel element either in the ATR or the ATR canal facility. Currently isotopic data for irradiated fuel elements, where the core calculation is performed in PDQ, is post-processed from PDQ and manually input (with the help of an MS-EXCELL spreadsheet) into a HELIOS input containing the geometric data for a single infinitely reflected fuel element. This single-fuel-element calculation calculates the k_{inf} for the fuel element and then generates the Hermes file using the HELIOS dump feature. Fresh fuel elements can be generated in this manner or defined separately using a default composition in the ATR model itself. Radioactive decay calculations in the canal are also performed using the single-fuel-element model. HELIOS allows for pure decay but forces at least one time-step to be performed with finite power, and a minimum of two flux calculations. The work-around for this was to perform the decay calculation then deplete for one hour at ~40 Watts. All single-fuel-element calculations result in a dumped Hermes file to be loaded into the main ATR model. Following full core cycle depletion, the 40 fuel element compositions are dumped again into new Hermes files representing the end-of-cycle.

During the course of proofing this database management process, we found that the currently released version of the HELIOS pre-processor, AURORA, had insufficient array allocation for the number of material definitions required in our ATR model. This was fixed by receiving an alpha version of AURORA from Studsvik with the array allocation increased.

2.4 Current Calculation Results

Sam Bays (INL)

2.4.1 Critical Eigenvalue Calculation

Since HELIOS is a two-dimensional code, it was necessary to characterize the reactivity worth of the axial reflection in the 2D model. This was done by starting with the available three-dimensional model, written in Monte Carlo Nth Particle (MCNP), which is distributed with the IRPhE ATR 1994 CIC benchmark. MCNP is a continuous space angle and energy software based on the Monte Carlo method for modeling radiation transport. This 3D model was first converted to use the universe feature in MCNP to allow the top and bottom-most surfaces were drawn in to +/- 0.5 cm about the fueled portion's axial mid-plane. The vacuum boundary condition for these surfaces was also changed to specularly reflective.

The IRPhE documentation recommends the MCNP model for verification purposes only as a template for a user to develop his/her own validation model. Still, the MCNP model was generated at INL and its pedigree is well characterized. In fact, a modeling error was detected in the MCNP model regarding the position of the regulating rods that is not documented in most recent revision of the IRPhE documentation. In the benchmark, the regulating rods are fully withdrawn. However, the MCNP model has these two rods halfway inserted. Furthermore, the ATR neck-shim and regulating rods have an aluminum follower that trails the hafnium poisoned annulus as the poison section is pushed out of the core by drive mechanisms beneath the core. The MCNP has this aluminum annulus modeled as water as opposed to the mostly aluminum follower (see Figure 2.3). These geometry errors were corrected. Table 2.1 shows the critical eigenvalue of these model modifications. Note that the difference between the as-distributed IRPhE model and the IRPhE corrected model is about 0.16%, equivalently ~\$0.25 assuming a

$\beta_{\text{eff}}=0.0065$, which is the approximate worth of one regulating rod, as should be expected. Also note the change made upon the model to assign the entire geometry to a universe had zero impact on the k-eff. The conversion of the 3D model to a 2D axially reflected model was 3.41%, equivalently \$5.24 for the assumed beta.

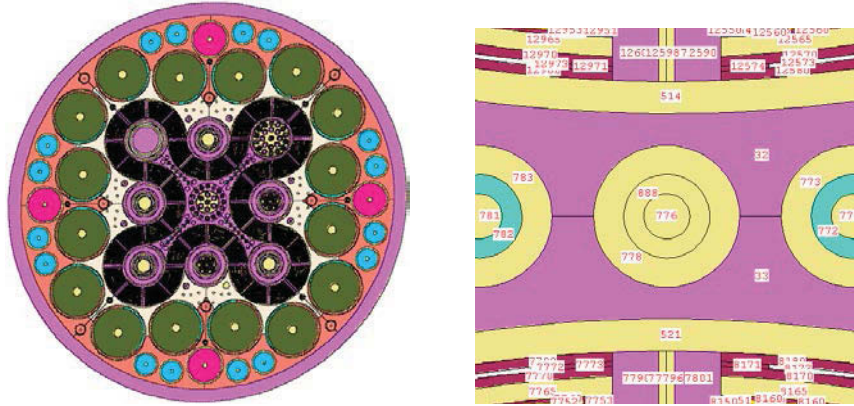


Figure 2.3. IRPhE ATR 1994 CIC MCNP model (L), South-West regulating rod taken just below fueled mid-plane (R). Cell 888 should be the same material as the neck-arm which is the purple color not water which is the tan. This modeling error in the IRPhE distribution was corrected for this work.

Table 2.1. Critical eigenvalue reported by MCNP5 code for conversion from a 3D to 2D model.

<u>Case</u>	<u>k-eff</u>	<u>STDEV</u>	<u>Description</u>
IRPhE	0.99935	0.00014	As distributed
IRPhE corrected	1.00096	0.00014	IRPhE model with corrections
With Universes	1.00096	0.00014	Corrected IRPhE model with universes
Two Dimensional	1.03565	0.00014	3D universe model converted to 2D

2.4.2 Versioned Model Benchmark Comparison

Given the added number of OSCC azimuthal meshes to Version 1 over that of Version 0 it is important to re-baseline the Version 1 model against the 1994 CIC. Table 2.2 shows the 2D critical eigenvalue reported by the MCNP 2D model versus the Version 0 and Version 1 HELIOS models. Even though the exact pedigree of the HELIOS geometry and compositions is not known, the relative error between the

Rev. 4 MCNP 2D model and the Version 0 HELIOS model, believed to be Rev. 0, is about 0.16% or equivalently \$0.24. The relative error between Version 0 and Version 1 is 0.22% or equivalently \$0.34%. This means that the total discrepancy between codes and models is roughly \$0.59 (the value of about two neck-shims). These results are promising given the HELIOS model representation of the ATR 1994 CIC benchmark has not been rigorously checked by any current or recent member of the ATR Modeling Update Project. However, it is interesting to note that the addition of much finer azimuthal discretization of the OSCC's resulted in such a large increase in predicted reactivity worth. This has prompted further space, energy and angle refinement sensitivity studies to determine the true model fidelity.

Table 2.2. Critical eigenvalue reported by HELIOS compared to MCNP 2D case.

<u>Case</u>	<u>k-eff</u>	<u>Description</u>
MCNP 2D	1.03565	2D IRPhE MCNP model
Version 0	1.0373	Version 0 HELIOS model
Version 1	1.039605	Version 1 HELIOS model

Note: The MCNP model is assumed current to Revision 4 of the IRPhE benchmark. The overwhelming majority of the HELIOS geometry was made at about the same time as Revision 0 but it is not explicitly known to be a valid model of the benchmark.

2.4.3 As-Run Results

As an initial approach for physics testing of the HELIOS code to confirm its capabilities for modeling the ATR, we performed a set of experiment-independent depletion analyses for the ATR cycles that have been run since the inception of the Modeling Update project in August 2009. To do this we used operational log data for OSCC, neck-shim pattern and lobe-power measurements by the N-16 detection system. This data is recorded by ATR Operations on an hourly basis. We created an MS-EXCEL spreadsheet for analyzing this data. The spreadsheet consists of a list of logical tests for binning the hourly data into discrete core-states and burn-steps. Each core state represents a significant change in core control configuration or lobe power level. A core state is used to establish the flux distribution and neutron spectrum that exists over a given burn-step. The main thrust of these “As-Run” calculations was to generate a short input for each cycle of interest (Cycle 145A1, Cycle 145B1, Cycle 146A1, Cycle 146B1, Cycle 147A1, Cycle 148A1, Cycle 148B1, Cycle 149A1 and Cycle 149B1). The important information necessary to generate the short input for a given cycle is: OSCC rotations (discretized into 3.75° increments), neck-shim pattern, and power level for each state. Also, required is the drum mapping of core states to burn-steps (i.e., a burn-step represents the amount of burnup that the fuel experiences while in a given core state).

Figure 2.4 shows the k-eff and burnup results for all As-Run cycle depletions. In the figure, every red circle represents a HELIOS transport calculation to be performed. As can be seen in the k-eff trends, the Version 1 model with no axial buckling correction to the calculated eigenvalue is consistently close to the critical eigenvalue reported by the Version 1 ATR 1994 CIC HELIOS model. The authors of the Version 0 model had determined an axial geometric value of $B_g^2=5.33 \times 10^4$ as a correction factor to give the benchmark model a k-eff near one. Using this value, we also found that the As-Run calculations were near one.

An important caveat must be brought forward at this point. Though these calculations currently have the correct OSCC, neck-shim and system power levels for each core state, the Version 1 model, by intent, is still lacking experiment design features. Experiments account for a non-dismissible reactivity component and power sharing in the ATR. Their absence may explain why the reactivity curve near end-of-cycle

tends to trend up despite the fact that fuel fissile depletion and fission product poison accumulation should cause a general downward trend. It should be noted that towards the end-of-cycle, the OSCC drums typically tend to be rotated outward at a rate faster than earlier in the cycle. This is why there are so many short burn-steps clustered together in most of the cycles plotted in Figure 2.4. This rotation likely would have been to compensate for experiment depletion in various flux traps. Since in this initial test the flux traps were modeled per the 1994 CIC configuration intentionally, rotation of the OSCC's out near the end of cycle would result in a positive reactivity insertion artifact. This artifact should disappear as the as-auilt experiment configurations for each cycle are added to the Version 1 model.

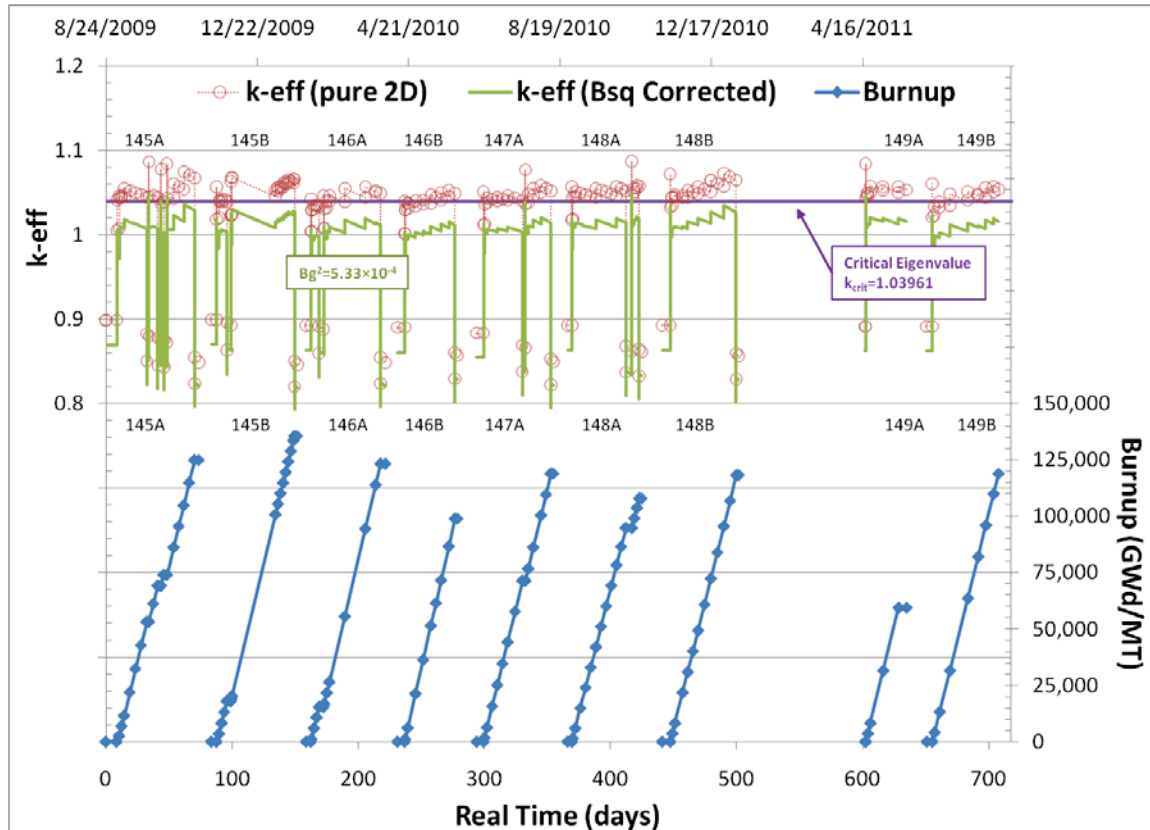


Figure 2.4. k-eff and burnup trend for current As-Run Version 1 models. (Note: Experiment locations such as flux traps are defaulted to the ATR 1994 CIC core in order to assess only the depletion and fuel shuffling capabilities of the HELIOS system, independent of reactivity variations that result from having a different set of experiments in each cycle.)

Finally, it should be noted that the isotopic data transferred from PDQ to represent fuel elements that were in the reactor prior to Cycle 145 contains only a few explicit isotopes. These are the significant isotopes of uranium and plutonium, and a few neutronically important fission product isotopes such as Xe-135, Nd-147, Pm-147, Pm-148, 148m, Pm-149, and Sm-149. All other fission product information is contained in a lumped fission product model that is macroscopically depleted in PDQ. Therefore, the negative reactivity worth of these lumped fission products from assemblies previously irradiated prior to Cycle 145A1 is not represented in the HELIOS as-run calculations.

2.4.4 Model Implementation Considerations

Experiment Design: Since HELIOS is a two-dimensional code, a methodology needs to be established for determining the correct axially averaged composition and dimension of features within experiment locations. In the current PDQ methodology, a reactivity equivalency strategy is used. We could adopt this strategy but refine it to model experiments to much higher geometric detail than is currently done with PDQ.

Fuel Element Design: Another model refinement will be to correctly model the “YA” elements when and where they are used in a cycle. YA elements have no fuel material in Plate 19 and are used near the end of the Be reflector lifetime to minimize exposure to the thin ligaments of Be separating the OSCC’s from the serpentine fuel. They can also be used at any time to reduce local reactivity and power peaking in any given location in the serpentine.

Beryllium Depletion: The current version of the HELIOS code does not model Beryllium transmutation chains. However, the large volume of the ATR core occupied by the reflector leads to a large negative reactivity effect as neutron poisons are generated from Beryllium depletion. The reflector Beryllium depletion is modeled in the current methodology with PDQ. We have yet to determine if the HELIOS code needs to be updated to accommodate Beryllium depletion. Alternatively, the reflector could be depleted using an external code, such as Origen-S, and the compositions updated prior to the next cycle’s core design calculations. This is considered acceptable given the small reactivity effect per cycle. The Beryllium depletion reactivity decrement is a cumulative effect over many cycles of operation.

Model Refinement: Given the large reactivity worth discovered by changing the azimuthal mesh of the OSCCs, we have undertaken an effort to explore mesh-refinement in the fuel plates to ensure enough detail is provided for supporting “hot-stripe” evaluation. We are also planning to evaluate quadrature used in the current coupling of structures, energy group structures, Collision Probability versus Long Characteristics. All results reported here were for the Collision Probability method. The next section describes the current model refinement implementation to ensure that no experiment irradiation facilities are cut by line-of-symmetry currently used for current coupling of structures and/or sub-systems.

2.5 Geometric Refinement Implementation

Doug Crawford (INL)

The ATR-HELIOS model received from Studsvik required changes to be made to the geometry. The changes to the ATR-HELIOS model geometry will improve the ability to model experiments, make routine changes of materials in and out of the ATR and will improve the overall accuracy of the ATR-HELIOS model. The reason that the geometry changes improve calculation accuracy is because the current coupling across the center of the circular-cylindrical-system (CCS for short) split across 2 structures (structure = STR in the HELIOS code language) is not the same as modeling the full CCS in one STR. For fuel-bearing CCS’s, it is not even close. The current ATR-HELIOS model makes it difficult to put any experiment in the reflector positions i.e. I-positions, because it would require construction of two half-experiments and then piece the two of them together with a connection operator (CNX operator), which is not advisable, either. After reviewing the ATR-HELIOS model from Studsvik, the geometry changes that would be necessary to remedy the issue are: I, B and A-position changes as well as the N-16 positions. The N-16 ports are used to back calculate a flux value based on the ^{16}N activity measured.

To show the changes to be made to the ATR-HELIOS model a series of figures have been created. Figures 2.5 through 2.10 show pieces of the ATR-HELIOS model, where changes made to these specific pieces will increase the fidelity and accuracy of the ATR-HELIOS model. These pieces of the ATR shown in Figures 2.5 through 2.10 are STRs in the current ATR-HELIOS model. Each figure is taken from the ORION viewer (ORION is software that is part of the subset of programs within the overall HELIOS software).

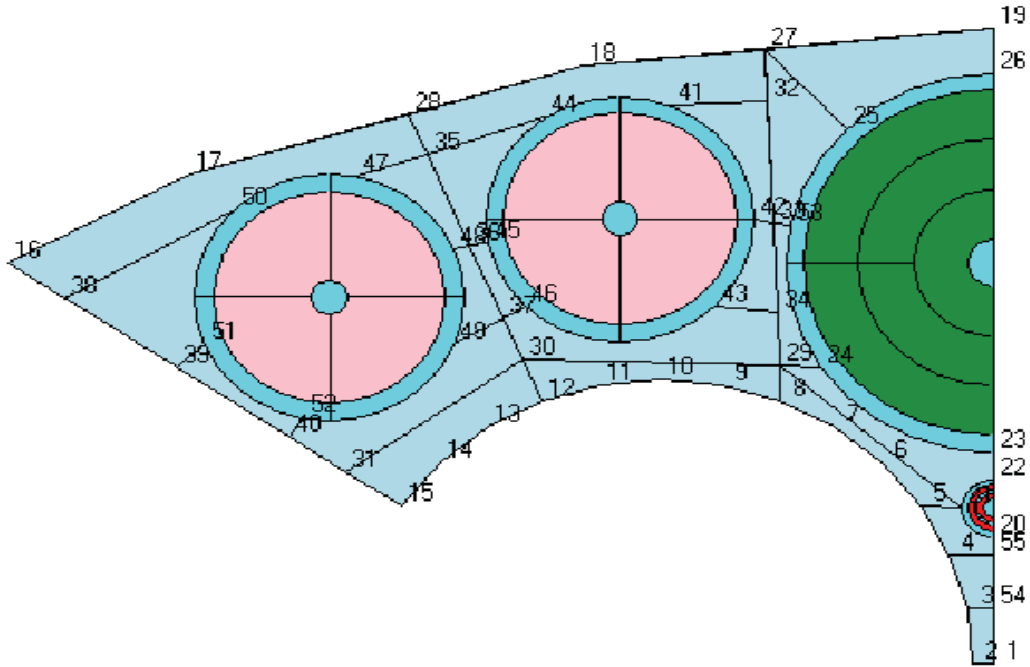


Figure 2.5 Left structure of the ATR HELIOS model showing the I-position and N-16 port cut in half

Figure 2.5 is a picture of a STR that represents a section of the beryllium reflector of the ATR. The numbering on the figure is the node labels that describe and carve out the non-CCS regions of the STR and the STR periphery. This STR is the upper left beryllium reflector with two medium I-positions, half of the N16-port and half of a large I-position imbedded in to the STR. The cut-in-half circle in green is half of the large I-position, or half of the large I-position CCS. The red and turquoise half circles are half of the N16-port CCS.

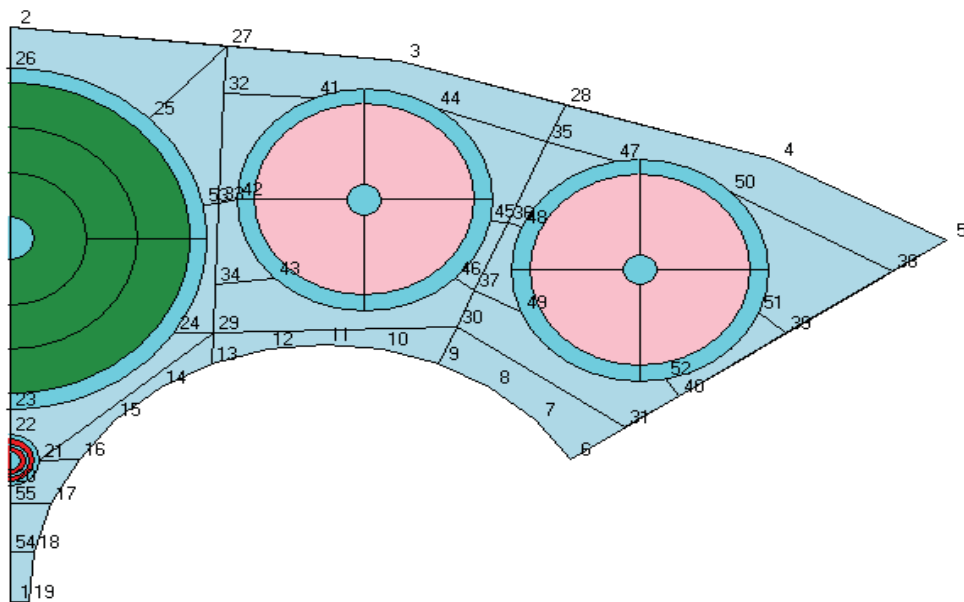


Figure 2.6 Right structure of the ATR HELIOS model showing the I-position and N-16 port cut in half

Figure 2.6 is the mirror reflection of Figure 2.5. Figure 2.6 also shows the node labels that define this STR. Figure 2.6 represents the other half that needs to be merged with the STR in Figure 2.5. Both STRs in Figures 2.5 and 2.6 sit on top of the outer shim control drums at the north, south, east and west of the ATR.

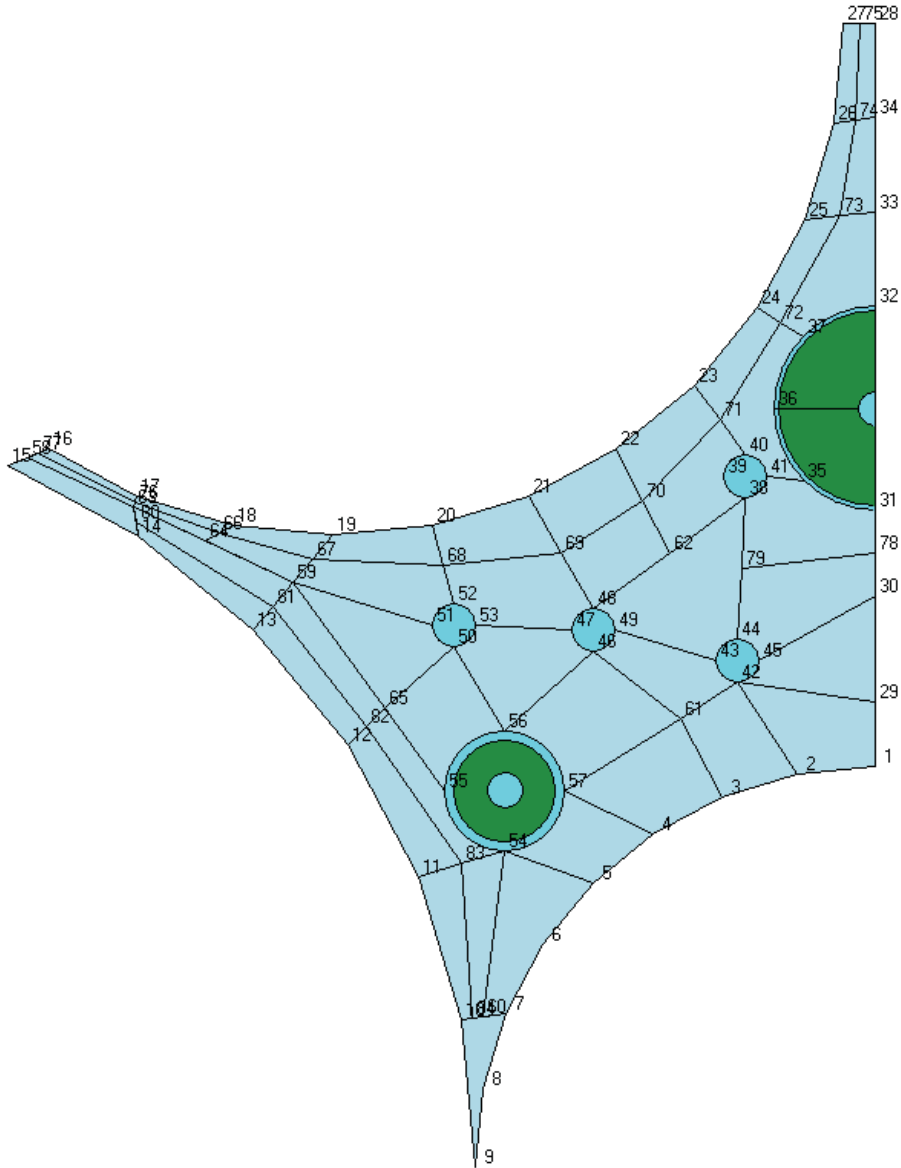


Figure 2.7 Left inner beryllium reflector with half of the large B-position

Figure 2.7 is the left inner beryllium reflector with half of a large B-position CCS, water cooling channel CCSs and a small B-position CCS. This STR sits between the outer shim control cylinder and the north, south, east and west flux traps on the left hand side. The green cut-in-half CCS is the large B-position CCS that needs to be merged together.

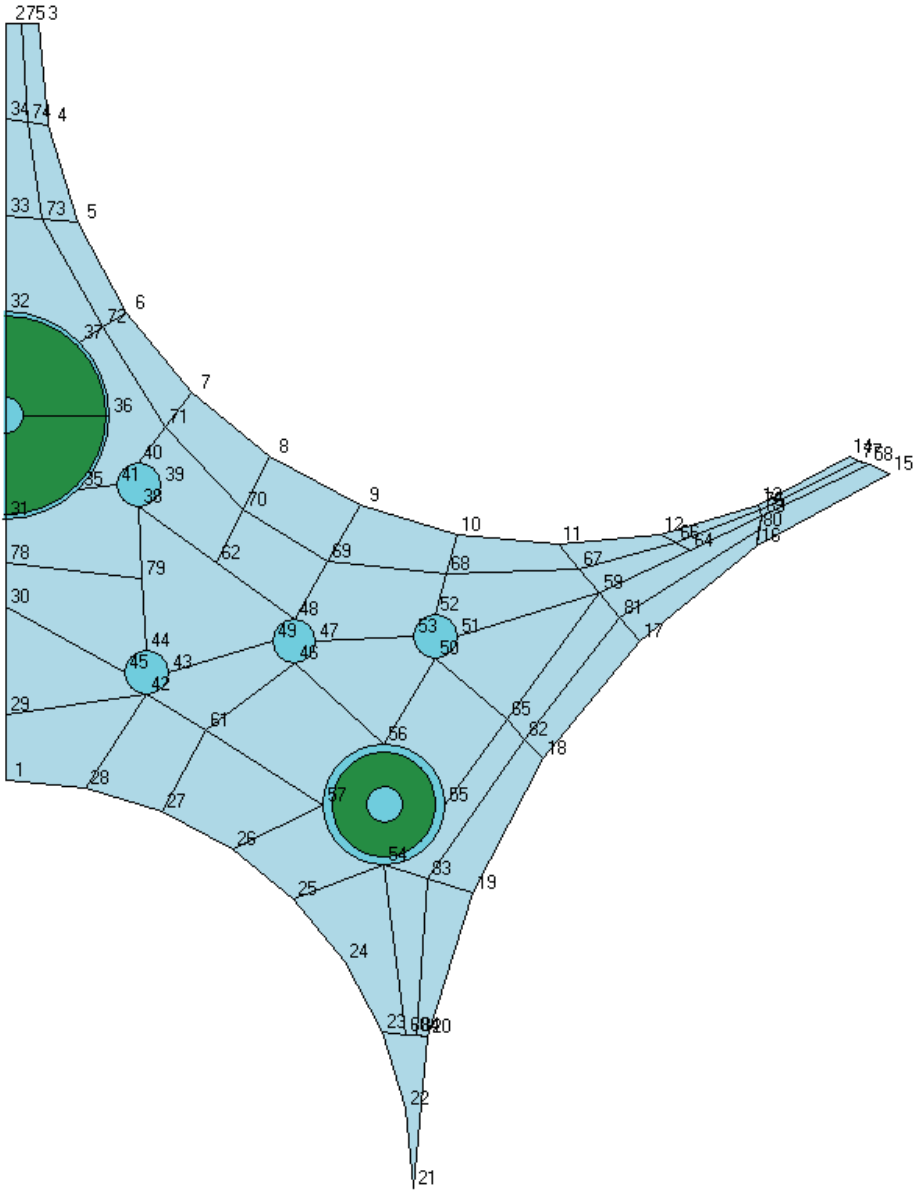


Figure 2.8 Right inner beryllium reflector with half of the large B-position, mirror image of Figure 2.7

Figure 2.8 is the mirror image of Figure 2.7 and it contains the other half of the large B-position that will be merged together. This STR is the right half of the beryllium reflector that sits between the outer shim control cylinder and the north, south, east and west flux traps.

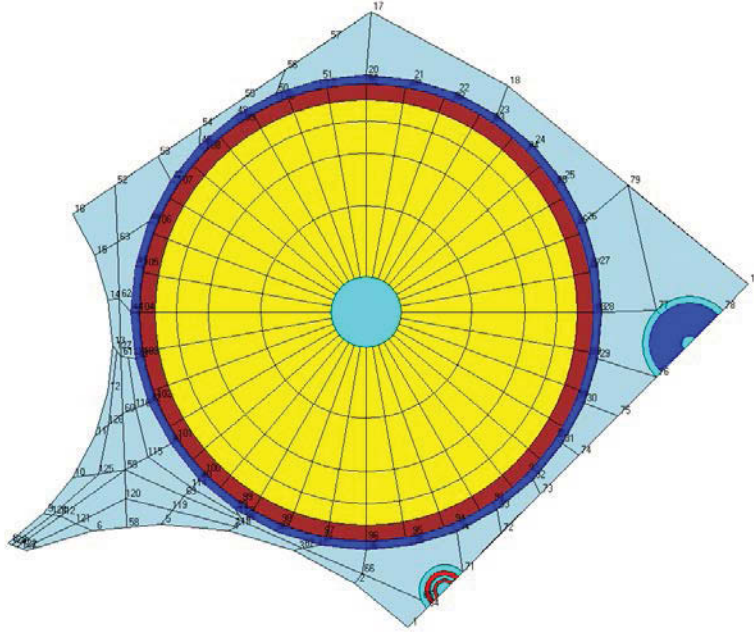


Figure 2.9. Beryllium reflector with outer shim cylindrical control, half N16-port and half small I-position

Figure 2.9 is the STR with the outer cylindrical control shim, half of a N16-port and half of a small I-position within beryllium reflector.

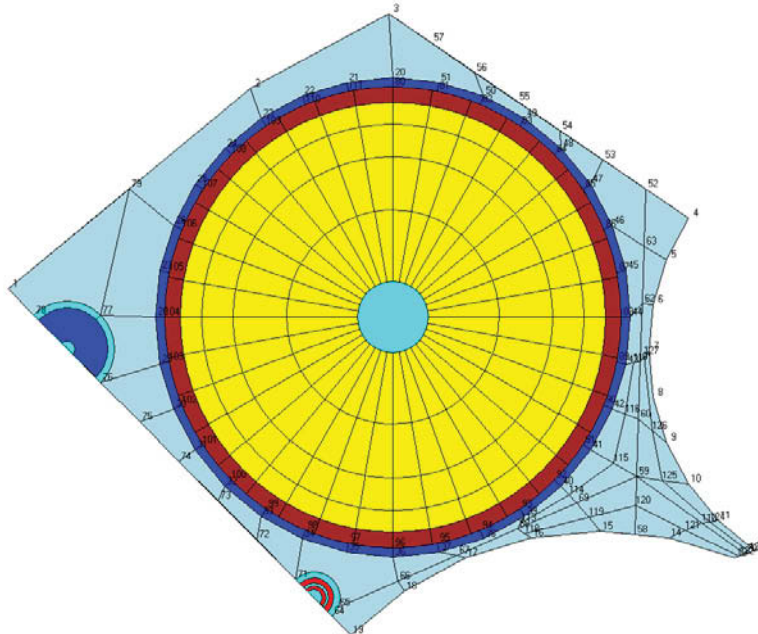


Figure 2.10. Beryllium reflector with outer shim cylindrical control, half N16-port and half small I-position, mirror image of Figure 2.9

Figure 2.10 is the mirror image of Figure 2.9 and contains half of a N16-port and half of a small I-position.

To merge the two half CCSs in Figures 2.9 and 2.10, the OSCCs will need to be cut out of the STRs and two new STRs will need to be created: 1st STR that contains the full N-16 port CCS and a 2nd STR that contains the small I-position CCS. In the next section the process of refinement is outlined with figures to show the steps of the process of merging the structures shown in Figure 2.5 and Figure 2.6 to make the large I-position CCS a single CCS instead of two halves.

2.5.1 Geometric Refinement Method for Baseline HELIOS Models

The process to knit one half to the other half (shown in Figure 2.11) is laborious and requires careful attention to detail due to the nature of the HELIOS code and the ATR-HELIOS model. The reasoning behind the process to merge existing STRs together instead of creating a new ATR-HELIOS model is: to take advantage of the work that Studsvik already produced (to avoid reinventing the wheel so to speak) and given the time frame to complete the modeling it seemed to be quicker to use the existing ATR-HELIOS model. The flexibility of the HELIOS software allows a change like; merging two STRs together is because a new STR or subsystem made of STRs can be connected to the existing ATR-HELIOS model and thus creates an improved version of the model. A general process to make the STR changes to improve the HELIOS model is outlined below:

1. Isolate the two halves to be merged together (there are 3 pairs of ATR STRs that need to be merged and reconnected to the model) into a new input file, this requires reading through the ATR.inp and ATR.set files to locate the name of the STR and the parameters (PAR in HELIOS code language) associated with the STR.
2. Determine the nodes that will need to be removed, merged or created to define the new STR or STR's from the two halves
3. Re-mesh and renumber the nodes according to the new periphery of the new STR, also in this step make sure to renumber all of the interior nodes as well and make sure the names of the non-CCS regions are named the same as the original material assignment name
4. Get all of the CCS regions, instead of half of them into the new structure
5. Iterate over steps 1-4 by following the error messages from AURORA and/or ORION (subset of software within the HELIOS software) until input file is error free
6. Once the input file is error free, open up the ORION viewer and look at the .hrf file corresponding to the input file to correct any visual/user mistakes AURORA did not catch, i.e. a node assignment is incorrect or a radii of a ring in a CCS is incorrect due to user-input error
7. Once the new STR or set of STR's is error free and matches the geometry of the two merged pieces, take the new STR and connect it back into the overall ATR-HELIOS model with a new CNX operator and run the new version in HELIOS. If the correct parameters are used to define the new STR it should fit into the ATR-HELIOS model if not, then review steps 1-6 again until the new STR/subsystem fits.

The reasoning behind making a new input file via this method is to be able to view the new STR or subsystem in ORION, before trying to connect the new STR/subsystem into the ATR-HELIOS model. ORION is a subset of the HELIOS software that allows the user input to be viewed, which Figures 2.5 through 2.10 are generated by ORION. ORION is not a GUI, it allows the user to see what was created in an input/set file combination. Before an input/set file can be seen in ORION the files must be read by AURORA (error free) and then if the input/set file is error free in ORION, then a graphic of the input can be seen. Seeing (in ORION) the input of the new STR/subsystem and comparing it to the current STR's in the ATR-HELIOS model provides the visual-user input check that the new STR/subsystem needs to be

able to connect to the ATR-HELIOS model. This process requires a visual check that the new STR/subsystem has similar dimensions as the old STR because it is very easy to make a user error due to the fact that AURORA will allow any geometry the user can define. The problem arises when a “strange but error free” geometry file from AURORA is then processed by HELIOS will crash because the geometry does not follow the “clockwise from the north rule” HELIOS uses to calculate the neutron current (see the AURORA/HELIOS methods pdfs for STR and CCS operators). The final check to make sure the new STR fits is to connect the new STR/subsystem with a new CNX operator in the ATR-HELIOS model and running the new version of the model in HELIOS error free.

2.5.2 Illustration of Refinement Process

Step 1: Locate all of the parameters needed for the STR’s for this piece of the ATR-HELIOS model. This is done by finding/searching for all of the parameter names needed from the ATR.inp and ATR.set files to make the new STR. Figures 2.5 and 2.6 provide a view of the number of parameters that need to be found, roughly 65 for each STR. The F4 search made this step possible because of the size of the ATR.inp and ATR.set files; there is not a good way to quickly scan visually to gather all of the parameter names associated with the STR’s in question. To see what the STR parameters from the Studsvik ATR-HELIOS model look like see the 1st set of HELIOS code in Appendix A. The STR parameter for the left outer beryllium reflector begins with: “\$LoBeR = PAR...” This is in the middle of the code text. The names of the other parameters that support the node parameter names are at the top of the code text.

The HELIOS code shows all of the parameters needed to define the two STRs represented by Figures 2.5 and 2.6. Because the HELIOS code requires a “self-made mesh”, this ultimately requires many parameters to describe a simple piece as can be seen in Figures 2.5 and 2.6. Many of the parameters in the example shown above have layers of naming associated with it. For example parameter name “\$N4LU1x” is built up of several parameters: “\$N4LU1x = PAR (“(6*(\$xdrum3+\$xdrum*\$si5625)+1*(\$xtki/2*(\$si3375+\$si2250)))/7”)”. The Studsvik ATR-HELIOS model is created around all of these parameter names. The simplest of parameters are the distances or multipliers in numeric format to create the other parameters, i.e. “\$si3375 = PAR (“0.55557 02330 19602”)”. For the HELIOS code to work properly each parameter name inside the STR must be included and used appropriately according to the precision of the numerics used in each parameter i.e. 15 decimal places, to ensure the models continuity. Future versions of the ATR-HELIOS model, all of these parameter names must be used correctly inside the STR parameter, or the model will not run.

Step 2 and Step 3 of the process go together in an iterative way. Step 2 requires eliminating, creating or merging nodes together. This seems straight forward except that once a node is removed or a new node added it must be kept track of so step 3 of the process can be completed correctly. The example below will illustrate this.

In Figures 2.5 and 2.6 it is seen that nodes 1, 54, 55, 20, 22, 23, 26 and 19 from Figure 2.5 need to be merged with nodes 1, 54, 55, 22, 23, 26. To keep track of the nodes requires a bookkeeping strategy of sorts or a completely new renumbering strategy, either way it is necessary to keep track of the number of nodes needed to make the new STR, or the connection (CNX) in step 7 cannot be made. Labeling, copying and pasting the STR’s in a separate file has been useful to keep track of the nodes. Most of the nodes are labeled with a number commented out of the working HELIOS code, i.e.

```
("$xtki*$si2250", "$xtki*$si6750")           ! 1 !
("$xtki/2*($si3375+$si2250)", "$xtki/2*($si5625+$si6750)") ! 2 !
("$xdrum3+$xdrum*$si5625", "$ydrum3+$xdrum*$si3375")    ! 3 !
("$xdrum3+$xdrum*$si4500", "$ydrum3+$xdrum*$si4500")    ! 4 !
```

```

("$xImed2-$medIpolyr*$co4500", "$yImed2-$medIpolyr*$si4500") ! 5 !
("$xImed2-$medIpolyr*$co6000", "$yImed2-$medIpolyr*$si6000") ! 6 !
("$xImed2-$medIpolyr*$co7500", "$yImed2-$medIpolyr*$si7500") ! 7 !
("$xImed2-$medIpolyr*$co0900", "$yImed2-$medIpolyr*$si0900") ! 8 !
("$xImed2+$medIpolyr*$co7500", "$yImed2-$medIpolyr*$si7500") ! 9 !

```

In the sample code above each node's number is commented out (by the user) with exclamations on either side. These numbers represent the x, y pair number that the HELIOS software uses for each node assignment. Only if the node numbers are labeled correctly will the user be able to make the correct STR that will connect (CNX) into the ATR-HELIOS model. The sample code shows the 1st 9 nodes in the STR, which the first nodes listed in a STR parameter, are the periphery nodes. The periphery nodes must be kept track of for connection purposes as well as defining non-CCS regions. If one of the nodes is removed which is what is needed to merge STR's together and two nodes replace the missing node the numbering would need to be as follows:

```

($lrgIplyr      , "$yIlar")           ! 1 !
( "$lrgIplyr*$co1500" , "$yIlar+$lrgIplyr*$si1500") ! 2 !
("$xtki*$si2250" , "$xtki*$si6750")           ! 3 !
("$xtki/2*($si3375+$si2250)" , "$xtki/2*($si5625+$si6750)") ! 4 !
("$xdrum3+$xdrum*$si5625" , "$ydrum3+$xdrum*$si3375") ! 5 !
("$xdrum3+$xdrum*$si4500" , "$ydrum3+$xdrum*$si4500") ! 6 !
("$xImed2-$medIpolyr*$co4500", "$yImed2-$medIpolyr*$si4500")! 7 !
("$xImed2-$medIpolyr*$co6000", "$yImed2-$medIpolyr*$si6000")! 8 !
("$xImed2-$medIpolyr*$co7500", "$yImed2-$medIpolyr*$si7500")! 9 !
("$xImed2-$medIpolyr*$co0900", "$yImed2-$medIpolyr*$si0900")! 10 !
("$xImed2+$medIpolyr*$co7500", "$yImed2-$medIpolyr*$si7500")! 11 !

```

Now there are 11 nodes in the new STR that are needed to define the periphery of the STR and the rest of the nodes (not shown here) will need to be renumbered. The non-CCS regions in a STR are outlined by the nodes themselves, so to make sure the new STR is readable by AURORA and ORION the correct node numbers must be kept track of. An example of the HELIOS code showing the node numbering to define a non-CCS region is below:

```

1,2,3,54,           refl; ! Right      !
3,4,55,54,         refl;
4,5,21,20,55,      refl;
5,6,7,8,29,21,     refl;
21,29,24,23,22,    refl;
24,29,33,53,       refl;
53,33,27,25,       refl;
25,27,19,26,       refl;

28,18,27,32,41,44,35,  refl; ! Middle      !
41,32,33,42,       refl;
43,42,33,34,       refl;
34,29,30,37,46,43,  refl;
37,36,45,46,       refl;
36,35,44,45,       refl;

```

```

9,10,11,12,30,29,8,      refl; ! Middle Bottom !
16,17,28,35,47,50,38,   refl; ! Left      !
35,36,48,47,            refl;
36,37,49,48,            refl;
37,30,31,40,52,49,      refl;
40,39,51,52,            refl;
15,31,30,12,13,14,      refl ! Left Bottom !
)

```

Each string of numbers separated by commas represents the path HELIOS needs to follow to calculate the neutron or gamma current in that region across each line segment the nodes define. The numbering must be chosen a specific way to define a non-CCS region. Choosing the numbering is specified in the HELIOS user’s manual under AURORA Input STR operator. For example: “1, 2, 3, 54, refl” defines the beryllium in the lower part of the neck region in Figure 2.5. The rest of the numbers in the non-CCS region code define the other beryllium regions that are not defined by the CCS. All of the non-CCS regions need to be labeled with a material identifier so it is simpler to place a material assignment for that region; in this case the identifier is “refl”, where the parameter name “refl” is used in a material overlay command, OVLM as the material beryllium.

Once Steps 1-5 are finished, now an ORION graphic of the input can be seen, Figure 2.11 is the final result of merging the STRs represented by Figures 2.5 and 2.6. The two structures have been merged together by coding a new subsystem along with new node assignments, which define 12 new structures versus the two structures shown in Figures 2.5 and 2.6. The 12 new structures will be put into a new subsystem that will act as a new structure (STR) inside the ATR model. The new subsystem still needs to be merged into the ATR-HELIOS model. Figure 2.11 visually looks similar to Figures 2.5 and 2.6 if they were placed side by side.

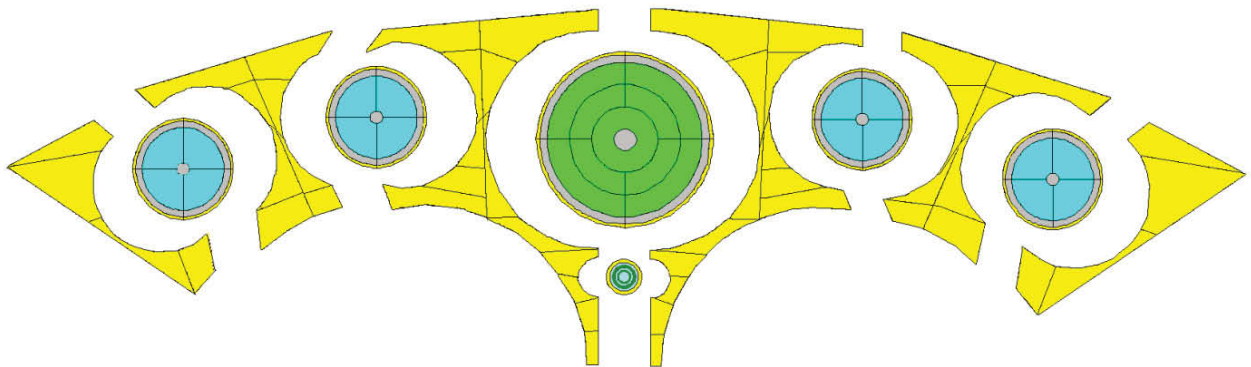


Figure 2.11. The two STRs from Figure 2.5 and Figure 2.6 put together with the new STRs that make the new subsystem to be put into the ATR-HELIOS model

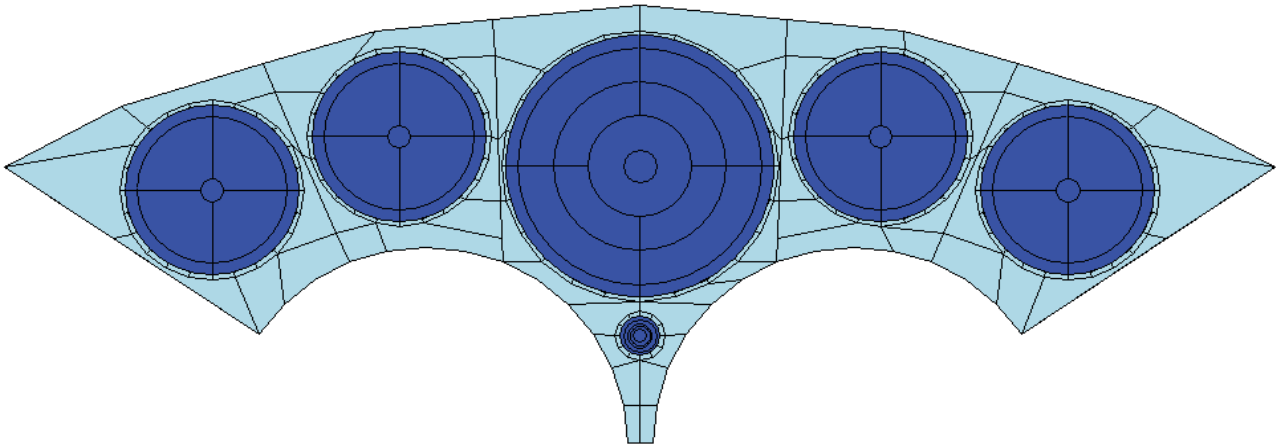


Figure 2.12 The new subsystem put together with a CNX operator

Figure 2.12 is from the ORION viewer. This new subsystem (seen in Figure 2.12) is a match of the two STRs from Figures 2.5 and 2.6. This new subsystem can be put into the ATR-HELIOS model.

2.5.2 Future Geometric Refinement Work

More model refinements like the process outlined for merging the STRs represented by Figure 2.5 and Figure 2.6 need to be completed. Connecting the STRs represented by Figures 2.7 and 2.8 together and to change STRs in Figure 2.9 and 2.10 will require following the same process. The process takes patience and persistence because this is a “hand meshed work” and the pieces need to match the existing naming scheme for each parameter imbedded into the existing ATR- HELIOS model. The step of searching for the parameter names for each node pair in the STRs and the CCS radii parameter names inside the STR has been partially completed, for the inner beryllium reflector but still needs to be completed for the N-16 port and small I-position CCS form the OSCC STRs.

Unfortunately, a user cannot treat the ORION viewer like an interactive GUI, the user can only view what is created absolutely error free according to the AURORA software the users mind is the 1st interactive GUI and then once there are no errors in AURORA/ ORION then the results of the users “mind STR” can be seen in ORION. At this point there is not a quicker way to improve the geometry of the ATR-HELIOS model and therefore improve the accuracy and fidelity of the model.

The path forward is to keep working the process to make the improvements (not perfect process certainly), and integrate the changes into a new ATR-HELIOS model version and carefully connect (CNX) all of the STRs back together.

2.6 Verification and Validation Suite

Kurt Hamman (INL)

HELIOS is a 2-D commercial reactor physics code developed by Studsvik Scandpower. The code is just one of several codes being evaluated as part of the Advanced Test Reactor (ATR) Core Modeling Update Project. ATR is a highly-heterogeneous light-water and beryllium moderated, beryllium reflected, light-water cooled system with full enriched (93% ^{235}U) plate-type fuel elements arranged in a serpentine pattern, whose features require the use of a very sophisticated modelling tool such as HELIOS.

The radial distribution of fuel, reflective material, and absorbers primarily contribute to the heterogeneity of the ATR; but, several reactivity control rods are known to contribute to the axial heterogeneity. For example, the 5 vertically withdrawn safety rods, which use hafnium (cadmium is the safety rod poison in ATRC) as a poison material extend 3 inches into the top of the fuel meat; and of the 24 vertically withdrawn hafnium neck shim rods, 23 are fully withdrawn, while one (i.e. regulating rod) is partially inserted into the core. Yet, the ATR has an inherent axial cosine-shaped flux distribution. In short, although the ATR has a 3-D geometry, the axial flux distribution coupled with uniform axial fuel/moderator/reflector/absorber distribution reduces the uncertainty in modeling the ATR as a 2-D geometry.

Regardless, modeling a reactor with heterogeneity in the axial plane (i.e. 3-D) contributes to additional uncertainty and ultimately places restrictions on the use of the code. Additionally, it should be expected that locating 2-D validation studies will be challenging, especially given the 3-D characteristics of most reactor experiments.

2.6.1. Code Validation Considerations

Several key validation considerations were considered as part of the overall development of the validation protocol.

1. Although verification, the process of verifying that the simulation accurately represents the model, is an important step in the verification and validation (V&V) process, the responsibility for software verification primarily resides with the commercial code vendors. Validation, determining that the results of the simulation are an accurate representation of the real world, primarily resides with the analyst.
2. Model/code verification should precede any validation exercise
3. Validated code has meaning only under the context of
 - a class of nearby problems (e.g. with flux and adjoint spectra that are similar to those of ATR)
 - specified variables (e.g. k_{eff} , flux distribution, spectral measurements)
 - specified level of accuracy (e.g. $k_{\text{eff}} = 0.9985 \pm 0.0001$)
4. Direct code validation is a process where code predictions are compared with physical experiments characteristic of the intended use of the code (i.e. a class of nearby problems). That is HELIOS code validation should include integral experiments having characteristics similar to those of the ATR.
5. Indirect code validation (i.e. benchmark) occurs when a previously validated code (e.g. MCNP) is used as a benchmark (e.g. to compare k_{eff}).

2.6.2. HELIOS Constraints

The following constraints were considered in the process of determining validation experiments:

1. Validation experiments will be required to be suitable for 2-D analysis by HELIOS.
2. The initial development of the HELIOS model of the ATR has been based on the 1994 CIC integral benchmark (Kim et al., 2008). The base model thus reflects a well-defined critical configuration at the time of the most recent measurements for which reliable and publically-available benchmark data have been published (Kim et al., 2008). This benchmark will continue to be a primary resource for validation.
3. There is a large collection of verified and validated benchmark cases for HELIOS. The specifications and input files for these benchmark cases are available from the code vendor.
4. The models used in the development must be verified and validated against existing data and reference calculations, and against new measured validation data as warranted. Computational uncertainties should be quantified using modern sensitivity/uncertainty analysis and least-squares adjustment techniques.
5. New data on flux distribution and spectral measurements within the reactor, and on burnup of fuel previously use in the reactor, will be needed to support model validation.

2.6.3. Experiments Evaluated

The ATR 1994 CIC configuration and supporting 1994 ATRC configurations, along with new ATRC experiments currently being conducted (see Sections 3 and 4 of this report) are the primary resource for validation. Additional benchmark experiments should have some similarities (e.g. plate fuel, highly enriched) to these experiments. Note that several minor errors (e.g. incorrect geometry and fuel densities) have been discovered since the 1994 CIC benchmark was originally published. Therefore all corrections that have been made to the benchmark since its original publication will be incorporated into the HELIOS models prior to final validation certification.

Numerous other integral experiments were also evaluated for possible use in connection with HELIOS validation. Most are documented in the IRPhE and ICSBEP Handbooks. Additionally, researchers at operating reactors including MURR (University of Missouri Research Reactor) and HFIR at ORNL (High Flux Isotope Reactor at Oakridge National Laboratory) were contacted regarding the availability of criticality benchmark experiments for those facilities. Experiments currently under consideration for formal incorporation into the HELIOS validation suite are listed in Table 2.3. A brief description of why each integral experiment was chosen for consideration is provided below.

The SPERT-D and SPERT-III experiments were chosen for validation studies due to having some significant and useful similarities (see Table 1) to the ATR benchmark. Note that each experiment evaluation as currently published provides only a k_{eff} value and indirect validation (i.e. benchmarking) using other reactor physics codes such as MCNP and KENO. Flux distribution and spectral measurements are not always provided.

In addition to published benchmarks, we will use measured ATR fuel burnup data as an indirect validation of the relevant depletion parameters. The Methods Update project includes development of a

non-invasive method for measuring irradiated ATR fuel burnup *in situ* using gamma spectroscopy (see Section 5 of this report). By comparing isotopic activities for key isotopes between measurements and HELIOS, an error function can be generated corresponding to the time-integrated history of cross-section multiplied against flux for when the fuel element was being irradiated.

Table 2.3 Evaluated Experiments under consideration for HELIOS validation studies

Experiment	Identifier	Location & Date	Fuel wt.%	Fuel	Clad	Coolant	Moderator	Reflector	Notes	Benchmark Codes (k _{eff} data)
ATR	HEU-MET-THERM-022	INL/1994	U-235 93	Plate (U-Al alloy)	Al	Water	Water	Beryllium	1	none none MCNP
SPERT-D	HEU-MISC-THERM-001	ORNL/1965	U-235 93.17	Plate (U-Al alloy)	Al	Water	Water	Water	2	KENO MONK-7B MCNP
SPERT-D	HEU-MISC-THERM-001	ORNL/1965	U-235 93.17	Plate (U-Al alloy)	Al	Uranyl Nitrate	Uranyl Nitrate	Uranyl Nitrate	3	KENO MONK-7B MCNP
SPERT-III	HEU-COMP-THERM-022 (Case 1)	INL/1959	U-235 93.2	Plate (UO ₂ / SST matrix)	SST	Water	Water	Water	4	KENO none MCNP
Task 5	INL/EXT-10-19940	INL/2010	U-235 93	Plate (U-Al alloy)	Al	Water	Water	Beryllium	5	none none none

Notes on experiment criticality conditions:

1. ATR operating conditions during criticality: OSCC @ 51.8° ; 22 shim rods fully inserted; 2 regulating rods fully withdrawn; 6 safety rods fully withdrawn (i.e. 3" below top of fuel meat)
2. Experimenter raised H₂O height, drained water, added fuel plates, raised H₂O height to criticality. The critical mass was determined by interpolation between slightly supercritical and slightly subcritical states.
3. Experimenter raised uranyl nitrate height, drained solution, added fuel plates, raised uranyl nitrate height to criticality. The critical mass was determined by interpolation between slightly supercritical and slightly subcritical states.
4. Experimenter raised H₂O height to criticality (Case 1) went critical at 34" (2" below top fuel meat)
5. In-Canal ATR Fuel Exposure Validation Measurements as described in Section 5.

2.7. Semi-Analytic Benchmarks for HELIOS

Doug Crawford (University of Utah), Barry Ganapol (University of Arizona)

In addition to the integral experiment validation suite described above, the Methods Upgrade project the development of a limited set of additional analytic benchmarks for supplementary verification of HELIOS in certain ranges of variables important to the ATR application. Although this effort was initiated late in the Fiscal Year and much remains to be done, some preliminary results and discussion are included in this section for informational purposes.

2.7.1. HELIOS Infinite Medium Benchmark

For verification purposes, a simple eigenvalue model was created with HELIOS to compare to semi-analytic benchmarks. The model is a simple homogeneous box of 5 cm in length, filled with UO₂. The model was made to compare to the solution of the standard slowing down equations. Both neutron cross section library files hy049n18g201.dat and hy177n48g201.dat from Studsvik Scandpower were used to calculate an eigenvalue for the system. The system is made with reflected boundary conditions that represent an infinite medium. The AURORA input file and the Zenith input file were created to compare, cross sections and other parameters as well as the eigenvalue: macroscopic absorption cross section, nu (number of fission neutrons produced per incident neutron) multiplied by the macroscopic fission cross

section, the scatter p0 matrix, the p1 scatter matrix, buckling value and four different eigenvalues; *kinf*, *kinfb*, *eigv* and *eigvb2* (see Zenith manual chapter 2 Table I: Data types for use in the SEL operator p18-20).

Quick explanations of the four different eigenvalues and infinite multiplication values calculated in HELIOS are as follows:

- *kinf* - infinite multiplication factor for calculated system, without any buckling
- *kinfb* - infinite multiplication factor for calculated system in the critical spectrum, i.e., with critical buckling applied
- *eigv* - calculated eigenvalue from the transport calculation
- *eigvb2* - calculated eigenvalue from the transport calculation with the input buckling applied

The major comparison point for the benchmark is the infinite multiplication factor (*kinf*) derived from the slowing down equation .

Details of the input file for this benchmark are as follows: 5cm length side, homogeneous UO2 as the fuel, fully reflected boundaries, a zero buckling factor initially and the buckling factor that is calculated by HELIOS is turned on initially, meaning it is included in two of the four Eigenvalue calculations, *eigvb2* and *kinfb*.

The infinite box model created in HELIOS was run with two different library files created by Studsvik as mentioned above. The box geometry was calculated with the current coupled collision probability method with both library files: the 49 energy group libraries file (hy049n18g201.dat) and with the 177 energy group library file (hy177n48g201.dat). *kinf* for the 49 energy group calculation is 1.5241, *kinfb* = 1.6004, *eigv* = 1.5241 and *eigvb2* = 0.2244 and the 177 group calculation *kinf* is 1.5088, *kinfb* = 1.58433, *eigv* = 1.5088 and *eigvb2* = 0.22215 which is not surprising that the two different library files give different answers. The HELIOS box model should give *kinf* = *kinfb*, since this was an infinite model.

The following was done to see whether the box created truly acted like an infinite medium.

- The length of the side of the box was varied to 1cm and 10cm no change in the eigenvalues for either library file was observed.
- Activated the feature in HELIOS to add a buckling factor into the calculation and again no change in the eigenvalues.
- Tried using the specular reflected boundary conditions instead of a diagonal albedo matrix boundary condition and still no change

From the trials above it was apparent that the HELIOS box model acted like an infinite slab/box as desired.

It should be noted that it is possible for *kinfb* to be larger than *kinf*. This is caused by leakage - when we (via the HELIOS software) apply the critical buckling, more fast neutrons than thermal neutrons will leak out of the system. This can significantly soften the spectrum so that, when we (via the HELIOS software) calculate the system-averaged nu-sigma-fission and sigma-absorption weighted with the critical spectrum, we can get a larger infinite multiplication factor”.

There is an option to turn off the critical buckling calculation internally generated by the HELIOS software and when this was done the various eigenvalue calculation methods (*kinf*, *kinfb*, *eigv*, and *eigvb2*) agree and are equal, in the case of the 177 group library the value is 1.5088 and for the 49-group library 1.5241.

Unfortunately, we were unable to match the eigenvalue found by the semi analytical benchmark described next.

2.7.2. Theory

As indicated, the initial eigenstate benchmark considered is for a homogeneous mixture of fissile fuel and moderator. The appropriate eigenstate slowing down equation is

$$\Sigma(E)\phi(E) = \int_0^{\infty} dE' \Sigma_s(E' \rightarrow E)\phi(E') + \frac{\chi(E)}{k} \int_0^{\infty} dE' \nu(E') \Sigma_f(E')\phi(E') \quad (1)$$

For demonstration purposes, elastic scattering for both the fissile and moderator material is initially assumed for this simple mixture. In the multigroup form, Eq (1) is approximated by

$$\Sigma_g \phi_g = \sum_{g'=1}^G \Sigma_{g'g} \phi_{g'} + \frac{\chi_g}{k} \sum_{g'=1}^G \nu \Sigma_{fg'} \phi_{g'}, \quad (2a)$$

And therefore for a non-zero (positive) solution to this homogeneous equation, we must have

$$\sum_{g'=1}^G \left[\Sigma_g \delta_{gg'} - \left(\Sigma_{g'g} + \frac{\chi_g}{k} \nu \Sigma_{fg'} \right) \right] \phi_{g'} = 0. \quad (2b)$$

More directly, in a vector form, Eq(2b) becomes

$$\mathbf{H}\boldsymbol{\phi} = \frac{1}{k} \boldsymbol{\chi} \mathbf{f}^T \boldsymbol{\phi}, \quad (3)$$

where

$$\mathbf{H} \equiv \left\{ \Sigma_g \delta_{gg'} - \Sigma_{g'g}, g, g' = 1, \dots, G \right\}$$

$$\boldsymbol{\phi} \equiv \left\{ \phi_g \right\}$$

$$\boldsymbol{\chi} \equiv \left\{ \chi_g \right\}$$

$$\mathbf{f} \equiv \left\{ \nu \Sigma_{fg} \right\}.$$

Formally solving this equation gives

$$\boldsymbol{\phi} = \frac{1}{k} \mathbf{H}^{-1} \boldsymbol{\chi} F, \quad (4a)$$

Where the scalar has been defined as

$$F = \mathbf{f}^T \boldsymbol{\phi}. \quad (4b)$$

Then, multiplying Eq (4a) by \mathbf{f}^T

$$\mathbf{f}^T \boldsymbol{\phi} = F = \frac{1}{k} \mathbf{f}^T \mathbf{H}^{-1} \boldsymbol{\chi} F,$$

And canceling the scalar gives the following explicit representation for the eigenvalue:

$$k = \mathbf{f}^T \mathbf{H}^{-1} \boldsymbol{\chi}. \quad (5)$$

To find the flux and an independent confirmation, we use Eq (4a) in the form

$$\mathbf{H}\phi = \frac{1}{k}\mathbf{B}\phi \quad (6a)$$

giving

$$\left[\mathbf{H}^{-1}\mathbf{B} - k\mathbf{I} \right] \phi = 0 \quad (6b)$$

Indicating that k is also the eigenvalue of the matrix $\mathbf{H}^{-1}\mathbf{B}$. The normalized scalar flux $\phi_1 \equiv 1$ is achieved by first letting $\phi_G \equiv 1$ and from Eq(6b) solving

$$\sum_{g'=1}^{G-1} \left[\Sigma_g \delta_{gg'} - \left(\Sigma_{g'g} + \frac{\chi_g}{k} \nu \Sigma_{fg'} \right) \right] \phi_{g'} = - \left[\Sigma_g \delta_{Gg} - \left(\Sigma_{Gg} + \frac{\chi_g}{k} \nu \Sigma_{fG} \right) \right]. \quad (7)$$

Finally,

$$\phi_g \rightarrow \frac{\phi_g}{\phi_1}. \quad (8)$$

2.7.3. HELIOS Spectral Benchmark Results

The initial HELIOS benchmark considers a homogeneous UO_2 fuel in a reflected box using the HELIOS 49 group cross section set. The first task is to adapt the HELIOS output to the HELIOSA code. This is performed electronically, by searching for the following key-words in the HELIOS output:

```
wd(1) = 'avesgmtr'
wd(2) = 'avesgm'
wd(3) = 'avesgmnu'
wd(4) = 'avespctr'
wd(5) = 'avescttr'
wd(6) = 'fl'
```

for the *transport cross section*, *absorption cross section*, *nu times the fission cross section*, *fission spectrum*, *scattering block* and the *flux*. The HELIOS input is then read into memory and arranged into appropriate columns in file *o71.dat* to be read by HELIOSA. Note that no modification of the HELIOS output is necessary.

Before generating the *o71* output file, the consistent total scattering cross section, including anisotropy, is obtained from

$$\Sigma_{sg} = \frac{\Sigma_{trg} - \Sigma_{ag}}{1 - \bar{\mu}_0}, \quad (10)$$

(Assuming all U235 fuel) where

$$\bar{\mu}_0 = \frac{A_{235}\bar{\mu}_{0,U} + A_{O_2}\bar{\mu}_{0,O_2}}{A_{235} + A_{O_2}}; \quad \bar{\mu}_{0,A} \square \frac{2}{3A}. \quad (10a)$$

The total cross section then becomes $\Sigma_g = \Sigma_{sg} + \Sigma_{ag}$.

The group flux from the HELIOS calculation is shown in Figure 2.13. To check the HELIOS calculation, k was determined from

$$k = \frac{\sum_{g=1}^G v \Sigma_{fg} \phi_g}{\sum_{g=1}^G \Sigma_{ag} \phi_g} \quad (10b)$$

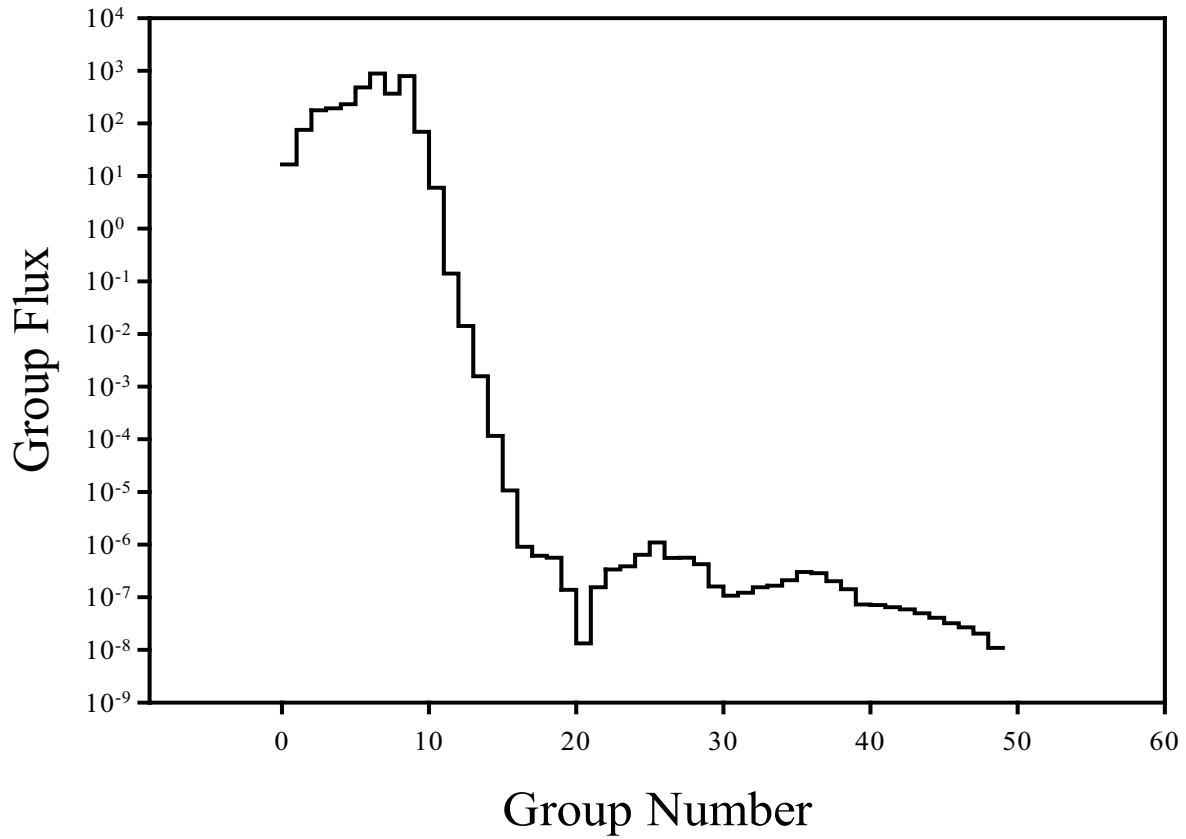


Figure 2.13. Group flux from HELIOS.

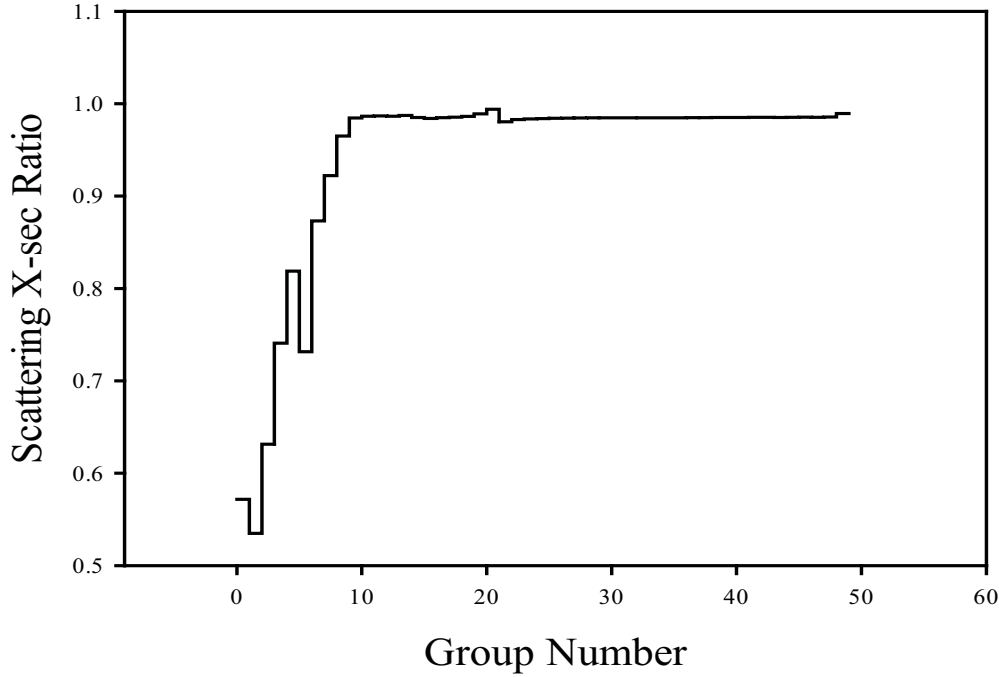


Figure 2.14. Scattering X-sec ratio.

which nearly confirms the *kinfb* entry in the HELIOS output as 1.60035. As a further check, the normalization of the group scattering cross section, which should be the sum of all outscatter to all other groups:

$$\sum_{g'=1}^G \Sigma_{gg'} , \quad (11a)$$

which is assessed through the ratio

$$r_{sg} = \frac{\Sigma_{sg}}{\sum_{g'=1}^G \Sigma_{gg'}} \quad (11b)$$

shown in Figure 2.14. As observed, the normalization holds to about 2% for most of the spectrum. At the high-end, it completely fails. At this time we are not sure why conservation fails.

A final check is found from Eq(2a), whose residual

$$R_{1g} \equiv \Sigma_g \phi_g - \sum_{g'=1}^G \Sigma_{g'g} \phi_{g'} - \frac{\chi_g}{k} \sum_{g'=1}^G \nu \Sigma_{fg'} \phi_{g'} , \quad (12a)$$

should vanish-- but as seen from Figure 2.15, this is not the case. A smaller residual is found when the scattering correction is included in the transfer cross section

$$R_{2g} \equiv \Sigma_g \phi_g - \sum_{g'=1}^G r_{sg'} \Sigma_{g'g} \phi_{g'} - \frac{\chi_g}{k} \sum_{g'=1}^G \nu \Sigma_{fg'} \phi_{g'} . \quad (12b)$$

Equation (12b) is consistent with total balance and should be the correct formulation as confirmed by the lower residual.

As shown in Table 2.4, when the original data is processed by the above theory, a k much smaller than the value from HELIOS is found. This observation is reinforced by the flux plot of Figure 2.16 indicating some negative flux values. To observe the effect of anisotropic scattering $\bar{\mu}_0$ was set to zero giving a much higher k (2.41...) than HELIOS. Some values of the flux are negative for this case also. The large sensitivity to anisotropy is not physically reasonable but may indicate the necessity of the higher moments to be included in the analytical calculation.

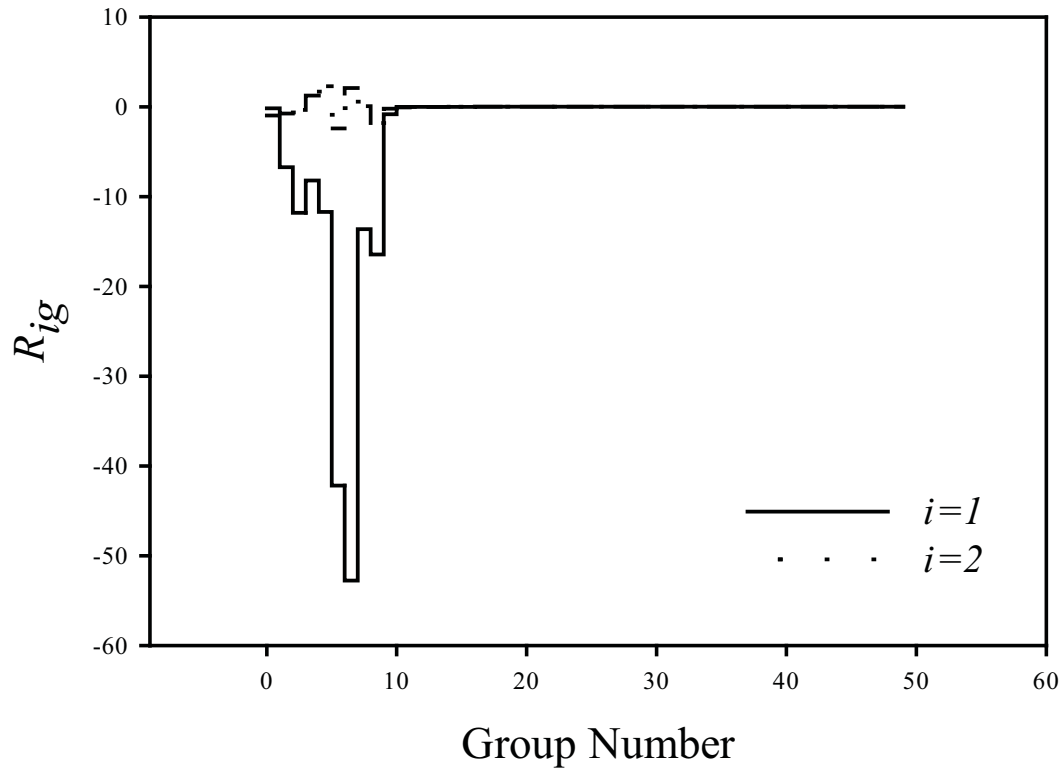


Figure 2.15. Multigroup residuals with (2) and without (1) scattering correction.

Table 2.4 K- comparison for various approximations

<i>Mode</i>	<i>k</i>
HELIOS	1.5241
Original	0.35056
Isotropic	2.41477

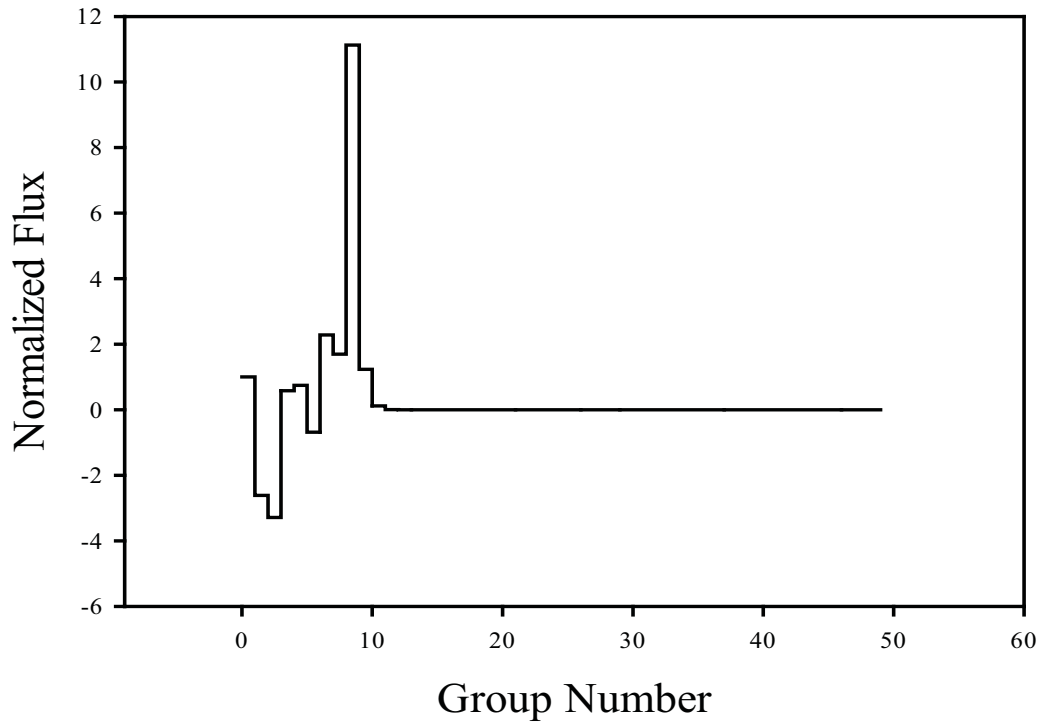


Figure 2.16 Analytical flux for original HELIOS data

Finally, if the scattering correction is enforced, we arrive at the last entry in Table 2.5, which is now much closer to the HELIOS *kinfb* value.

Table 2.5 *k*- comparison with scattering X-sec consistency

<i>k-Mode</i>	<i>k</i>
<i>Kinf</i>	1.5241
<i>Kinfb</i>	1.6004
Corrected	1.6023

However, upon further examination of the HELIOS output, there is a second *k* reported *kinf* whose exact meaning is unknown at this time. However, for all analytical cases, the multigroup equation [Eq (2a)] is satisfied to machine accuracy.

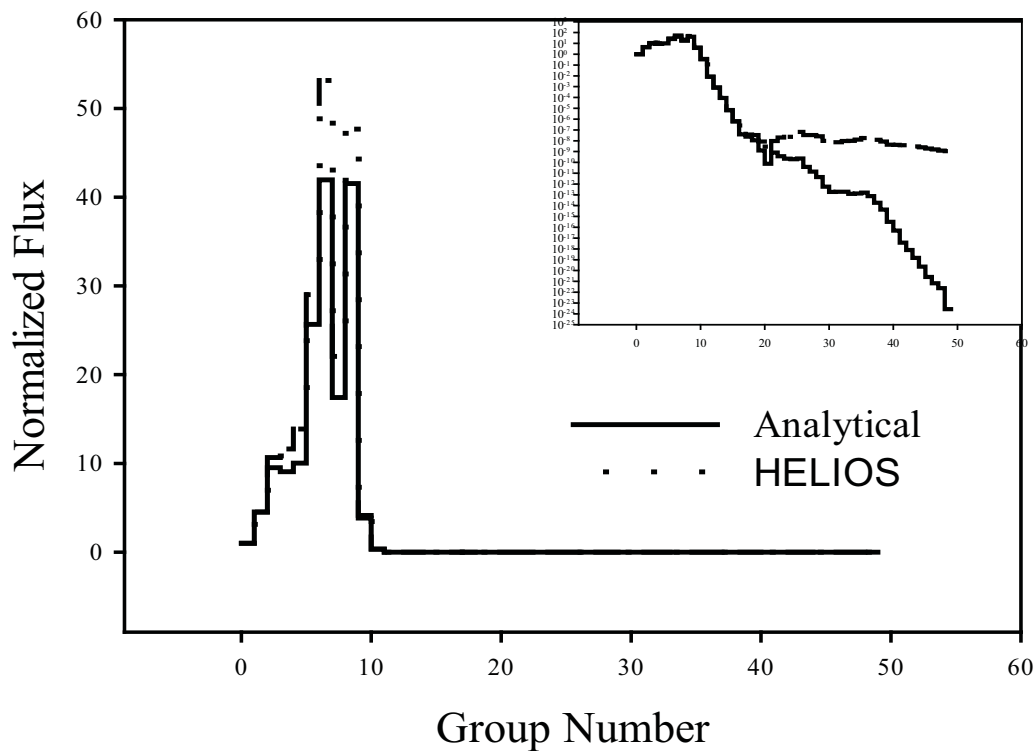


Figure 2.17. Normalized flux comparison.

A normalized flux comparison between the semi-analytical benchmark and HELIOS is shown in Figure 2.17. Reasonable agreement is observed at the high energies, but there is no agreement at low energies. It can be concluded at this point that the origin of the *kinf* entry as well as the importance of anisotropy needs to be resolved.

2.8 Model and Software Configuration Control

Sam Bays (INL), Kurt Hamman (INL)

Version control software helps to maintain and track changes to documents, source and input files such that any revision of any document can be retrieved at any point in time. There are several version control software packages available. SubversionTM is a popular version control utility that establishes a centralized document repository on a dedicated server. Subversion stores the history of all changes made to files stored in this centralized repository. Starting in May 2011, the HELIOS executables, source code, documentation and data-libraries were entered into a Subversion-controlled central repository. Along these lines, the most recent version (i.e., snapshot) of the HELIOS code with cross-section libraries was installed on a self-maintained computer system.

At the same time all modeling efforts were consolidated to reference one base model, Version 1, which was also entered into the Subversion repository. The original base model transmitted by Studsvik which

is the grandfather to all miscellaneous work prior to May 2011 was also archived as Version 0 but is treated as a snapshot only and is not part of any on-going development work.

The second phase of our software quality assurance plan is to establish a robust version controlled issue tracking system. Issue tracking software is a common best practice in software engineering for the purpose of reporting code/model deficiencies as well as resolution documentation. TRAC, a web-based (wiki) tracking system has been identified to perform this function. There are many issue-tracking software packages available. However, TRAC is known to be used by other DOE software/model development projects, e.g. Consortium for Advanced Simulation of Light Water Reactors (CASL), and is supported at Idaho National Laboratory. TRAC enables issues and action items to be organized in terms of priority, schedule as well as their relationship with reporting Milestones. TRAC is version controlled such that all issues raised cannot be deleted from record. TRAC can also directly interface with a Subversion repository.

3.0 HIGH-FIDELITY MODELS TO SUPPORT VALIDATION EXPERIMENTS IN THE ATRC

During the year extensive progress was made in the development of various models of the ATRC using the new modeling code suite. These models are to be used as aids in validation experiment design as well as for direct code and model validation as described in this section and in Section 4.

3.1 MCNP5 Modeling to Support ATRC Validation Experiments

Joseph Nielson (INL)

MCNP5 (Goorley et al., 2003) is a continuous-energy Monte Carlo Code developed at Los Alamos National Laboratory. The MCNP ATRC full core model was created to support experiment validation. It is similar to the published full core ATR1994 Core Internals Changeout (CIC) Benchmark model (Kim and Schnitzler, 2008). During FY-11 that model was modified to match the configuration of the ATRC. Significant differences exist between the current ATR configuration and the ATRC, due primarily to evolutionary changes in the ATR configuration over the course of several core internal change-outs (CICs) and fuel design changes. Neutronically, the most significant differences between the cores are the fuel design, operating conditions and the flux trap loadings. ATRC element fuel plates are uniformly loaded with boron, whereas the ATR uses boron for power peaking control only in the four innermost and four outermost plates. The ATR operates at a high power density with forced cooling under pressurized conditions, while the ATRC is an unpressurized pool type reactor that operates at a power generally less than 1000 watts with cooling by natural convection. Hence, ATRC coolant is full density water, and coolant, moderator (water and beryllium) and fuel can be assumed to remain at room temperature [Bess, 2009]. The other significant difference between the ATR and ATRC is the contents of the irradiation positions. Flux trap contents can not only influence core reactivity but also the relative power distribution between the five core lobes. For Irradiations 1-4 described in Section 4, conducted as new validation experiments in connection with the Methods Update Project, the contents of the Northwest (NW) flux trap are well characterized. For remaining flux traps, various INL Test Plan documents and other resources were used to identify the current contents.

The ATRC also contains a number of additional cooling channels in the beryllium reflector that were removed from the ATR in an earlier CIC. Furthermore, the ATRC uses five cadmium-plated safety rods while the ATR uses six hafnium-plated safety rods.

Two confirmatory configurations were first modeled based on certain ATRC experiments conducted in connection with 1994 ATR CIC. The first configuration, referred to as 94-2, is similar in experiment loading to the ATR 1994 CIC model, with the exception of the fuel loading, which consisted of Mark IV fuel elements. The 94-2' configuration replaced the Mark IV fuel elements with the current Mark VII fuel elements. A listing of the experiment loadings for these configurations is presented in Table 3.1.

The MCNP calculated eigenvalues for the 94-2 and 94-2' are 0.98924 ± 0.00009 and 0.98565 ± 0.00009 , respectively. Additionally, the calculated element powers for the 94-2 case were measured, and subsequently calculated using MCNP. A comparison of the measured and calculated values is presented in Figure 3.1. The calculated power split measurements are in good agreement with the measured values. The maximum difference between the measured lobe power and the calculated lobe power occurs in the NE lobe at -3.3%. The calculated eigenvalue is slightly lower than critical. Additional model refinements are planned as part of the project. However, the model does show good agreement with measured values and demonstrates that the model is adequate for use.

The ATRC MCNP model was then modified to represent the current experiment configuration with the Mark IV fuel elements and the insertion experiments into the NW flux trap for Modeling Update Project

Irradiations 1, 3 and 4. A complete description of these experiments is presented in Section 4. The ATR core configuration for Irradiations 1 through 3 is presented in Table 3.2. A diagram of the MCNP geometry for ATRC is shown in Figure 3.2.

The foil holding strips used in Irradiations 1 and 2 were modeled with the following configuration:

- First holding strip, lower position, stacked bare foils Au-105 and Mn/Cu-206.
- First holding strip, upper position, Cd-covered foil stack containing foils In-60, Au-111, W-R20-1-1, Co-R20-3-4, Mn/Cu-204, Cu-510, and Sc-501.
- Second holding strip, lower position, Cd-covered foil stack containing foils In-61, Au-112, W-R20-1-2, Co-R20-3-5, Mn/Cu-205, Cu-511, and Sc-502.
- Second holding strip, upper position, stacked bare foils Au-106 and Mn/Cu-207
- Place Cu/Au flux wires in the six wire positions of each foil holding strip as indicated.

In addition to the foils and flux wires in the holding strip, Cu/Au wires were placed in Channel 10 of fuel elements 32, 34, 36, and 38. These wires were included in the MCNP model and the appropriate reaction rates were tallied in the model.

Experiment 2 was similar to Experiment 1, except the foils and Cd cover were removed from the NW test train. Experiment 2 was modeled by “voiding” out the foils and wires, but keeping the flux and reaction rate tallies in those regions. MCNP allows for tallying reaction rates in voided regions by allowing the user to tally the flux in the region and simply multiplying the flux by the appropriate microscopic cross-section for the material of interest. This allows for calculation of the unperturbed (i.e. unshielded) fluxes and reaction rates in the experiment.

A diagram of the MCNP model in the NW flux trap for Irradiation 1 is shown in Figure 3.3. The calculated keff for the core configuration of Irradiation 1 is 0.98928 ± 0.00002 . The individual Cu/Au wires and the foils were modeled to calculate the fluxes and reaction rates at those positions. The reaction rates are calculated using the recent International Reactor Dosimetry Files (IRDF) cross-section libraries for each reaction of interest. The microscopic shielded cross-section can be determined by dividing the MCNP calculated reaction rate tally by the flux tally. Each tally was broken down into the 48 energy groups corresponding to the BUGLE series of standard cross section libraries (Roussin, 1980) with one extra group to cover the highest energy range between 17.3 MeV and 20 MeV since the MCNP5 library extends to 20 MeV but the standard BUGLE structure stops at 17.3 MeV. A listing of the energy groups used for the tallies is presented in Table 3.3. The tallied reaction rates and flux in each energy group were used to provide a set of 48 group cross-section that can be used as part of the validation protocol described in Section 4.0.

Irradiation 3 was intended to measure additional details of the fast neutron spectrum. The foils were placed inside an enriched B-10 sphere to shield the foils from thermal neutrons. The following foils were modeled inside the B-10 sphere: Rh-104, In-526, Ti-1002, Ni-1004, Zn-502, Fe-505, Cu-509, Nb-1005. The reaction rate tallies and flux tallies were used to calculate the 48 group cross-sections. A diagram of the MCNP Experiment 3 configuration is shown in Figure 3.4. The calculated keff for the configuration of Irradiation 3 is 0.99037 ± 0.00002 . Irradiation 4 was modeled based on the configuration listed in Table 3.5. Standard $^{235}\text{U}(10\%)/\text{Al}$ fission wires used for wires were inserted into all of the odd elements at the axial midplane following standard ATRC “flux run” procedures. In addition Au/Cu flux wires, described in detail in Section 4 were inserted into elements 12, 14, 16, 18, 32, 34, 36, and 38 at the axial midplane. These wires are designed to obtain spectral detail rather than gross fission rate.

MCNP calculated power splits were compared with measured values from the fission wires. The calculated keff for the configuration of Irradiation 4 is 0.99157 ± 0.00002 . A comparison of the MCNP element power split results to the measured values is shown in Figure 3.5. The results indicate that the calculated power in the NWFT is slightly higher (8.0%) than the measured values based on the fission wires placed in the odd-numbered elements as part of the standard flux measurement protocol used for both ATRC and ATR. Additional model refinement is planned in FY-12 and detailed spectral analysis for the even-numbered fuel elements containing Au/Cu wires will be conducted as discussed further in Section 4.

Table 3.1. Experiment configuration for the 94-2 Benchmark.

Facility	Loading
Flux Traps	
NW	LIPT and 3.5-inch diameter aluminum filler
E	Safety rod, Chopped Dummy IPT (CDIPT), and Small Irradiation Housing Assembly (SIHA) with aluminum baskets containing three LSA cobalt capsules in all 7 positions.
S	Safety rod, Chopped Dummy IPT (CDIPT), and Small Irradiation Housing Assembly (SIHA) with aluminum baskets containing three LSA cobalt capsules in all 7 positions.
NE	LIHA with LSA cobalt capsule mockups in positions 3 through 6, 10 through 13, and 23 and aluminum filler assemblies in positions 1, 2, 7, 8, 9, 14, and 15 through 22.
N	Safety rod, Standard Inpile Tube (SIPT), flow tube, and 1.5-inch diameter aluminum filler
W	Safety rod, Standard Inpile Tube (SIPT), and water filled flow tube
SW	Safety rod, Standard Inpile Tube (SIPT), flow tube, and 1.5-inch diameter aluminum filler
C	SIHA with aluminum filler assemblies in positions 1 through 6 and a LSA cobalt capsule mockup in position 7
SE	Dummy Flux Trap Filler, SIPT, flow tube and water-filled flow tube
A Irradiation Facilities	
A-1 thru A-8	Aluminum filler
A-9 through A-12	Aluminum filler
B Irradiation Facilities	
B-1 through B-8	"Y" aluminum flow restrictor
H Irradiation Facilities	
H-2 and H-10	Empty flux monitor wire holders
H-3 and H-11	N-16 flow tube mockup
H-1, H-4, H-5, H-6, H-7, H-8, H-9, H-12, H-13, H-14, H-15 and H-16	Aluminum basket containing three LSA cobalt capsules
I Irradiation Facilities	
I-1 through I-20	Aluminum filler except for positions I-3 and I-9 which contain log count rate detector thimbles
Fuel Elements	Forty ATRC standard fuel elements
Neck Shims	All inserted

Bottom underlined number is power normalized to 250W.
 Red number is the measured value given in the ECAR
 Green number is the percentage difference between the two

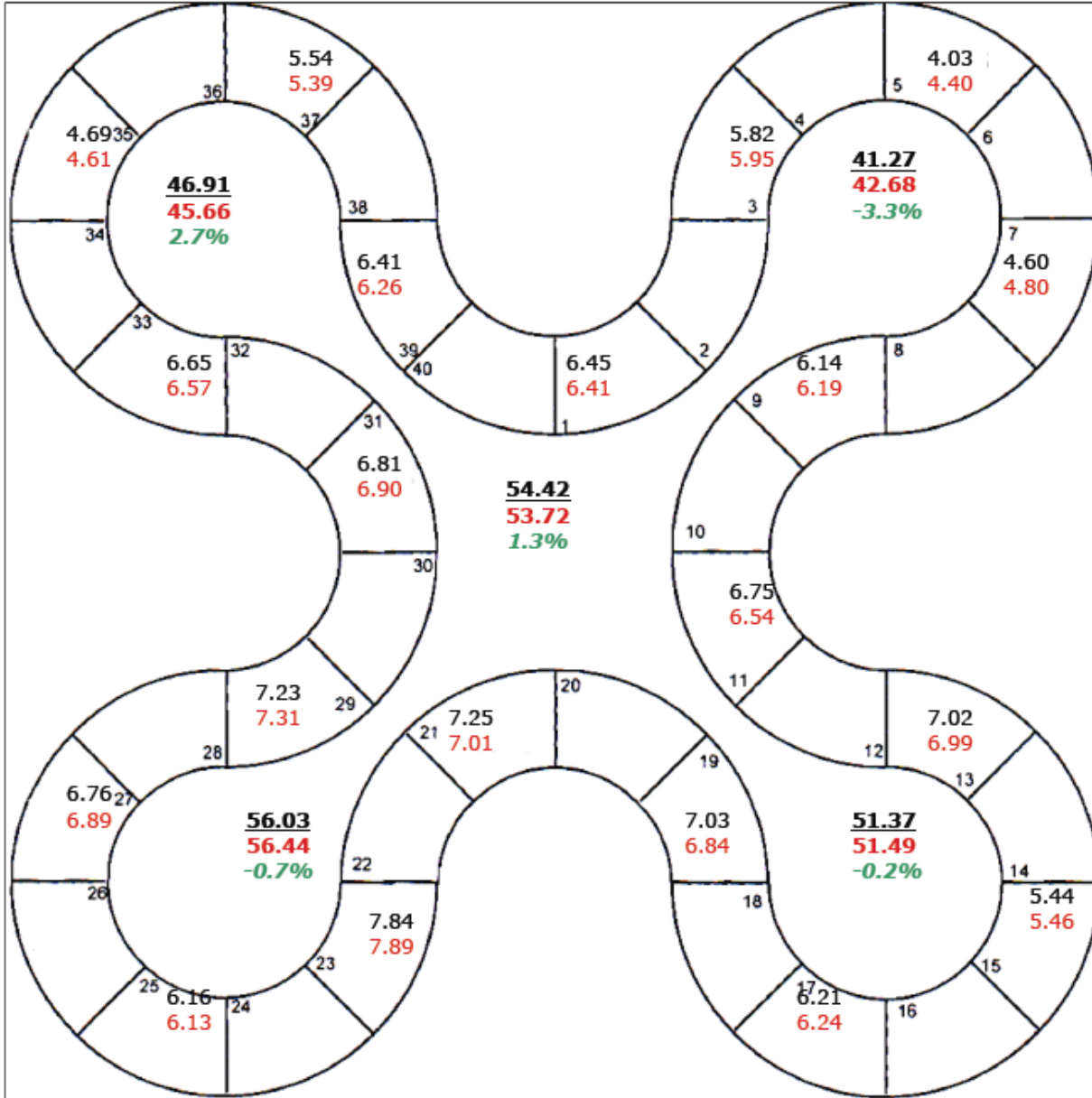


Figure 3.1. Comparison of the calculated (MCNP5) and measured power splits from the 94-2 configuration.

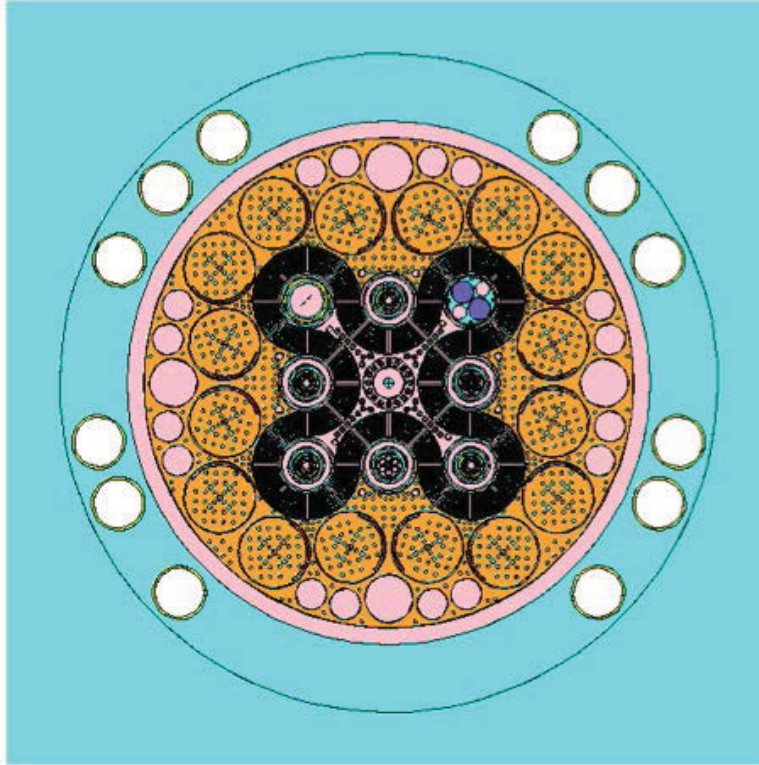


Figure 3.2. MCNP generated cross-section of the ATRC model (x-y planes).

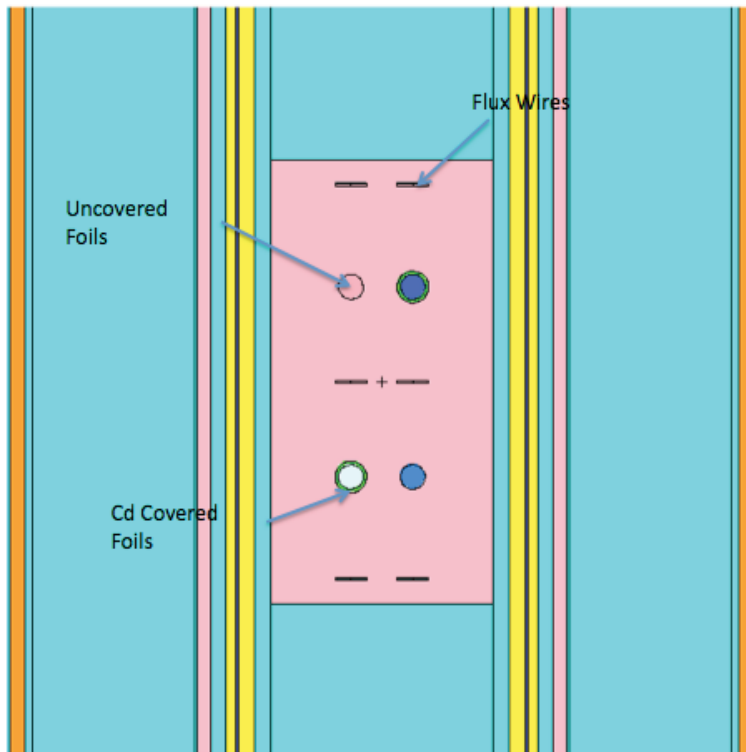


Figure 3.3 MCNP Cross-Section of Hardware used for Irradiation 1 (x-z planes).

Table 3.2. Configuration for Modeling Update Irradiation 1.

Facility	Loading
Flux Traps	
NW	LIPT and NW experiment configuration
E	Safety rod, Chopped Dummy IPT (CDIPT), and Small Irradiation Housing Assembly (SIHA) with aluminum baskets containing three LSA cobalt capsules in all 7 positions.
S	Safety rod, Chopped Dummy IPT (CDIPT), and Small Irradiation housing Assembly (SIHA) with three LSA cobalt capsules in aluminum basket in S-7 position and six aluminum fillers in S-1 thru S-6
NE	Multiple Irradiation Capsule Experiment (MICE) facility with fueled MICE PRIME 1 capsule mockups in NW and SE positions; MICE filler plugs in the NE and SW positions. Shrouding described in Bettis letter B-MT(EDT)I-1171 and B-MT(EDT)I-1309
N	Safety rod, Standard Inpile Tube (SIPT), flow tube, and 1.5-inch diameter aluminum filler
W	Safety rod, Standard Inpile Tube (SIPT), flow tube, and 1.5-inch diameter aluminum filler
SW	Safety rod, Standard Inpile Tube (SIPT), flow tube, and 1.5-inch diameter aluminum filler
C	AFIP Dummy Test with one -inch diameter hole
SE	Dummy Flux Trap Filler, SIPT, flow tube with aluminum spacer, and 1.5-inch diameter aluminum filler
A Irradiation Facilities	
A-1 thru A-8	LSA Cobalt
A-9 through A-12	Aluminum filler
B Irradiation Facilities	
B-1 through B-8	"Y" aluminum flow restrictor
H Irradiation Facilities	
H-2 and H-10	Empty flux monitor wire holders
H-3 and H-11	N-16 flow tube mockup
H-1, H-4, H-5, H-6, H-7, H-8, H-9, H-12, H-13, H-14, H-15 and H-16	Aluminum basket containing three LSA cobalt capsules
I Irradiation Facilities	
I-1 through I-20	Aluminum filler except for positions I-3 and I-9 which contain log count rate detector thimbles
Fuel Elements	Forty ATRC standard fuel elements
Neck Shims	All inserted

Table 3.3. Energy group structure used for MCNP tallies.

Group	Upper Energy	Lower Energy
1	2.00E+01	1.73E+01
2	1.73E+01	1.42E+01
3	1.42E+01	1.22E+01
4	1.22E+01	1.00E+01
5	1.00E+01	8.61E+00
6	8.61E+00	7.47E+00
7	7.47E+00	6.07E+00
8	6.07E+00	4.97E+00
9	4.97E+00	3.68E+00
10	3.68E+00	3.01E+00
11	3.01E+00	2.73E+00
12	2.73E+00	2.47E+00
13	2.47E+00	2.37E+00
14	2.37E+00	2.35E+00
15	2.35E+00	2.23E+00
16	2.23E+00	1.92E+00
17	1.92E+00	1.65E+00
18	1.65E+00	1.35E+00
19	1.35E+00	1.00E+00
20	1.00E+00	8.21E-01
21	8.21E-01	7.43E-01
22	7.43E-01	6.08E-01
23	6.08E-01	4.98E-01
24	4.98E-01	3.69E-01
25	3.69E-01	2.97E-01
26	2.97E-01	1.83E-01
27	1.83E-01	1.11E-01
28	1.11E-01	6.74E-02
29	6.74E-02	4.09E-02
30	4.09E-02	3.18E-02
31	3.18E-02	2.61E-02
32	2.61E-02	2.42E-02
33	2.42E-02	2.19E-02
34	2.19E-02	1.50E-02
35	1.50E-02	7.10E-03
36	7.10E-03	3.35E-03
37	3.35E-03	1.58E-03
38	1.58E-03	4.54E-04
39	4.54E-04	2.14E-04
40	2.14E-04	1.01E-04
41	1.01E-04	3.73E-05
42	3.73E-05	1.07E-05
43	1.07E-05	5.04E-06
44	5.04E-06	1.86E-06
45	1.86E-06	8.76E-07
46	8.76E-07	4.14E-07
47	4.14E-07	1.00E-07
48	1.00E-07	0.00E+00

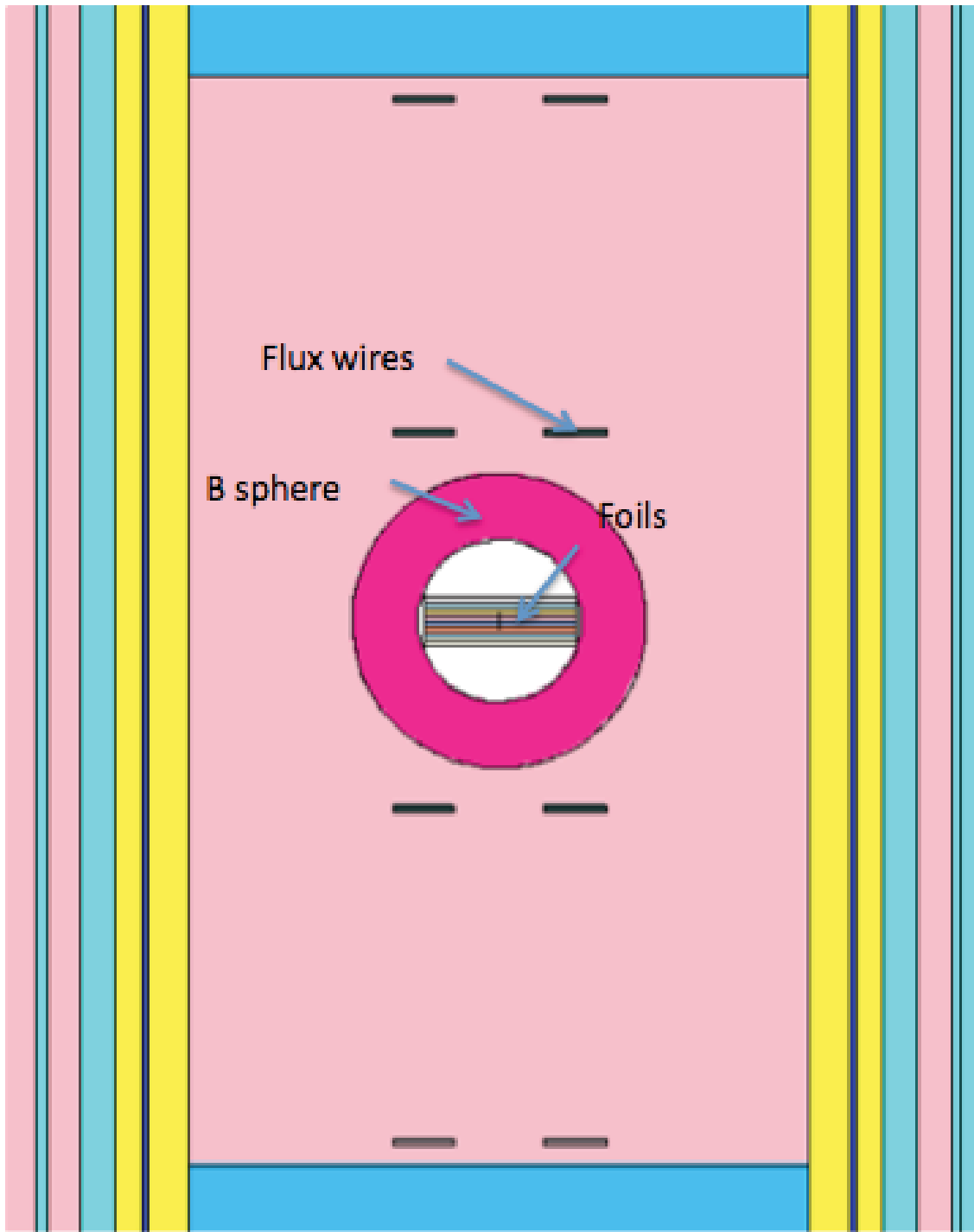


Figure 3.4. MCNP generated cross-section of NW LIPT hardware used for Irradiation 3 (y-z planes).

Bottom underlined number is power normalized to 250W.
 Red number is the measured value given in the ECAR
 Green number is the percentage difference between the two

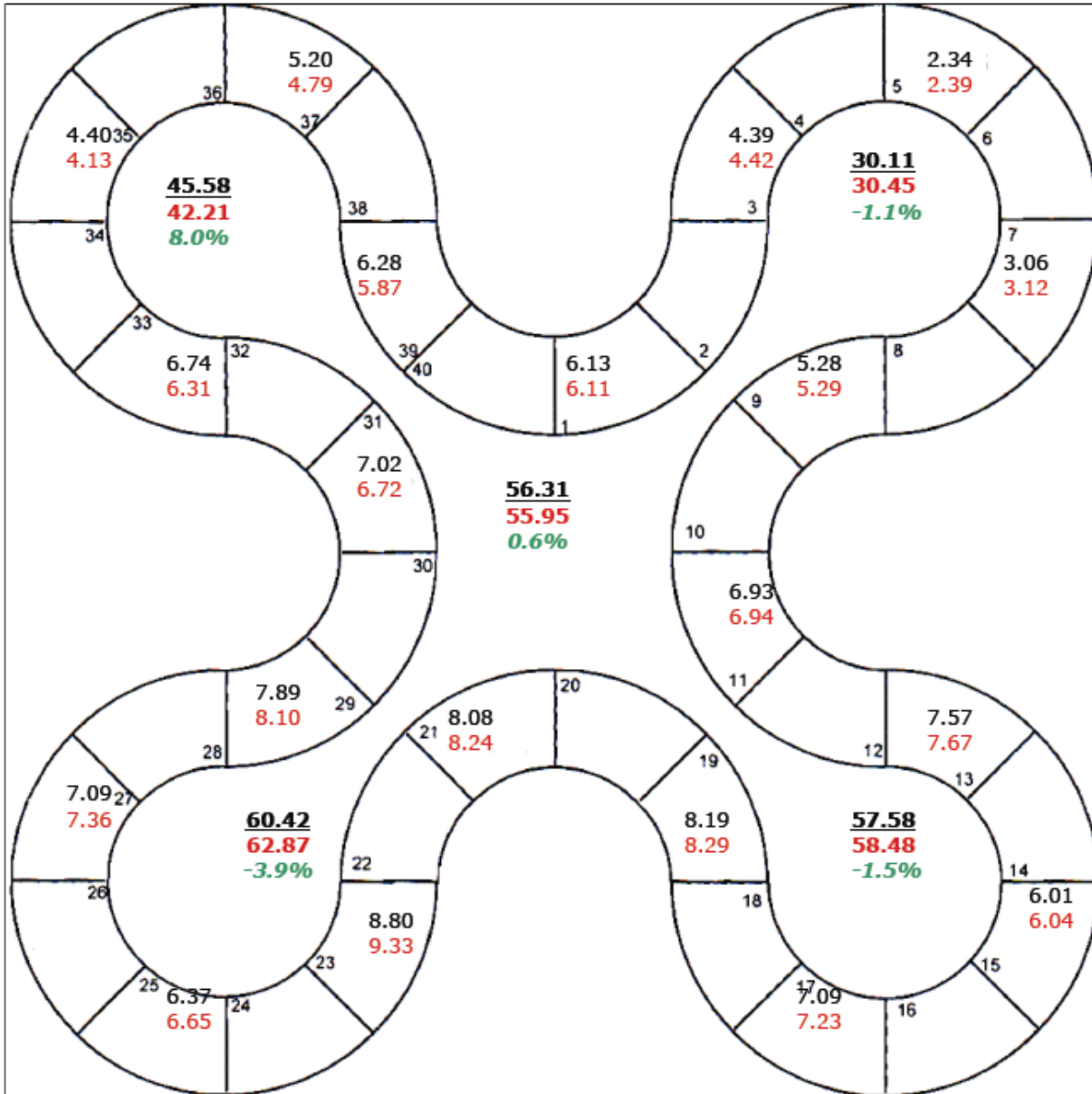


Figure 3.5. Comparison between the MCNP calculated power splits and measured power splits for ATRC Irradiation 4.

Table 3.4. Listing of reactions and MCNP cross-sections used in the analysis.

Experiment	Foil/Wire	Isotope	MCNP ZAID	MCNP Reaction Number
1	MnCu206	Mn-55	25055.34y	102
1	MnCu207	Mn-55	25055.34y	102
1	MnCu204	Mn-55	25055.34y	102
1	MnCu205	Mn-55	25055.34y	102
1	Cu-510	Cu-63	29063.34y	102
1	Cu-511	Cu-63	29063.34y	102
1	Au105	Au-197	79197.34y	102
1	Au106	Au-197	79197.34y	102
1	Au111	Au-197	79197.34y	102
1	Au112	Au-197	79197.34y	102
1	In60	In-115	49115.34y	11102
1	In61	In-115	49115.34y	11102
1	In60	In-115	49115.34y	10004
1	In61	In-115	49115.34y	10004
1	W2011	W-186	74186.34y	102
1	In60	In-115	49115.34y	10004
1	In61	In-115	49115.34y	10004
1	W2012	W-186	74186.34y	102
1	Co-R-20-3-4	Co-59	27059.34y	102
1	Co-R-20-3-5	Co-59	27059.34y	102
1	Sc501	Sc-45	21045.34y	102
1	Sc502	Sc-45	21045.34y	102
1	Flux Wire 1	Au-197	79197.34y	102
1	Flux Wire 2	Au-197	79197.34y	102
1	Flux Wire 3	Au-197	79197.34y	102
1	Flux Wire 4	Au-197	79197.34y	102
1	Flux Wire 5	Au-197	79197.34y	102
1	Flux Wire 6	Au-197	79197.34y	102
1	Flux Wire 7	Au-197	79197.34y	102
1	Flux Wire 8	Au-197	79197.34y	102
1	Flux Wire 9	Au-197	79197.34y	102
1	Flux Wire 10	Au-197	79197.34y	102
1	Flux Wire 11	Au-197	79197.34y	102
1	Flux Wire 12	Au-197	79197.34y	102
1	Flux Wire 13	Au-197	79197.34y	102
1	Flux Wire 14	Au-197	79197.34y	102
1	Flux Wire 15	Au-197	79197.34y	102
1	Flux Wire 16	Au-197	79197.34y	102

1	Flux Wire 1	Cu-63	29063.34y	102
1	Flux Wire 2	Cu-63	29063.34y	102
1	Flux Wire 3	Cu-63	29063.34y	102
1	Flux Wire 4	Cu-63	29063.34y	102
1	Flux Wire 5	Cu-63	29063.34y	102
1	Flux Wire 6	Cu-63	29063.34y	102
1	Flux Wire 7	Cu-63	29063.34y	102
1	Flux Wire 8	Cu-63	29063.34y	102
1	Flux Wire 9	Cu-63	29063.34y	102
1	Flux Wire 10	Cu-63	29063.34y	102
1	Flux Wire 11	Cu-63	29063.34y	102
1	Flux Wire 12	Cu-63	29063.34y	102
1	Flux Wire 13	Cu-63	29063.34y	102
1	Flux Wire 14	Cu-63	29063.34y	102
1	Flux Wire 15	Cu-63	29063.34y	102
1	Flux Wire 16	Cu-63	29063.34y	102
3	Rh103 foil	Rh-103	45103.34y	10004
3	In115 foil	In-115	49115.34y	10004
3	Ti47 foil	Ti-47	22047.34y	103
3	Ti46 foil	Ti-46	22046.34y	103
3	Ti48 foil	Ti-48	22048.34y	103
3	Ni58 foil	Ni-58	28058.34y	103
3	Zn64 foil	Zn-64	30064.34y	103
3	Fe54 foil	Fe-54	26054.34y	103
3	Fe56 foil	Fe-56	26056.34y	103
3	Cu63 foil	Cu-63	29063.34y	107
3	Nb93 foil	Nb-93	41093.34y	10016

Table 3.5. ATRC configuration for Irradiation 4.

Facility	Loading
Flux Traps	
NW	LIPT and 3.5-inch diameter aluminum filler
E	Safety rod, Chopped Dummy IPT (CDIPT), and Small Irradiation Housing Assembly (SIHA) with aluminum baskets containing three LSA cobalt capsules in all 7 positions.
S	Safety rod, Chopped Dummy IPT (CDIPT), and Small Irradiation housing Assembly (SIHA) with three LSA cobalt capsules in aluminum basket in S-7 position and six aluminum fillers in S-1 thru S-6
NE	Multiple Irradiation Capsule Experiment (MICE) facility with fueled MICE PRIME 1 capsule mockups in NW and SE positions; MICE filler plugs in the NE and SW positions. Shrouding described in Bettis letter B-MT(EDT)I-1171 and B-MT(EDT)I-1309
N	Safety rod, Standard Inpile Tube (SIPT), flow tube, and 1.5-inch diameter aluminum filler
W	Safety rod, Standard Inpile Tube (SIPT), flow tube, and 1.5-inch diameter aluminum filler
SW	Safety rod, Standard Inpile Tube (SIPT), flow tube, and 1.5-inch diameter aluminum filler
C	AFIP Dummy Test with one -inch diameter hole
SE	Dummy Flux Trap Filler, SIPT, flow tube with aluminum spacer, and 1.5-inch diameter aluminum filler
A Irradiation Facilities	
A-1 thru A-8	LSA Cobalt
A-9 through A-12	Aluminum filler
B Irradiation Facilities	
B-1 through B-8	"Y" aluminum flow restrictor
H Irradiation Facilities	
H-2 and H-10	Empty flux monitor wire holders
H-3 and H-11	N-16 flow tube mockup
H-1, H-4, H-5, H-6, H-7, H-8, H-9, H-12, H-13, H-14, H-15 and H-16	Aluminum basket containing three LSA cobalt capsules
I Irradiation Facilities	
I-1 through I-20	Aluminum filler except for positions I-3 and I-9 which contain log count rate detector thimbles
Fuel Elements	Forty ATRC standard fuel elements
Neck Shims	All inserted

3.2 KENO Modeling to Support ATRC Validation Experiments

Mark DeHart (INL) and Jorge Navarro (University of Utah)

In FY10, The development, verification, and initial validation of a KENO-VI model of the ATR was completed based on the IRPhE benchmark specification for the ATR 94-CIC core configuration (Kim and Schnitzler, 2008). During FY-11 the model was modified to match the ATRC configuration, much as was described in the previous section for the MCNP model.

3.2.1 ATRC Model Development

KENO-VI models were developed for both the Irradiation 1 and the Irradiation 4 configurations. Figure 3.6 provides an illustration of the KENO-VI model of the ATRC with beryllium and water regions removed to be able to visualize other structures. Figure 3.7 shows a cutaway of the KENO-VI model for the configuration of Irradiation 1, cut at the plane between halves of the irradiation wire/foil holder in the NW flux tram. Flux wires located in fuel positions are not visible in this figure. The Irradiation 4 configuration is similar, with the exception of the loading of the NW flux trap; Irradiation 4 used a solid aluminum dummy in the NW position, and added a number of flux wires in 3 radial locations in each of 8 fuel elements.

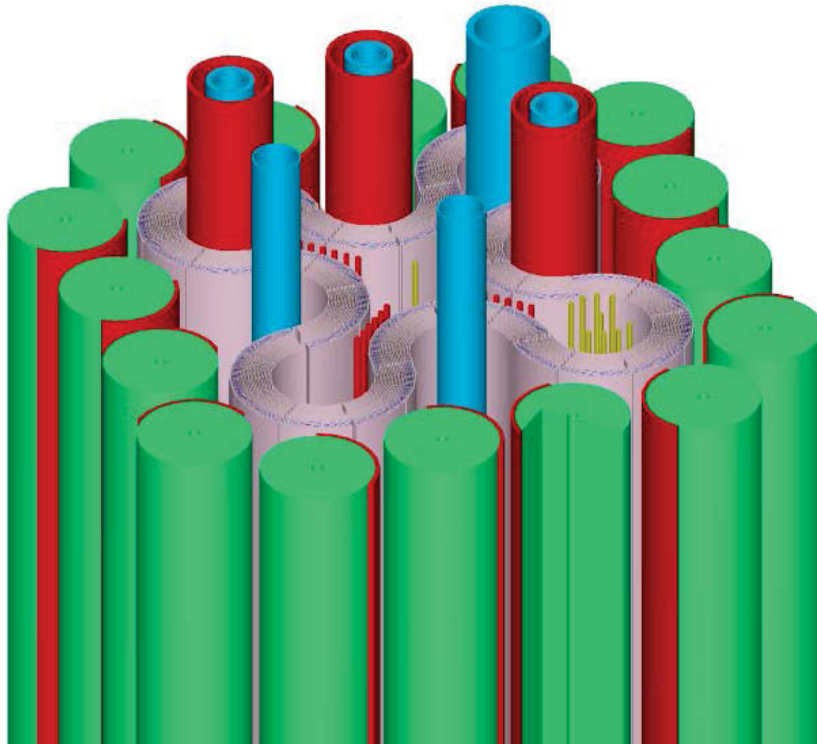


Figure 3.6. KENO-VI representation of ATRC with water and beryllium regions removed.

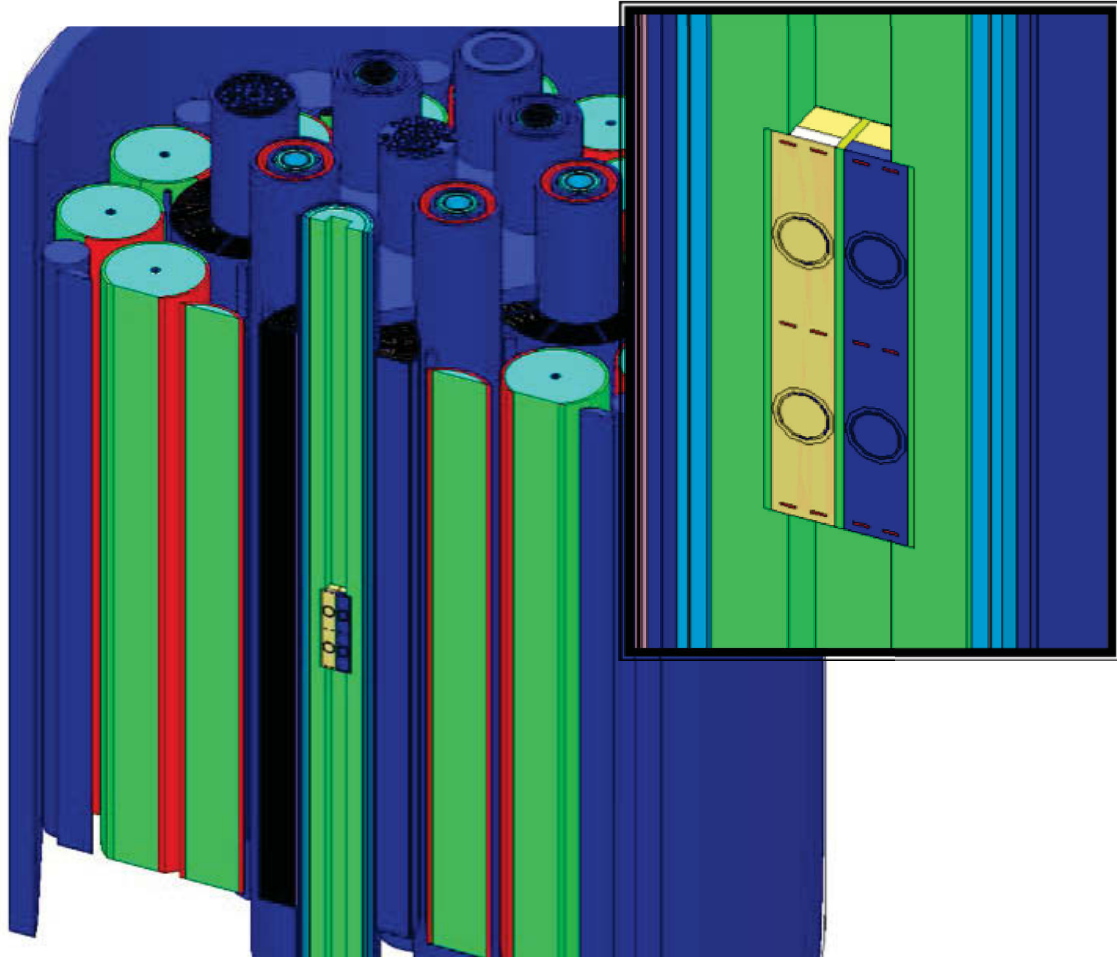


Figure 3.7. KENO-VI representation of Irradiation1 configuration.

3.2.2 Analysis Approach

Multigroup calculations performed in this work were based on a modified version of the BUGLE-80 group structure referred to here as the BUGLE+ library. The BUGLE (Broad User Group Library ENDF/B, Roussin, 1980) library was originally developed for LWR shielding and dosimetry calculations; the BUGLE-80 release was a coupled neutron-gamma library with 47 neutron energy groups and 20 gamma groups, and was derived (Hunter, 1994) from a 199-neutron/42-gamma group library named VITAMIN-E (Versatile Integrated Techniques using AMPX and MINX for Investigating Neutronics ENDF/B). In the current work, the 47-neutron-group structure was expanded to provide additional thermal resolution. Beginning with the SCALE ENDF/B-VII 200/53-group library (which has evolved from VITAMIN-E and remains a superset of the original 47/20 energy group BUGLE structure), a revised cross section library was generated collapsed to 53 neutron energy groups; the gamma cross sections are not needed in this work and were not carried into the new BUGLE+ library. Table 3.6 provides the energy group structure for the BUGLE+ library.

Table 3.6. Group structure for BUGLE+ cross-section library.

Group No.	Upper Energy (eV)	Group No.	Upper Energy (eV)
1	2.0000E+07	28	6.7379E+04
2	1.4918E+07	29	4.0868E+04
3	1.2214E+07	30	3.1828E+04
4	1.0000E+07	31	2.6058E+04
5	8.6071E+06	32	2.4176E+04
6	7.4082E+06	33	2.1875E+04
7	6.0653E+06	34	1.5034E+04
8	4.9659E+06	35	7.1017E+03
9	3.6788E+06	36	3.3546E+03
10	3.0119E+06	37	1.5846E+03
11	2.7253E+06	38	4.5400E+02
12	2.4660E+06	39	2.1445E+02
13	2.3653E+06	40	1.0130E+02
14	2.3457E+06	41	3.7266E+01
15	2.2313E+06	42	1.0677E+01
16	1.9205E+06	43	5.0435E+00
17	1.6530E+06	44	3.0590E+00*
18	1.3534E+06	45	1.8554E+00
19	1.0026E+06	46	1.1253E+00*
20	8.2085E+05	47	8.7643E-01
21	7.4274E+05	48	4.1399E-01
22	6.0810E+05	49	1.8400E-01*
23	4.9787E+05	50	1.0000E-01
24	3.6883E+05	51	4.0000E-02*
25	2.9721E+05	52	1.4500E-02*
26	1.8316E+05	53	5.0000E-03*
27	1.1109E+05	-	1.0000E-05

* New energy boundaries added to BUGLE-80 structure to create BUGLE+ library.

The first attempt to calculate fluxes was performed using KENO-VI with 10,000 generations of 2000 neutrons per generation (2×10^7 total neutrons) after skipping 500 generations. Because KENO-VI is not able to run in parallel, this calculation required several days of CPU time, and yielded unacceptable statistics for the flux wires and foils in the NW LIPT. KENO-VI does allow for user specified biasing for certain materials, but support staff at ORNL (Petrie, 2010) recommended against using biasing within KENO-VI for flux wires located within the fuel region. Hence, it was decided that a purely KENO-VI approach would not be feasible. However, within the SCALE system, the MAVRIC sequence has been developed to facilitate calculations of this nature. MAVRIC (Monaco with Automated Variance

Reduction using Importance Calculations) uses the Monaco Monte Carlo computer code for shielding calculations, with variance reduction; this feature enables the code to obtain statistically similar results as a standard Monte Carlo code in shorter periods of time. MAVRIC uses a hybrid technique based on a Consistent Adjoint-Driven Importance Sampling (CADIS) methodology that combines a discrete ordinates method with Monte Carlo calculations. The MAVRIC sequence performs a three-dimensional coarse mesh discrete ordinates calculation using Denovo to obtain energy and position dependent adjoint fluxes that are then used to build an importance map. The information obtained by Denovo (importance map and biased source) is then passed to Monaco within the MAVRIC calculational sequence.

To model Irradiation 1 a two-step process was performed in order to determine the flux and activation of the experiment foils, experiment flux wires and fuel wires. First a neutron source distribution is generated using KENO-VI; this source is used to drive a fixed-source MAVRIC calculation to obtain fluxes in wires and foils. The results of the calculations were then used in calculations to obtain adjusted “best-estimate” two-group and six-group fluxes at each target location as described in Section 4.

The first step consisted of a KENO-VI calculation within the SCALE CSAS6 sequence, using 1300 generations of 2000 neutrons per generation (skipping the first 300 generations for source convergence) and the BUGLE+ library. The CSAS6 sequence performs a complete analysis that includes generation of problem-dependent cross sections and the calculation of k-eff. The generation of problem-dependent cross sections itself is a multistep process that first invokes BONAMI to perform resonance self-shielding calculations in the unresolved resonance range using the Bondarenko shielding factor method. This is followed by a CENTRM 1-D discrete ordinates calculation that uses point-wise cross section data to calculate point-wise fluxes in the resolved resonance energy range and Multigroup cross-sections above and below resonance energies. Finally, PMC uses the point-wise flux solution from CENTRM to generate multigroup cross sections. The resultant cross-section library was then used by KENO-VI to perform a neutron transport simulation to estimate the neutron source distribution on a three dimensional Cartesian mesh.

The second step in the process was to create a MAVRIC sequence input to calculate the fluxes within foils and wires. The MAVRIC sequence performs a complete system analysis including the same multistep process used by CSAS6 to generate problem dependent multigroup cross section data using BONAMI, CENTRM and PMC. The multigroup cross sections generated were then used by the Denovo module within MAVRIC to perform a discrete ordinates calculation to determine the adjoint fluxes as function of energy and location. The adjoint fluxes were then used by MAVRIC to build the importance map needed by the Monte Carlo module Monaco to perform a fixed source calculation to obtain the desired fluxes. Monaco shares the same geometry specification as KENO-VI, thus the MAVRIC sequence case was built using the same geometry model that was used in the CSAS6 case. MAVRIC also read the source mesh created with KENO-VI as a starting neutron source.

Monaco offers three different options to tally fluxes: region, mesh and point detectors. For this particular problem point detector tallies were selected because they yielded the best statistics for a given run time. Point detectors tallies are regions in which Monaco computes the uncollided and collided flux for all the energy groups using variance reduction techniques. For this problem thirty-four point detectors were positioned inside each experiment foil material, fuel flux wire and experiment flux wire. Once the number and location of the point detectors were defined two different MAVRIC cases were run with 10,000 batches of 10,000 neutrons per batch. However, calculations were set to end after 7200 CPU-minutes (5 CPU-days). Monaco is programmed to do a normal termination following the first complete batch after the time limit is reached.

Two MAVRIC cases were prepared in order to obtain data for spectrum adjustment calculations. The first case represented the perturbed state; in which the foil and wire materials were defined based on

irradiation 1 experiment logbook notes. The second input modeled the unperturbed case in which the materials were voided for the experimental flux wires and foils, while the materials for the fuel flux wires were specified as water. For each calculation MAVRIC created individual output files for each detector in the form of text files that contained detailed energy-dependent distributions. The analysis of the results obtained so far with the SCALE 6.1 package are described in Section 4.

3.3 ATTILA Modeling to Support ATRC Validation Experiments

D. Scott Lucas (INL) and Mark DeHart (INL)

This section describes the ATTILA™ (ATTILA) Radiation Transport model validation effort during FY-11 via comparisons of calculated data to earlier measurements performed during the 1994 ATR Core Internals Changeout (CIC-94), and the ATRC 94-2 and ATRC 94-2' experiments. Models were also developed for FY-12 analysis of ATRC Irradiations 1 through 4, conducted during FY-11 as part of the Modeling Update Project.

For purposes of the present discussion, validation with respect to experimental data includes:

1. Having a correct physical model of the problem.
2. Having reliable nuclear data (“cross section input”) can represent experimental behavior without “tuning” the model to the data.
3. Being able to prove convergence of the code and model for finer grids with respect to the experimental data.
4. Being able to “illustrate” the results with plots and 3D representations that are discernible by plant staff and operations, i.e., one picture is worth a thousand words.

3.3.1 Model Description

The ATTILA code is a three dimensional neutron transport code that uses the Linear Discontinuous Galerkin (LDG) solution technique which is second order spatially accurate for point quantities and third order accurate for integral quantities, such as reaction rates. Geometry is represented in ATTILA using Para Solid™ (PS) files made from models in Solid Works™ (SW). Solid Works™ is a CAD/CAM code, similar to ProE or Inventor. The model is made in SW and saved to a Para Solid™ file that can be read into ATTILA to be used for meshing. The meshing tool in ATTILA is from Simmetrix, it allows surface meshing with triangles and quads and volume meshing with Tetrahedral finite elements. The 3D and “thin 3D” (basically 2D transaxial) Solid Works™ models for ATR and ATRC used in this work are shown in Figures 3.8 through 3.15 below. The meshes in the models vary from one hundred thousand tetrahedra to five million depending on a thin 3D or a full 3D model with reflectors.

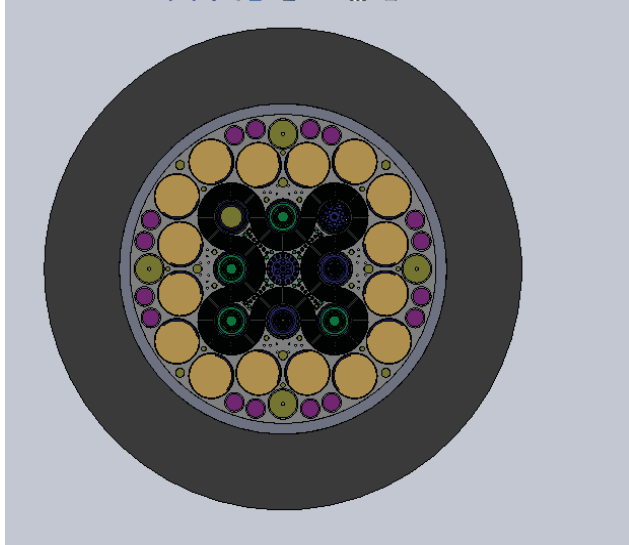


Figure 3.8 ATR CIC-94 SW model

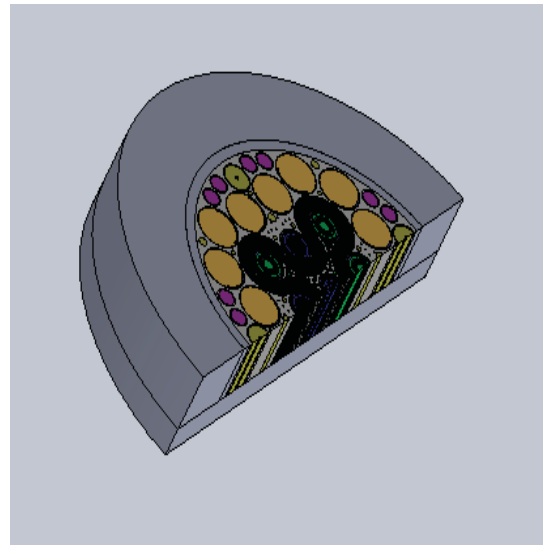


Figure 3.9 ATRC CIC-94 & reflectors

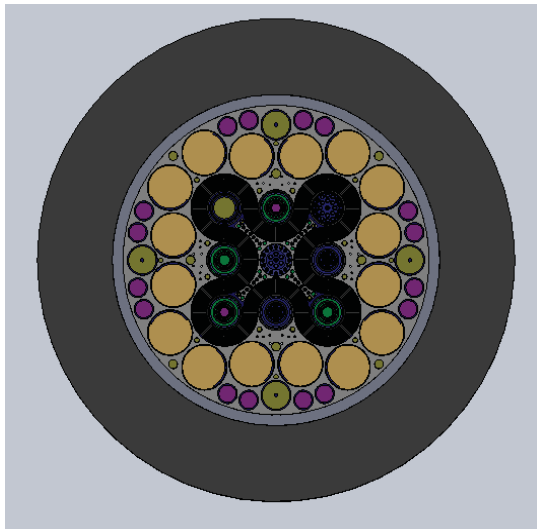


Figure 3.10 ATRC 94-2 model

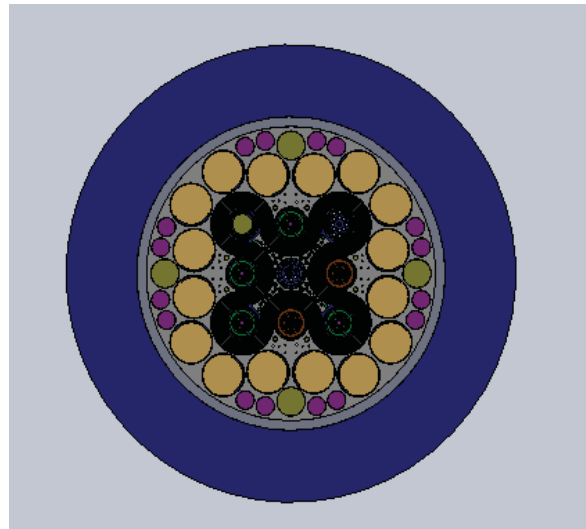


Figure 3.11 ATRC 94-2' model

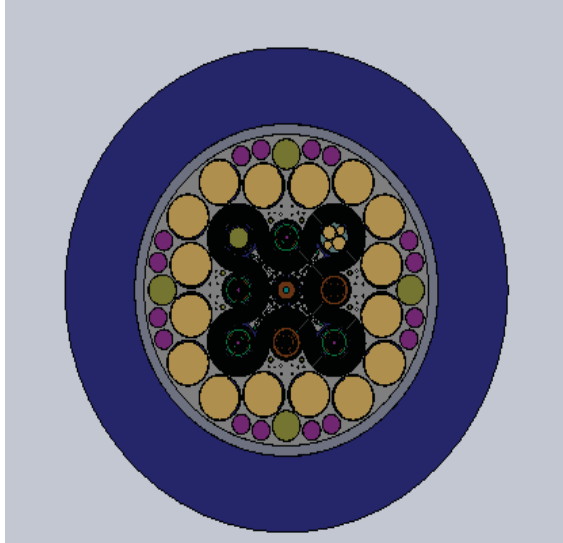


Figure 3.12 ATRC Irradiation 4 model

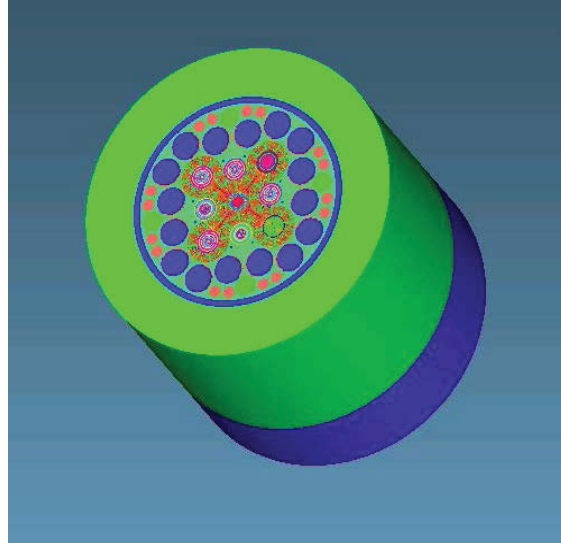


Figure 3.13 ATRC Irradiation 4 3D model

3.3.2 Results and Comparisons

All calculations were performed with a discrete ordinates S4 angular integration (quadrature) and P3 scattering. The calculations used a convergence criterion of 0.0001 with 100 inner and 50 outer iterations. The calculations were performed for CIC-94, 94-2, 94-2' and for Irradiation 4 of the current ATRC experiment series.

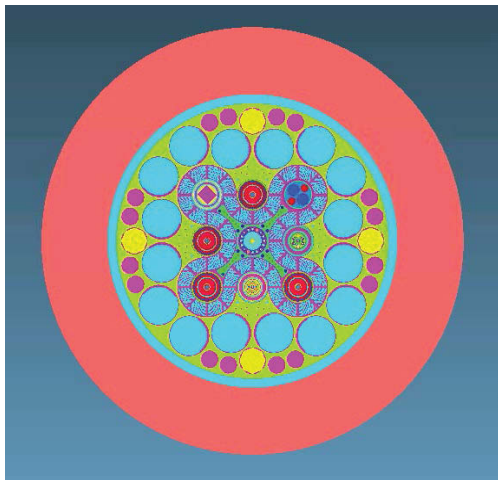


Figure 3.14 ATRC Irradiation 1 3D model.

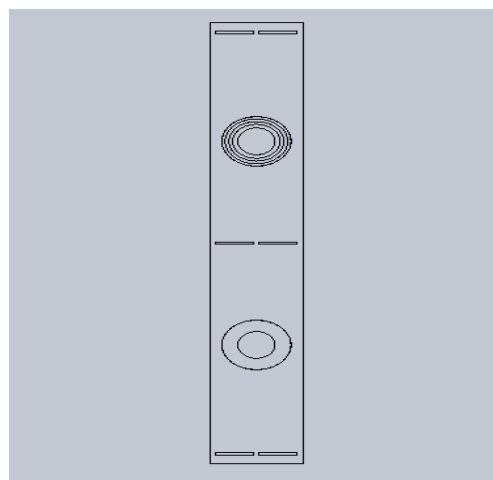


Figure 3.15 ATRC Irradiation 1 foil positioning plate model

3.3.2.1 ATR & ATRC Model Comparisons

The first results are those shown for the ATR CIC-94 comparisons. Figure 3.16 shows fuel element power distribution comparisons for MCNP, ATTILA and the ATR and ATRC data. This model used 64 CPU's on the Ice storm Cluster and ran for approximately two hours. The computed critical eigenvalue (K_{eff}) was 1.01.

The next results that were obtained are for the ATRC CIC-94 model compared to the ATRC CIC-94 data directly, shown in Figure 3.17. This model was executed on a Windows PC using one hundred inner and fifty outer iterations, collapsed to nine energy groups using the spectral averaging in ATTILA. The run took three hours. The calculated K_{eff} is 1.02. Table 3.7 shows the relevant data. Figures 3.18 and 3.19 show the flux map and the geometry.

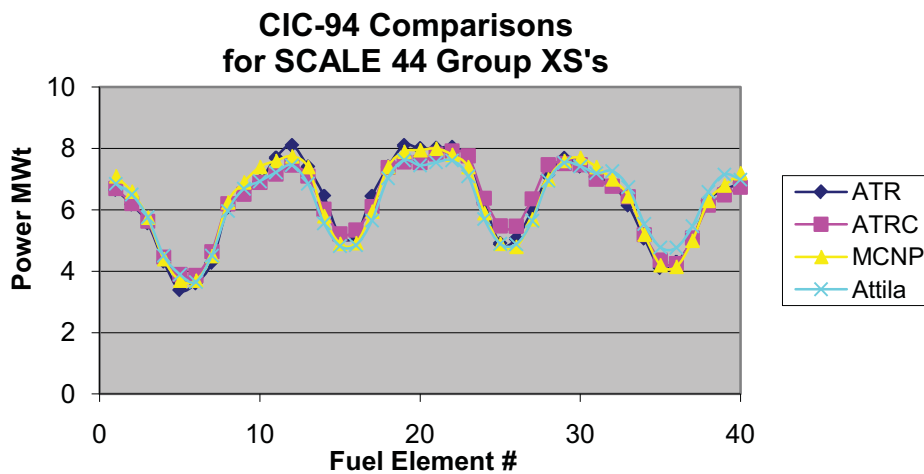


Figure 3.16 ATR ATTILA model results compared to CIC-94 data

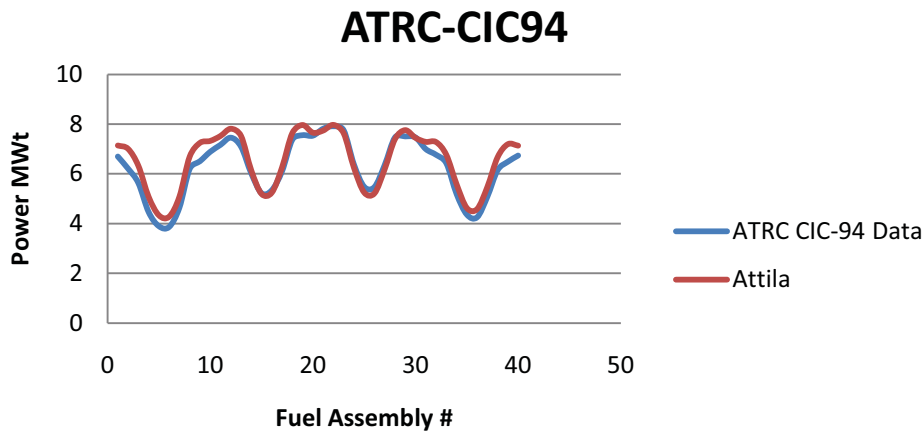


Figure 3.17 ATRC ATTILA model results compared to CIC-94 data

Table 3.7 ATRC CIC-94 ATTILA iteration data.

Summary for outer iteration:	50
Relative delphi	: 1.727E-02
Relative balance	: -4.270E-06
Spectral radius	: 0.935
k eigenvalue	: 1.021E+00
Lambda minus one	: 6.981E-08

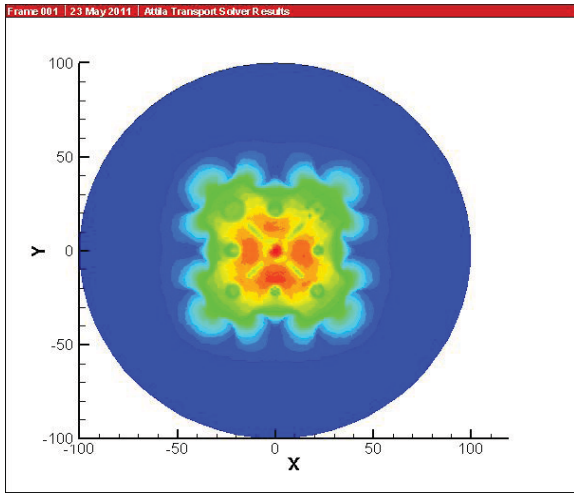


Figure 3.18 ATRC 94 CIC flux Map

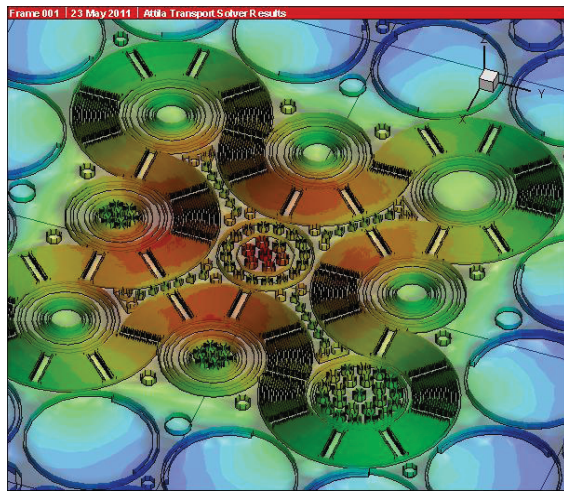


Figure 3.19 ATRC 94 CIC geometry

3.3.2.2 ATRC 94-2 Model Comparison

The next comparison is for the ATRC 94-2 experiment. The reference for the model is that of McCracken, et al. (1994). The reference describes the fuel, flux trap assemblies and shim positions used in the experiment. This reference was used for both the 94-2 and 94-2' tests. For both 94-2 and 94-2' tests, the data is only given for every other fuel assembly. Symmetry about the flux traps was used for plotting the experimental data with the calculations. The ATTILA results are computed for each fuel assembly. The comparisons are shown in Figure 3.20 and 3.21. Table 3.8 provides a summary of the calculation.

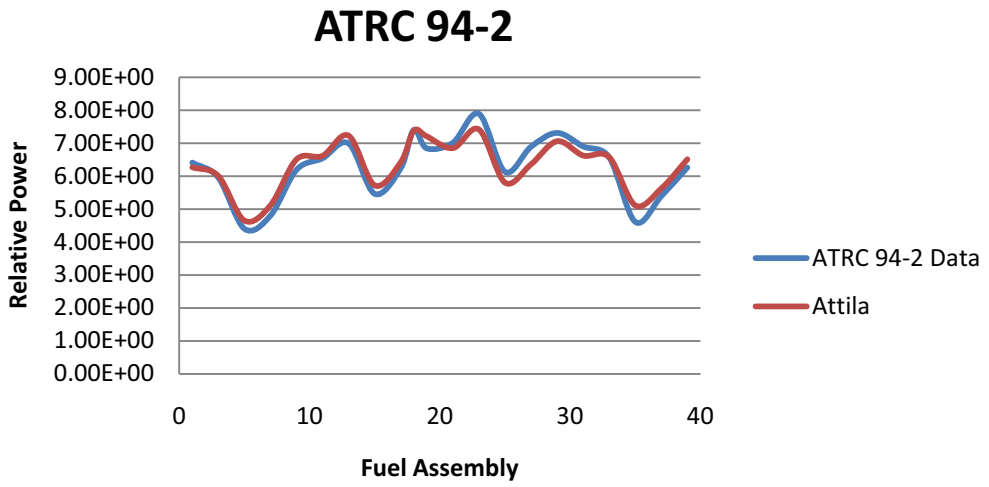


Figure 3.20 ATRC CIC 94-2 element power results

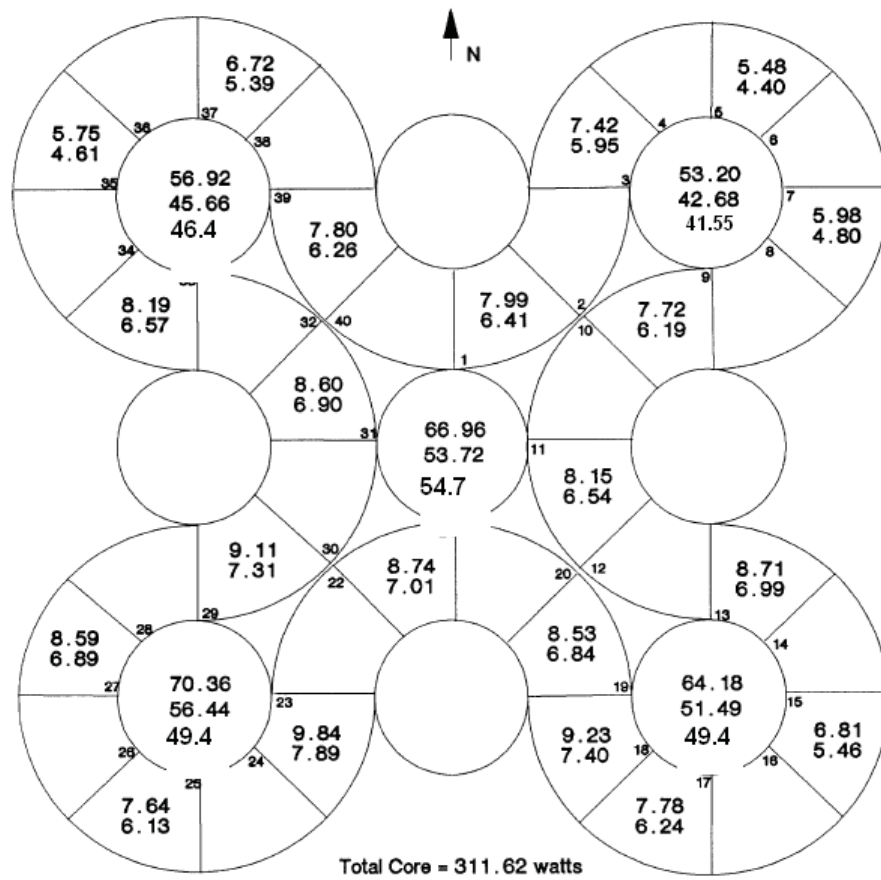


Figure 3.21. ATRC CIC 94-2 lobe power results

Table 3.8 ATTILA iteration summary for ATRC CIC 94-2

k Eigenvalue Search Summary:
 Outer Iterations : 50
 Converged k-eff : 1.0418250
 Converged Lambda - 1 : 4.076E-06

3.3.2.3 ATRC 94-2' Model Comparison

The ATRC 94-2' model ran for approximately two hours on a Windows PC with two CPU's for the Bugle+ 53 Group cross-section library and approximately twenty two minutes with 64 CPU's on Ice storm for the SCALE 44 Group library. A convergence criterion of 0.0001 was used for both runs. The results for each run are shown in Tables 3.9 and 3.10.

Table 3.9 ATTILA iteration summary for ATRC 94-2' with Bugle+ library

Summary for outer iteration: 179
 Relative delphi : 9.914E-05
 Relative balance : -1.574E-07
 Spectral radius : 0.926
 k eigenvalue : 1.000E+00
 Lambda minus one : 1.612E-11
 k Eigenvalue Search Summary:
 Outer Iterations : 179
 Converged k-eff : 1.0003399
 Converged Lambda - 1 : 1.612E-11

Table 3.10 ATTILA iteration summary for ATRC 94-2' with SCALE 44 group library

Summary for outer iteration: 162
 Relative delphi : 9.634e-05
 Relative balance : -1.748e-09
 Spectral radius : 0.947
 k eigenvalue : 1.103e+00
 Lambda minus one : 5.420e-09
 Run time (s) : 1318.7145
 k eigenvalue search summary
 Outer iterations : 162
 Converged k-effective : 1.1028063
 Converged lambda - 1 : 5.420e-09

A comparison of the two runs with differing cross-section libraries is shown in Figure 3.22. Tables 3.9 and 3.10 along with Figure 3.22 indicate that the Bugle library produces better results for the 94-2' experiment. Figures 3.23 and 3.24 show the ATTILA model geometry and the flux plot for the comparison to experiment 94-2'.

Attila 94-2' SCALE Bugle53 & SCALE 44 Group XS's

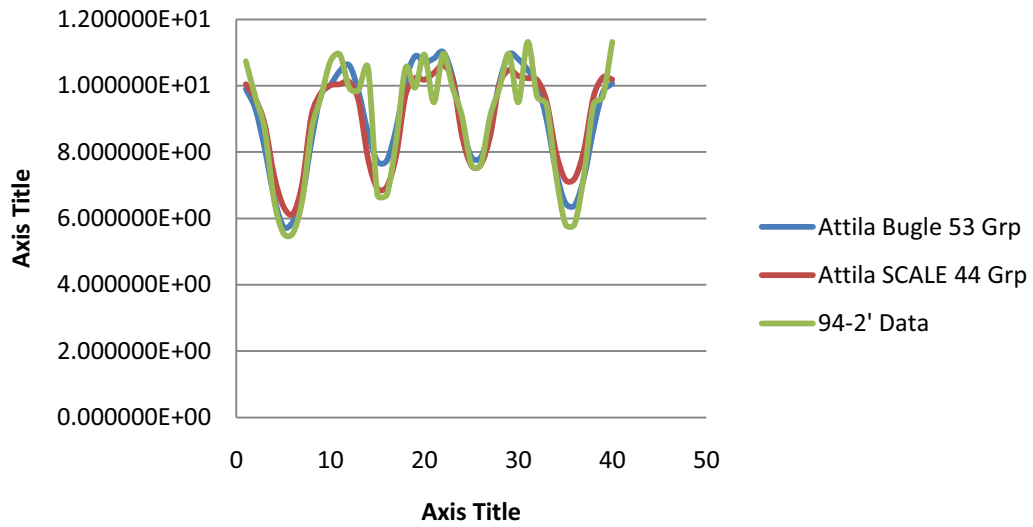


Figure 3.22 ATTILA element power results for ATRC 94-2'.

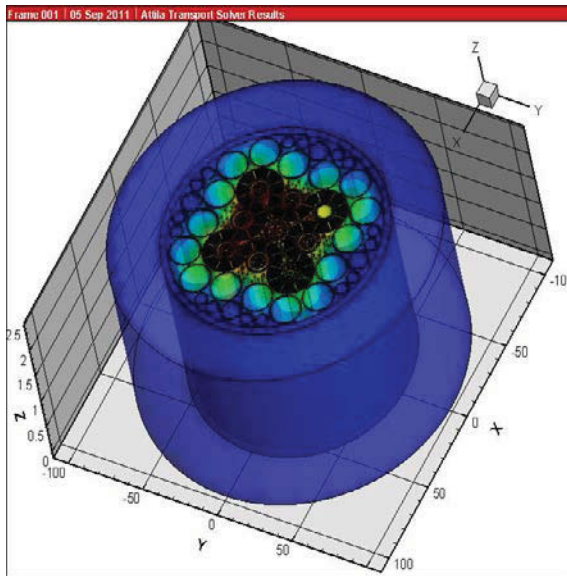


Figure 3.23 ATTILA geometry for ATRC 94-2'

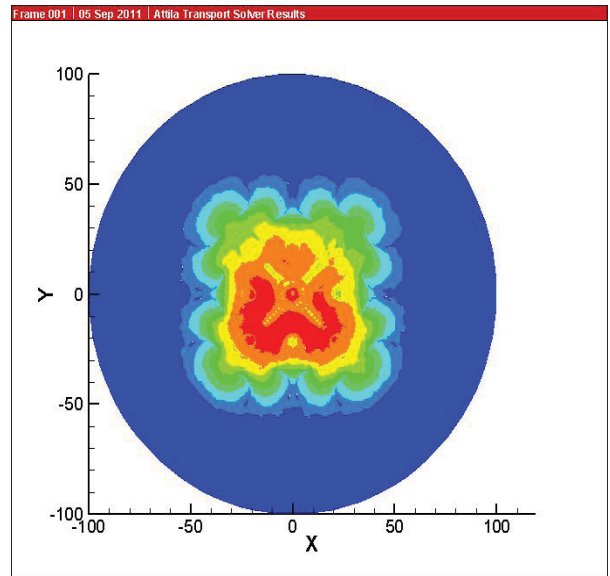


Figure 3.24 ATTILA flux map for ATRC 94-2'

3.3.2.4 Initial ATRC Irradiation 4 Model Comparison

ATRC Irradiation 4 used Au/Cu wires at three locations in eight even numbered fuel elements at the axial midplane. These were elements 12, 14, 16, and 18 surrounding the SE IPT and elements 32, 34, 36, and 38 surrounding the NW LIPT. The wires were placed as shown in Figure 3.25. The construction of the SW model used horizontal wires from the mid position extending leftward, exactly as they were placed in the element. The wires were modeled as unstructured objects in SW (unstructured means the code is not restricted in doing the meshing) for easier meshing in ATTILA.

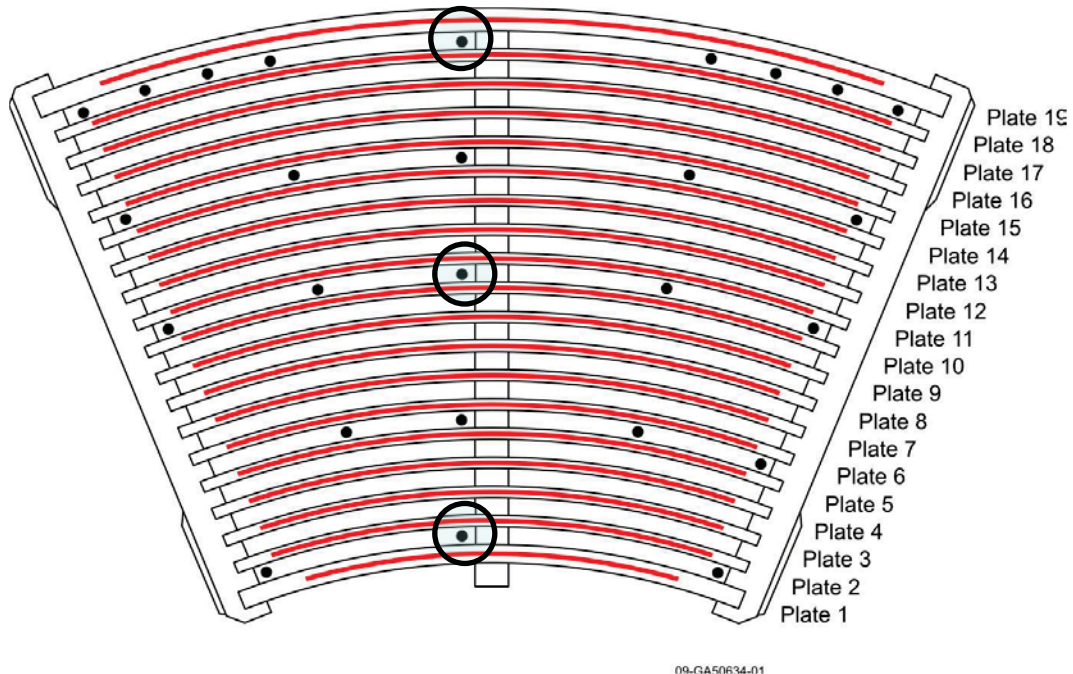


Figure 3.25. ATRC Fuel Element showing available flux wire positions and the three instrumented positions used for Irradiation 4.

Two ATTILA cases were executed for Irradiation 4, the thin 3D and the full 3D with reflectors, both using the Bugle 53 Group cross-section set. The thin 3D model used 135,000 tetrahedral elements for the mesh and the full 3D model used three million elements in the mesh. The thin 3D model was executed on a Windows Laptop with 2 CPU's in 45 minutes using nine energy groups and the 3D model took approximately three hours with 128 CPU's on the Ice storm cluster for both the un-perturbed and perturbed flux cases. These cases were performed due to the post processing program used. The results for the computed power distribution are shown in Figures 3.26 and Figure 3.27. The data from the 3D case with reflectors and the full 53 Group Bugle+ library will also be used in FY-12 for direct least-squares validation against the measured flux wire data as discussed in Section 4.

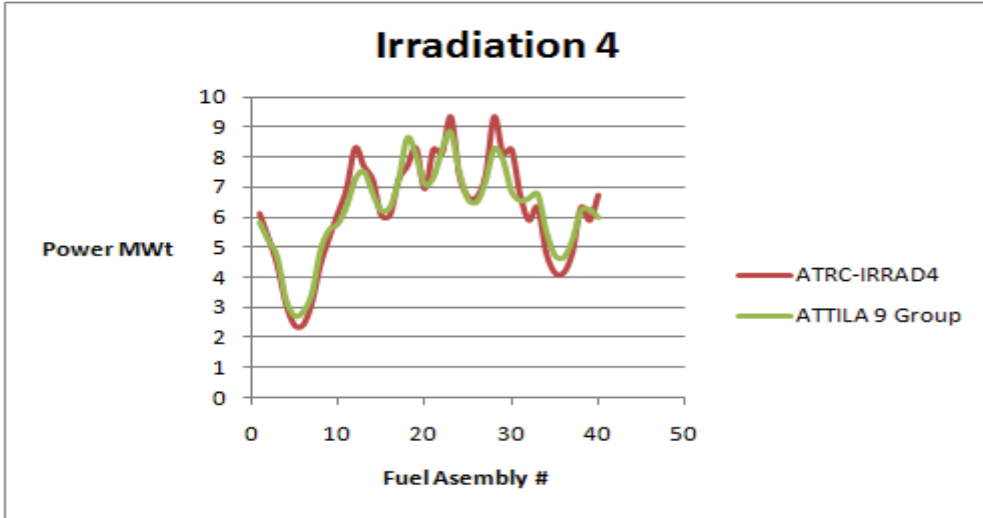


Figure 3.26. Irradiation 4 element power distributions

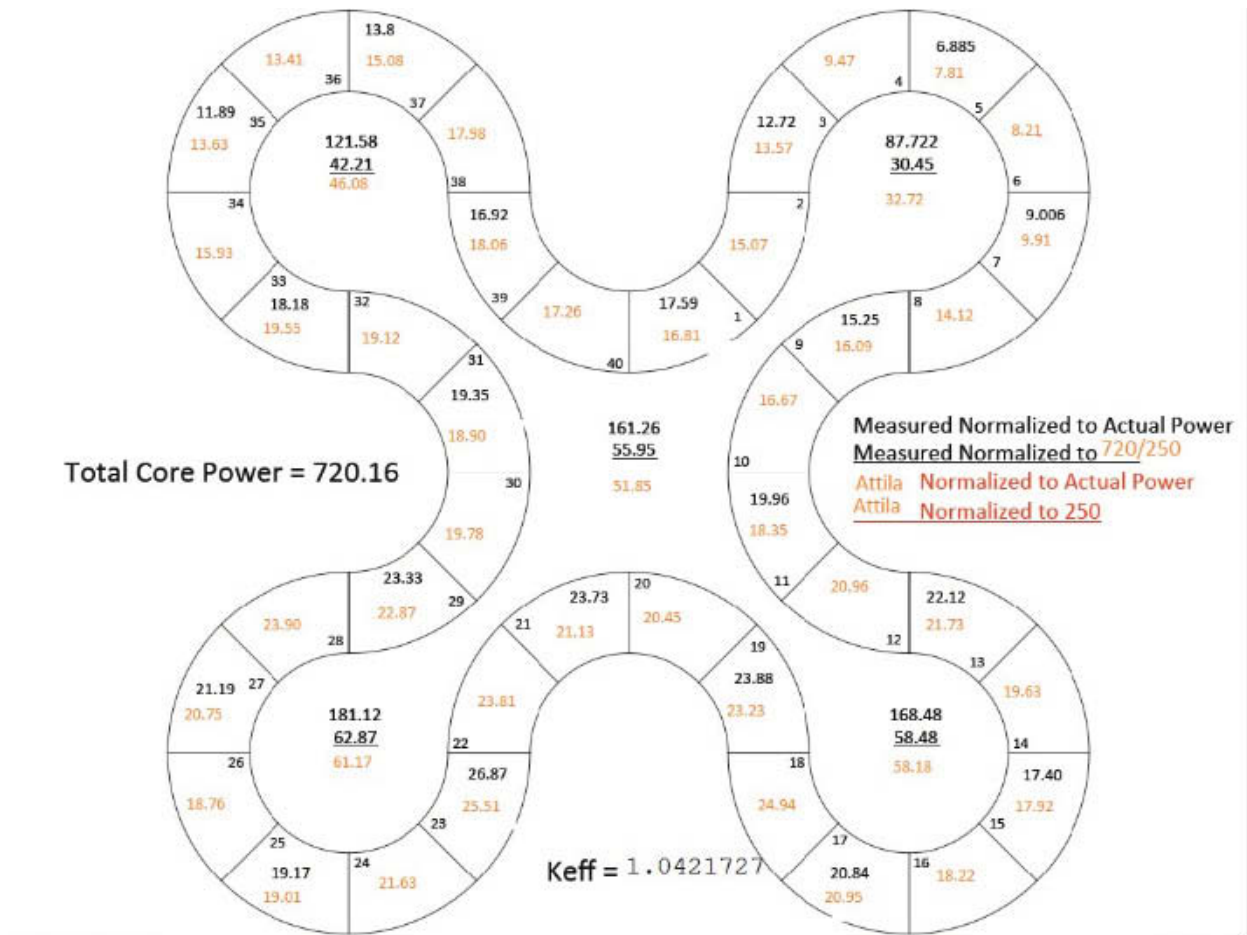


Figure 3.27. Irradiation4 power distribution comparison.

3.3.2.5 ATRC Irradiation 1 Model

A model for the ATRC Irradiation 1 configuration was also constructed for use in FY-12. The North West Flux Trap Large Inpile Tube (LIPT) contains an aluminum holder with various foils and Cu/Au wires as described in Section 4. The SW model of the holder with foils and wires is shown in Figure 3.28. The solid and meshed foils and wires are shown in Figures 3.29 and 3.30. The seven layer meshed model of the NW LIPT insert with 3.5 million elements is shown Figure 3.31.

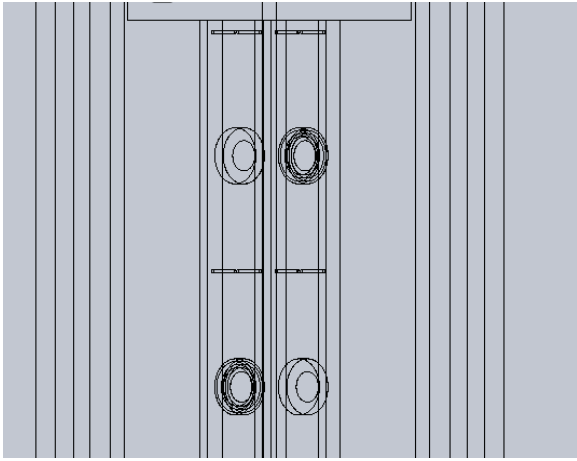


Figure 3.28. SW model of foil positioning plate

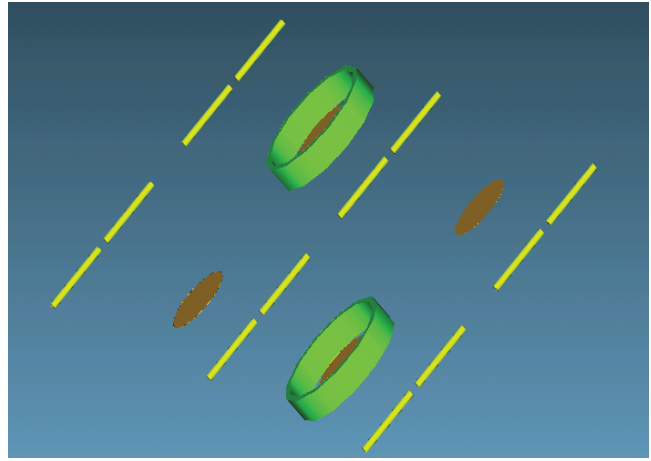


Figure 3.29. Foils and wires used in Irradiation 1

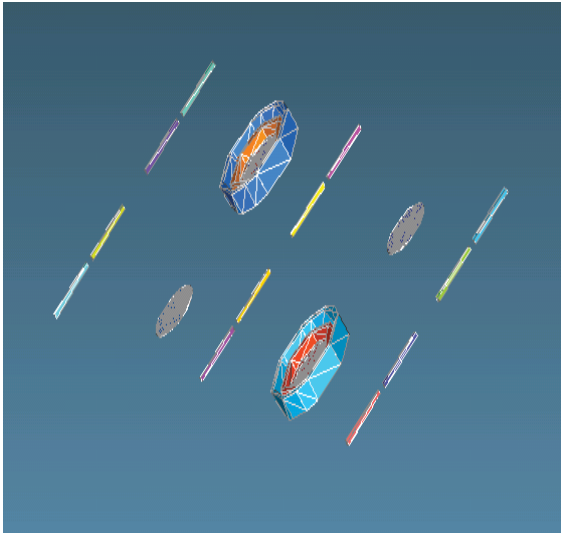


Figure 3.30. Meshed foils and wires

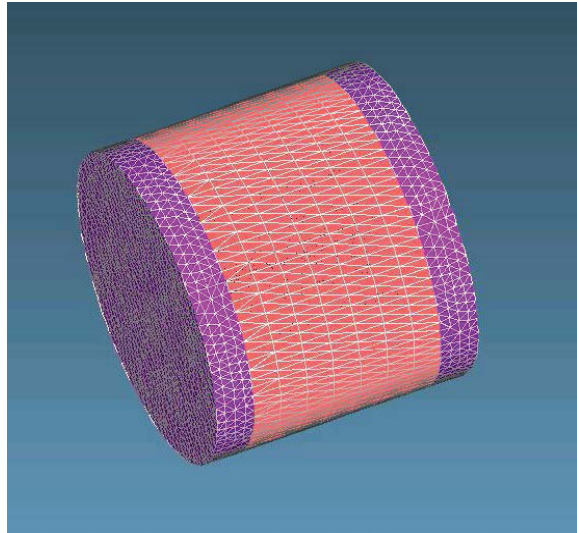


Figure 3.31. 3D meshed LIPT insert model

3.3.3 Summary

The comparisons of ATTILA to the available data at this point indicate that it can readily be used as a 3D and as a thin 3D (quasi-2D) analysis too for various ATR and ATRC applications, especially for experiment support and model validation. The meshing capability has improved greatly along with runtime enhancements.

3.4 NEWT Modeling to Support ATRC Validation Experiments

James Parry (INL)

The NEWT (New ESC-based Weighting Transport code) computer code as a multigroup discrete-ordinates transport code with flexible meshing capabilities that allow two-dimensional neutron transport calculations using complex geometric models. The NEWT differencing scheme is based on the Extended Step Characteristic (ESC) approach for spatial discretization on an arbitrary mesh structure. Newt collapses cross section libraries into specified group structures for each nuclide in each material mixture in the model. Cross sections are flux weighted by using the average flux in the mixture (material) for each energy group in the library. As part of the SCALE code package (Bowman, 2011), NEWT is capable of performing fuel burnup calculations using the ORIGEN-S module of SCALE.

3.4.1 NEWT ATRC Model Development

A full core two-dimensional (2D) model of the Advanced Test Reactor Critical Facility (ATRC) was generated for the NEWT computer code (Figure 3.32). The model is based on the information provided in the ATR Critical Facility Core Reconfiguration (McCracken et al. 1994). Four different ATRC core configurations were modeled in NEWT. The four configurations were designated as 94-1, 94-2, 94-2', and 94-3. Configurations 94-1 and 94-2 use what is designated as standard ATRC fuel elements, which nominally contain 975 g of U-235. Each plate contains boron as a burnable poison. Configurations 94-2' and 94-3 both use what is designated as zone loaded fuel elements which are the standard ATR Mark VII fuel elements. There are 3 different experiment loadings for the four core configurations. Configuration 94-1 has a unique experiment loading. The experiment loading for configurations 94-2 and 94-2' are identical and different than the 94-1 configuration. Only the driver fuel type is different between the 94-2 configuration and the 94-2' configuration. Configuration 94-3 has a unique experiment loading that is different from both the 94-1 configuration and the 94-2 and 94-2' configurations.

Results from the developed NEWT models were compared to the experimental data published in ATR Critical Facility Core Reconfiguration (McCracken et al. 1994). The K_{eff} for each of the configurations is provided in Table 3.11 with the assumption that each core configuration measured K_{eff} was equal to 1.000. The power distribution for configurations 94-1, 94-2, and 94-3 are compared to the measured distributions in Figure 3.33 through Figure 3.35. The results of these comparisons indicate the models represent the actual core reasonably well at this point in the development.

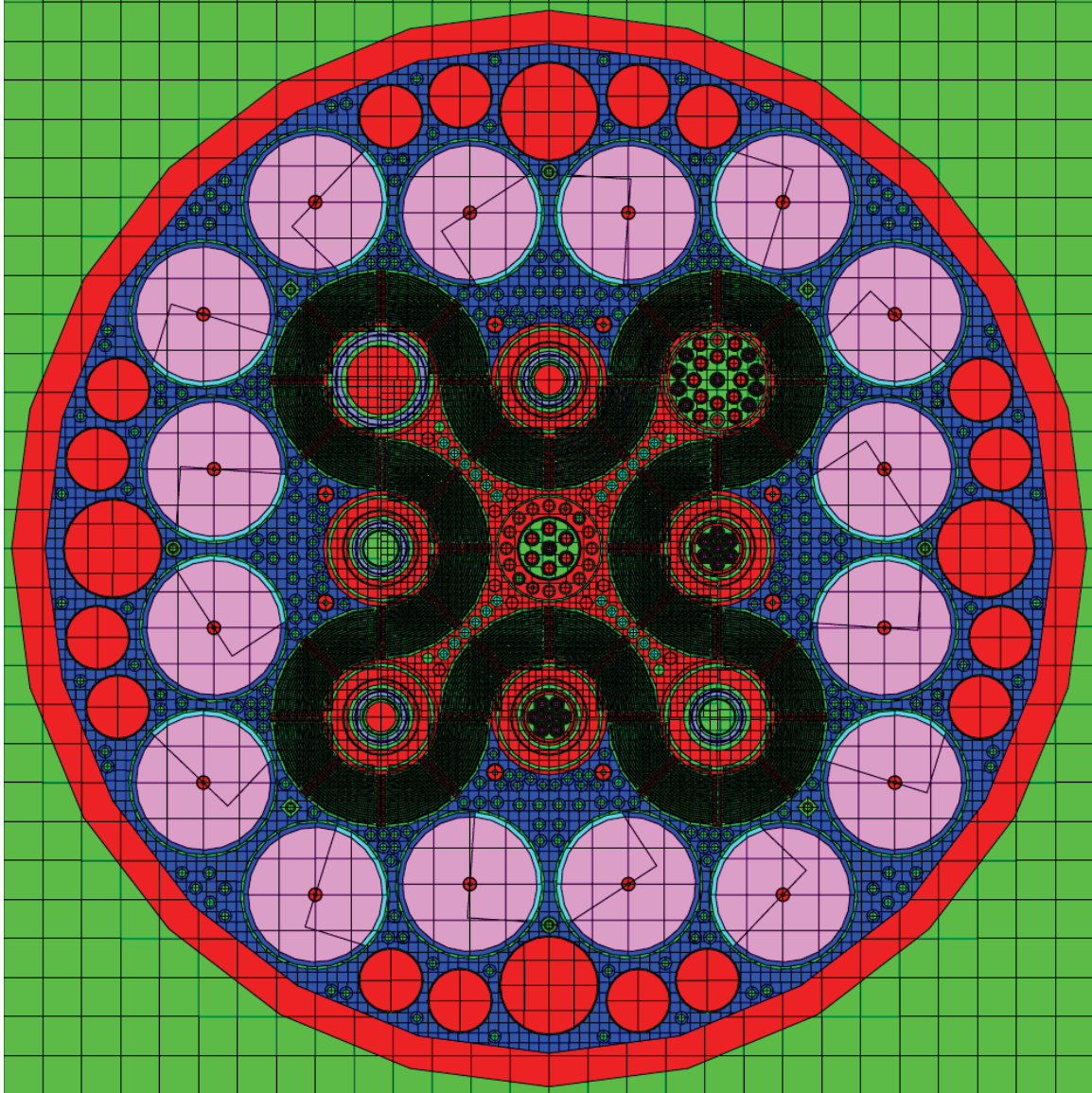


Figure 3.32. NEWT model of the ATRC.

Table 3.11. Calculated K_{eff} for the NEWT models of the four different ATRC configurations.

Configuration	NEWT K_{eff}
94-1	0.9942
94-2	0.9895
94-2'	0.9921
94-3	0.9908

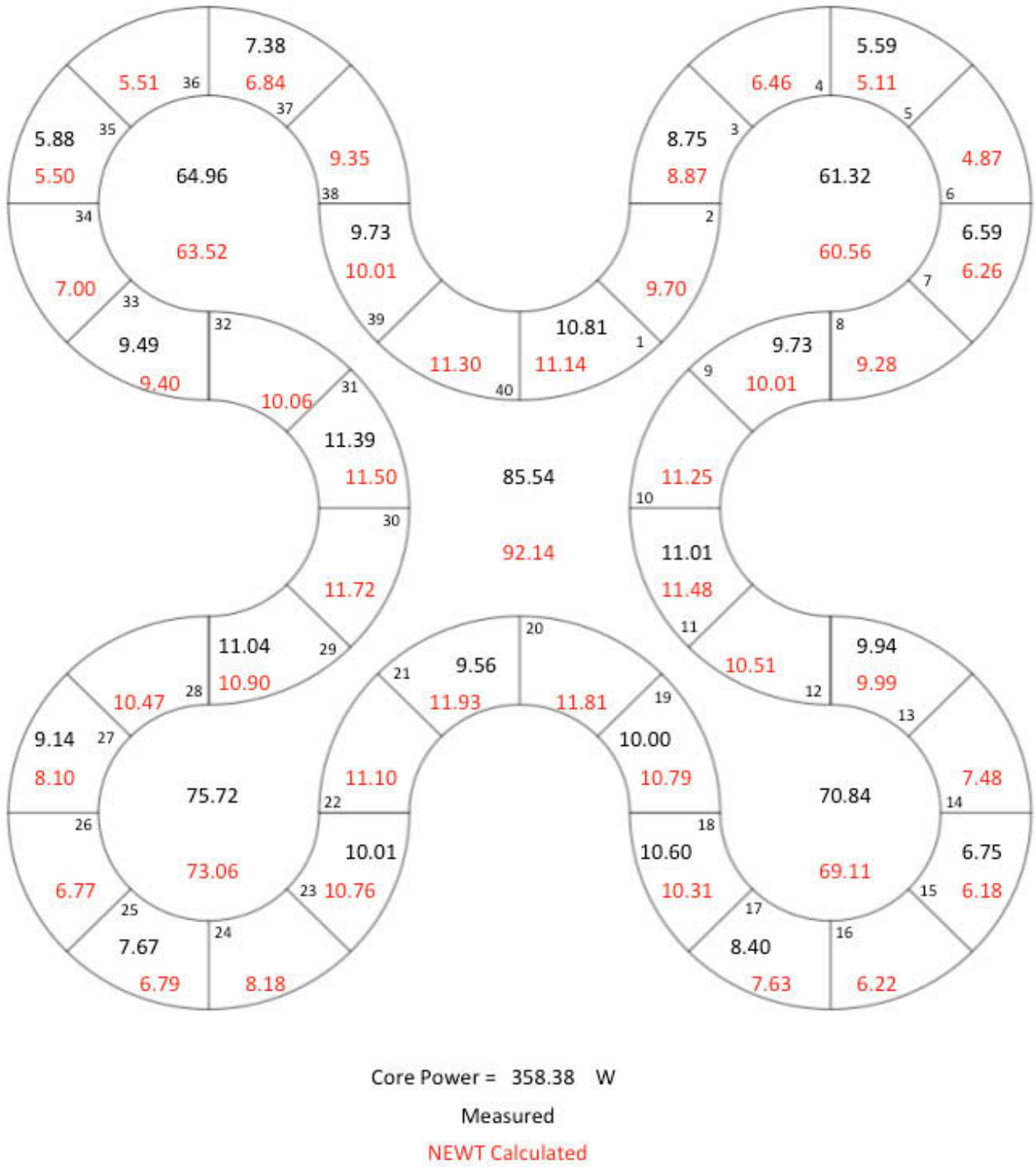
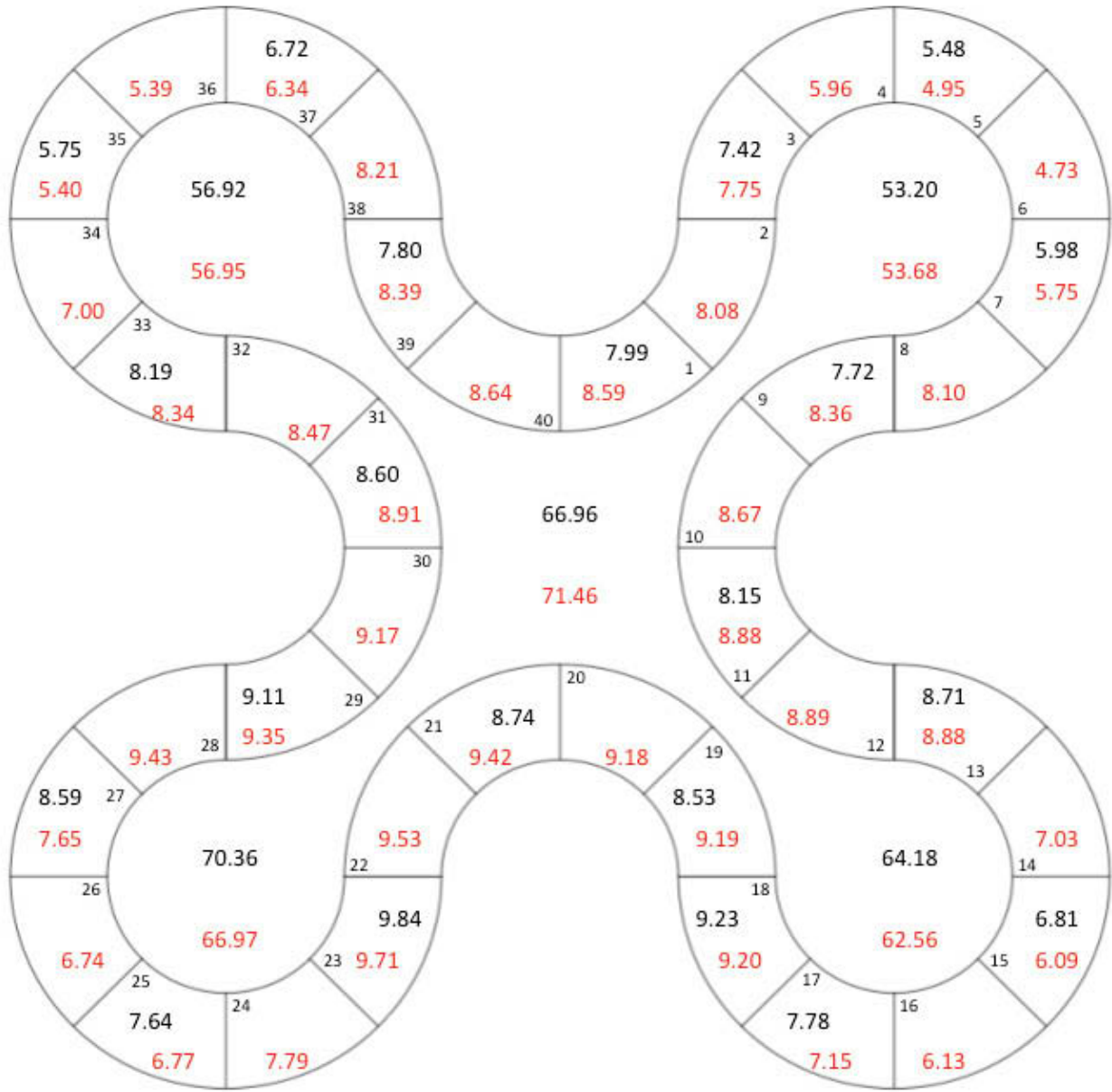


Figure 3.33. Power distribution for ATRC configuration 94-1.



Core Power = 311.62 W

Measured

NEWT Calculated

Figure 3.34. Power distribution for ATRC configuration 94-2.

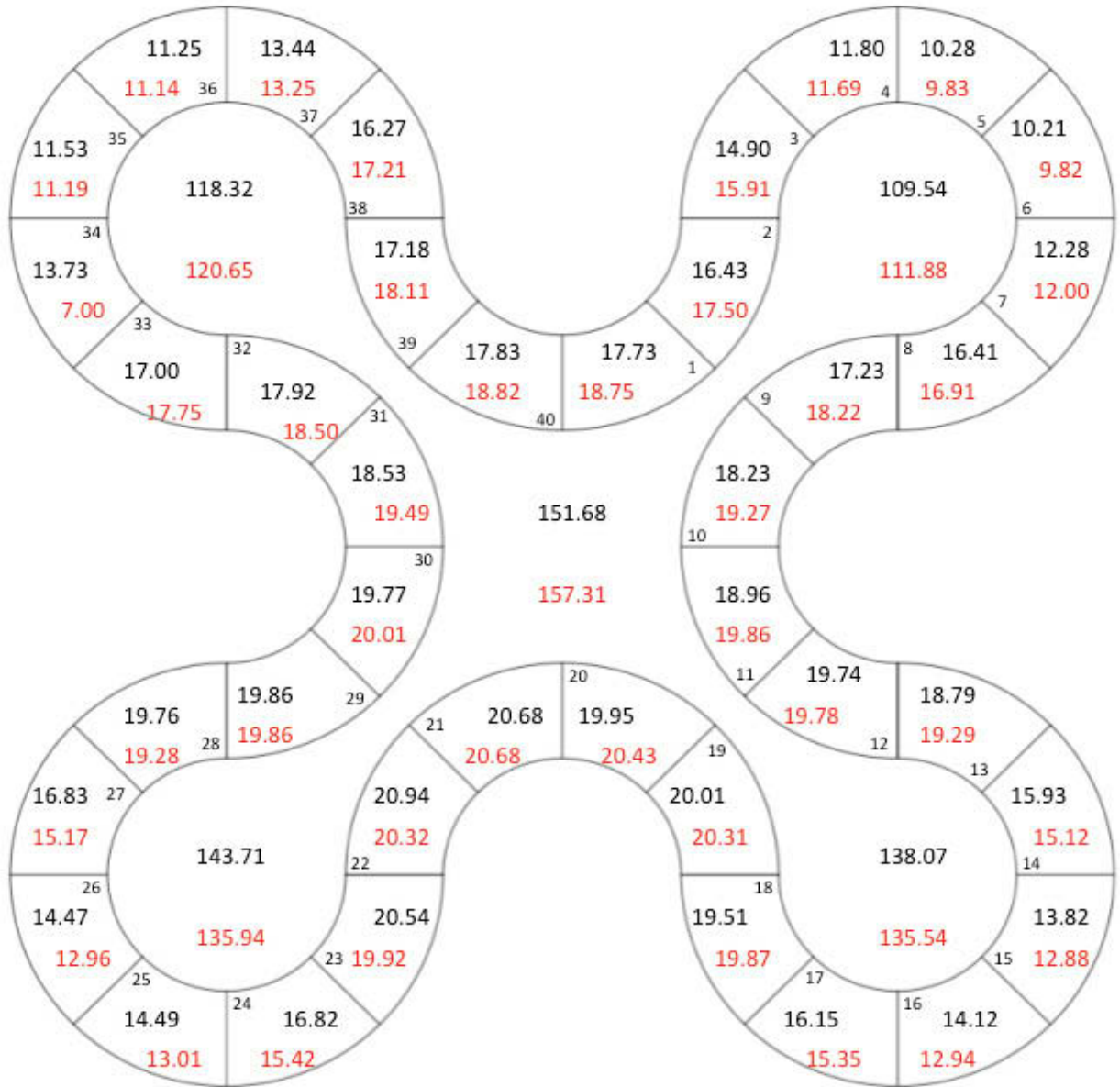


Figure 3.35. Power distribution for ATRC configuration 94-3.

The NEWT model of the ATRC was then modified to more closely represent the current ATRC core configuration for Modeling Update validation Irradiations 1-4. Specifically, the northeast lobe was modified to more closely represent the MICE experiment mockup currently contained in the northeast flux trap (Figure 3.36). A lobe power comparison and element power comparison is provided in Figure 3.37 for the NEWT model before the NE flux trap modification and in Figure 3.38 after the NE flux trap modification. The improvement in results is apparent from these two figures. The latter model will be used to support Irradiation 4 of the current validation experiment series.

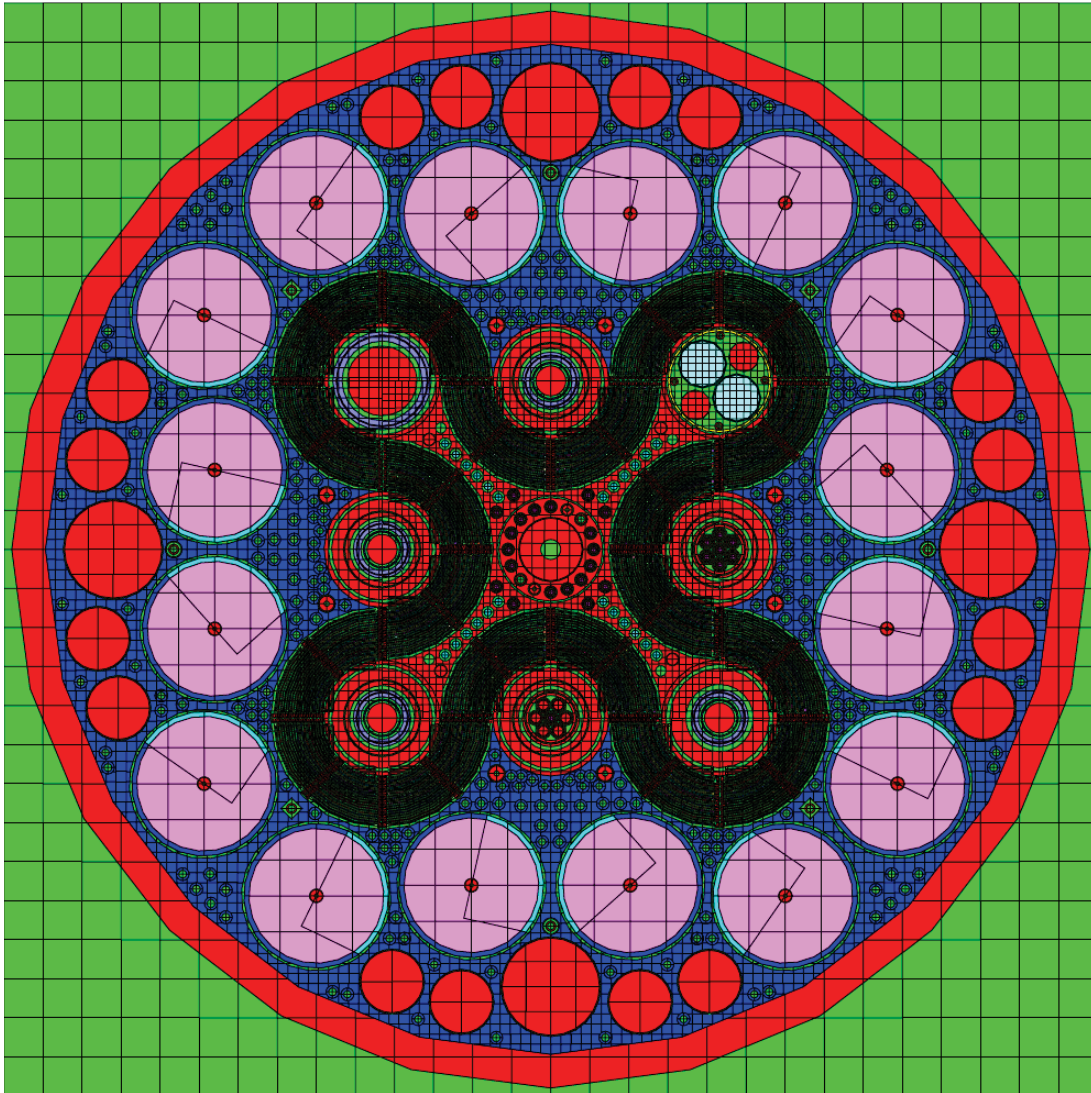
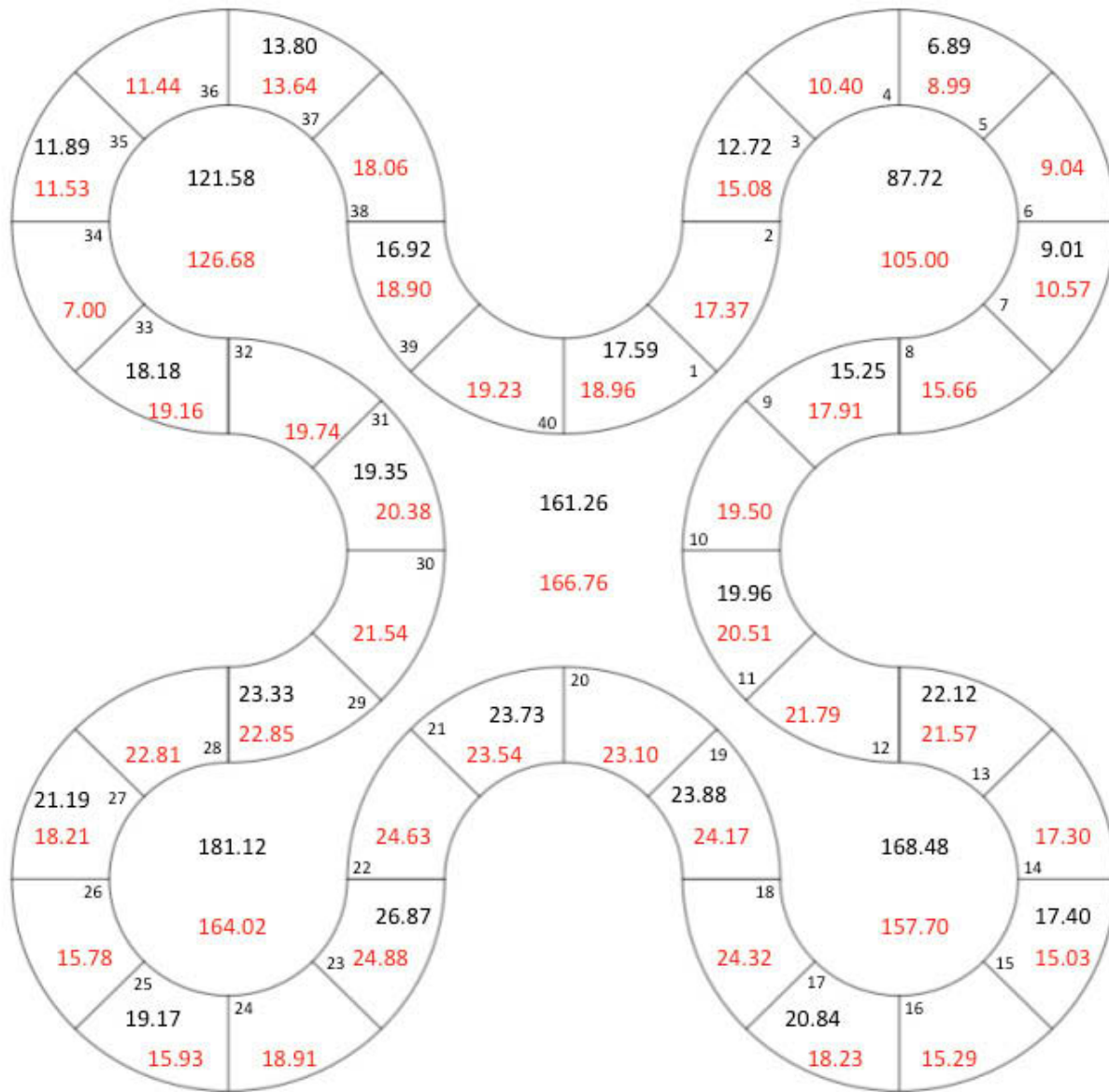


Figure 3.36. NEWT model of ATRC with a current representation of the NE flux trap contents.



Core Power = 720.16 W

Measured

NEWT Calculated

Figure 3.37. Power distribution comparison of the previous NEWT ATRC model and current easurements for Irradiation 4.

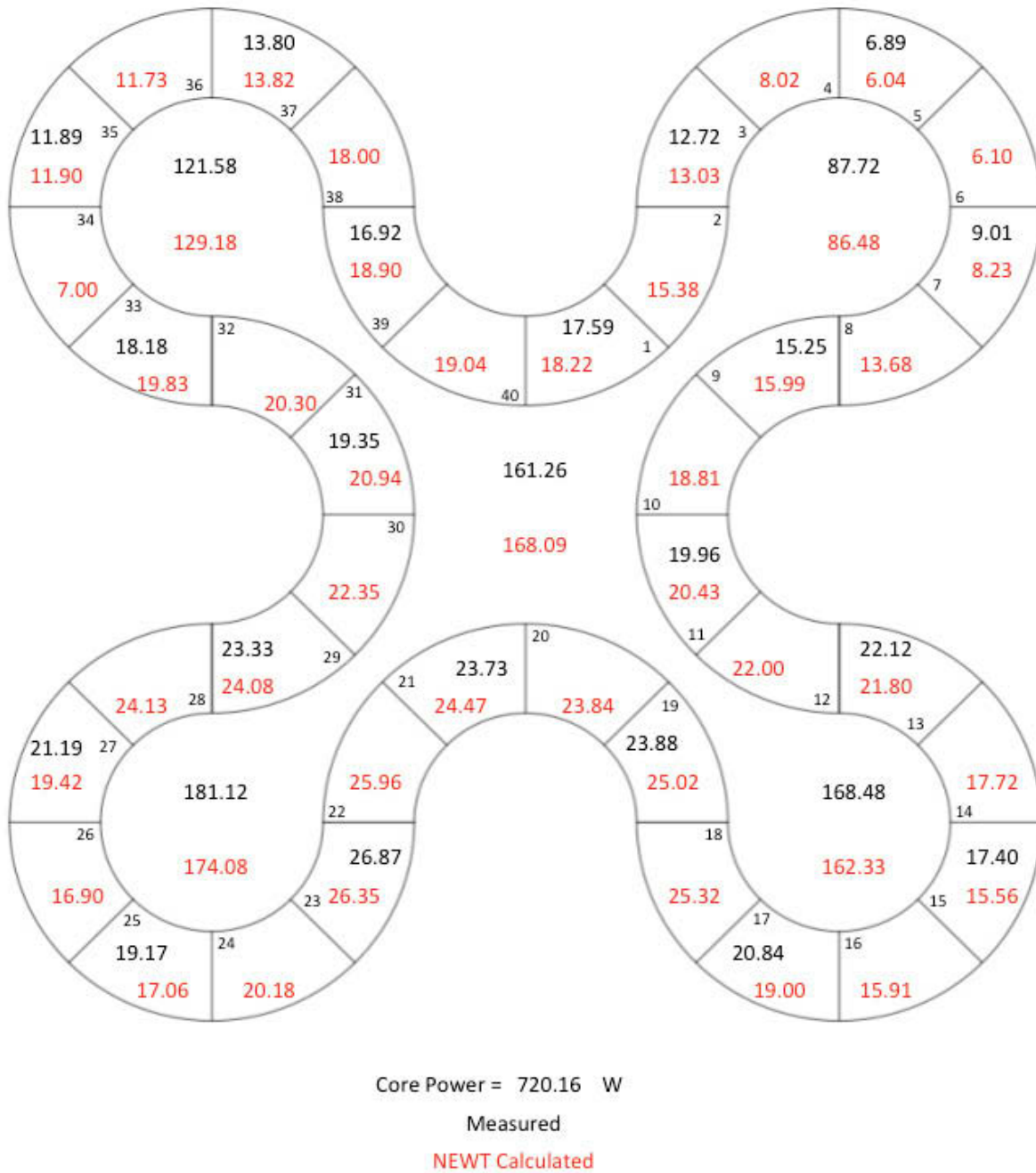


Figure 3.38. Power distribution comparison of the modified NEWT ATRC model and current measurements for Irradiation 4.

3.4.2 Experiment Support Using NEWT

NEWT will be used to support the ATR Methods Update validation experiments in ATRC as well as several planned ISU/INL DOE Nuclear Energy University program (NEUP) instrumentation experiments in the ATRC. NEWT is able to calculate neutron flux and neutron reaction rates for materials in the ATRC. The NEWT model of the ATRC has also been modified to include flux wire positions in the ATRC fuel elements to support Irradiation 4 of the current validation series (see Figure 3.39). Neutron spectra and Au/Cu reaction rates for each of the modeled flux wires will be calculated in NEWT for spectral adjustment calculations during FY-12 based on measurements described in Section 4.

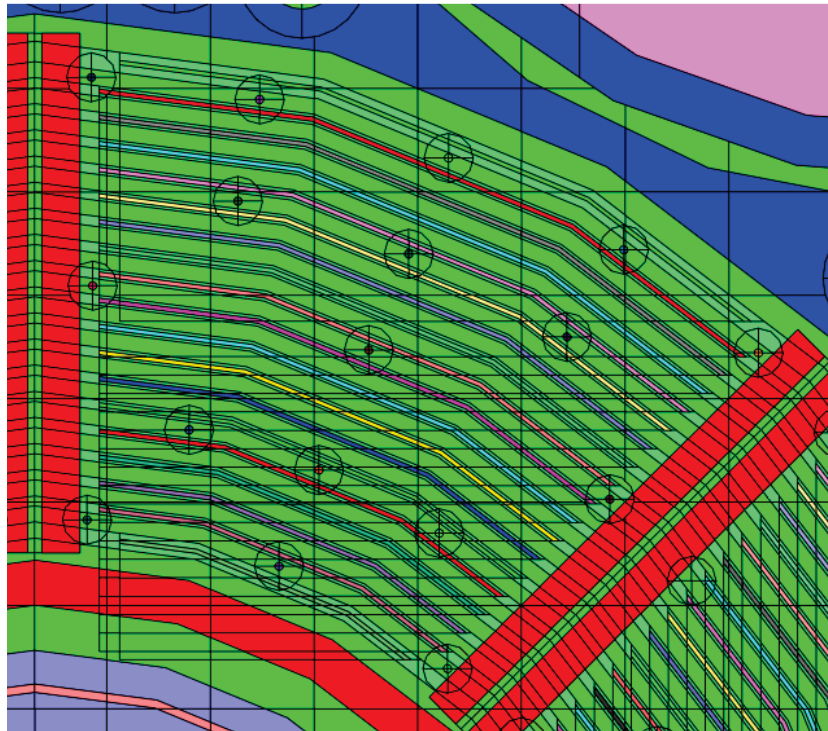


Figure 3.39. Flux wire positions in the NEWT model of the ATRC.

The newt ATR model has been run with Au/Cu wires in fuel elements 12, 14, 16, 18, 32, 34, 36, and 38. The model was run with the standard scale 44 group library, the ENDF/B-VII 238 group library, and the ENDF/B-VII 200 group neutron library. The NEWT calculated power distribution using the ENDF/B-VII 200 group neutron library was compared to the measured power split distribution for irradiation 4 (separately determined using standard $^{235}\text{U}/\text{Al}$ flux wires in the odd-numbered elements) as shown in Figure 3.40. The 200 group library was run in Scale 6.1 while the other libraries were run in Scale 6.0. Table 3.12 presents some typical normalized neutron flux and neutron cross sections for copper in the Au/Cu flux wires from the NEWT output, which can be used for validation of models and codes. The reaction rates in Table 3.12 are calculated by multiplying the normalized neutron flux by the neutron cross section for each energy group.

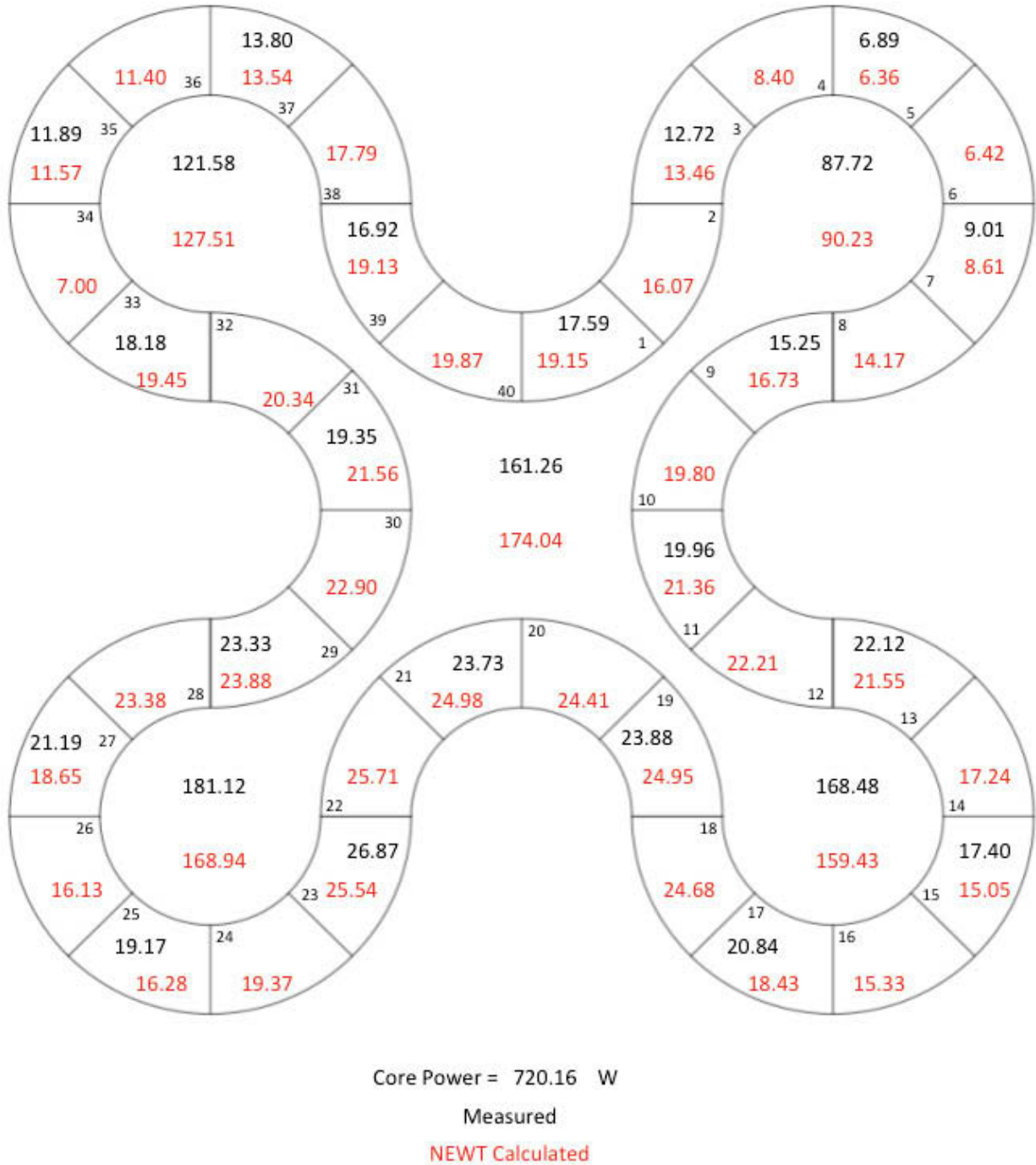


Figure 3.40. Power distribution for the NEWT model with the 200 neutron group ENDF/B-VII cross sections compared to the measured power distribution for ATRC validation Experiment 4.

Table 3.12. Some Typical neutron flux and cross sections extracted from the NEWT output for the ATRC experiment 4 model using the 200 group neutron cross section library.

Upper Energy (eV)	Group Flux	Reaction Rate	Cross Section (barns)
2.00E+07	1.56E-09	1.37E-10	8.75E-02
1.42E+07	6.41E-09	6.92E-10	1.08E-01
1.22E+07	3.57E-08	3.97E-09	1.11E-01
1.00E+07	7.80E-08	8.01E-09	1.03E-01
8.61E+06	1.72E-07	1.59E-08	9.29E-02
7.41E+06	4.92E-07	4.23E-08	8.59E-02
6.07E+06	9.40E-07	7.49E-08	7.97E-02
4.97E+06	2.46E-06	1.68E-07	6.86E-02
3.68E+06	2.37E-06	1.29E-07	5.45E-02
3.01E+06	1.47E-06	6.56E-08	4.45E-02
2.73E+06	1.64E-06	6.26E-08	3.83E-02
2.47E+06	8.08E-07	2.74E-08	3.39E-02
2.37E+06	1.54E-07	5.00E-09	3.24E-02
2.35E+06	8.84E-07	2.71E-08	3.07E-02
2.23E+06	2.56E-06	6.52E-08	2.54E-02
1.92E+06	2.72E-06	5.27E-08	1.94E-02
1.65E+06	3.63E-06	5.69E-08	1.57E-02
1.35E+06	5.00E-06	7.28E-08	1.45E-02
1.00E+06	3.08E-06	4.49E-08	1.46E-02
8.21E+05	1.67E-06	2.43E-08	1.45E-02
7.43E+05	3.12E-06	4.54E-08	1.45E-02
6.08E+05	2.65E-06	3.96E-08	1.50E-02
4.98E+05	3.16E-06	5.31E-08	1.68E-02
3.69E+05	2.22E-06	4.27E-08	1.93E-02
2.97E+05	4.06E-06	9.68E-08	2.38E-02
1.83E+05	3.28E-06	9.29E-08	2.84E-02
1.11E+05	2.71E-06	8.35E-08	3.08E-02
6.74E+04	2.32E-06	6.80E-08	2.93E-02
4.09E+04	8.97E-07	3.44E-08	3.83E-02
3.18E+04	1.01E-06	4.74E-08	4.69E-02
2.61E+04	3.18E-07	1.72E-08	5.40E-02
2.42E+04	4.06E-07	2.05E-08	5.05E-02
2.19E+04	1.45E-06	7.34E-08	5.07E-02
1.50E+04	2.75E-06	2.20E-07	7.99E-02
7.10E+03	2.62E-06	1.96E-07	7.47E-02
3.35E+03	2.56E-06	3.21E-07	1.25E-01
1.58E+03	4.15E-06	8.47E-07	2.04E-01
4.54E+02	2.43E-06	6.51E-08	2.68E-02
2.14E+02	2.39E-06	8.25E-08	3.46E-02
1.01E+02	3.10E-06	2.15E-07	6.95E-02
3.73E+01	3.74E-06	5.47E-07	1.46E-01
1.07E+01	2.13E-06	5.41E-07	2.54E-01
5.04E+00	2.80E-06	1.13E-06	4.05E-01
1.86E+00	2.11E-06	1.33E-06	6.29E-01
8.76E-01	2.17E-06	1.99E-06	9.20E-01
4.14E-01	5.13E-06	8.63E-06	1.68E+00
1.00E-01	8.69E-06	3.26E-05	3.75E+00

The NEWT ATRC model also has geometric units created for the cadmium covered foils and bare foils used in Irradiation 1 (Figure 3.41). The model with these 3-dimensional experiments will be used in FY-12 to determine how well a 2D computer code can model 3D experiments and will allow investigation of 2D modeling methods that will improve the ability of the 2D codes to capture 3D effects. Irradiation 3 with the spectral shifting boron sphere and activation foils will also be modeled. These models will serve as aids in direct validation of the HELIOS models used for fuel management as described in Section 2.

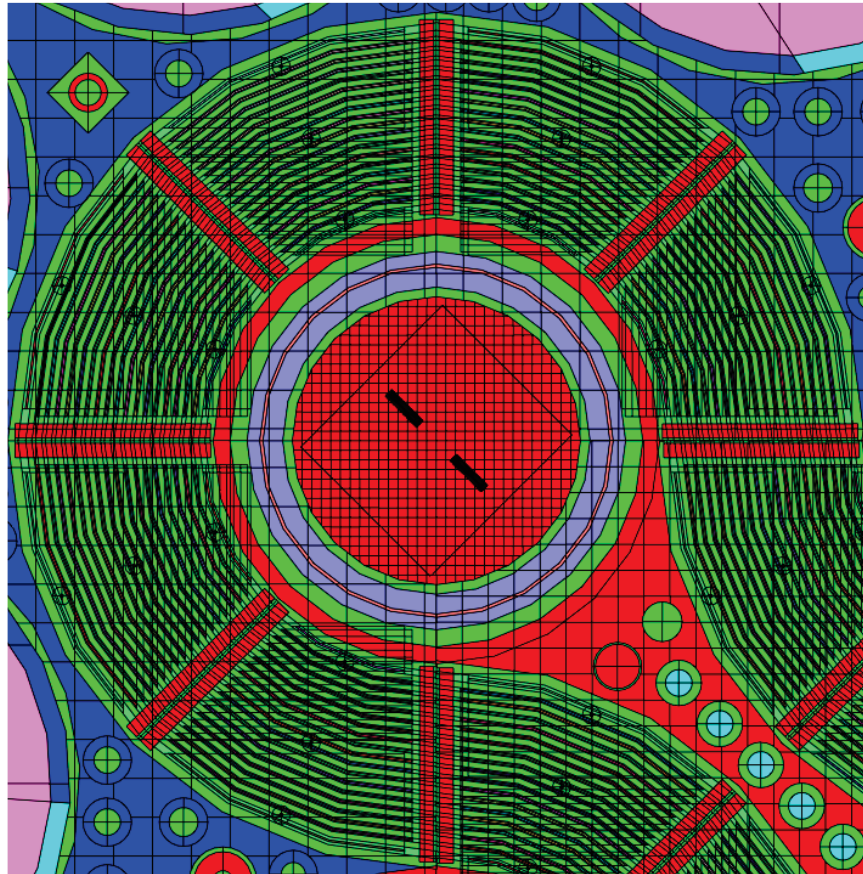


Figure 3.41. NEWT model with the bare and cadmium covered foils in the NW flux trap for ATRC validation Irradiation 1.

3.5 HELIOS ATRC Model Description for ATRC Irradiation 4 Analysis

Bryon Curnutt (INL)

As discussed in Section 2, a HELIOS model of the post 1994 CIC ATR core is well into development for ATR CSAP applications. The primary task of the HELIOS ATRC model development is to make the materials, and geometry changes to the ATR HELIOS model to match the ATRC core. This includes conversion of the post 1994 CIC ATRC core loading (94-2 loading) to the current ATRC core loading (09-1 loading). Table 3.13 provides a comparison between the 94-2 and 09-1 ATRC core loadings.

Table 3.13. 09-1 ATRC Core Loading versus 94-2 ATRC Core Loading

Facility	09 -1 Loading (Irradiation 4)	94-2 Loading (1994 CIC)	Difference
Flux Traps			
NW	LIPT and 3.5-inch diameter aluminum filler	LIPT and 3.5-inch diameter aluminum filler	None
E	Safety rod, Chopped Dummy IPT (CDIPT), and Small Irradiation Housing Assembly (SIHA) with aluminum baskets containing three LSA cobalt capsules in all 7 positions.	Safety rod, Chopped Dummy IPT (CDIPT), and Small Irradiation Housing Assembly (SIHA) with aluminum baskets containing three LSA cobalt capsules in all 7 positions.	None
S	Safety rod, Chopped Dummy IPT (CDIPT), and Small Irradiation housing Assembly (SIHA) with three LSA cobalt capsules in aluminum basket in S-7 position and six aluminum fillers in S-1 thru S-6	Safety rod, Chopped Dummy IPT (CDIPT), and Small Irradiation Housing Assembly (SIHA) with aluminum baskets containing three LSA cobalt capsules in all 7 positions.	Remove 6 Al filler assemblies, insert 6 LSA Co assemblies
NE	Multiple Irradiation Capsule Experiment (MICE) facility with fueled MICE PRIME 1 capsule mockups in NW and SE positions; MICE filler plugs in the NE and SW positions. Shrouding described in Bettis letter B-MT(EDT)I-1171 and B-MT(EDT)I-1309	LIHA with LSA Cobalt capsule mockups in positions 3 thru 6, 10 thru 13, and 23 and aluminum filler assemblies in positions 1, 2, 7, 8, 9, 14, and 15 thru 22	Remove MICE tests and facility, insert LIHA with LSA Co/aluminum filler assemblies as designated in preceding column
N	Safety rod, Standard Inpile Tube (SIPT), flow tube, and 1.5-inch diameter aluminum filler	Safety rod, Standard Inpile Tube (SIPT), flow tube, and 1.5-inch diameter aluminum filler	None
W	Safety rod, Standard Inpile Tube (SIPT), flow tube, and 1.5-inch diameter aluminum filler	Safety rod, Standard Inpile Tube (SIPT), and water-filled flow tube	Remove 1.5-inch diameter aluminum filler
SW	Safety rod, Standard Inpile Tube (SIPT), flow tube, and 1.5-inch diameter aluminum filler	Safety rod, Standard Inpile Tube (SIPT), flow tube, and 1.5-inch diameter aluminum filler	
C	AFIP Dummy Test with one -inch diameter hole		
SE	Dummy Flux Trap Filler, SIPT, flow tube with aluminum spacer, and 1.5-inch diameter aluminum filler	Dummy Flux Trap Filler, SIPT, and water-filled flow tube diameter aluminum filler	Remove aluminum spacer and 1.5-inch diameter aluminum filler
A Irradiation Facilities			
A-1 thru A-8	LSA Cobalt	Aluminum Filler	Remove LSA Cobalt and install aluminum fillers
A-9 through A-12	Aluminum filler	Aluminum Filler	None
B Irradiation Facilities			
B-1 through B-8	"Y" aluminum flow restrictor	"Y" aluminum flow restrictor	None
H Irradiation Facilities			

Facility	09 -1 Loading (Irradiation 4)	94-2 Loading (1994 CIC)	Difference
H and H-10	Empty flux monitor wire holders	Empty flux monitor wire holders	None
H-3 and H-11	N-16 flow tube mockup	N-16 flow tube mockup	None
H-1, H-4, H-5, H-6, H-7, H-8, H-9, H-12, H-13, H-14, H-15 and H-16	Aluminum basket containing three LSA cobalt capsules	Aluminum basket containing three LSA cobalt capsules in H-1, H-4, H-5, H-7, H-8, H-9, H-12, H-13, H-15, and H-16 Empty flux monitor wire holders in H-6 and H-14	Remove LSA Co in H-6/H-14, insert MT FMWHs
I Irradiation Facilities			
I-1 through I-20	Aluminum filler except for positions I-3 and I-9 which contain log count rate detector thimbles	Aluminum filler except for positions I-3 and I-9 which contain log count rate detector thimbles	None
Fuel Elements	Forty ATRC fuel elements (Mark IV)	Forty ATRC fuel elements (Mark IV)	
Neck Shims	All inserted	All inserted	See below

3.5.1 Geometric Considerations

Of particular note is that there is a major difference in the physical configuration between the hafnium sections of the neck shims in ATR and ATRC. The ATRC hafnium sections were obtained from the ATR Critical Experiment and are smooth-surfaced rods; the hafnium sections for the ATR are fluted and have a hole through the center. Figure 3.42 below shows the core mid plane cross sections of the ATR and ATRC neck shims. The locations of the neck shims are shown in Figure 3.43 on the following page.

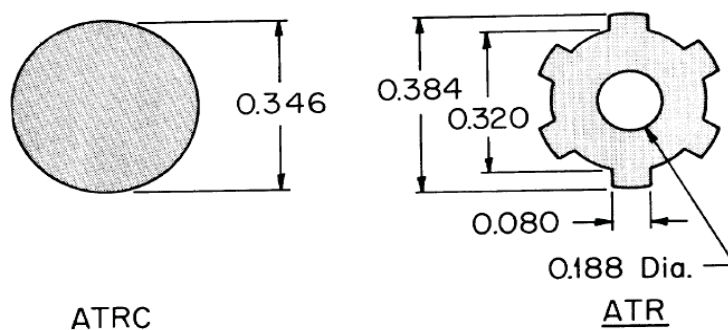


Figure 3.42. Cross Section Comparison of ATRC and ATR Hafnium Neck Shims

According to Henscheid, 1967, “the hafnium sections of the neck shims from the ATR Critical Experiment were turned down to a diameter of 0.346 inch and now have practically the same reactivity effect as the ATR hafnium neck shims”. Although the ATR and ATRC neck shims are said to have the same reactivity, the geometry of the neck shims in the HELIOS ATRC model was changed to reflect the differences.

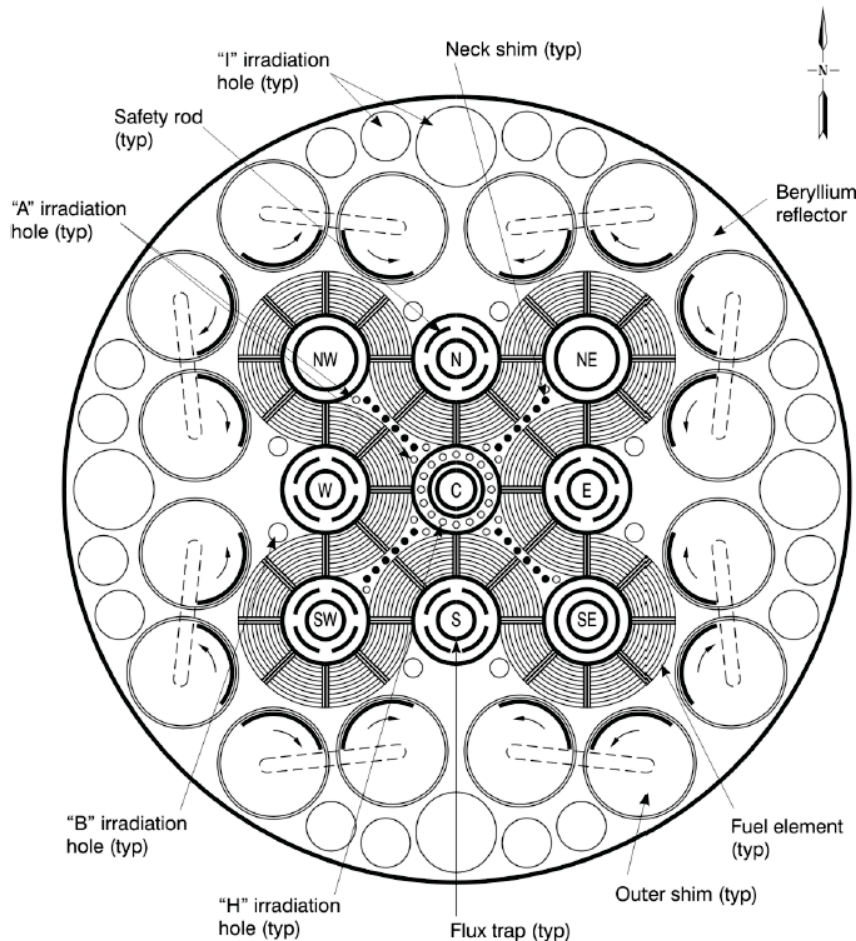


Figure 3.43. ATRC Core Cross Section

There are several other key geometric differences between ATR and ATRC. ATRC does not have any small “I” or large “B” capsule irradiation facilities. The HELIOS ATRC model has been changed to reflect this difference. ATRC has four “Outer-A” capsule irradiation facilities whereas ATR has eight Outer-A facilities. The additional A positions in ATR are located in the neck shim housing assembly adjacent to the A positions shown in Figure 3.43. The HELIOS ATRC model has been changed to reflect this difference.

The normal fuel loading for the ATRC core consists of 40 Mark IV fuel elements. Mark IV type fuel elements are an older design of ATR fuel element no longer manufactured. Prior to the 1994 CIC, ATRC

was loaded with 40 new Mark VII fuel elements, physics testing was performed, and then ATRC was reloaded with the older Mark IV fuel elements. The HELIOS ATR 1994 CIC reference model consists of 40 unburned Mark VII type “7F” fuel elements. A Mark IV fuel element will be modeled in HELIOS in order to load the HELIOS ATRC core with the correct elements. The Mark IV fuel element has a U_3O_8 aluminum fuel matrix loaded with a nominal 975 grams ^{235}U and 0.81 grams ^{10}B . The fuel and boron are loaded with a uniform density of 1.23 gm/cm^3 of ^{235}U throughout the fuel. Although the geometry of the Mark IV and Mark VII elements are nearly identical, there are significant differences in the density and nominal ^{235}U and ^{10}B loading, which bring forth significant differences in reactivity and reactivity feedback mechanisms. Because there is no change in geometry, the model of the Mark VII element can be modified with material overlays and density changes to correctly model the Mark IV fuel elements.

3.5.2 Near-Term Applications of the HELIOS ATRC Model

Irradiation 4 was one of four experiments performed in ATRC during FY-11 to support the V&V efforts of the ATR Methods Upgrade project for ATR, as discussed in more detail in Section 4. ATRC Test Plan TP-1-11 provided the appropriate ATRC core loading (09-1 Core Loading) for Irradiation 4 and provided the ATRC operations staff with a written plan necessary to install the experiment hardware and reactivity data for use in the preparation of reactor core changes. Table 3.13 compares the 1994 CIC ATRC core loading to the core loading of Irradiation 4 as noted earlier. The most significant difference between the two loadings in regard to HELIOS modeling requirements for Irradiation 4 is the Multiple Irradiation Capsule Experiment (MICE) in the NE flux trap. In the case of the 1994 CIC the NE flux trap was loaded with a large in-pile housing assembly (LIHA) with 22 separate capsule irradiation facilities loaded with either aluminum fillers or Low Specific Activity (LSA) cobalt as shown in Table 3.13. Before Irradiation 4 can be simulated with the HELIOS ATRC model the MICE experiment must be correctly modeled in the NE flux trap.

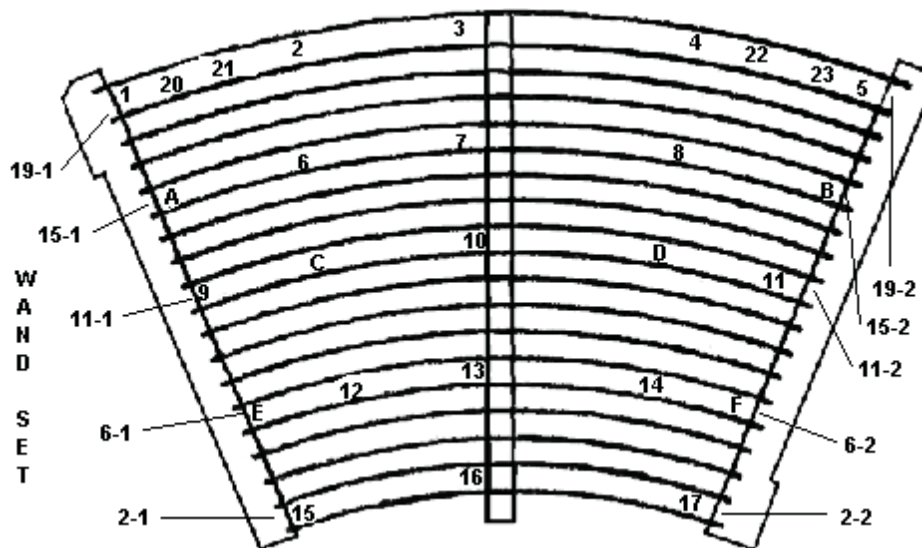


Figure 3.44. Flux Wire and Wand Positions

During Irradiation 4 the ATRC was run at 720.16 W (ECAR-1401) for 20 minutes. Seventeen (17) 40-mil diameter, ¼ inch long 10% enriched U-Al wires were loaded at the axial midplane in each of the 20 ATRC fuel elements in the odd numbered fuel element positions. Additionally, Au/Cu wires (described in Section 4) were loaded in wire positions 3, 10, and 16 in ATRC fuel elements 12, 16, 18, 32, 34, 36, and 38. Figure 3.44 shows a core mid-plane cross section of an ATRC fuel element with wand and flux wire positions labeled.

After the HELIOS ATRC model has been verified to have the correct materials, fuels, geometry and core loading, Irradiation 4 will be simulated. The data from the HELIOS run will then be compared to the results from the gamma spectroscopy performed on the Cu/Au wires and the gross beta counting performed on the ²³⁵U fission wires. The fuel elements in the HELIOS ATRC model will be represented with the wire loadings described above. The wires in the fuel elements become individual regions that can be burned and tracked in HELIOS. Isotope edit sets in the HELIOS output processor ZENITH will provide the isotopic data from the flux run for each fission wire. The isotopic data from the HELIOS output can then be compared to results from the actual flux run, in which some of the fission wires were examined by gamma spectroscopy. A gross beta analysis was also performed on each fission wire using standard techniques (Durney and Kauffman, 1967) to provide the element power data reported in ECAR-1401. This information will also be compared to the computational results from the HELIOS model. Finally, the Cu/Au wire saturation activities will be used in a least-squares adjustment procedure (see Section 4) to produce spectral validation data at the locations of the Au/Cu wires.

4.0 VALIDATION EXPERIMENTS IN THE ATRC

David W. Nigg (INL), Joseph Nielsen (INL), Ben Chase (INL), Troy Unruh (INL), Tony LaPorta (INL), Jorge Navarro (INL), Mark DeHart (INL), Kirk Stueve (INL), Craig Jackson (INL), Ron Murray (INL)

Validation protocols for the various computational models are based on neutron activation spectrometry as described in this section, and on post-irradiation burnup measurements for selected fuel elements as described in Section 5. Some basic equipment for activation experiments in the Northwest Large In-Pile Tube (NW LIPT) and in the fuel elements was fabricated during FY-2010, and initial scoping measurements using this hardware were completed during FY-2011. Additional equipment was fabricated during FY-2011 to enable activation measurements in the southeast flux trap that will be conducted during FY-2012. Ultimately a complete set of experimental apparatus and associated standard validation measurement protocols using neutron activation spectrometry will be available for future code and model validation measurements as needed in both the ATRC and, when feasible, in the ATR itself. The work described here builds on extensive previous relevant INL experience at the ATR (e.g. Rogers and Anderl, 1995) as well as at other research reactor and accelerator facilities worldwide (e.g. Nigg et al., 2000).

4.1 Methods and Materials

Neutron activation spectrometry is based on the fact that different elements (and different isotopes of the same element) placed in a neutron field will capture and scatter neutrons selectively with respect to the incident neutron energy. Some elements are primarily sensitive to capture of thermal neutrons, others have strong capture resonances in the epithermal energy range, while others exhibit interaction energy thresholds for inelastic scatter, secondary neutron and charged particle emission, and fission, below which essentially no interactions occur. If the neutron interaction product for a particular nuclide is radioactive, then the induced radioactivity of a sample of that nuclide placed in a neutron field will be largely proportional to the neutron flux at energies where interactions are most likely to occur in the sample. If different materials having different sensitivities to neutrons as functions of energy are activated in the same field it is ultimately possible to reconstruct a measured neutron spectrum from the induced activities. The level of spectral detail that can be reliably obtained generally corresponds to the number of different materials, and different interactions in the same materials, that are available.

As an example to illustrate the underlying physics of activation spectrometry, Figure 4.1 shows the capture cross section for ^{197}Au , which has a relatively high thermal neutron capture component as well as a prominent capture resonance at about 5 electron volts (eV). Capture of neutrons in a small sample (typically a foil or wire) of ^{197}Au produces ^{198}Au , which undergoes beta decay with emission of a prominent 411 keV gamma ray. The strength of this gamma ray is proportional to the neutron capture rate, which is for the most part proportional to the flux of neutrons at thermal energies and at 5eV. If the sample is placed inside a cover made of cadmium, which absorbs essentially all incident thermal neutrons, then the interaction rate of the gold sample will be proportional to the neutron flux above thermal energies, primarily at 5 eV where the resonance occurs. The thermal and above-thermal neutron fluxes can then be separated by converting the measured induced activities to saturation activities (i.e. activation rates per atom), subtracting the activation rate of the cadmium-covered sample from that of the bare sample and computing the corresponding thermal-neutron and total neutron fluxes. This is the classic cadmium difference method and in effect it yields a two-energy group (thermal and above-thermal) spectrum. Elemental gold also exhibits several very useful and convenient threshold interactions for secondary neutron emission. These include (n,2n) up through (n,6n), extending up to about 60 MeV (Nigg et al., 2000).

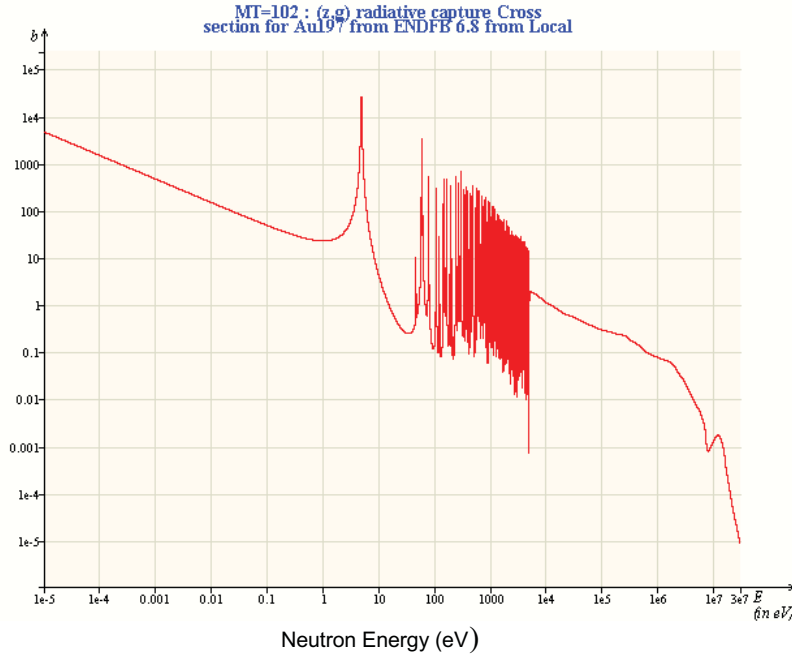


Figure 4.1. Capture cross section (barns) of ^{198}Au . (Source: OECD Janis 2.1)

As another example, cross section data for ^{115}In are shown in Figure 4.2. This nuclide (96% abundance in natural indium) captures thermal neutrons and it also has a strong neutron capture resonance at about 1 eV. In both cases neutron capture produces radioactive ^{116}In , which emits three prominent gamma rays with energies of 416, 1097 and 1293 keV. In addition it will form an isomer by inelastic scatter of neutrons having energies above about 400 keV. This yields $^{115\text{m}}\text{In}$, which decays back to the ground state by emission of a 336 keV gamma ray. Hence the inelastic scatter rate (and thus the neutron flux above the 400 keV threshold) is proportional to the measured activity of the 336 keV gamma ray while the activities of the other three gamma rays, which are associated with a different half-life since they are emitted by a different radionuclide (^{116}In) are largely proportional to the neutron flux at thermal energies and at 1 eV. If an indium foil is covered with cadmium, the thermal neutron capture rate is suppressed as described previously for gold. As a result, this single nuclide can be used to obtain information in three different energy ranges of the neutron spectrum of interest.

In the general case, a number of different activation responses (typically 8-12) are typically measured using a variety of nuclides having different sensitivities to neutrons in the thermal, resonance, and fast energy ranges. This permits the reconstruction of additional spectral detail in the unfolding process. Materials found useful for ATRC applications include gold and indium as described above as well as tungsten, manganese, cobalt, copper, and scandium for thermal and epithermal neutron measurements and several other materials having threshold interactions for fast-neutron measurements, as will be described later.

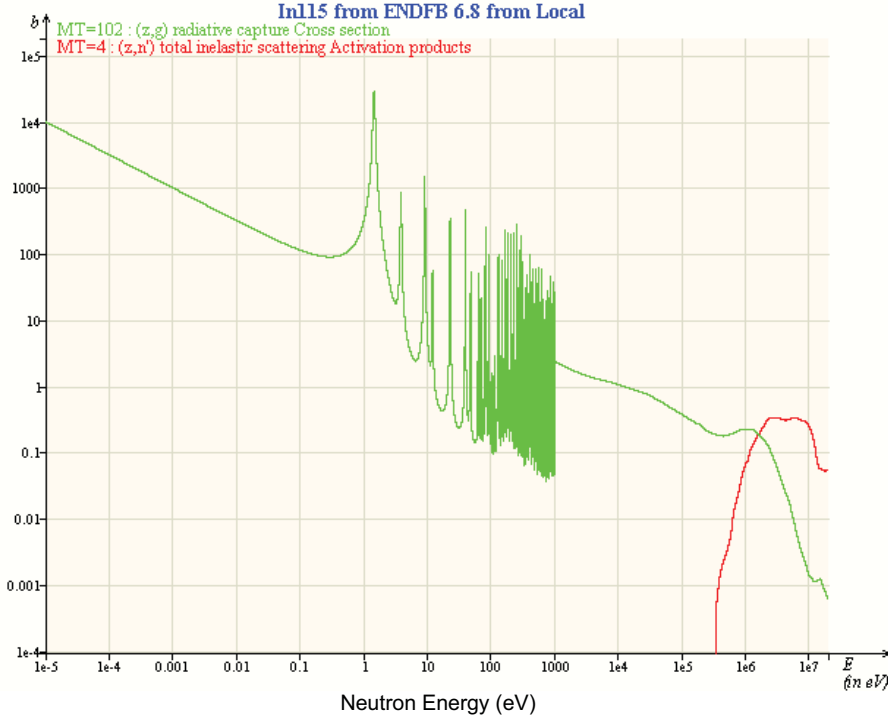


Figure 4.2. Capture (Green) and inelastic scatter (Red) cross sections (barns) of ¹¹⁵In. (Source: OECD Janis 2.1)

We now consider some essential mathematical details of neutron activation spectrometry. In general, the volume-average activation rate per atom for a foil or wire dosimeter placed in a neutron flux field may be calculated as:

$$R = \int_0^{\infty} \sigma_d(E) \Psi_d(E) dE \quad (1)$$

where $\sigma_d(E)$ is the microscopic activation cross section of interest for the dosimeter material, as a function of neutron energy and $\psi_d(E)$ is the volume-average scalar neutron flux existing within the active dosimeter, again as a function of energy, and accounting for self-shielding effects, if any. Equation 1 can also be expressed as:

$$R = \int_0^{\infty} \sigma_d(E) \left(\frac{\Psi_d(E)}{\Psi(E)} \right) \Psi(E) dE = \int_0^{\infty} \sigma_d(E) P_d(E) \Psi(E) dE \quad (2)$$

where $\psi(E)$ is the unperturbed neutron flux that would exist at the measurement location in the absence of the flux perturbations caused by the dosimeter itself and any surrounding spectral modification devices and other structures placed in the field (Cd covers, foil and wire positioning devices, etc).

It may be noted here that, as a practical matter, the function $P_d(E)$ in Equation 2 can be determined independently from $\Psi(E)$ if desired since it is simply a flux ratio. In this case $\Psi(E)$ on the far right hand side of Equation 2 can be any appropriate *a-priori* free-field unperturbed flux estimate that is then modified by the self-shielding function $P_d(E)$.

Equation 2 may be written as a summation rather than as an integral by partitioning the range of the energy variable into a number of discrete contiguous energy groups:

$$R = \sum_{j=1}^{NG} a_j \phi_j \quad (3)$$

where NG is the total number of energy groups, with

$$a_j = \frac{\int_{EL_j}^{EH_j} \sigma_d(E) P_d(E) \Psi(E) dE}{\int_{EL_j}^{EH_j} \Psi(E) dE} \quad (4)$$

and

$$\phi_j = \int_{EL_j}^{EH_j} \Psi(E) dE. \quad (5)$$

where EL_j and EH_j are the lower and upper energy limits of energy group j .

If additional dosimeter materials are placed in the field, or if a particular material exhibits more than one independent activation response (e.g. gold or indium as noted earlier) then Equation 3 may be written as a system of equations:

$$R_i = \sum_{j=1}^{NG} a_{ij} \phi_j \quad (6)$$

where R_i is the total activation rate for interaction i and a_{ij} is the activation constant from Equation 4 for reaction i due to neutrons in energy group j . There will be a total of NF equations, where NF is the total number of activation responses available.

Effective shielded cross sections $\sigma_d(E)$ and the corresponding shielded and unshielded *a-priori* neutron fluxes suitable for computing the function $P_d(E)$ in the above equations may be obtained by any of several well-established neutron transport modeling techniques and nuclear data libraries. A typical approach involves computation of application-specific cross sections and *a-priori* fluxes for each dosimeter in the neutron field using continuous-energy Monte Carlo techniques, e.g. MCNP. This is crucial if self-shielding or mutual shielding (as in a stack of foils) is significant. It is also sometimes possible to use highly-dilute foils (Auterinen et al., 2004) to avoid the need for shielding corrections, facilitating the direct application of standard dosimetry cross section libraries. The Monte Carlo calculations for

dosimeter packages generally include only the dosimeters and surrounding support structure with a boundary condition that represents the incoming space, angle- and energy-dependent incident neutron source, precomputed using a Monte Carlo or deterministic computational model of the entire reactor. The global reactor computations may be done with MCNP, or with a standard multidimensional discrete-ordinates code such as DORT (Rhodes and Childs, 1988, Wheeler et al., 1990) or in the case of ATR, with any of the more advanced transport codes described in Section 2 of this Annual Report.

The system of activation equations, Eq. 6, may be written out in matrix form as:

$$\begin{bmatrix} a_{11} & a_{12} & a_{13} & \cdots & a_{1NG} \\ a_{21} & a_{22} & a_{23} & \cdots & a_{2NG} \\ a_{31} & a_{32} & a_{33} & \cdots & a_{3NG} \\ \vdots & \vdots & \vdots & & \vdots \\ \vdots & \vdots & \vdots & & \vdots \\ a_{NF1} & a_{NF2} & a_{NF3} & & a_{NFNG} \end{bmatrix} \begin{bmatrix} \phi_1 \\ \phi_2 \\ \phi_3 \\ \vdots \\ \phi_{NG} \end{bmatrix} = \begin{bmatrix} R_1 \\ R_2 \\ R_3 \\ \vdots \\ R_{NF} \end{bmatrix} \quad (7)$$

or, more compactly:

$$[A][\Phi] = [R] \quad (8)$$

Equation (7) is exact, provided that the reaction rates R_i , the activation constants a_{ij} and the group fluxes ϕ_j all correspond to the same self-consistent *a-priori* model. If experimentally measured reaction rates for each interaction R_i are substituted into Equation (7), a solution of the resulting new system of equations for adjusted fluxes corresponding to the measured reaction rates may also be obtained under certain conditions.

If $NF = NG$ in Equation 7 then the matrix $[A]$ is square, its inverse will ordinarily exist, and the unknown flux vector may be obtained by any standard solution method that converges, provided that the rows of $[A]$ are linearly-independent to a sufficient degree and the measured reaction rates are sufficiently precise. In physical terms the former requirement implies that the response functions (cross sections) for the activation interactions used in the measurement must be selected such that they have sufficiently different shapes as functions of energy. Spectral modification devices (e.g. cadmium covers) can also be used to force linear independence. It may be noted that positive fluxes are not guaranteed to result from this procedure, but if the elements of $[A]$ are computed in a sufficiently valid, physically-realistic manner for the specific measurement configuration, and if the measured reaction rates are accurately determined, a positive solution will generally be obtained. In practice this situation ($NF=NG$) is exemplified by the previously-noted cadmium difference method, which can readily be shown to be a special case of Equation 7, with only two rows in the matrix, one for the bare foil and one for the covered foil. It also typically occurs when measuring pointwise fluxes at resonance energies (Harker et al., 1992) using stacks of foils, and when measuring simple spectra using flux wires composed of alloys of two materials with different spectral responses, such as copper and gold (as is done in the present work), or manganese and gold.

There are two possibilities for the situation where NF , the number of available activation response functions, is not equal to NG , the number of energy groups for which it is desired to obtain unfolded fluxes. If $NF < NG$ the problem is underdetermined and additional information must be introduced in some manner to permit a constrained solution. Typically this involves the numerical modification of an input *a-priori* spectrum by any of several well-developed algorithms to produce an adjusted flux vector that yields calculated responses corresponding to the best overall fit to the measured data in some sense. Some of these methods involve introduction of the covariance matrix associated with the *a-priori* flux, while others are more empirical in nature, based on physical intuition. If $NF > NG$ the problem is overdetermined and the “extra” information that is thereby available can be incorporated into the direct algebraic determination of a unique “best-estimate” solution for the adjusted group fluxes and their propagated uncertainties using a least-squares procedure based on the so-called “normal equations” (Meyer, 1975).

The underdetermined methods for spectral unfolding allow the estimation of a spectrum having more energy detail than the number of linearly independent activation responses, but these approaches do not necessarily produce a unique solution – many solutions can be possible from the same input data. Introduction of *a-priori* covariance information in effect constrains the solution to a single physically realistic optimum in a least squares sense. Several adjustment codes based on this approach have been developed. A popular example is the LSL code (Stallman 1986). If the covariance information required for the underdetermined least-square adjustment procedures is not available, other somewhat more empirical iterative adjustment techniques are widely used, one popular example being the method described by Draper (1971), implemented as an option in the SAND-II code (McElroy and Berg, 1967). Effective use of all underdetermined methods requires good physical insight and intuition, since the form of the input *a-priori* spectrum and its assumed uncertainty, as well as the iteration strategy used to produce a solution, can have a significant influence on the results.

Neutron activation spectrometry can be applied to any neutron field for which suitable activation responses can be measured. It is used on a regular, but somewhat limited, basis for flux characterization in most experiments irradiated in the ATR, generally using nickel and cobalt wires. A full spectral characterization of the ATR has not been done since 1986 (Rogers and Anderl 1995). The activation method is capable of high precision and accuracy ($1\sigma < 5\%$) when uncertainties are carefully managed throughout every step of the process. Precautions to be taken include:

- Use of high-purity, accurately assayed dosimeter materials
- Careful weighing, preparation and handling of the foil packages to ensure accurate knowledge of the foil masses and to avoid contaminants
- Careful recording of the activation and post-irradiation decay times of the foils
- Irradiation at constant flux if at all possible, with appropriate corrections for any time-dependence of the flux.
- Accurate, reproducible calibration of gamma spectrometers used for measurement of the foil activities, using certified, traceable standards.
- Use of good techniques for the foil activity measurements in order to minimize uncertainties due to coincidence summing, counting geometry etc.
- Thoughtful selection and application of unfolding techniques

- Use of multiple unfolding techniques to verify consistency

It is also important to recognize that activation measurements for code validation, especially in the case of thermal neutron fields, must be planned and interpreted very carefully due to the possibility of large flux gradients that can depend on the specific geometry of the reactor, which can change with time (e.g. as a result of shim rotation in the ATR). As a result, reproducibility can be an issue and self consistent comparison with the calculation being validated is crucial – i.e. be sure you are really calculating and measuring the same quantity.

4.2 Conduct of ATRC Validation Protocol Experiments 1-3 during FY-2011

In the initial phase of the experimental campaign described here various sets of activation foils and wires were irradiated in the NW LIPT of the ATRC, with a “balanced“ outer shim critical configuration. Three 20-minute ATRC reactor runs at 600 watts were required for this phase. Activation responses used are listed in Table 4.1. The first irradiation was targeted on the thermal and epithermal neutron energy range and included duplicate bare Au and Mn foils and duplicate cadmium-covered In, Au, W, Mn, and Cu foil packages. The second irradiation was conducted primarily to experimentally confirm the anticipated small effect of the cadmium-covered foil packages used in Irradiation 1 on the local flux in the NW LIPT. The third irradiation was designed to provide additional spectral detail in the energy range above about 300 keV using a set of In, Ti, Ni, Zn, Fe, and Nb foils contained within a spectral shifting shield composed of boron. The foils are standard 12.7 mm (0.5”) diameter foils with thicknesses ranging from 0.0254 mm (1 mil) to 0.127 mm (5 mil). They were selected from a very well-characterized inventory of foils used at the INL over a period of many years. All foils were positioned at the axial core midplane within a standard ATRC NW LIPT insert. Figure 4.1 shows this insert, separated into its two components, as well as a standard Cd foil cover and the B spectral shifter, which is a hollow sphere of sintered boron, enriched to approximately 90% in ^{10}B , with an inside diameter of approximately 2.5 cm (1”), an outside diameter of 5 cm (2”), and a nominal mass of 115 grams. It prevents essentially all neutrons having energies of less than about 10 keV from reaching the foil package inside.

Table 4.1. Activation interactions of interest for ATR model validation applications.

Neutron Interaction	Nominal Mass and Composition of Standard Foil	Half-life of Product of Interest	Energy Range of Primary Response	Activation Gamma Energy of Interest (keV)
$^{115}\text{In} (n, \gamma) ^{116}\text{In}$	25 mg, 100% In	54 Minutes	1 eV Resonance	1293,1097, 416
$^{197}\text{Au} (n, \gamma) ^{198}\text{Au}$	60 mg, 100% Au	2.694 Days	Thermal & 5 eV Resonance	412
$^{186}\text{W}(n, \gamma) ^{187}\text{W}$	60 mg, 100% W	23.9 Hours	18 eV Resonance	686
$^{55}\text{Mn}(n, \gamma) ^{56}\text{Mn}$	50 mg, 80% Mn, 20% Cu	2.578 Hours	Thermal & 340 eV Resonance	847
$^{63}\text{Cu} (n, \gamma) ^{64}\text{Cu}$	140 mg, 100%Cu	12.7 Hours	Thermal & 1 keV Resonance	511 (Positron)
$^{115}\text{In} (n, n') ^{115m}\text{In}$	25 mg, 100% In	4.486 Hours	0.5 MeV Threshold	336.3
$^{47}\text{Ti} (n, p) ^{47}\text{Sc}$ $^{46}\text{Ti} (n, p) ^{46}\text{Sc}$ $^{48}\text{Ti} (n, p) ^{48}\text{Sc}$	157 mg, 100% Ti	3.349 Days 83.81 Days 43.7 Hours	1.0 MeV Threshold 3.5 MeV Threshold 5.5 MeV Threshold	159.4 1121,889 984,1312,1038
$^{58}\text{Ni} (n, p) ^{58}\text{Co}$	286 mg, 100% Ni	70.88 Days	1.2 MeV Threshold	811
$^{64}\text{Zn} (n, p) ^{64}\text{Cu}$	117 mg, 100% Zn	12.7 Hours	1.5 MeV Threshold	511 (Positron)
$^{54}\text{Fe} (n, p) ^{54}\text{Mn}$ $^{56}\text{Fe} (n, p) ^{56}\text{Mn}$	132 mg, 100% Fe	312.2 Days 2.578 Hours	1.5 MeV Threshold 5.0 MeV Threshold	834.8 847
$^{93}\text{Nb} (n, 2n) ^{92m}\text{Nb}$	270 mg, 100%Nb	10.13 Days	6.0 MeV Threshold	935

Note: All elements listed have their natural isotopic abundances.

The foils were positioned within the ATRC NW LIPT insert using specialized insert fittings fabricated by the INL Machine Shop for this purpose. Foils used for thermal and epithermal neutron measurements during Irradiation 1 were placed in covered aluminum strips (Figure 4.3). These strips fit into the square holder shown on the left-hand side of Figure 4.4, which fits, in turn, into the square cavity in the cylindrical LIPT insert on the right hand side of Figure 4.4. The Cd-covered packages were placed in the upper position in the first strip and in the lower position in the second strip. The upper and lower positions were reversed for the bare foil packages. This enabled quantification and averaging of flux differences that that may exist between the upper and lower positions due to axial gradients. The insert also contains “dummy” strips in the other eight positions as shown. These dummy strips are designed so that the fully-assembled insert will have the same metal to water ratio as it will have in the case of the third irradiation, where the boron sphere positioning device is substituted in the place of the foil holding strips and dummies used in the first and second irradiations. Copper/gold (1.55% Au by weight) flux wires were also placed at specific locations within the strips as shown in Figure 4.3. These wires are 1 mm in diameter and approximately 0.635 cm (0.25”) in length. They each contain approximately 45 milligrams of copper and 0.7 milligrams of gold. The wires are used to obtain a common measure of the fast and thermal neutron flux in the experiment hardware from one irradiation to another. Final assembly of the foil positioning strips consists of fastening the cover strips in place using aluminum machine screws. Figure 4.4 shows the foil positioning strips mounted in the standard NW LIPT test train inserts.

Co-normalization of the NW lobe power in the three separate reactor runs was accomplished using the measured activation of copper/gold flux wires in the circled position shown in Figure 4.5 between Fuel Plates 10 and 11 (referred to as “Wire Position 10”) at the axial core midplane of the four even-numbered elements surrounding the NW flux trap (Elements 32, 34, 36, 38). These wires are identical to those used in the NW LIPT as described above.

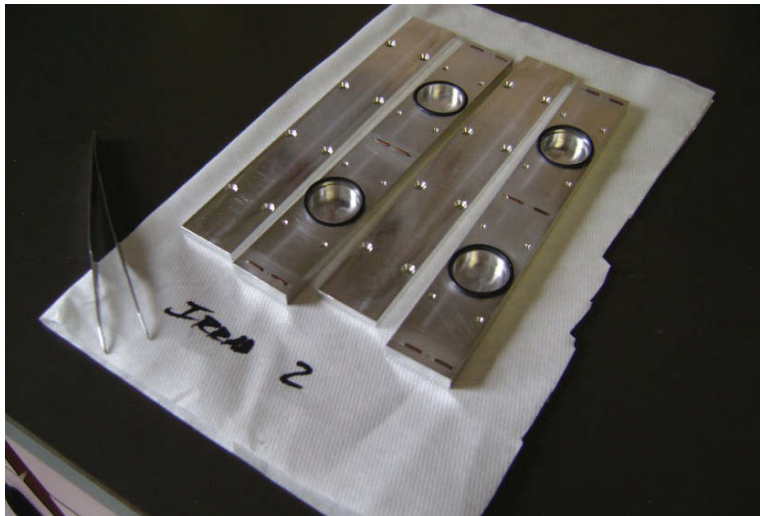


Figure 4.3 Foil positioning strips for the bare and cadmium-covered foil packages. Foils are placed in the circular indentations and duplicate flux wires are placed in the indented slots at each end and in the middle of each strip. The covers are then fastened in place with machine screws.

A second set of foil positioning strips was prepared for Irradiation 2, with flux wires in the various positions as before, but without foil packages. This arrangement represents the assumed “unperturbed” LIPT configuration, which is required in the spectral unfolding and adjustment process. For the third irradiation the package of threshold interaction foils was suspended at the center of the boron spectral shifting shield, which was then placed in a second insert fitting as shown in Figure 4.6. This insert fitting also has 8 positions for flux wires. Another view of the assembled inserts and fittings is shown in Figure 4.7.



Figure 4.4. Foil positioning strips and dummy strips mounted in the standard NW LIPT test train insert.

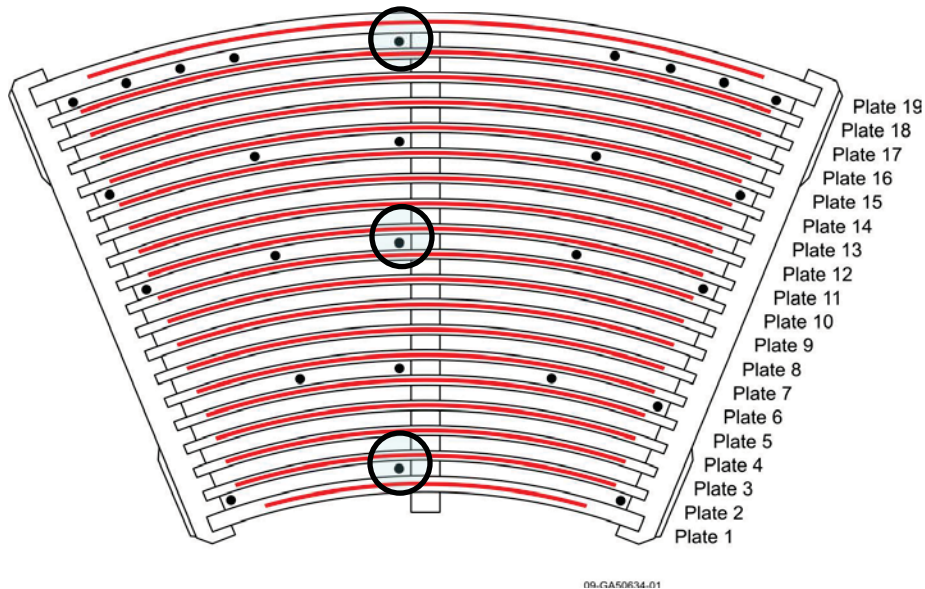


Figure 4.5. ATRC Fuel Element showing available flux wire positions. The circled position in the center was used for power normalization in Irradiations 1-3 as discussed in the text.



Figure 4.6. Fitting for positioning of boron sphere. Duplicate flux wires are placed in the indented slots at each end and just above and below the boron sphere. The two halves are then bolted together.



Figure 4.7. Combined view of the various components of the NW LIPT Neutron Activation Spectrometry apparatus.

The typical experimental arrangement for the NW LIPT, referred to as a Test Train, consists of the midplane insert described above plus several hollow aluminum spacer sections that are assembled together axially and then put inside of an aluminum shroud that fits inside of the NW LIPT. Figure 4.8 illustrates how the test train is assembled for positioning in the NW LIPT with the center section aligned with the axial active core midplane.

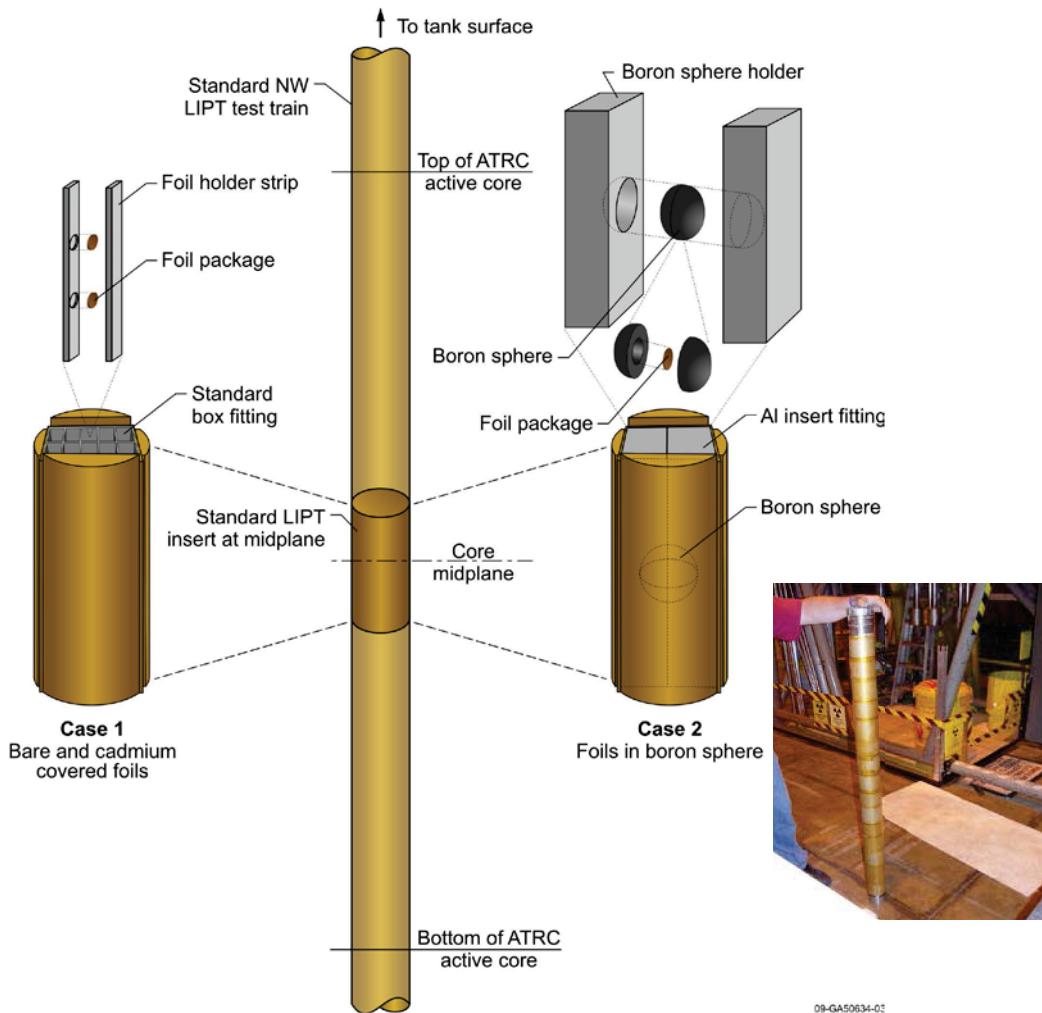


Figure 4.8. Positioning of test train components in the ATRC Northwest Large In-Pile Tube insert. The inset photo shows the entire assembled test train. Case 1 was the configuration for Irradiations 1 and 2. Case 2 was the configuration for Irradiation 3.

4.3 Experimental Results and Least-Squares Adjustment Analysis

The first two irradiations were successfully conducted in late September 2010 at the ATRC. Irradiation 3 was conducted in late April 2011. The activities of the foils and wires were measured at the INL Radiation Measurements Laboratory (RML) according to standard RML procedures using ORTEC HPGe

gamma spectrometers. Some detailed results for the first irradiation and for the first and third irradiations combined are summarized here.

4.3.1 Measured Foil and Wire Responses

Table 4.2 shows the measured saturation activities per atom for all foils whose responses were used in the spectral adjustment procedures reported here. The measured results are arranged in descending order of neutron energy sensitivity. Total activity measurement uncertainties (counting statistics plus detector calibration) are in the range of 4-6% (1σ) for the foils used in Irradiation 1 and 6-10% for those used in Irradiation 3.

Table 4.2. Measured foil saturation activities – ATRC Irradiations 1 and 3.

Response	Irradiation	Spectral Modifier	Measured $\sigma\Phi$
Nb(n,2n)	3	Boron Sphere	2.64E-19
Ti-48 (n,p)	3	Boron Sphere	1.35E-19
Fe-56 (n,p)	3	Boron Sphere	5.12E-19
Ti-46 (n,p)	3	Boron Sphere	5.00E-18
Ti-47 (n,p)	3	Boron Sphere	1.17E-17
Fe-54 (n,p)	3	Boron Sphere	4.10E-17
Zn-502 (n,p)	3	Boron Sphere	2.05E-17
Ni-1004 (n,p)	3	Boron Sphere	5.72E-17
In-(n,n')	3	Boron Sphere	1.30E-16
In(n,n')	1	Cadmium	1.24E-16
In(n,n')	1	Cadmium	1.23E-16
Cu(Res)	1	Cadmium	3.44E-16
Cu(Res)	1	Cadmium	3.54E-16
Mn(Res)	1	Cadmium	9.52E-16
Mn(Res)	1	Cadmium	1.01E-15
W(Res)	1	Cadmium	2.79E-14
W(Res)	1	Cadmium	2.86E-14
Au(Res)	1	Cadmium	4.90E-14
Au(Res)	1	Cadmium	5.09E-14
In(Res)	1	Cadmium	8.03E-14
In(Res)	1	Cadmium	8.57E-14
Au(Th)	1	None	1.07E-13
Au(Th)	1	None	1.09E-13
Mn(Th)	1	None	8.74E-15
Mn(Th)	1	None	8.26E-15

Table 4.3 shows the saturation activities for the Au/Cu flux wires in the NW LIPT hardware as well as in the four surrounding fuel elements. The ratio of the gold activity relative to the copper activity for each wire is shown in the last column. This activity ratio, also referred to as a “spectral index” provides a simple indication of the relative “hardness” of the neutron spectrum to which the wire has been exposed since copper is relatively more sensitive to thermal neutrons but gold is roughly equally-sensitive to thermal and above-thermal neutrons. In the case of a fully-thermalized neutron field where essentially all neutrons are in equilibrium with the surroundings and essentially all above-thermal neutrons have been eliminated this ratio will asymptotically approach the ratio of the Au and Cu cross sections at 2200 m/s, assuming no spatial self-shielding. This asymptotic ratio is approximately 22.1 (i.e. 98.74 barns divided by 4.47 barns). Any departure from the described asymptotic spectral conditions will cause this ratio to increase, primarily due to increased resonance capture in gold. For example it can be seen from Table 4.3 that the Au/Cu ratio is in the range of 51 in the upper wire locations within the NW LIPT hardware. This non-asymptotic ratio reflects the fact that the cadmium ratio for the NW LIPT measurement location is approximately 2, as can be seen from the data in Table 4.2. In the middle locations of the insert this ratio increases to approximately 60. This is an indication of the axial attenuation by aluminum of thermal neutrons streaming vertically into the NW LIPT insert from the water-filled regions above and below.

Table 4.3. Measured flux wire saturation activities – ATRC Irradiation 1.

Wire Location ¹	¹⁹⁷ Au(n,γ) σΦ (±3%)	⁶³ Cu(n,γ) σΦ (±3%)	Spectral Ratio Au/Cu (±5%)
NW LIPT Upper 1L	1.70E-13	3.36E-15	50.41
NW LIPT Upper 1R	1.76E-13	3.29E-15	53.47
NW LIPT Upper 2L	1.74E-13	3.33E-15	52.32
NW LIPT Upper 2R	1.60E-13	3.11E-15	51.53
NW LIPT Middle 1L	1.61E-13	2.62E-15	61.25
NW LIPT Middle 1R	1.58E-13	2.73E-15	57.87
NW LIPT Middle 2L	1.63E-13	2.68E-15	60.60
NW LIPT Middle 2R	1.51E-13	2.65E-15	57.08
NW LIPT Lower 1L	1.75E-13	3.71E-15	47.21
NW LIPT Lower 1R	1.73E-13	3.42E-15	50.63
NW LIPT Lower 2L	1.71E-13	3.56E-15	47.89
NW LIPT Lower 2R	1.83E-13	3.64E-15	50.36
LIPT Average	1.68E-13	3.18E-15	52.86
Fuel Element 32	1.58E-13	1.64E-15	96.23
Fuel Element 34	1.13E-13	1.14E-15	99.06
Fuel Element 36	9.07E-14	8.73E-16	103.84
Fuel Element 38	1.36E-13	1.30E-15	104.40
Core Average	1.24E-13	1.24E-15	100.37

¹ Location “Upper 1L” denotes the wire position at the upper end of Foil Strip 1, Left Side, etc.

Table 4.4 shows the saturation activities of the Au/Cu wires used in Irradiation 2. This irradiation was exactly the same as Irradiation 1 except that only the wires were included in the NW LIPT hardware – the foil positions were empty. It can be seen that the NW LIPT wire activities are very similar at all locations, with very a slight apparent relative increase in the copper activities relative to the gold activities. This indicates that the presence of the foils and their cadmium covers has only a very small (if any) effect on the absolute flux and spectrum within the NW LIPT hardware. It can also be seen that the activities of the wires in the surrounding core fuel elements are essentially identical for the two irradiations. This indicates that the NW lobe was operating at the same total power for both irradiations, as desired. Finally it is interesting to note from the spectral index data in both tables that the neutron spectrum in the core fuel elements is significantly harder than in the NW LIPT. This is as expected, since the NW LIPT and its immediate surroundings provide some moderation of neutrons entering the LIPT region from the surrounding fuel.

Table 4.4. Measured wire saturation activities – ATRC Irradiation 2.

Wire Location ¹	¹⁹⁷ Au(n,γ) σΦ (±3%)	⁶³ Cu(n,γ) σΦ (±3%)	Spectral Ratio Au/Cu (±5%)
NW LIPT Upper 1L	1.82E-13	3.50E-15	51.93
NW LIPT Upper 1R	1.78E-13	3.40E-15	52.44
NW LIPT Upper 2L	1.75E-13	3.54E-15	49.48
NW LIPT Upper 2R	1.74E-13	3.57E-15	48.67
NW LIPT Middle 1L	1.74E-13	2.92E-15	59.48
NW LIPT Middle 1R	1.69E-13	2.93E-15	57.61
NW LIPT Middle 2L	1.65E-13	2.93E-15	56.32
NW LIPT Middle 2R	1.64E-13	2.83E-15	57.96
NW LIPT Lower 1L	1.88E-13	3.84E-15	48.89
NW LIPT Lower 1R	1.81E-13	3.60E-15	50.34
NW LIPT Lower 2L	1.79E-13	3.50E-15	51.03
NW LIPT Lower 2R	1.83E-13	3.86E-15	47.33
LIPT Average	1.76E-13	3.37E-15	52.22
Fuel Element 32	1.67E-13	1.62E-15	103.52
Fuel Element 34	1.13E-13	1.16E-15	97.47
Fuel Element 36	9.63E-14	9.00E-16	106.92
Fuel Element 38	1.28E-13	1.32E-15	96.57
Core Average	1.26E-13	1.25E-15	100.89

¹ Location “Upper 1L” denotes the wire position at the upper end of Foil Strip 1, Left Side, etc.

Table 4.5 shows the wire activities and spectral indices for Irradiation 3. This irradiation was conducted to obtain data about the spectrum above the ^{115}In inelastic scatter threshold (approximately 300 keV). The NW LIPT insert fitting (Figure 4.5) was somewhat different for this irradiation and the boron sphere was used to eliminate interfering interactions from thermal and resonance neutron interactions in the enclosed foils. The significant additional spectral hardening caused by the boron sphere is apparent from the spectral index data in the last column of Table 4.5. In addition, it appears from the data for the core flux wires that the NW lobe was operating at a slightly higher power during Irradiation 3 compared to irradiations 1 and 2. This could be an indication of a slightly higher total reactor power, a slightly greater tilt of the power distribution toward the NW LIPT, or some combination of both in the case of irradiation 3, which was run approximately 6 months after Irradiations 1 and 2. In any event, this information was used to renormalize the foil data from Irradiation 3 slightly downward when combining the Irradiation 3 foil activities with the corresponding foil data from Irradiation 1 to obtain a full range adjusted neutron spectra as described in the following section (the foil activities shown in Table 4.2 reflect this renormalization).

Table 4.5. Measured flux wire saturation activities – ATRC Irradiation 3.

Wire Location ¹	$^{197}\text{Au}(n,\gamma) \sigma\Phi (\pm 3\%)$	$^{63}\text{Cu}(n,\gamma) \sigma\Phi (\pm 3\%)$	Spectral Ratio Au/Cu ($\pm 5\%$)
NW LIPT Upper L	1.69E-13	3.14E-15	53.96
NW LIPT Upper R	1.69E-13	3.12E-15	54.25
NW LIPT Upper Middle L	1.35E-13	1.99E-15	67.73
NW LIPT Upper Middle R	1.26E-13	1.98E-15	63.57
NW LIPT Lower Middle L	1.32E-13	2.00E-15	66.12
NW LIPT Lower Middle R	1.30E-13	2.02E-15	64.49
NW LIPT Lower L	1.70E-13	3.12E-15	54.59
NW LIPT Lower R	1.73E-13	3.20E-15	53.97
LIPT Average	1.51E-13	2.57E-15	58.58
Fuel Element 32	1.88E-13	1.84E-15	102.06
Fuel Element 34	1.29E-13	1.28E-15	100.52
Fuel Element 36	9.88E-14	1.01E-15	97.96
Fuel Element 38	1.47E-13	1.44E-15	102.37
Core Average	1.41E-13	1.39E-15	101.04
Core Average I3/I1	1.13 ($\pm 5\%$)	1.12 ($\pm 5\%$)	-

¹ Location “Upper L” denotes the upper left-hand flux wire position, etc.

4.3.2 Spectral Adjustment (MCNP5 *A-Priori*)

Table 4.6 shows a 6-group adjusted neutron spectrum unfolded from the results of Irradiation 1 alone, using the combined activities of the bare Au and Mn foils and the cadmium-covered In, Au, W, and Mn foils, but not the copper foils. The indium foil provided two linearly-independent responses (capture, and inelastic scatter resulting in excitation of the 336 keV metastable state). There were thus a total of 7 duplicate linearly independent responses included in the determination of the spectrum shown in Table 4.6. The adjusted spectrum was determined using a variance-weighted overdetermined least-square fitting procedure specifically adapted by the INL (Nigg et. al, 2000) for this type of application. Additional detail of this adjustment technique is provided in Appendix B. The elements of the 14 x 6 unfolding matrix and the *a-priori* flux vector for the adjustment procedure were computed using an MCNP5 model of the experimental apparatus as it was positioned in the NW LIPT. The nature of the adjustment algorithm is such that the fluxes shown in Table 4.6 represent a variance-weighted least-squares best estimate spatial average flux over the four foil positions in the apparatus, corrected for the perturbing effect of the cadmium covers and the foils themselves. The bias of the *a-priori* model for the conditions being calculated is the difference between the *a-priori* flux and the adjusted flux, with its corresponding uncertainty. It can be seen that in this case the adjustment tended to reduce the total flux by about 13% with a concurrent small degree of hardening (shift toward the higher-energy groups) that appears to be of limited statistical significance. The chi-squared parameter for the adjustment shows an excellent fit, with a possible indication of over-conservatism in the quantification of uncertainty in the underlying foil reaction rate measurements. Table 4.7 shows the measured, *a-priori*, and adjusted (i.e. computed using the adjusted flux vector) foil saturation activities. It can be seen that the adjusted activities are very consistent with the corresponding measurements.

Table 4.6. Six-group neutron flux spectrum from foils – Northwest Large In-Pile Tube, Irradiation 1, 600W. MCNP5 *a-priori*.

Energy Group	Upper E (eV)	Lower E (eV)	<i>A-Priori</i> Group Flux(n/cm ² -s)	Adjusted Group Flux (n/cm ² -s)	Propagated Flux Uncertainty (1 σ)
1	2.0000E+07	2.9720E+05	1.11E+09	9.22E+08	2.9%
2	2.9720E+05	3.7267E+01	1.25E+09	1.12E+09	8.3%
3	3.7267E+01	1.0677E+01	1.44E+08	1.57E+08	4.4%
4	1.0677E+01	1.8554E+00	2.00E+08	2.00E+08	3.6%
5	1.8554E+00	4.1399E-01	1.82E+08	1.58E+08	4.0%
6	4.1399E-01	1.0000E-05	9.64E+08	8.05E+08	3.5%
Total Fast Flux (Groups 1-5)	2.0000E+07	4.1399E-01	2.89E+09	2.55E+09	3.8%
Fast/Thermal Ratio			3.00	3.17	5.2%

Note: χ^2 per degree of freedom = 0.44

Table 4.7. Measured, *a-priori*, and adjusted foil interaction rates for Irradiation 1

Foil	Measured $\sigma\Phi$	<i>A-Priori</i> $\sigma\Phi$	Adjusted $\sigma\Phi$
In(n,n')	1.2400E-16	1.4956E-16	1.2394E-16
In(n,n')	1.2300E-16	1.4850E-16	1.2306E-16
Mn(Res)	9.5200E-16	1.0689E-15	9.8332E-16
Mn(Res)	1.0100E-15	1.0689E-15	9.8237E-16
W(Res)	2.7900E-14	2.7000E-14	2.8850E-14
W(Res)	2.8600E-14	2.5828E-14	2.7523E-14
Au(Res)	4.9000E-14	5.0076E-14	4.9046E-14
Au(Res)	5.0900E-14	5.1595E-14	5.0545E-14
In(Res)	8.0300E-14	9.0925E-14	8.0545E-14
In(Res)	8.5700E-14	9.6628E-14	8.5474E-14
Au(Th)	1.0700E-13	1.2010E-13	1.0809E-13
Au(Th)	1.0900E-13	1.2115E-13	1.0917E-13
Mn((Th)	8.7400E-15	1.0013E-14	8.4622E-15
Mn(Th)	8.2600E-15	1.0003E-14	8.4522E-15

Tables 4.8 and 4.9, Tables 4.10 and 4.11, and Tables 4.12 and 4.13 respectively show 2-group adjusted neutron spectra and reaction rates determined from the results of Irradiation 1 using the combined activities of the four Au/Cu wires in the upper, middle, and lower axial wire levels. Thus in these cases there were two quadruplicate linearly independent responses included in the determination of the spectrum for each of the three axial levels. The elements of the 8 x 2 unfolding matrix and the *a-priori* flux vector at each axial level were computed using same MCNP5 model of the experimental apparatus as was used for the foils. Once again it can be seen that the adjustments tended to reduce the total flux at each axial level but in these cases with a concurrent small degree of spectral softening, that once again is of limited statistical significance. It is also interesting to note that both the *a-priori* and the adjusted spectra in the middle wire positions are significantly shifted toward the higher-energy group compared to the spectra determined for the upper and lower positions. This again reflects the fact that thermal neutrons entering the top and bottom of the insert fitting from the water above and below are preferentially absorbed in the aluminum structure of the fitting, consistent with the earlier discussion based solely on the various wire activities alone.

Table 4.8. Two-group neutron flux spectrum from upper four wires – Northwest Large In-Pile Tube, Irradiation 1, 600W. MCNP5 *a-priori*.

Energy Group	Upper E (eV)	Lower E (eV)	<i>A-Priori</i> Group Flux(n/cm ² -s)	Adjusted Group Flux (n/cm ² -s)	Propagated Flux Uncertainty (1σ)
1	2.0000E+07	4.1399E-01	2.69E+09	2.00E+09	6.2%
2	4.1399E-01	1.0000E-05	1.14E+09	9.03E+08	3.0%
F/T Ratio			2.36	2.21	6.9%

Note: χ^2 per degree of freedom = 1.67

Table 4.9. Measured, *a-priori*, and adjusted foil interaction rates for upper wires in Irradiation 1

Wire Location	Measured $\sigma\Phi$	<i>A-Priori</i> $\sigma\Phi$	Adjusted $\sigma\Phi$
NW LIPT Upper 1L – Au	1.70E-13	2.36E-13	1.79E-13
NW LIPT Upper 1R – Au	1.76E-13	2.15E-13	1.64E-13
NW LIPT Upper 2L – Au	1.74E-13	2.25E-13	1.71E-13
NW LIPT Upper 2R – Au	1.60E-13	1.99E-13	1.53E-13
NW LIPT Upper 1L – Cu	3.36E-15	4.12E-15	3.26E-15
NW LIPT Upper 1R – Cu	3.29E-15	4.13E-15	3.26E-15
NW LIPT Upper 2L – Cu	3.33E-15	4.22E-15	3.33E-15
NW LIPT Upper 2R – Cu	3.11E-15	4.11E-15	3.25E-15

Table 4.10. Two-group neutron flux spectrum from middle four wires – Northwest Large In-Pile Tube, Irradiation 1, 600W. MCNP5 *a-priori*.

Energy Group	Upper E (eV)	Lower E (eV)	<i>A-Priori</i> Group Flux(n/cm ² -s)	Adjusted Group Flux (n/cm ² -s)	Propagated Flux Uncertainty (1σ)
1	2.0000E+07	4.1399E-01	2.95E+09	2.30E+09	3.7%
2	4.1399E-01	1.0000E-05	9.35E+08	7.46E+08	2.8%
F/T Ratio			3.16	3.08	4.6%

Note: χ^2 per degree of freedom = 0.248

Table 4.11. Measured, *a-priori*, and adjusted foil interaction rates for middle wires in Irradiation 1

Wire Location	Measured $\sigma\Phi$	<i>A-Priori</i> $\sigma\Phi$	Adjusted $\sigma\Phi$
NW LIPT Middle 1L - Au	1.61E-13	2.05E-13	1.61E-13
NW LIPT Middle 1R - Au	1.58E-13	1.97E-13	1.55E-13
NW LIPT Middle 2L - Au	1.63E-13	2.11E-13	1.66E-13
NW LIPT Middle 2R - Au	1.51E-13	1.94E-13	1.52E-13
NW LIPT Middle 1L - Cu	2.62E-15	3.38E-15	2.69E-15
NW LIPT Middle 1R - Cu	2.73E-15	3.33E-15	2.65E-15
NW LIPT Middle 2L - Cu	2.68E-15	3.36E-15	2.68E-15
NW LIPT Middle 2R - Cu	2.65E-15	3.34E-15	2.66E-15

Table 4.12. Two-group neutron flux spectrum from lower four wires – Northwest Large In-Pile Tube, Irradiation 1, 600W. MCNP5 *a-priori*.

Energy Group	Upper E (eV)	Lower E (eV)	<i>A-Priori</i> Group Flux (n/cm ² -s)	Adjusted Group Flux (n/cm ² -s)	Propagated Flux Uncertainty (1 σ)
1	2.0000E+07	4.1399E-01	2.68E+09	1.99E+09	5.0%
2	4.1399E-01	1.0000E-05	1.13E+09	9.96E+08	3.1%
F/T Ratio			2.37	2.00	5.9%

Note: χ^2 per degree of freedom = 0.758

Table 4.14 shows an 8-group adjusted neutron spectrum unfolded from the results of Irradiation 1 (this time including the copper foils) combined with those of Irradiation 3, which enables some additional spectral detail in the higher-energy range. In this case there were 25 responses used for the adjustment, with 7 duplicates and 1 triplicate (¹¹⁵In(n,n')), for a net total of 16 linearly-independent responses. The results are very consistent with the earlier 6-group results. Table 4.15 shows the measured, *a-priori*, and adjusted foil saturation activities for this case. Once again the adjusted activities are very consistent with the corresponding measurements.

Table 4.13. Measured, *a-priori*, and adjusted foil interaction rates for lower wires in Irradiation 1. MCNP5 *a-priori*.

Wire Location	Measured $\sigma\Phi$	<i>A-Priori</i> $\sigma\Phi$	Adjusted $\sigma\Phi$
NW LIPT Lower 1L - Au	1.75E-13	2.23E-13	1.77E-13
NW LIPT Lower 1R - Au	1.73E-13	2.09E-13	1.67E-13
NW LIPT Lower 2L - Au	1.71E-13	2.10E-13	1.67E-13
NW LIPT Lower 2R - Au	1.83E-13	2.40E-13	1.90E-13
NW LIPT Lower 1L - Cu	3.71E-15	4.12E-15	3.57E-15
NW LIPT Lower 1R - Cu	3.42E-15	4.12E-15	3.57E-15
NW LIPT Lower 2L - Cu	3.56E-15	4.19E-15	3.62E-15
NW LIPT Lower 2R - Cu	3.64E-15	4.11E-15	3.56E-15

Table 4.14. Eight-group neutron flux spectrum from foils – Northwest Large In-Pile Tube, Irradiations 1 and 3 combined, 600W. MCNP5 *a-priori*.

Energy Group	Upper E (eV)	Lower E (eV)	<i>A-Priori</i> Flux (n/cm**2-s)	Adjusted Flux (n/cm**2-s)	Propagated Uncertainty (1 σ)
1	2.00E+07	1.92E+05	2.98E+08	2.72E+08	4.25%
2	1.92E+05	2.97E+05	8.16E+08	5.89E+08	13.4%
3	2.97E+05	4.54E+02	9.59E+08	7.29E+08	8.04%
4	4.54E+02	3.73E+01	2.92E+08	2.70E+08	10.18%
5	3.73E+01	1.07E+01	1.44E+08	1.57E+08	4.40%
6	1.07E+01	1.86E+00	2.00E+08	2.00E+08	3.51%
7	1.86E+00	4.14E-01	1.82E+08	1.58E+08	4.00%
8	4.14E-01	1.0000E-05	9.64E+08	8.05E+08	3.51%
Total Fast Flux (Groups 1-7)	2.0000E+07	4.1399E-01	2.89E+09	2.36E+09	4.35%
Fast/Thermal Ratio			3.00	2.93	5.59%

Note: χ^2 per degree of freedom = 0.70

Table 4.15. Measured, *a-priori*, and adjusted foil interaction rates for Irradiations 1 and 3 combined. MCNP5 *a-priori*.

Response	Spectral Mod.	Measured $\sigma\Phi$	<i>A-Priori</i> $\sigma\Phi$	Adjusted $\sigma\Phi$
Nb(n,2n)	Boron Sphere	2.64E-19	2.76E-19	2.52E-19
Ti-48 (n,p)	Boron Sphere	1.35E-19	1.64E-19	1.49E-19
Fe-56 (n,p)	Boron Sphere	5.12E-19	5.65E-19	5.15E-19
Ti-46 (n,p)	Boron Sphere	5.00E-18	6.21E-18	5.66E-18
Ti-47 (n,p)	Boron Sphere	1.17E-17	1.15E-17	1.02E-17
Fe-54 (n,p)	Boron Sphere	4.10E-17	4.65E-17	4.22E-17
Zn-502 (n,p)	Boron Sphere	2.05E-17	2.22E-17	2.02E-17
Ni-1004 (n,p)	Boron Sphere	5.72E-17	6.36E-17	5.73E-17
In-(n,n')	Boron Sphere	1.30E-16	1.46E-16	1.23E-16
In(n,n')	Cadmium	1.24E-16	1.50E-16	1.26E-16
In(n,n')	Cadmium	1.23E-16	1.49E-16	1.25E-16
Cu(Res)	Cadmium	3.44E-16	4.17E-16	3.50E-16
Cu(Res)	Cadmium	3.54E-16	4.09E-16	3.44E-16
Mn(Res)	Cadmium	9.52E-16	1.069E-15	9.84E-16
Mn(Res)	Cadmium	1.01E-15	1.069E-16	9.81E-16
W(Res)	Cadmium	2.79E-14	2.70E-14	2.89E-14
W(Res)	Cadmium	2.86E-14	2.58E-14	2.75E-14
Au(Res)	Cadmium	4.90E-14	5.01E-14	4.90E-14
Au(Res)	Cadmium	5.09E-14	5.16E-14	5.06E-14
In(Res)	Cadmium	8.03E-14	9.09E-14	8.06E-14
In(Res)	Cadmium	8.57E-14	9.66E-14	8.55E-14
Au(Th)	None	1.07E-13	1.20E-13	1.08E-13
Au(Th)	None	1.09E-13	1.21E-13	1.09E-13
Mn(Th)	None	8.74E-15	1.00E-14	8.46E-15
Mn(Th)	None	8.26E-15	1.00E-14	8.45E-15

4.2.3 Spectral Adjustment (KENO-VI *a-priori*)

Table 4.16 shows some preliminary six-group spectral adjustment results for the NW LIPT using the same foil data as before, but with the unfolding matrix elements and *a-priori* flux computed using the previously-described KENO-VI model of the ATR and the NW LIPT experimental hardware. Similar adjusted results were obtained, although the adjustments to the *a-priori* flux were significantly larger than was the case when MCNP5 was used, especially in the resonance energy range (Groups 3-5). This is likely due to the completely different nature of the cross section library used for the KENO-VI model, and will be a subject of further investigation during FY-12.

Table 4.17 shows the measured, *a-priori*, and adjusted foil saturation activities for this case. Once again the adjusted activities are very consistent with the corresponding measurements, although the larger adjustments required for some of the resonance interactions are apparent.

Table 4.16. Six-Group Neutron flux spectrum from foils – Northwest Large In-Pile Tube, Irradiation 1, 600W. KENO-VI *a-priori*.

Energy Group	Upper E (eV)	Lower E (eV)	<i>A-Priori</i> Group Flux(n/cm ² -s)	Adjusted Group Flux (n/cm ² -s)	Propagated Flux Uncertainty (1σ)
1	2.00E+07	2.97E+05	1.50E+09	1.07E+09	3.01%
2	2.97E+05	3.73E+01	1.77E+09	1.29E+09	5.51%
3	3.73E+01	1.07E+01	1.82E+08	1.24E+08	3.62%
4	1.07E+01	1.85E+00	2.42E+08	1.14E+08	3.56%
5	1.85E+00	4.14E-01	2.08E+08	7.66E+07	4.54%
6	4.14E-01	1.00E-05	6.40E+08	8.68E+08	4.03%
Total Fast Flux (Groups 1-5)	2.00E+07	4.14E-01	3.90E+09	2.68E+09	2.93%
Fast/Thermal Ratio			6.10	3.09	5.2%

Table 4.17. Measured, *a-priori*, and adjusted foil interaction rates for Irradiation 1. KENO-VI *a-priori*.

Foil	Measured $\sigma\Phi$	<i>A-Priori</i> $\sigma\Phi$	Adjusted $\sigma\Phi$
In(n,n')	1.2400E-16	1.7193E-16	1.2254E-16
In(n,n')	1.2300E-16	1.7468E-16	1.2449E-16
Mn(Res)	9.5200E-16	1.5051E-15	9.2438E-16
Mn(Res)	1.0100E-15	1.6942E-15	1.0327E-15
W(Res)	2.7900E-14	4.2198E-14	2.8444E-14
W(Res)	2.8600E-14	4.1670E-14	2.8011E-14
Au(Res)	4.9000E-14	1.0110E-13	4.9690E-14
Au(Res)	5.0900E-14	1.0323E-13	5.0702E-14
In(Res)	8.0300E-14	2.1473E-13	8.2595E-14
In(Res)	8.5700E-14	2.1627E-13	8.3363E-14
Au(Th)	1.0700E-13	1.4567E-13	1.0656E-13
Au(Th)	1.0900E-13	1.4395E-13	1.0713E-13
Mn((Th)	8.7400E-15	7.1640E-15	8.3972E-15
Mn(Th)	8.2600E-15	7.3488E-15	8.6613E-15

4.3 Future Work

A fourth irradiation was also completed during FY-2011, with a focus on flux spectrum measurements and power distribution measurements in the core fuel elements using Au/Cu and $^{235}\text{U}/\text{Al}$ flux wires, respectively. Some details of this irradiation were summarized in Section 3.5.2. Data from these measurements remain to be processed and reported. For the longer term, fabrication of an additional set of foil and wire positioning devices was also recently completed for use in the Southeast In-Pile Tube (SE IPT), diametrically across the reactor core from the NW LIPT. The new hardware contains one foil positioning strip, identical to the ones used in the NW LIPT hardware. Two additional spectral measurements will be conducted with this new apparatus, along with the NW LIPT apparatus, in place. In the first of these, the NW LIPT hardware will be the same as described for Irradiation 1, and the SE IPT hardware will be constructed of solid aluminum, with water above and below, similar to the arrangement with the NW LIPT hardware. This provides a true three-dimensional situation for neutron transport, with thermal neutrons passing into the experiment hardware from above and below. In the second of these irradiations the eight dummy foil holder strips will be removed from the NW LIPT hardware and the SE IPT hardware will make use of a second insert fitting that is designed to have only 20% solid aluminum by volume in its structure, allowing water to fill the remaining 80% of the volume around the foils and wires. This will permit a measurement that is more-two-dimensional in terms of spectral changes along the vertical axes of the NW and SE flux traps. In both cases the core fuel elements will also be heavily instrumented with Au/Cu and U/Al wires, and various least-squares techniques for statistically combining the ^{235}U fission rate with the Au and Cu capture rates at each instrumented core fuel location to produce an improved estimate for the adjusted neutron flux spectrum that is also rigorously tied to the local fission rate will be explored. Taken together the six irradiations will form the basis for a flexible and repeatable validation experiment protocol applicable to all of the computational neutron transport tools included in the new suite.

5.0 FEASIBILITY TESTING FOR ATR FUEL BURNUP MEASUREMENT SYSTEM

Rahmat Aryaeinejad (INL) and Jorge Navarro (University of Utah)

State of the art neutronics modeling tools currently being phased into use for computational support of Advanced Test Reactor (ATR) operations and safety analysis will require fuel element isotopic and burnup validation data. Although this information may be retrievable from existing records to some extent, confirmatory burnup measurements for the large inventory of used fuel elements stored in the canal will be required. A suitable non-invasive fuel burnup measurement system will also permit validation measurements for new fuel elements as a tool for quality assurance of the new models as they come into general use for ATR operations support.

1.1 Introduction

In FY10, as a part of the ATR life extension program (LEP), feasibility measurements were carried out on some selected fuel elements in the ATR canal to determine whether it is possible to get a meaningful gamma-ray spectrum of very hot fuels, identify the fission isotopes, establish a method for burnup calibration for long cooling times (1-3 years) and investigate the best way to measure burnup for short cooling times (< 6 months) fuels. A combination of these two calibrations can, in principle, be used to determine the burnup for fuels between these two cooling times (6-12 months). The study consisted of measuring very short, short, and long cooling time fuel elements at the ATR canal. Three different types of gamma-ray detectors of HPGe, LaBr₃, and High Pressure Xenon gas (HPXe) and two system configurations (above and under water) were used in this feasibility study. The idea was to investigate which detector and system configuration would be better suited for different scenarios and how to establish burnup and cooling time calibrations using experimental isotopic ratio and ORIGEN 2.2 burnup calculations.

The results of feasibility study in FY-10 (Nigg, et al., 2010) far exceeded expectations and established the proof-of-concept for non-invasive measurement of burnup for ATR fuel elements. It was found that several isotopic ratios and absolute measurements could be used to predict ATR fuel burnup and cooling times. We have determined the burnup calibrations for three different types of HPGe, LaBr₃, and HPXe detectors. The results also showed the linear relationship between the ¹³⁴Cs/¹³⁷Cs ratio and the burnup for all three detectors. For the first time, we also found a new activity ratio of ¹³⁴Cs/¹⁴⁴Ce has a linear relationship with the burnup. Although, our detection system was not setup for absolute activity measurement, we looked at the activity of some fission products. Among them ¹³⁴Cs and ¹³⁷Cs isotopes found to have linear relationship with the burnup and therefore they can be used as burnup monitors for the ATR fuel. We also investigated to see which other isotopic ratios or absolute activities can be used to determine the fuel element cooling time. The ¹⁴⁴Ce/¹³⁷Cs ratio, ¹⁴⁴Ce, ⁹⁵Zr, and ⁹⁵Nb showed a linear relationship as a function of cooling time. The comprehensive data analysis of these data was continued in FY-11 and the results indicated that the burnup measurement system is performing well and that using the above the water configuration is the right way to design a permanent system. This configuration also makes the design simpler and less expensive. In addition, the results of the study clearly showed that a permanent system would improve the quality of data tremendously with much smaller uncertainty and therefore would be able produce better results that can be compared with the results of calculations from the ORIGEN code as well as the new reactor models that are currently being developed in the overall Methods Update project.

In the first half of FY-11, we completed the analysis of all the data taken during the previous year and also completed the conceptual design of a permanent burnup monitor system. The program execution plan to build this system was submitted to DOE-HQ on January 31, 2011 (document ID: PLN-3721). The

second half of FY-11 was dedicated to measurements on the two short cooling time fuel elements from Cycle 145a that were set aside for us. However, in order to establish the burnup calibration reference we also needed to do measurements on several other fuel elements that we used before for this purpose. Monitoring these fuels every six months provided us with valuable information about the fission product decay and also led to shortening the length of the project by 6-12 months. This is because there was no need to wait months to measure the long half-life fission product yields. All measurements were done with both HPGe and LaBr₃ detectors in above the water configuration during April and May 2011. The analysis of these data was completed. The results definitely confirmed the results obtained in the feasibility studies. We found new isotopic ratios for burnup and cooling time determination. We also found new fission product isotopes that can be used to determine cooling time for short cooling time fuels between six to twelve months.

Below we will discuss the apparatus and methods used for non-destructive fuel burnup measurements performed at the INL ATR canal facility and show some results. At the end of this report we will summarize the recommended approach to the design and construction of a permanent burnup measurement system for future production use. Additional details can be found in the 2011 program execution plan noted previously.

1.2 Background and Conceptual Feasibility Study Results

The use of gamma-ray spectrometry for the passive, non-destructive determination of spent fuel burnup and cooling time has been common in domestic and international safeguards for decades (Reily et al., 1991; Ramalho and Payne, 1979; Phillips et al., 1980; Lebrun and Bignan, 2001). These techniques usually rely on ratios of various fission products rather than absolute concentration measurements. This is because ratios is geometry-independent and can generally be determined more accurately. Also, the fission product ratios measured by gamma-ray spectrometry can be directly compared with those computed by a validated isotope build up and model calculations code such as ORIGEN (Croff et al., 1980). This code uses the data provided with either the operator-declared irradiation and cooling history, or a generic set of irradiation and cooling times to confirm the irradiation history.

The absolute gamma-ray activity of a particular fission product, or the ratio of the particular isotopes, is used to measure the fuel burnup. This depends on the fuel element cooling time. No matter which technique is used, there ideally should be a linear relationship between the absolute isotope activity or isotopes ratio and the burnup value. The burnup calibration is obtained by measuring fuel elements with different burnup, well known irradiation history, and cooling times. The burnup is then plotted versus the absolute activity or isotopes ratio to obtain a linear burnup calibration curve. Finally, the burnup for unknown fuel element is simply derived from this calibration curve. For long cooling times fuels (> 9 months), the absolute activity of ¹³⁷Cs or ratio of some fission product isotopes such as ¹³⁴Cs/¹³⁷Cs or ¹⁵⁴Eu/¹³⁷Cs is used. However, for short cooling time fuels (< 6 months), the absolute measurement of activity of ⁹⁵Zr, ¹⁰⁶Ru, ¹⁴⁴Ce, or ¹⁴⁰La may be required.

It is very important to emphasize here that all measurements were done with the detection system hanging with the crane and the detector position was controlled using ropes attached to the front and the back of detection system. Thus the exact detector positioning was not as well controlled as it would be in a permanent system. This was done for the preliminary feasibility measurements in order to avoid the expense of building a tower structure with motors to place the detection system at an exact location. The purpose was to determine whether the preliminary results are promising before committing to build an expensive tower structure.

1.2 Measurement Setup

In this section, we briefly describe the types of detectors used, waterproof housing and collimators of the detection system, and finally the measurement configurations.

Historically, detector of choice for very high-resolution gamma-ray spectroscopy has been Hyper-Pure Germanium detectors (HPGe). Other alternatives are to use room temperature inorganic scintillators or high pressure gas detectors.

For fuel burnup measurements the detection system must be rugged, not very sensitive to environmental temperature extremes. It should preferably operate at room temperature if possible and must have a better energy resolution than commonly used NaI scintillator detector. Within the last few years, several promising detector candidates have emerged that offer resolution between that of HPGe and NaI. In particular, two alternate room temperature detector types are now available as commercial detector products offering energy resolution in the range of 2.5% to 3.5% (which is at least factor of 2 better than the NaI detector) with acceptable efficiency for many applications. These are lanthanum bromide LaBr₃ (Ce activator) scintillation detector and high pressure xenon (HPXe) gas detector.

For the feasibility study, we used three types of HPGe, LaBr₃, HPXe and detectors as shown in Figure 5.1. Two different sizes of HPGe detectors (40% efficient and 25% efficient) and two different sizes of LaBr₃ (1"x1" and 2"x2") were utilized in our measurements. We used 1.5" in diameter and 4" long HPXe detector made by Constellation Technology. This detector consists of the ionization chamber filled with a Xenon gas plus 0.3% H₂ mixture at the density of 0.35 g/cm³ and gas pressure of 650 psi (44 atmospheres). This detector has energy resolutions of 2.7% and 2.0% for the ¹³⁷Cs 662-keV peak and the ⁶⁰Co 1332-keV peak, respectively. The performance of these detectors has been tested to determine which one is better suited for specific cooling times and burnup. In some cases like very short cooling time it is absolutely necessary to use an HPGe detector because of many close-by gamma rays that cannot be resolved using the other two detectors. However, for fuels with a long cooling time the less expensive LaBr₃ or HPXe detector is more likely sufficient.



Figure 5.1. Detectors used in this study.

Figure 5. 2 shows the waterproof housing, collimators, and detector holder used in the measurements. The housing is made of aluminum and is 9" in diameter and 16" long. It consists of cylinder attached to the front and back plates. The back plate has a cables port, which attached to the PVC tube for sending HV, preamplifier and signal cables through and then to electronics modules outside the water. Other parts are support a rod made of stainless steel (attached to the front and back plates) and crane hook for lifting the housing. Inside the housing there is a collimators holder to make sure everything is centered along the housing cylinder axis. The collimator system is made of bismuth (Bi) that contains several different pieces for a multi-purpose functionality that can accommodate different types and sizes

of detectors. This includes the 40% HPGe, 25% HPGe, 1"x1" LaBr₃, 2"x2" LaBr₃, and HPXe gas detectors used in this study. The collimator system consists of two 2"-thick Bi discs, collimator insert in the front, and one 1.5"-thick Bi cylinder in the back. Not shown in this figure, there is also an additional

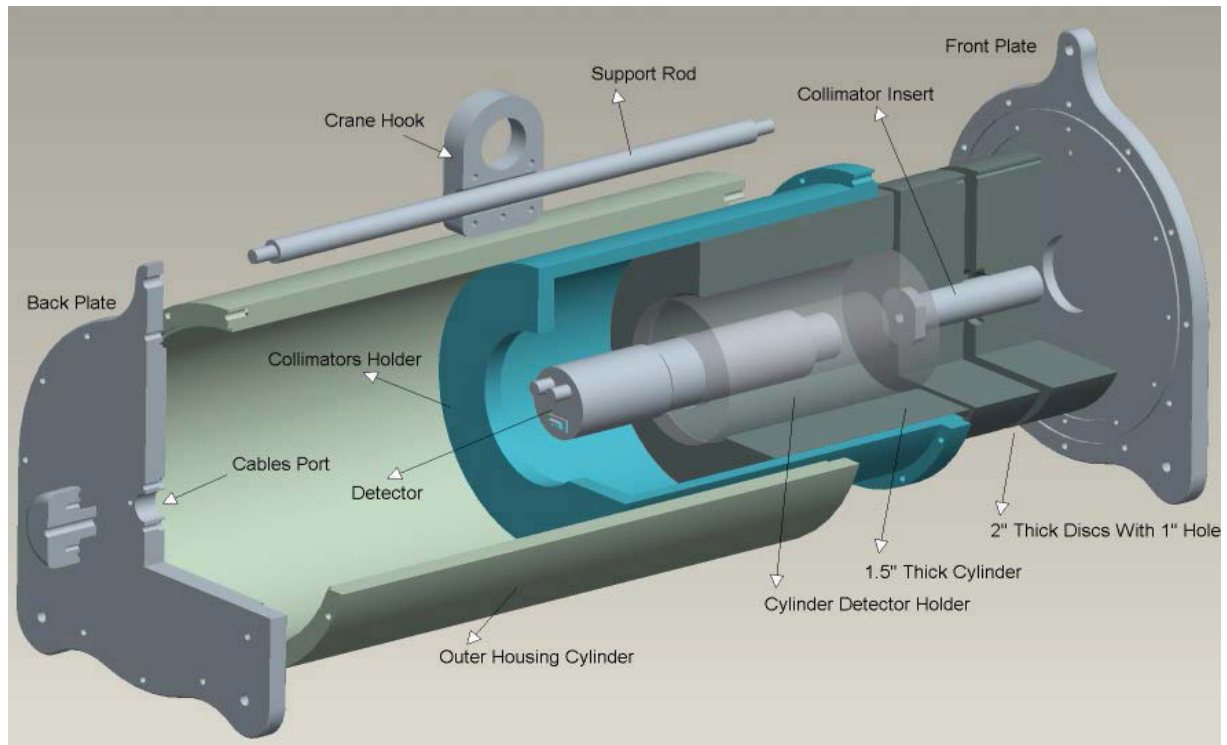


Figure 5.2. Waterproof housing and collimators.

0.5" Bi sleeve that can be inserted inside the bigger cylinder when smaller detectors are used to provide more shielding around the detector. In fact, this Bi sleeve was used in all of our measurements. Different collimator inserts with different shape and sizes were used to determine which ones deliver the best results under different measurement scenarios.

In the feasibility study the measurements were performed with both underwater and above-water configurations. The analysis was focus on determining which detector configuration provides better

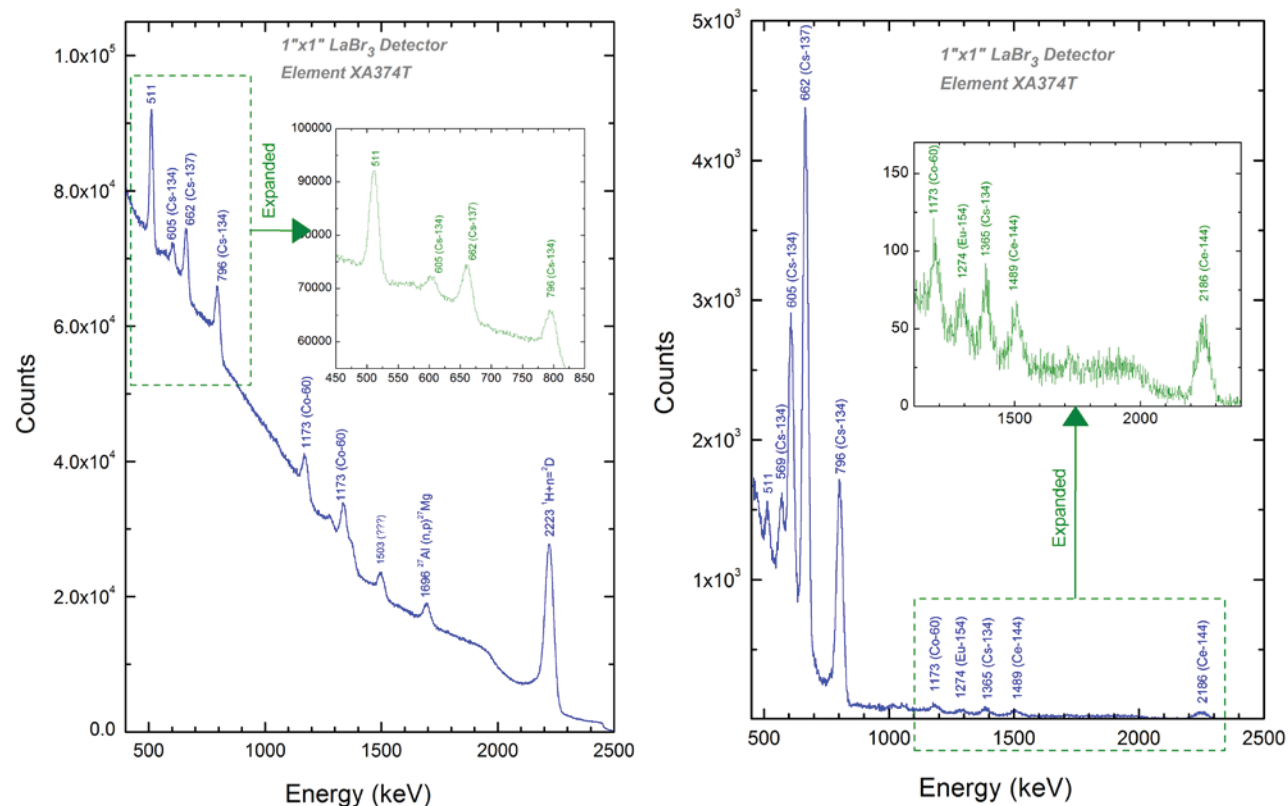


Figure 5.3. Spectra taken with the LaBr₃ detector under the water (left) and above the water (right) results. Figure 5.3 shows spectra of element XA374T taken with the LaBr₃ detector in two different configurations of under the water (left) and above the water (right), respectively. The detection system in the under the water measurements was placed at 4.0 ft from the fuel element XA374T. By comparing the two spectra it is very clear that quality of spectrum is much better for the above the water measurements, especially for low energy gamma rays like 605 keV of ¹³⁴Cs and 662 keV of ¹³⁷Cs peaks. This is mainly due to the fact that gamma rays are severely attenuated going through the water in the under-water measurement. Gamma attenuation is higher in the underwater detector setup due to 4 feet of water that gamma rays have to travel before reaching the detector. While in the above the water setting gamma rays need to travel only 6 inches of water. Another important distinction between these two spectra is the existence of the hydrogen neutron-capture peak at 2223 keV in the under the water measurement (see Figure 5.3 left). The neutrons are produced from alphas (emitted from actinides) reaction with low-Z materials and also from spontaneous fission of even-mass actinides. This peak was not observed in the above water spectrum due to the shorter distance between the fuel element and pipe (less water between), and also due to the long 15 feet of air within the collimated pipe that this gamma ray has to travel to reach the detector. In under the water configuration there is 4 feet of water between the fuel element and the detector and therefore one expect to see more neutron interaction with hydrogen, which translates to very strong 2223-keV peak.

In conclusion, the comparison of these two spectra shows much better results can be obtained using the above the water configuration. Therefore, measurements in FY-11 were performed only in this configuration as shown in Figure 5.4.

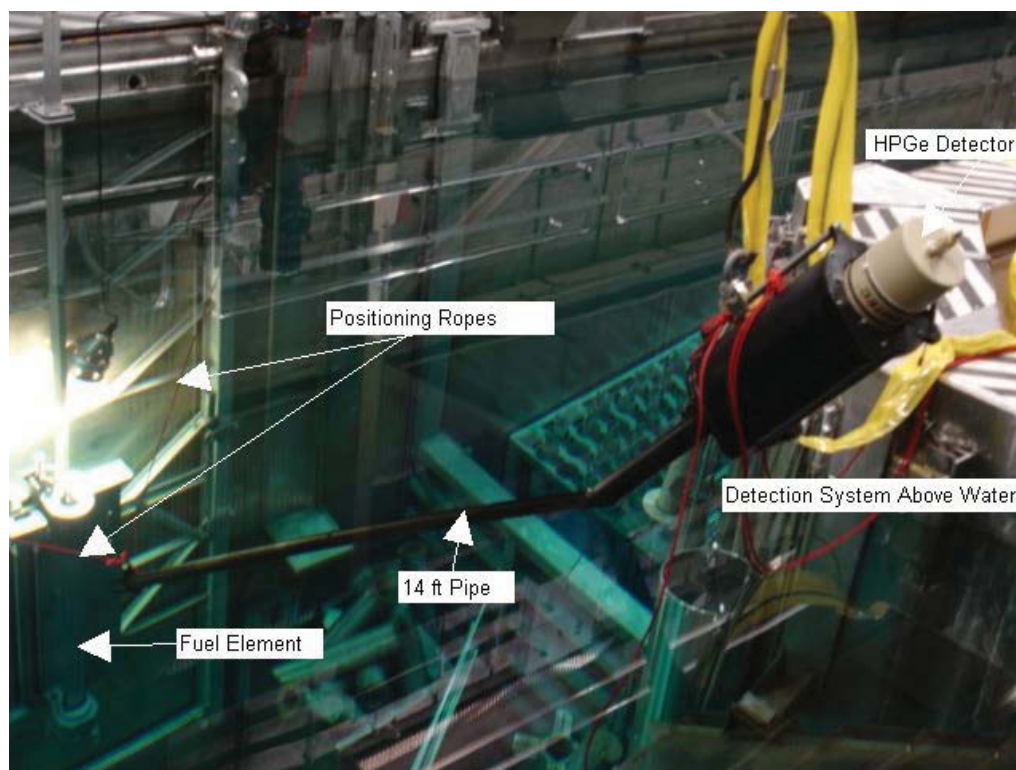


Figure 5.4. Above the water configuration.

The fuel elements were placed inside the turning table vertically, with the plate number 19 facing the detector. The detector was viewing a small section fuel assembly allowed through small aperture in the collimator insert. The detection system was lowered with the crane to the desire position and ropes attached to the front and back of the lifting rod controlled the position of the detection system. A long 14-foot pipe with the 2.5" inches in diameter was attached to the front of detection system housing. This pipe was water-sealed with air inside. Inside the pipe at the end additional collimation system made of Bi was added in order to collimate gamma rays emitted from the fuel element through the pipe. Here again, collimator inserts with different aperture were utilized to decrease or increase the gamma-ray flux going through the pipe. For example, the collimator pipe with a small collimator insert hole allows the detector to view small section of the fuel assembly and therefore the pipe can be moved closer to the fuel element.

In our study the ORIGEN 2.2 computer code was used to calculate burnup and depletion rates along with fission products isotopes activities of ATR fuel elements. The objective was to correlate experimental isotopic activity or isotopic ratios with ORIGEN fuel burnup values to create calibration curves that would create a tool to predict fuel burnup of ATR fuels. Correlations are necessary because determining burnup directly from gamma spectroscopy is a difficult task.

1.2.1 Measurement Techniques

An efficient and reliable fuel management program requires having on-site accurate information concerning fuel elements without having to completely rely on computer codes. An integral part of any on-site fuel management system has to involve non-destructive techniques that can provide burnup and cooling time information of fuel elements without the need of expensive destructive chemical tests. Non-

destructive methods are a more attractive tool than chemical tests because they are faster, cheaper and most importantly they preserve the integrity of the fuel.

The use of gamma-ray spectrometry for the passive, non-destructive determination of spent fuel burnup and cooling time has been common in domestic and international safeguards for decades. These techniques usually rely on ratios of various fission products rather than absolute activity measurements. This is because ratios are geometry-independent and can generally be determined more accurately. Also, the fission product ratios measured by gamma-ray spectrometry can be directly compared with those computed by a validated isotope build up and decay model code such as ORIGEN.

Two of the most important parameters for fuel management are burnup and cooling time since discharge of fuel assemblies. Burnup of the fuel is among the most valuable pieces of information that ideally can be obtained by knowing the initial material composition and comparing it to the amount of fissile material left in the fuel at the end of the reactor power cycle. However, performing a procedure that can effectively and directly measure the leftover material is very difficult. The ^{235}U content cannot be directly measured because gamma rays from the fission products dominate the spectrum by roughly 7 orders of magnitudes, which mask the ^{235}U gamma rays. One of the feasible and simpler ways is to use gamma-ray spectroscopy to indirectly estimate burnup by using the spontaneous emission of gamma-rays emitted from the fission products.

There are about 10 major isotopes produced in fission process that can be measured after fuel discharge. Table 5.1 lists these dominant isotopes, along with their half-lives and gamma rays. Only strong gamma rays are listed. In this table, the decay half-life, fission yields (per 100 fission disintegrations), Gamma-ray relative intensity (in black) and gamma-ray emission probability (in red) are reported. In addition to the fission product gamma rays, gamma rays from the activation of fuel cladding and structural materials such as ^{54}Mn , ^{58}Co , and ^{60}Co , not listed in this table, may be also present depending on type of reactor, and fuel kind.

Ultimately, the main objective of this study was to find correlations between experimental measurements and burnup or cooling time. Either absolute gamma-ray spectroscopy that measures the activity of one or more fission product isotopes, or relative measurements that determine the ratio of activities of two certain isotopes can be used to measure the fuel burnup. Absolute activity measurements require the careful and precise determination of the detection system efficiency calibration that is energy dependent. This means that being able to position the detection system at precise position all the time in order to obtain accurate results. Unfortunately, this was not possible with the crane system used in our study. However, with the proposed permanent system (discussed later) capable of positioning the detection system within 1/1000" accuracy, absolute measurements is easily achievable. However, we developed a technique in which burnup and cooling time calibrations were done at the specific distance that allow us to determine the burnup and cooling time of unknown fuel elements at the same distance independent of geometry. Here, the total area of a gamma-ray peak of interest would be directly proportional to absolute activity of the fission isotope.

Table 5.1. Fission fragments in spent fuel assemblies with their half-lives and associated main gamma rays from their decay. The % relative intensities are in black and the gamma-ray emission rates per 100 decays are in red. Only strong gamma rays are listed in this table.

Isotope	Half-Life	Fission Yields (%)	Main gamma rays (keV)
$^{140}\text{Ba} \rightarrow$ ^{140}La $^{140}\text{La} \rightarrow$ ^{140}Ce	12.75 d 1.68 d	6.2	537.26 (100%, 24.4%) 328.8 (19.6%, 20.3%), 487.0 (44.7%, 45.5%), 815.8 (24.2%, 23.3%), 925.2 (7.2%, 6.9%), 1596.2 (100%, 95.4%), 2521.4 (3.59%, 3.5%)
^{95}Zr	64.02 d	6.5	724.2 (80.6%, 44.2%); 756.7 (100%, 54.5%)
^{95}Nb	34.99 d	6.5	765.8 (100%, 99.8%)
^{144}Ce	284.5 d	5.5	133.5 (804%, 11.9%) 696.4 (100%, 1.3%); 1489.2 (21.4%, 0.3%); 2185.6 (57%, 0.7%)
^{103}Ru	39.27 d	3.0	497.1 (100%, 91.0%); 610.3 (7.4%, 5.8%)
^{106}Ru	1.02 yr	0.4	511.4 (100, 20.4%); 621.9 (48.8%, 9.9%); 873.5 (7.6%, 0.4%); 1050.5 (7.6%, 1.6); 1128.1 (1.98%, 0.4%); 1562.2 (0.8%, 0.2%)
$^{133}\text{Xe} \rightarrow$ $^{133}\text{Cs} + n \rightarrow$ ^{134}Cs	2.06 yr	6.7 ^a	569.3 (15.3%, 15.4%); 604.7(100%, 97.6%); 795.8 (87%, 85.5%); 801.8 (8.8%, 8.7%); 1038.5 (1.1%, 1.0%); 1167.9 (2.0%, 1.8%); 1365.1 (3.3%, 3.0%)
$^{154-xn}\text{Eu} +$ $xn \rightarrow ^{154}\text{Eu}$	8.59 yr	1.6 ^b	123.0 (100%, 40.6%); 247.9(16.8%, 6.9%); 996.3(30.3%, 10.5%); 1004.8(50.5%, 17.9%); 1274.4 (95.0%, 35.0%)
^{137}Cs	30.07 yr	6.2	661.6 (100%, 85.1%)

a) Fission yield is for the ^{133}Xe isotope

b) Fission yield is for the ^{153}Eu isotope.

Typically, a good burnup calibration can be achieved by selecting few fuel assemblies (4-5) with a wide range of burnup and cooling times and irradiation histories. The process was also focused on finding sets of elements that their burnups and activities or activity ratios yield linear correlations. The selection on the fuel was based on an analysis from results of exploratory studies made with ORIGEN 2.2. The exploratory studies performed with ORIGEN were the main tool to efficiently and effectively determine how many and which ATR fuel elements to measure. The selection was based primarily on analyzing ORIGEN results from several calculations performed on a series of elements with a wide range of burnups and cooling times. The ORIGEN Calculations told us which fission products isotopes to expect, their relative strength and their capability to correlate with burnup and cooling times. Then the burnup is plotted versus the absolute activity or isotopic ratio to obtain a linear calibration curve. Finally, the burnup for unknown fuel assembly is simply derived from this calibration curve. The ratios of certain radioisotope activities such as $^{134}\text{Cs}/^{137}\text{Cs}$ or $^{154}\text{Eu}/^{137}\text{Cs}$ are directly related to the fuel element burnup. In a study of measurements on 14 PWR fuel assemblies the $^{134}\text{Cs}/^{137}\text{Cs}$ ratio technique coupled with one destructive assay of burnup, provided burnup determinations with good accuracies and in some cases within 5% (Phillips et al., 1980).

1.2.2 ORIGEN Model Calculations

ORIGEN 2.2 is a point depletion and decay computer code used to simulate nuclear fuel cycles (Croff, et al., 1980). In this study ORIGEN 2.2 simulation code was used to calculate burnup and depletion rates along with fission products isotopes activities of ATR fuel elements. The objective was to correlate experimental isotopic activity or isotopic ratios with ORIGEN fuel burnup values to create calibration curves to predict fuel burnup of ATR fuels. Based on previous studies mentioned before and data analysis, numerous calibration curves using ORIGEN 2.2 burnup results in combination with experimental fission products absolute and isotopic ratio activities were created. Establishing the consistent relationships between activity measurements and burnup will ultimately allows us to experimentally determining ATR fuel elements burnup without the need of previous irradiation history or computer calculations.

1.2.3 Measurement Results

ATR uses uranium-oxide fuel, and its cycle times are relatively short. As a result, the fuel typically has little Pu buildup that could negatively impact radiation measurements. Additionally, ATR is typically operated at relatively constant power levels, so determination of fuel element power histories should be fairly straightforward. These will make the ATR burnup estimation process less complicated. The fuel elements measured were irradiated at the Advanced Test Reactor at the Idaho National Laboratory. Each element has 19 plates and approximately 1075 grams of ^{235}U . The measurements were performed at the canal adjacent to the reactor using five and two different gamma detectors in FY-10 and FY-11, respectively. The fuel elements were placed into a turn table fuel holder with plate number one facing towards the wall and the detector pointing at plate number nineteen.

In April and May of FY-11 we performed measurements on 4 and 6 fuel elements at the ATR canal. Two of the fuel elements were the ones set aside for us for burnup calibration of the proposed permanent system. Measurements on the other fuel elements were carried out in order to establish the burnup calibration reference. The data analyses of these measurements as well as ORIGEN calculations were completed. The measurements were done using the HPGe and LaBr₃ detectors in above the water configuration only. No measurements were performed with the HPXe gas detector.

Figure 5.5 shows typical spectra taken with the germanium detector divided into three groups, based on their cooling time. The first group contains measurements made on element XA815T that was in

thereactor for one cycle. Element XA815T was monitored with the high purity germanium detector for

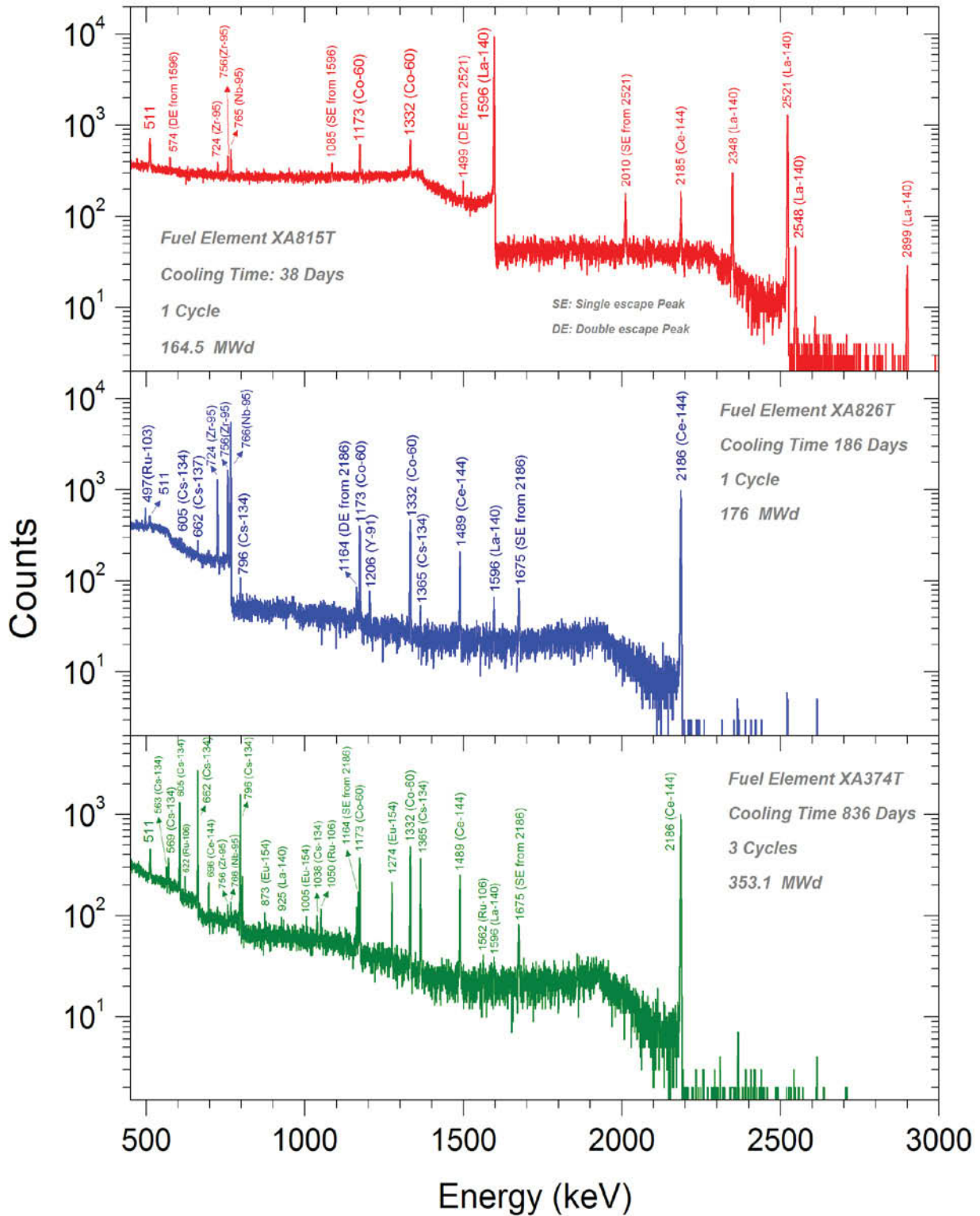


Figure 5.5. Spectra taken using the HPGe detector with very short (top), short (middle), and long (bottom) cooling time fuel elements.

two months. Measurements were taken every two weeks to monitor the decay history of the fission product isotopes. The top spectrum shows a spectrum taken with a 45% efficient HPGe detector after 38 days of cooling time. Due to high resolution of this detector the peaks of all the isotopes are very well separated. It can be seen that the spectrum is dominated by the gamma-ray emitted from the short-lived fission product isotope ^{140}La with a half-life of 12 days.

The second group of experiments consisted of measurements done on element XA826T, during a 5-month span. The element XA826T had been in the reactor for one cycle and the measurements with the high purity germanium detector started on March 17, 2010. Figure 5.5 middle spectrum is the data taken with the element Xa826T taken on May 10, 2010 using the HPGe detector. On that day, the cooling time was 186 days. This spectrum when compared to the top spectrum shows the natural decay behavior of the fuel fission products. The spectrum is dominated by the ^{95}Zr (64 days half-life) and ^{95}Nb (35 days half-life) peaks while the ^{140}La peaks are mostly decayed away. It can also be seen that the long lived ^{137}Cs and ^{134}Cs are starting to show up in the spectrum. Another dominating peak is ^{144}Ce , this peak was part of the XA-815T spectrum but due to the dominate role of ^{140}La isotope it was relatively a small peak.

The third group of experiments consisted of measurements on several elements with longer cooling times (6 months- 3.5 years). Figure 5.5 bottom spectrum shows the HPGe data taken for element XA374T. If we compare it to the previous two groups spectra indicates that almost all the short lived isotopes (^{140}La , ^{95}Zr , and ^{95}Nb) have decayed away. Most of the peaks in the bottomspectrum are due to long-lived isotopes. The strongest peaks come from ^{134}Cs , ^{137}Cs , and ^{144}Ce . Also, in this spectrum the ^{154}Eu gamma-ray peaks can be seen. From these spectra it is clear that all close-by gamma rays are easily resolved due to the high energy resolution.

The same measurements of above three fuel elements were also performed using LaBr_3 detector. The spectra taken with detector are shown in the Figure 5.6. The top spectrum is for very short cooling time fuel, middle spectrum is for short cooling time fuel, and bottom spectrum is for long cooling time fuel.

By comparing spectra shown in Figures 5.5 (HPGe data) and 6 (LaBr_3 data) taken with the same fuel elements it is clear that the high purity germanium spectrum has a far better energy resolution than the LaBr_3 spectrum. The better energy resolution of the HPGe detector makes it possible to resolve close-by peaks. This becomes very important for short cooling time fuels. In addition, the peak-to Compton (P/C) ratio is much better for the HPGe detector resulting in a better area definition, which reduces the measurement uncertainties.

1.2.4 Calibration Results

The data analysis was focus on calibration curves made with experimental absolute activity or isotopic activity ratio and theoretical burnup and cooling times. These calibrations are the main goal of our study because they will allow us to create mathematical relationships to predict ATR fuel burnup and to become a useful fuel management tool. There were a number of calibrations curves created most of them based on last year analysis and results reported by various authors. Four activity ratios and three absolute activity isotopes were identified as consistent burnup and cooling time monitors for ATR fuel elements.

This year analysis was based on a smaller set of data than fiscal year 2010 and the ratios and areas chosen were derived from last year results. The study consisted in analyzing three sets of experimental data taken with two different detectors and was mainly gear towards verifying the consistency of isotope ratios and areas that were previously determined as good cooling time and burnup ATR fuel monitors and also look at other fission isotopes not studied before.

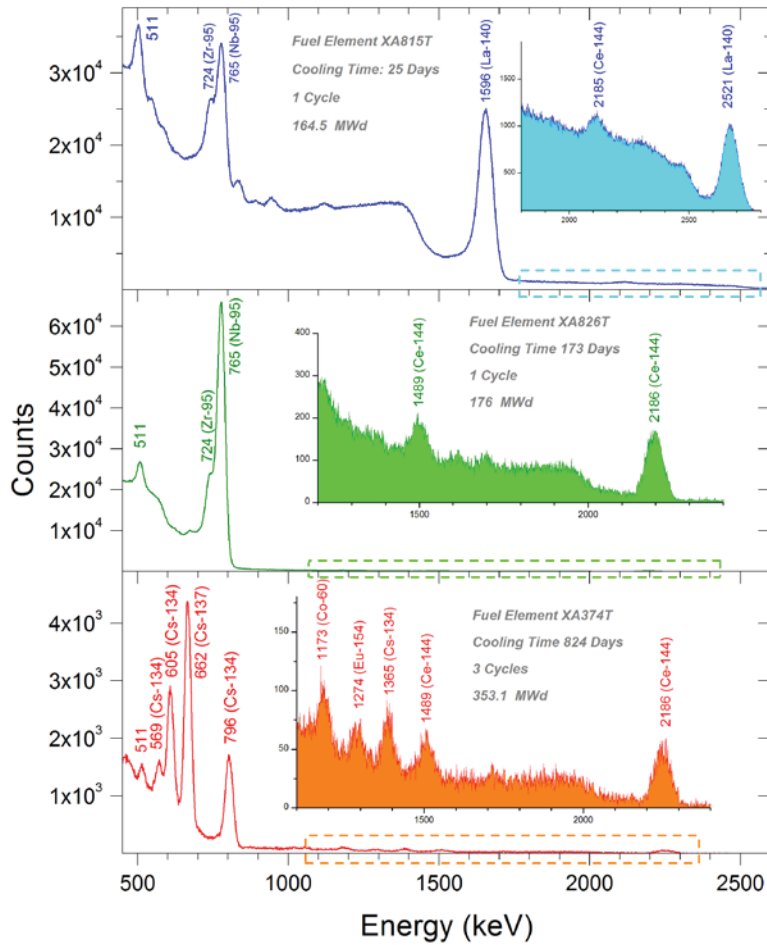


Figure 5.6. Spectra taken using the LaBr₃ detector with very short (top), short (middle), and long (bottom) cooling time fuel elements.

The data analysis was focus on three different data measurements sets taken with two different detectors (HPGe and LaBr₃). Nine elements were subject to measurements .The data analysis from last year allow us to narrow down the number of calibration curves that were performed. Gamma-ray peak used for calibration in each isotope is shown in Table 5.2.

Table 5.2. Gamma-ray peaks used for calibrations

Isotope	Half-life	Gamma-ray peak used for calibration (keV)
⁹⁵ Zr	64.02 d	756.7
⁹⁵ Nb	34.99 d	765.8
¹³⁴ Cs	2.06 yr	604.7
¹³⁷ Cs	30.07 yr	661.6
¹⁴⁴ Ce	284.5 d	2185.6

1.2.5 Burnup Calibrations

As discussed before quantitative characteristics of nuclear material in fuel cannot be measure directly from gamma radiation. Characteristics for determining burnup have to be estimated indirectly using indicators based on radiation from fission products. The basic approach is to correlate burn up with absolute activity, or activity ratios from long-lived fission product isotopes to indirectly determine the quantitative attributes of the fuel element.

The key to success of any approach to indirectly calculate quantitative characteristics from fission products indicators relies on being able to have dependable measurements along with burnup values from operations or depletion codes. Two of the burn-up calibration monitors ($^{134}\text{Cs}/^{144}\text{Ce}$ and ^{134}Cs) that we are using in this study have not been previously reported by other investigators.

The most consistent monitor in most studies done by other authors and also in our study last year was the activity ratio of $^{134}\text{Cs}/^{137}\text{Cs}$. The results can be seen in Figure 5.7, where experimental isotopic ratios for

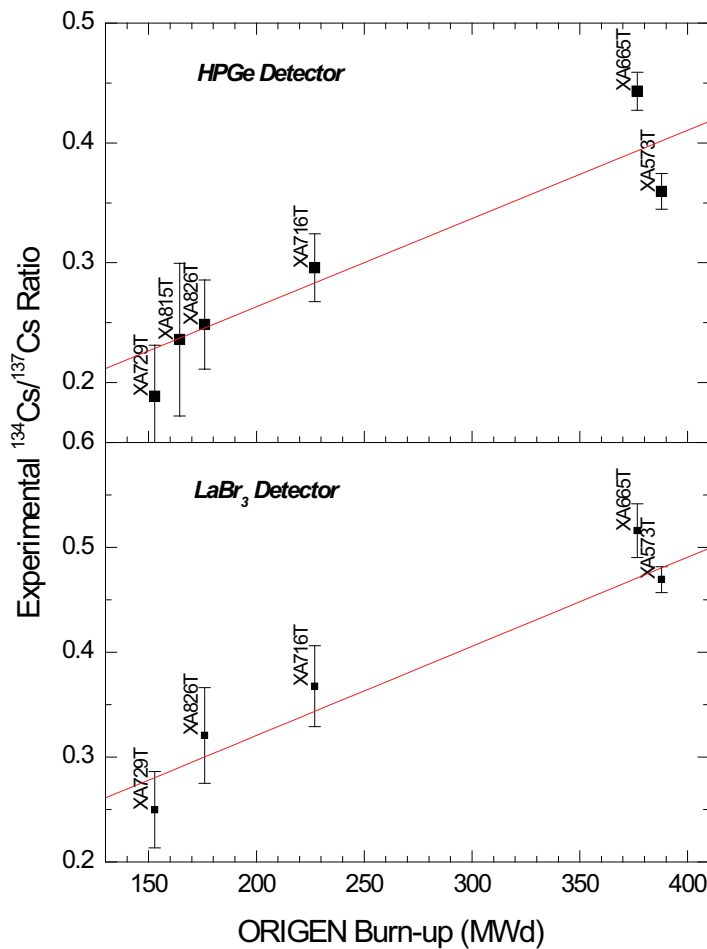


Figure 5.7. Experimental $^{134}\text{Cs}/^{137}\text{Cs}$ ratio as a function of fuel burnup for the HPGe detector (top) and the LaBr₃ (bottom) detectors.

ATR fuel elements were plotted against burnup calculated with ORIGEN. In this figure, it can be seen that for the same set of data taken with different detectors the two plots show a consistent linear trend.

Figure 5.8 show the performance of ^{134}Cs as a burn-up monitor for a set of elements taken with two different detectors (top HPGe and bottom LaBr_3) in two different dates. The trend shown by the two plots confirms the calibration monitor consistency and corroborates last year's results proving that ^{134}Cs can be an option to predict ATR fuel burnup.

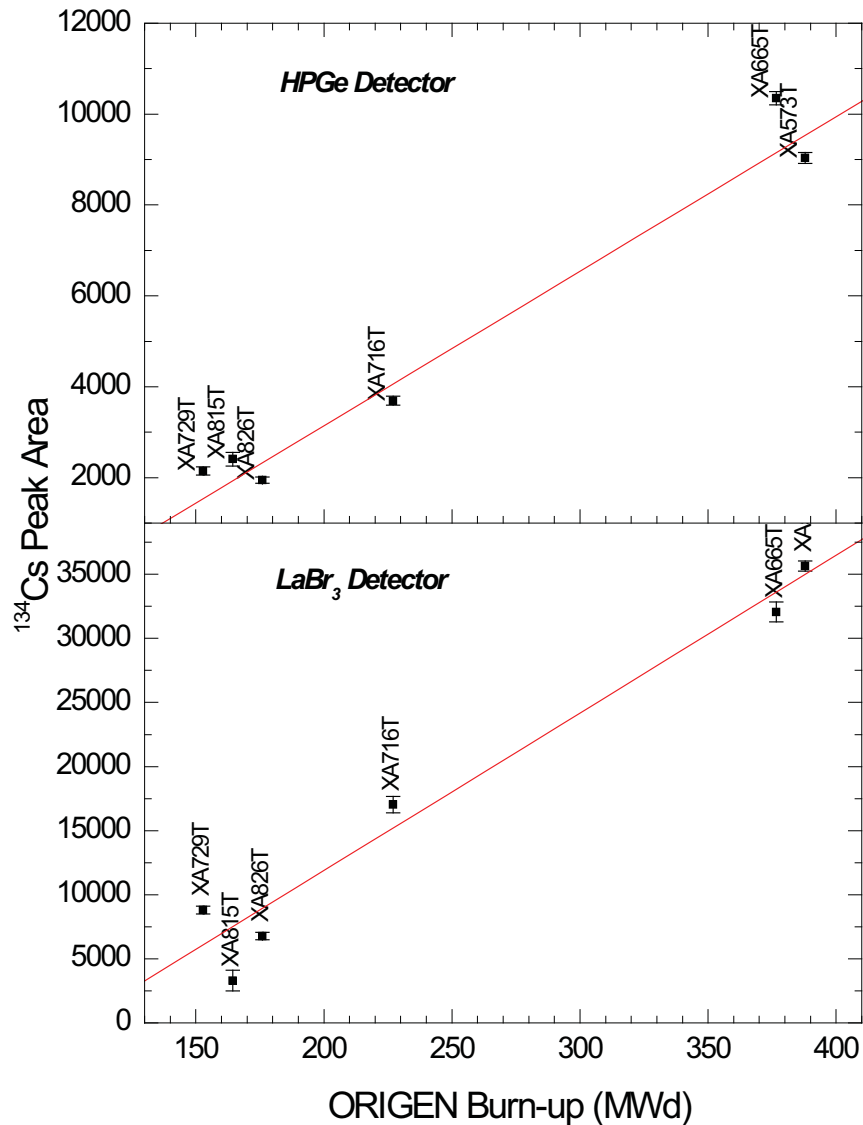


Figure 5.8. Experimental ^{134}Cs peak area as a function of fuel burnup for HPGe detector (top) and LaBr_3 (bottom) detectors.

The last burnup monitor used in this study was $^{134}\text{Cs}/^{144}\text{Ce}$ ratio. Figure 5.9 (top) shows a linear trend between the experimental ratio obtained with an HPGe detector and ORIGEN generated burn-up. The results shown in this figure corroborate the results obtained in last year analysis making $^{134}\text{Cs}/^{144}\text{Ce}$ ratio a good burnup monitor candidate for ATR fuel. Figure 5.9 (bottom) shows the ORIGEN calculated $^{134}\text{Cs}/^{144}\text{Ce}$ ratio as a function of fuel burnup.

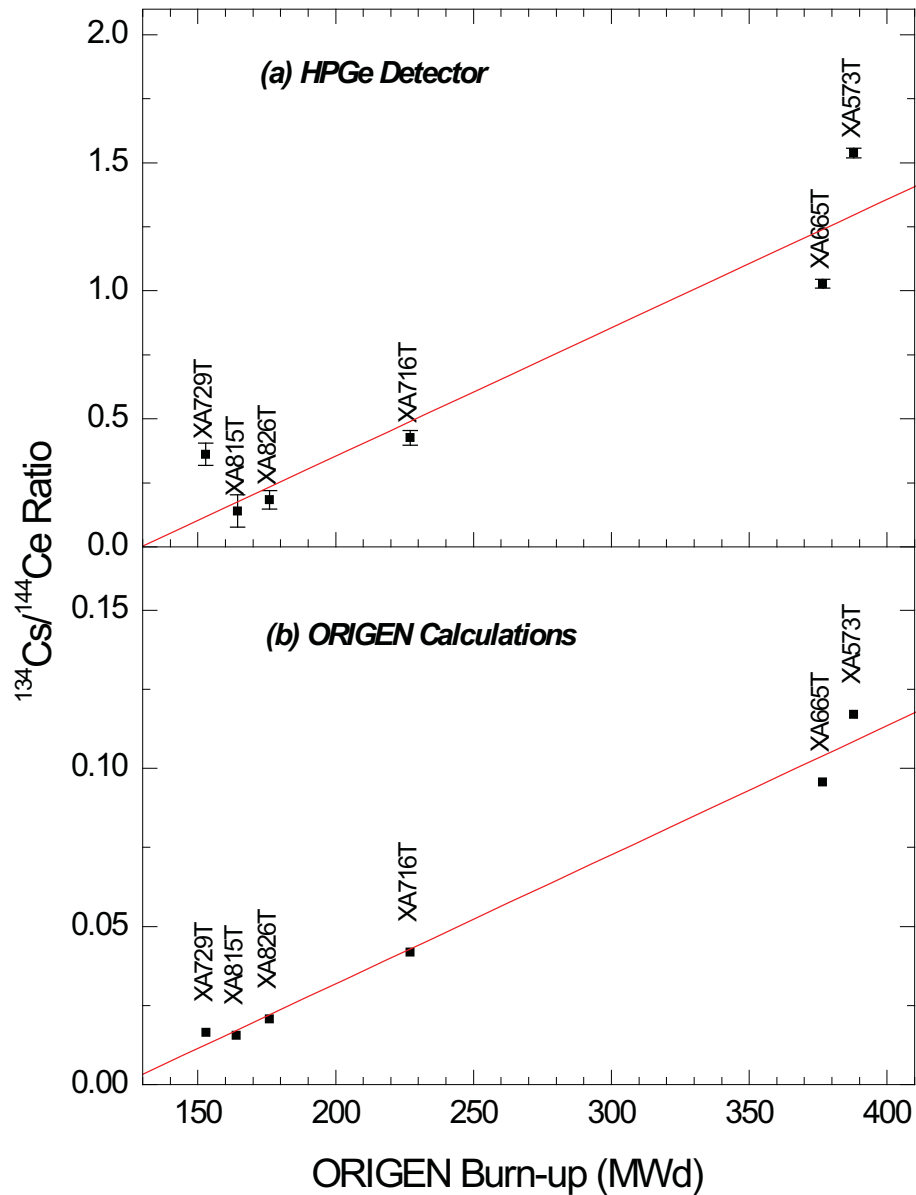


Figure 5.9. Experimental $^{134}\text{Cs}/^{144}\text{Ce}$ ratio (top) and ORIGEN calculated $^{134}\text{Cs}/^{144}\text{Ce}$ ratio as a function of fuel burnup.

The X axis in the two plots is the same so the analysis should be based on the Y axis and just by simply comparing the two of them it can be seen that the trend of the data points in both graphs are the same. For example in the top plot the $^{134}\text{Cs}/^{144}\text{Ce}$ ratio for the XA665T fuel element is below the line whereas this ratio is above the line for the XA573T. The same is through for the ORIGEN calculated ratio in the bottom plot. This simple comparison is a rough, crude and very preliminary ATR fuel geometry independent validation for ORIGEN using experimental data.

1.2.6 Cooling Time Calibrations

Six different cooling time calibrations curves were performed, as mention before these ratios and absolute areas were selected based on previously data analysis. Figure 5.10 shows the two calibration curves based on the experimental ratio of $\text{Log} (^{137}\text{Cs}/^{144}\text{Ce})$ vs cooling time.

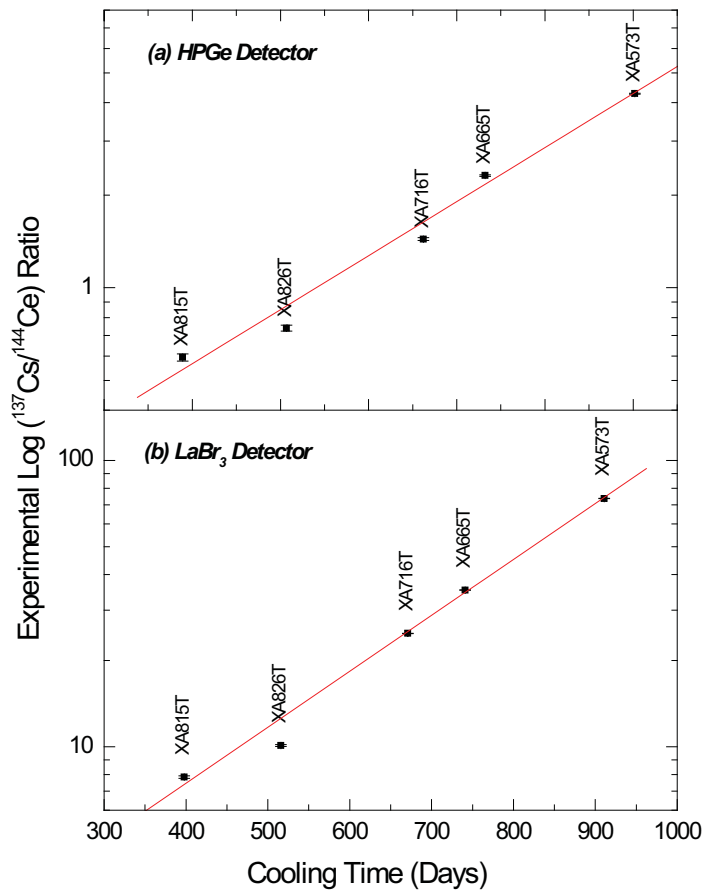


Figure 5.10. Experimental $^{137}\text{Cs}/^{144}\text{Ce}$ ratio as a function of fuel cooling time for the HPGe (top) and LaBr₃ (bottom) detectors.

The top plot is for the HPGe detector and the bottom plot is for the LaBr₃ detector. This particular ratio was not used previously in our analysis however our earlier studies indicated that the use of this ratio could yield high-quality cooling time calibration curves. By comparing these two calibration curves in this figure, it can be seen that the experimental $\text{Log} (^{137}\text{Cs}/^{144}\text{Ce})$ ratio in the two curves change linearly

with the cooling time. The fact that the two graphs taken with different detectors show the same trend for every element, shows the consistency of this particular ratio monitor.

Figure 5.11 depicts the next set of graphs of the area of ^{95}Zr (top plot) and the Log of $^{144}\text{Ce}/^{95}\text{Zr}$ ratio (bottom) to predict cooling time of ATR fuel elements. The experimental measurements were taken with the HPGe gamma-ray detector.

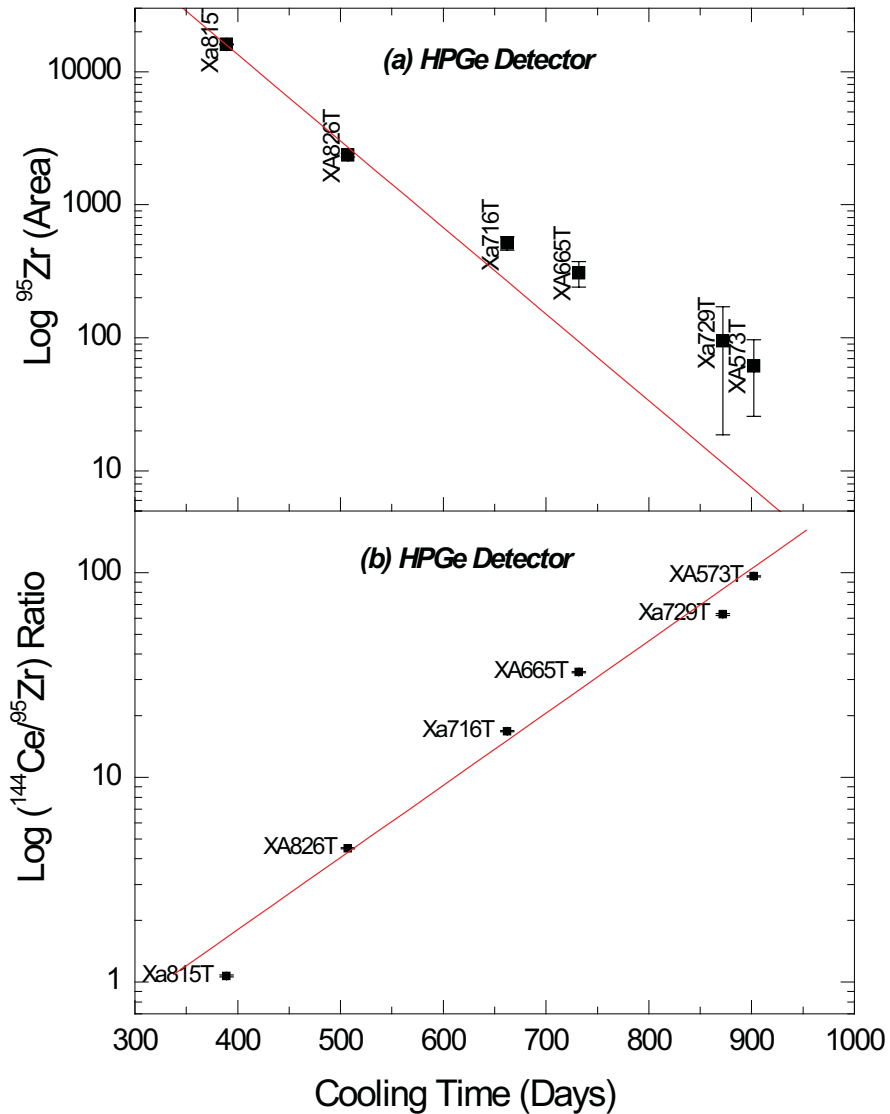


Figure 5.11. Experimental Log(^{95}Zr) area (a) and $^{144}\text{Ce}/^{95}\text{Zr}$ ratio (b) as a function of fuel cooling time.

As it can be seen in the top graph two data points after 700 days (XA729T and XA573T) deviate sharply from the linear trend. This deviation is due to the short half life of ^{95}Zr (64.02) limiting its

usefulness to short cooling time predictions. It is also important to mention here that the $^{144}\text{Ce}/^{95}\text{Zr}$ ratio (bottom plot) was not previously reported as a cooling time monitor.

Figure 5.12 contains two plots, the top plot shows the correlation between the experimental area of ^{95}Nb cooling time while the bottom plot is the correlation between $^{95}\text{Nb}/^{144}\text{Ce}$ ratio and cooling time.

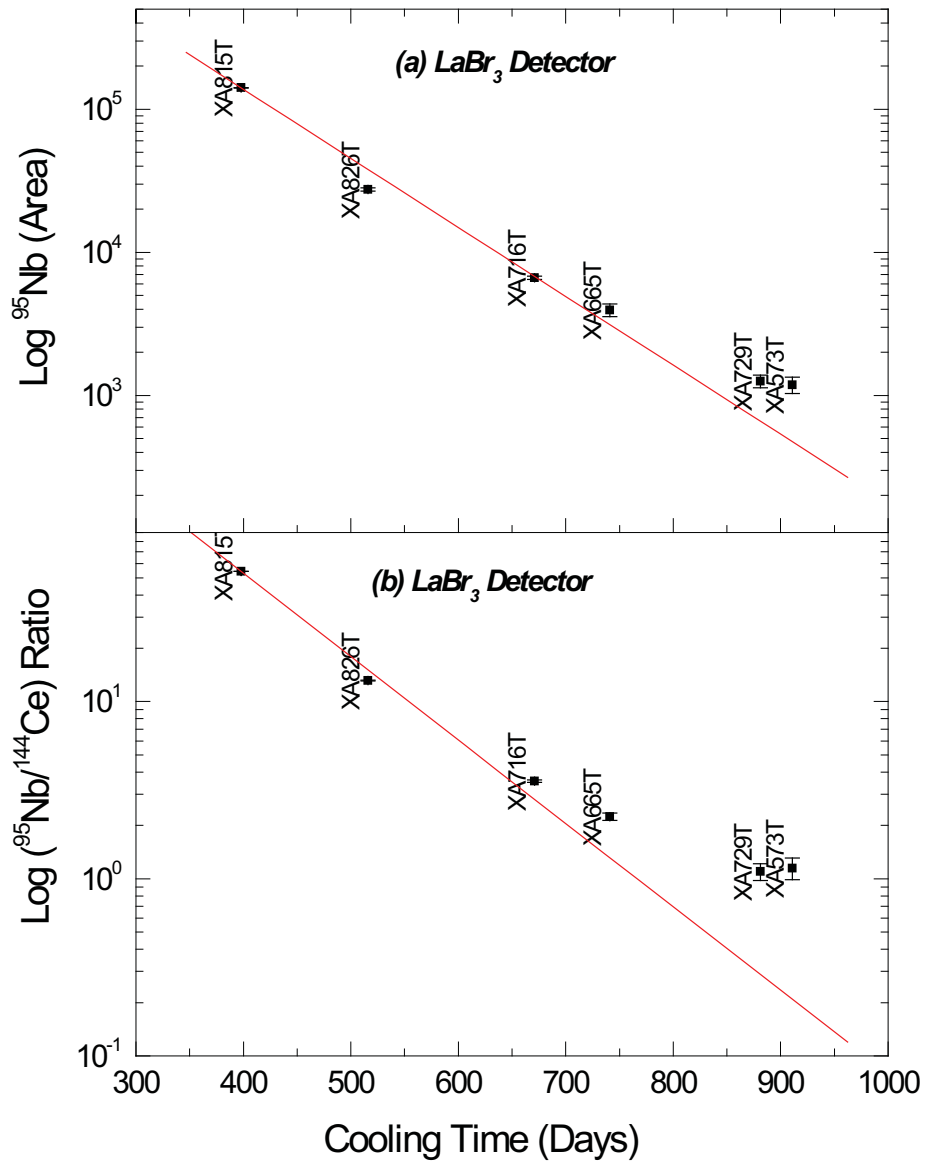


Figure 5.12. Experimental $\text{Log}(^{95}\text{Nb})$ area (a) and $^{144}\text{Ce}/^{95}\text{Nb}$ ratio (b) as a function of fuel cooling time using the LaBr_3 detector.

The two plots were generated with data taken with the LaBr_3 detector. Again here, like in the case of ^{95}Zr in Figure 5.11 (top), by analyzing the top plot in this figure it can be concluded that after

approximately 700 days ^{95}Nb cannot be used as a precise ATR fuel cooling time monitor, due to its short half-life of 34.4 days. The ^{95}Nb isotope area was used as a cooling monitor instead of the ^{95}Zr because the resolution of the LaBr_3 detector does not allow to accurately resolve the ^{95}Zr peak, this problem can be resolved by applying spectra enhancement techniques. The analysis of Figures 5.11 and 5.12 corroborates the results we obtained last year by confirming that ^{95}Zr and ^{95}Nb are consistent monitors for short cooling time fuel elements.

The final cooling time calibration monitor used in our study was ^{144}Ce as shown in Figure 5.13.

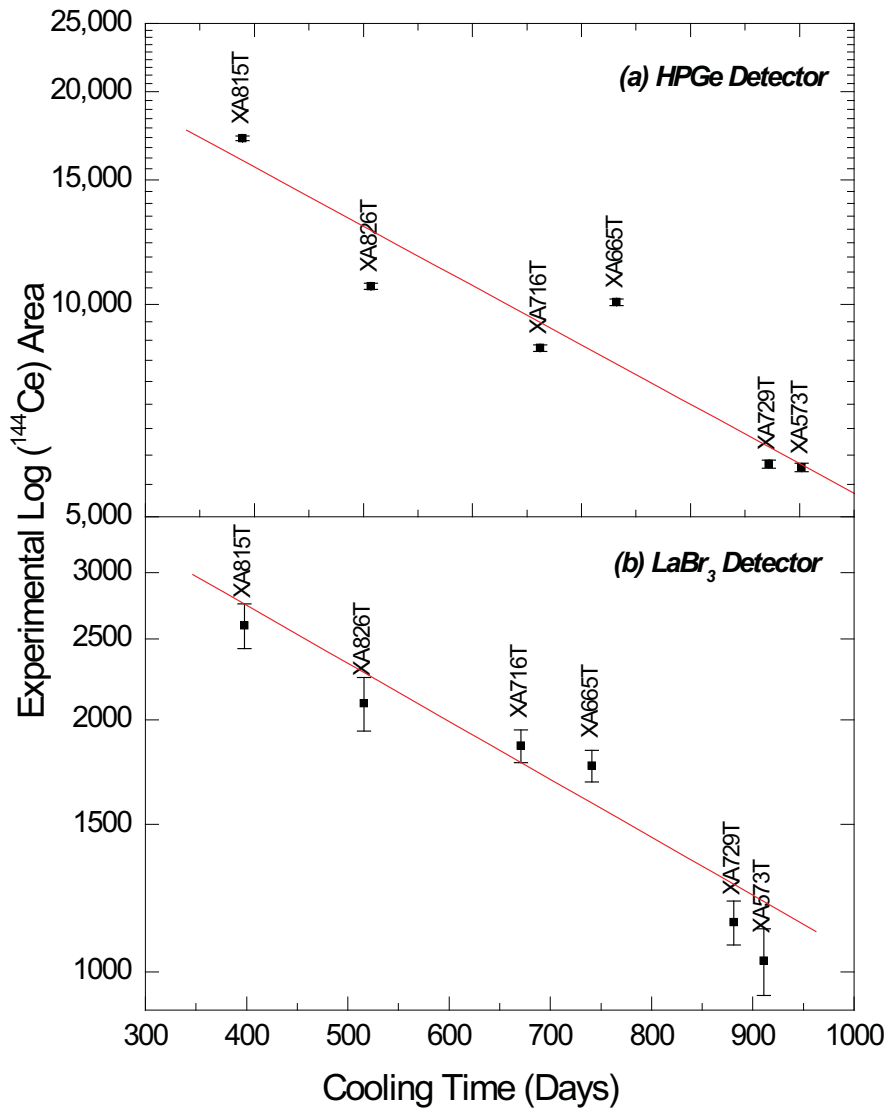


Figure 5.13. Experimental $\text{Log}(^{144}\text{Ce})$ area as a function of fuel cooling time for the HPGe (top) and LaBr_3 (bottom) detectors.

The top plot was taken with the HPGe detector and the bottom plot was made using data taken with the LaBr_3 . By analyzing Figure 5.13 it can be seen that in the two plots generated with two different

detectors with the same number of data points representing ATR fuel elements follow a linear trend. This analysis also confirms the results obtained in last year measurements. For the ^{144}Ce isotope we used the highest gamma peak at 2185.6 at higher end of gamma spectrum for our data analysis because there is no interference from other gamma rays. Because of the longer half-life of ^{144}Ce isotope (284.5 days), this gamma-ray peak can be used for a broader cooling time range up to two years.

1.2.7 Proposed Permanent System and Experimental Plans.

The impressive results of the feasibility study showed that the ATR fuel elements burnup as well as cooling time can be experimentally determined with the small uncertainties and we can now proceed to design, build the permanent system at the ATR facility. The conceptual design for a permanent ATR Fuel Burnup Measurement System (FBUMS) is shown in Figure 5.14.

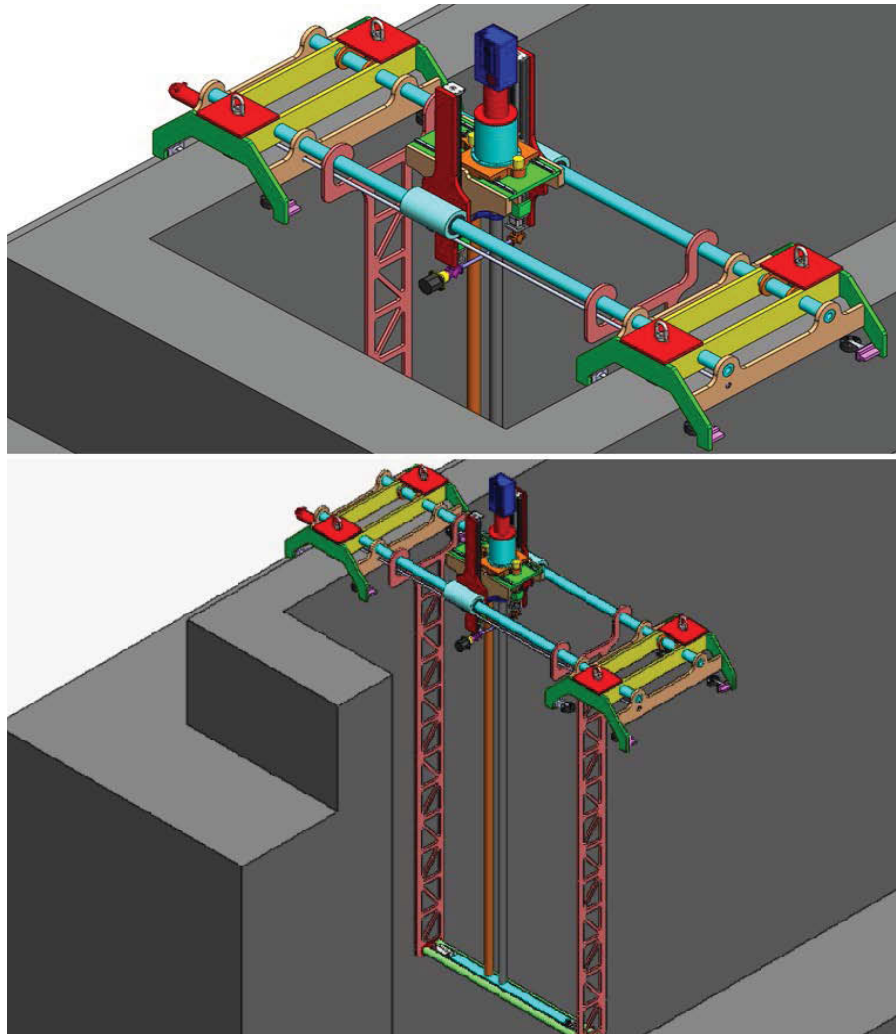


Figure 5.14. Conceptual design of a permanent fuel monitoring system.

This system would be consisted of the following major subsystems:

- X Scan Axis
- Lead Screw Trolley

- Detector Housing
- Two Down Pipes
- Fuel Element Carriage
- Computer Control System

It is capable moving the detection system and placing it exactly at desired spot with accuracy of 1/1000". The tower structure will be placed on the east side of canal. The system includes parallel rods to hold the detection system above the water and a U-shape structural frame in the water with the Fuel Element Carriage (FEC) at the bottom to hold a fuel assembly. Measurements will be done with detection system above the water and with the 14' collimated pipe attached to it. This makes the design simpler and less expensive. This is because outside the water and less expensive motors can be used to move the detection system in "X" and "Z" directions. By looking at the data analyzed so far we believe the existing housing collimator can be utilized for the permanent system.

FBUMS is configured as a two axis (X-Z) computer controlled scanning system. Two parallel 3" diameter stainless steel shafts form the X axis which spans the width of the ATR canal. Each end is mounted on a set of wheeled trucks with locks that will retain the FBUMS in position over the canal. A Lead Screw Trolley (LST) moves the detector system along the X axis. The trolley, positioned between the shafts, is incrementally driven back and forth. This movement is parallel and directly above the length of the fuel element suspended below. The X axis provides a trolley parking area at one end to accommodate fuel element loading in the Fuel Element Carriage (FEC) below. The ATR fuel element to be inspected will be supported horizontally in the FEC suspended approximately 14 feet below the canal water level. The FEC will automatically position and center the fuel element in the same position relative to the detector before every inspection cycle.

The Detector Housing Assembly (DHA) is mounted on two short horizontal slides on the X Scan Carriage (XSC) for manual positioning of the assembly over either Down Pipe Assembly (DPA). The DPAs are approximately 14 feet long, air filled pipes with different sized bismuth collimators located at the bottom end of the tubes. Shielding on the DPA insures both down pipes are covered at all times to prevent streaming radiation during inspection of the fuel elements, especially for the pipe that is not used.

The Z axis lifts the XSC, DHA and DPAs vertically, a maximum of 24 inches to increase the distance between the end of the pipe and consequently the HPGe Detector and the fuel element under inspection. A computer system will control the mechanical operation of the scanning system and also collect the spectral data from the detector system.

This system also allows us to do measurements along the fuel element to obtain the radiation profile for investigating the fuel burnup uniformity.

The system could be constructed over a period of three years. An immediate task during the first year would be to complete the final design of the permanent system and initiate fabrication as soon as possible. It is estimated that about 3 months would be required to build the tower system. The procurement of a mechanically cooled HPGe detector and associated digital signal processing would also be done as soon as possible because of required 3-months lead. The next step would be to install the whole system on the east side of the ATR canal. After the installation, the energy and efficiency calibrations of the detection system would be performed.

The burnup and cooling time calibrations would be done on two sets of fuel elements. The first set involves 7 fuel elements that we used for calibrations in the feasibility study with the burnup between 100 to 400 MWD ranging from 1-4 cycles irradiation in the reactor. This would enable us to compare the result with the feasibility study results and establishes the fact that the system is performing as expected

and with much better accuracy and smaller uncertainties. For the better calibrations we use the second set of the fuel elements containing 3-4 un-irradiated fuel elements. These fresh fuels will be put in the reactor at the same time in selected positions under controlled monitoring. After the first cycle these fuels will be characterized using three different types of detectors (HPGe, LaBr₃, HPXe). Next, we keep one of the fuel elements in storage and put the rest of fuel elements back in the reactor for the second cycle. During this cycle, we perform measurements every week on the other fuel element not in the reactor. After the second discharge we characterize all fuel elements and keep another discharged fuel in storage and put the rest of the 2-cycle fuels back in the reactor for the third cycle irradiation. During this cycle, we continuously monitor and perform measurements on the other two fuels not in the reactor. Finally, after the third discharge we continue our measurements of all fuel elements every week. A combination of these fuel elements and two other fuel elements that were set aside for feasibility study, should establish burnup and cooling time calibrations using both ratio and absolute methods. The results will be compared with the results of ORIGEN calculations as well as the new 3D modeling calculations if are available. If the results are insufficiently conclusive, some destructive fuel analysis may be needed to resolve the discrepancies and to validate the results.

For best burnup calibration we are planning to do fast scan of the fuel every 12" to obtain both gamma-ray and neutron radiation profiles. For this we are going to use the pocket-sized gamma/neutron radiation detector system developed at the INL (Aryaeinejad et al., 2004 and Aryaeinejad et al., 2009). This device is capable of scanning the fuel element and provides, simultaneously, the gamma-ray and neutron profiles in less than 10 minutes. The small waterproof housing need to be fabricated to put the detector inside of it and then attached it to the end of one of the down pipes. In addition, some modifications to the firmware and software are necessary to get the data and show the radiation profiles. If irradiation of the fuel is uniform then one would expect to see flat gamma-ray and neutron profiles. Otherwise, one needs to take the average of the burnup obtained at different locations of the fuel element.

The permanent system would have the following capabilities:

- Experimental fuel burnup measurements should in principle validate the new 3D ATR model calculation results. Measurements uncertainties will be very small (<5%).
- The activity ratio of fission product isotopes can be used to very accurately obtain burnup and cooling time for fuels greater than 9 months cooling time.
- For short cooling time fuel elements the absolute activity measurements can be used to obtain the burnup and cooling time.
- Occasional confirmatory destructive radiochemical analysis will be used to help resolve calibration discrepancies between experimental data and model calculation results as needed.
- This system will be automated so non-expert can operate the system and obtain results without the need for interpreting the data.

1.3 Conclusions

The successful feasibility study in FY-10 established that non-invasive method together with the carefully designed apparatus can be used to measure post-irradiation fuel element burnup and cooling time. This technique can be used both as an aid in characterizing the existing inventory of used elements stored in the ATR canal and more importantly to provide experimental validation data for the new ATR core modeling project and fuel cycle design models.

We have established several burnup calibrations for ATR fuel elements using LaBr₃, HPGe and HPXe detectors. The results showed that for the LaBr₃ and HPXe detectors can be used for burnup

measurements. We found that for high-enriched fuels there is a consistent linear relationship between the $^{134}\text{Cs}/^{137}\text{Cs}$ ratio and burnup for all three detectors. The analysis of the data also concluded that for ATR fuel elements the activity ratio $^{134}\text{Cs}/^{144}\text{Ce}$ has a linear relationship with burnup. The use of this ratio has not previously been reported as a burnup monitor. Also it is important to state that although the detection system was not setup for absolute activity measurement, a new method was developed to obtain geometry-independent burnup calibration using the ORIGEN 2.2 calculations without a need for precise absolute detector efficiency.

We looked at the activity of some fission products among them ^{134}Cs and ^{137}Cs isotopes were found to have a linear relationship with burnup and therefore they can be used as monitors for ATR fuel. We also investigated which other isotopic ratios and absolute activities can be used as ATR fuel cooling time monitors and it was determined that $^{144}\text{Ce}/^{137}\text{Cs}$ ratio, ^{144}Ce , ^{95}Zr , and ^{95}Nb showed a linear relationship as a function of cooling time for ATR fuel elements. The measurements results indicate that the detection system is performing very well and that using an above the water configuration is better suited for the ATR environment and needs, making it the recommended option to build the future permanent system.

6.0 REFERENCES

- Aryaeinejad, R. and Spencer, D.F., Pocket Dual Neutron/Gamma Radiation Detector, IEEE Trans. Nucl. Sci., vol. 51, no. 4, pp. 1667-1671, August 2004.
- Aryaeinejad, R. and Spencer, D.F., Standalone and Network Capable Pocket Radiation Detection System, Nuclear Instruments and Methods in Physics Research, A600, pp. 604-608, 2009.
- ATRC Test Plan, TP-1-11, Performance of the Annual Neutron Level Calibration, NW-160 Reactivity Measurements, and NW-AFM3 Flux Run
- Bess, J. D., "Preliminary Assessment of ATR-C Capabilities to Provide Integral Benchmark Data for Key Structural/Matrix Materials that May be Used for Nuclear Data Testing and Analytical Methods Validation," INL/EXT-09-15591, Idaho National Laboratory, July 2009.
- Bowman, S. M. (Ed.), *SCALE: A Modular Code System for Performing Standardized Computer Analyses for Licensing Evaluation*, ORNL/TM-2005/39, Version 6, Vols. I-III, Oak Ridge National Laboratory, Oak Ridge, Tennessee, January 2009. Available from Radiation Safety Information Computational Center at Oak Ridge National Laboratory as CCC-750.
- Breismeister J.F., 1999, "MCNP – A General Monte Carlo N-Particle Transport Code, Version 4C, LA-13709-M, Los Alamos National Laboratory, USA (1999).
- Briggs, 2010 - Briggs, J. B. (Ed.), *International Handbook of Evaluated Criticality Safety Benchmark Experiments*, NEA/NSC/DOC(95)03/I-IX, Organization for Economic Co-operation and Development - Nuclear Energy Agency (OECD-NEA), May 2010 Edition.
- Broadhead, B. L., Rearden, B. T., Hopper, C. M., Wagschal, J. J. and Parks, C. V., "Sensitivity- and Uncertainty-Based Criticality Safety Validation Techniques," *Nucl. Sci. Eng.* **146**, 340–366 (2004).
- Croff, A.J. "ORIGEN2 -- A Revised and Updated Version of the Oak Ridge Isotope Generation and Depletion Code," ORNL-5621, July 1980.
- DeHart, M. D., Advancements in Generalized-Geometry Discrete Ordinates Transport for Lattice Physics Calculations, A154.pdf in Proc. of PHYSOR–2006, American Nuclear Society Topical Meeting on Reactor Physics: Advances in Nuclear Analysis and Simulation, September 10–14, 2006, Vancouver, British Columbia, Canada.
- Draper Jr., E.L., Integral Reaction Rate Determinations - Part I: Tailored Reactor Spectrum Preparation and Measurement, Nuclear Science and Engineering, **48**:22-30 (1971).
- Durney, J. L. and N.C. Kaufman, Calculating Reactor Power from Activation Techniques as Applied to Unusual Fuel Geometry (ATRC), IN-1047, January, 1967
- ECAR-1401, RML Data Package Flux Run 11-1, TP 1-11, February 23, 2011
- Failla, G., "Private Communication D. S. Lucas & D. Nigg," August, 2010.

Goorley, T. Bull, J., Brown, F. et. al., Release of MCNP5_RSICC_1.30, MCNP Monte Carlo Team X-5, LA-UR-04-4519, Los Alamos National Laboratory, November 2004 and, X-5 Monte Carlo Team, MCNP—A General Monte Carlo N-Particle Transport Code, Version 5, Volume I, LA-UR-03-1987, Los Alamos National Laboratory, April 24, 2003 (Revised 6/30/2004) and Volume II, LA-CP-0245, Los

Harker, Y.D., Anderl, R.A., Becker, G.K., Miller, L.G., Spectral Characterization of the Epithermal Neutron Beam at the Brookhaven Medical Research Reactor, Nuclear Science and Engineering **110**:355-368 (1992).

Henscheid, J. W. and N.C. Kaufman, ATR Startup, Zero-Power Experiments, and Comparison with ATR Critical Facility, IN-1136, December, 1967

Hollenbach, D.F., Petrie, L.M., Landers, N.F., KENO-VI: A General Quadratic Version of the KENO Program, ORNL/TM-13011, Lockheed Martin Energy Research Corp., Oak Ridge National Laboratory, 1996.

Hunter, H. T., Slater, C. O., and White, J. E., “BUGLE-93 (ENDF/B-VI) Cross-Section Library Data Testing Using Shielding Benchmarks,” *Proceedings of the 8th International Conference on Radiation Shielding*, **2**, 840-847 (1994).

Kim, S. S. and Schnitzler, B. G., Advanced Test Reactor: Serpentine Arrangement of Highly Enriched Water-Moderated Uranium-Aluminide Fuel Plates Reflected by Beryllium” HEU-SOLTHERM-022, *International Handbook of Evaluated Criticality Safety Benchmark Experiments*, NEA/NSC/DOC(95)03, OECD-NEA (2008).

Lebrun, A. and Bignan, G. Nondestructive Assay of Nuclear Low-Enriched Uranium Spent fuels for Burnup Credit, Nuclear Technology, Vol. 135, p. 216-228 (Sept. 2001)

McClure, J. A., 1991. Results of Outer and Neck Shim Calibration Studies, TRA-ATR-542, EG&G Idaho, Inc., September 1991.

McCracken, R. T., Loret, L. S., 1994, Results of ATR Critical Facility Core Reconfiguration and Requalification Testing for Post-Core Internals Changeout Operation, Report No. PG-T-94-006, EG&G Idaho, Inc., June 1994.

McCracken, R., “Results of the ATR Critical Facility Core Reconfiguration and PG-T-94-006 Requalification Testing for Post-Core Internals Change-out,” PGT-94-006, June, 1994.

McElroy, W.N. and Berg, S., SAND-II Neutron Flux Spectra Determination by Multiple Foil Activation Iterative Method”, AWR-TR-67-41, Vol 1-4 (1967).

McGhee, J.M., Wareing, T.A., Barnett, D.J., ATTILA Version 5: User Manual, Transpire Inc., Gig Harbour WA, USA (2006).

Meyer, S.L., Data Analysis for Scientists and Engineers, John Wiley and Sons, 1975.

Nigg, D.W., Wemple, C.A., Risler, R., Hartwell, J.K., Harker, Y.D., Laramore, G.E., Modification of the University of Washington Neutron Radiography Facility for Optimization of Neutron Capture Enhanced Fast-Neutron Therapy, Medical Physics **27**:359-367 (2000).

Nigg, D.W., Aryaeinejad, R., Crawford, D.S., Griffith, G.W., Gross, B.J., Lucas, D.S., Nielsen, J.W., Navarro, J., Parry, J.R., Petersom, J., Steuhm, K., Advanced Test Reactor Core Modeling Update Project Annual Report for Fiscal Year 2010, INL/EXT-10-19940, Edited by David W. Nigg, September 2010.

Nigg, D.W. and Steuhm, K.A., Project Plan for the ATR Core Modeling Update, PLN-2852, Revision 2, Idaho National Laboratory, 2011.

Pautz, S., VERIFICATION OF TRANSPORT CODES BY THE METHOD OF MANUFACTURED SOLUTIONS: THE ATILA EXPERIENCE, LA-UR-01-1487.

Petrie, L. M., Personal Communication, Dec. 20, 2010

Pfeifer, C.J., PDQ Reference Manual II, WaPD-TM-947(L), 1971.

Phillips, J.R., et al., Application of Nondestructive Gamma-ray and Neutron Techniques for the Safeguarding of Irradiated Fuel Materials” LA-8212 (May 1980)

Press, W.H., Teukolsky, S.A., et al. Numerical recipes in C, Volume 2, The Press Syndicate of the University of Cambridge.

Radiation Safety Information Computational Center, NJOY99- Code System for Producing Pointwise and Multigroup Neutron and Photon Cross Sections from ENDF/B Data and AMPX77- Modular Code System for Generating Coupled Multigroup Neutron-Gamma Libraries from ENDF/B, Oak Ridge National Laboratory (<http://www-rsicc.ornl.gov>), 2010.

A. J. G. Ramalho and W. E. Payne, Spent Fuel Measurements using High Resolution Gamma Systems, Nuclear Materials Management, p. 76-82, Fall 1979.

D. Reilly, N. Ensslin, H. Smith, Jr., and S. Kreiner, Passive Nondestructive Assay of Nuclear Materials, NUREG/CR-5550 (LA-UR-90-732), March 1991.

Rempe, J.L., Nigg, D.W., Imel, G. R., Unruh, T., FY-10 Irradiation Experiment Plan for the ATR National Scientific User Facility – Idaho State University Project Evaluating Flux Sensors, PLN-3351, Revision 0, Idaho National Laboratory, 2010.

Roache, P., Code Verification by the Method of Manufactured Solutions, J. Fluids Eng., March 2002, Volume 124, Issue 1, 4.

Rogers, JW and Anderl, R.A., ATR Neutron Spectral Characterization, INEL-95/0494, November 1995.

Roth, P. A., 2010, Evaluation of ATR Cycle 145B Physics Analysis Inaccuracy, TEV-765, Idaho National Laboratory, March 2010.

Roussin, R.W., “BUGLE-80 Coupled 47-Neutron, 20 Gamma-Ray P3 Cross Section Library”, DLC-75, Radiation Shielding Information Center, Oak Ridge National Laboratory, USA (1980).

Stallmann, F.W., LSL-M2: A Computer Program for Least Squares Logarithmic Adjustment of Neutron Spectra, NUREG/CR-4349, ORNL/TM-9933, Oak Ridge National Laboratory, USA (1986).

Studsvik Scandpower, HELIOS Methods (Version 1.10), 2008.

Sutton, T.M., et al., The MC21 Monte Carlo Transport Code, Knolls Atomic Power Laboratory and Bettis Laboratory, LM-06K144, 2007.

Transpire, Inc. ATTILA Tutorial Package, Variance Reduction for MCNP & MCNPX.

Wachs, 2010 - Wachs, D. M., *Demonstration Control Plan for the RERTR Full-size Element*, PLN-2946, Rev. 0, Idaho National Laboratory, May 10, 2010

Wheeler, F.J., Parsons, D.K., Rushton, B.L., Nigg, D.W., Epithermal Neutron Beam Design for Neutron Capture Therapy at the PBF and BMRR Reactor Facilities, *Nuclear Technology*, **92**:106-118 (1990)

Williams, M.L., Rearden, B.T., SCALE 6 Sensitivity/Uncertainty Methods and Covariance Data, *Nucl. Data Sheets* **109** (2008), p. 2796.

Wilson, P., et al., State of the Art 3D Radiation Transport Methods for Fusion Energy Systems, *Fusion Engineering and Design*, Vol. 83, pgs. 824-833 (2008).

Appendix A – SAMPLE HELIOS INPUT FOR MERGED STRUCTURES

This is the parameter list needed to merge the two STRs together from the Studsvik ATR-Helios model.

```

THEL
!-----1-----2-----3-----4-----5-----6-----7-----!
case = CASE('lib-47u/RLBeR1.hrf'/ATR pieces')
!-----parameters from ATR.INP and ATR.SET to make RandLBeR structure-----!
!-----parameters from ATR.INP and ATR.SET to define LoBeR and RoBeR-----!

! ----- Beryllium reflector ----- !
! ----- Small water hole data ----- !
$rw hole = PAR("0.3155*2.54/2") ! Radius of water holes [cm] !
$xwh1 = PAR("0.959 *2.54") ! x-coordinate of hole 1 [cm] !
$ywh1 = PAR("$yBhole-0.499*2.54") ! y-coordinate of hole 1 [cm] !
$xwh2 = PAR("1.015*2.54") ! x-coordinate of hole 2 [cm] !
$ywh2 = PAR("$yBhole-1.851*2.54") ! y-coordinate of hole 2 [cm] !
$xwh3 = PAR("2.084*2.54") ! x-coordinate of hole 3 [cm] !
$ywh3 = PAR("$yBhole-1.631*2.54") ! y-coordinate of hole 3 [cm] !
$xwh4 = PAR("3.109*2.54") ! x-coordinate of hole 4 [cm] !
$ywh4 = PAR("$yBhole-1.596*2.54") ! y-coordinate of hole 4 [cm] !

! ----- Small/medium/large I holes ----- !
$rm dIho = PAR("8.255/2") ! O.R. of Med. I hole [cm] !
$xI sma = PAR("60.969*$si4500") ! x-coord small hole [cm] !
$yI sma = PAR("$xI sma") ! y-coord small hole [cm] !
$xI med1 = PAR("4.5 *2.54") ! x-coord medium hole 1 [cm] !
$yI med1 = PAR("(16.937+5.879)*2.54") ! y-coord medium hole 1 [cm] !
$xI med2 = PAR("8.0 *2.54") ! x-coord medium hole 2 [cm] !
$yI med2 = PAR("(16.937+4.853)*2.54") ! y-coord medium hole 2 [cm] !
$yI lar = PAR("(16.937+5.312)*2.54") ! y-coord large hole [cm] !

! ----- N16 holes ----- !
$R N16o = PAR("1.905/2") ! O.R. of N16 hole [cm] !
$y N16c = PAR("(16.937+2.062)*2.54") ! y-coord N16 round hole [cm] !
$x N16s = PAR("46.925*$si4500") ! x-coord N16 aquar hole [cm] !
$y N16s = PAR("$x N16s") ! y-coord N16 aquar hole [cm] !

! ----- Core reflector tank ----- !
$rtki = PAR("25.25*2.54") ! Inner radius core reflector tank [cm] !
$rtko = PAR("$rtki+1.6875*2.54") ! Outer radius core reflector tank [cm] !
! ----- !
$rdrum = PAR("7.50*2.54/2") ! Outer radius control drum hole [cm] !
$R CHfo = PAR("3.62*2.54") ! Outer radius control Hf ring [cm] !
$R CHfi = PAR("3.37*2.54") ! Inner radius control Hf ring [cm] !
$x drum3 = PAR("4.0*2.54") ! x-coordinate of centre of drum N3 [cm] !
$y drum3 = PAR("16.937*2.54") ! y-coordinate of centre of drum N3 [cm] !
$x drum4 = PAR("11.814*2.54") ! x-coordinate of centre of drum N4 [cm] !
$y drum4 = PAR("(16.937+0.532)*2.54") ! y-coordinate of centre of drum N4 [cm] !

$N4LU1x=PAR("(6*($xdrum3+$xdrum*$si5625)+1*($xtki/2*(($si3375+$si2250))))/7")!52x!
$N4LU1y=PAR("(6*($ydrum3+$xdrum*$si3375)+1*($xtki/2*(($si5625+$si6750))))/7")!52y!

$N4LU2x=PAR("(5*($xdrum3+$xdrum*$si5625)+2*($xtki/2*(($si3375+$si2250))))/7")!53x!
$N4LU2y=PAR("(5*($ydrum3+$xdrum*$si3375)+2*($xtki/2*(($si5625+$si6750))))/7")!53y!

$N4LU3x=PAR("(4*($xdrum3+$xdrum*$si5625)+3*($xtki/2*(($si3375+$si2250))))/7")!54x!
$N4LU3y=PAR("(4*($ydrum3+$xdrum*$si3375)+3*($xtki/2*(($si5625+$si6750))))/7")!54y!

$N4LU4x=PAR("(3*($xdrum3+$xdrum*$si5625)+4*($xtki/2*(($si3375+$si2250))))/7")!55x!
$N4LU4y=PAR("(3*($ydrum3+$xdrum*$si3375)+4*($xtki/2*(($si5625+$si6750))))/7")!55y!

$N4LU5x=PAR("(2*($xdrum3+$xdrum*$si5625)+5*($xtki/2*(($si3375+$si2250))))/7")!56x!
$N4LU5y=PAR("(2*($ydrum3+$xdrum*$si3375)+5*($xtki/2*(($si5625+$si6750))))/7")!56y!

```

```

$N4LU6x=PAR("(1*($xdrum3+$xdrum*$si5625)+6*($xtki/2*(Ssi3375+Ssi2250)))/7")!57x!
$N4LU6y=PAR("(1*($ydrum3+$ydrum*$si3375)+6*($xtki/2*(Ssi5625+Ssi6750)))/7")!57y!
$N4LV0x=PAR("( ($xlo+$xhi )+($xlo+$xhi*(1-$si1125)) )/2" ) ! 58x!
$N4LV0y=PAR("( ($xlo+$xhi*2)+($xlo+$xhi*(1+Ssi7875)) )/2" ) ! 58y!

$N4LV1x=PAR("(5*$N4LV0x+ 1*$N4LU1x)/6") ! 59x!
$N4LV1y=PAR("(5*$N4LV0y+ 1*$N4LU1y)/6") ! 59y!

$N4LV2x=PAR("(4*$N4LV0x+ 2*$N4LU1x)/6") ! 60x!
$N4LV2y=PAR("(4*$N4LV0y+ 2*$N4LU1y)/6") ! 60y!

$N4LV3x=PAR("(3*$N4LV0x+ 3*$N4LU1x)/6") ! 61x!
$N4LV3y=PAR("(3*$N4LV0y+ 3*$N4LU1y)/6") ! 61y!

$N4LV4x=PAR("(2*$N4LV0x+ 4*$N4LU1x)/6") ! 62x!
$N4LV4y=PAR("(2*$N4LV0y+ 4*$N4LU1y)/6") ! 62y!

$N4LV5x=PAR("(1*$N4LV0x+ 5*$N4LU1x)/6") ! 63x!
$N4LV5y=PAR("(1*$N4LV0y+ 5*$N4LU1y)/6") ! 63y!
$rlg1 = PAR(" 1.5875/2")
$rlg4 = PAR("11.5443/2")
$rlg5 = PAR("12.7000/2")
$rlg2 = PAR("(2*$rlg1+$rlg4)/3")
$rlg3 = PAR("( $rlg1+2*$rlg4)/3")
!-----TRIG parameters used for the coordinates of the ATR-----!
$pi = PAR("3.14159 26535 89793")
$f1125 = PAR("( $pi/16/$si1125)**0.5" ) ! Convert circle to polygon !
$si1125 = PAR("0.19509 03220 16128")
$si2250 = PAR("0.38268 34323 65089")
$si3375 = PAR("0.55557 02330 19602")
$si4500 = PAR("0.70710 67811 86548")
$si5625 = PAR("0.83146 96123 02545")
$si6750 = PAR("0.92387 95325 11287")
$si7875 = PAR("0.98078 52804 03230")

$tg2250 = PAR("0.41421 35623 73095")
$tg6750 = PAR("2.41421 35623 73090")

$si0257 = PAR(" 0.43388 37391 17558")
$si0514 = PAR(" 0.78183 14824 68030")
$si0771 = PAR(" 0.97492 79121 81824")
$si1028 = PAR(" 0.97492 79121 81824")
$si1285 = PAR(" 0.78183 14824 68030")
$si1542 = PAR(" 0.43388 37391 17558")
$si1800 = PAR(" 0.00000 00000 00000")
$si2057 = PAR(" -0.43388 37391 17558")
$si2314 = PAR(" -0.78183 14824 68030")
$si2571 = PAR(" -0.97492 79121 81824")
$si2828 = PAR(" -0.97492 79121 81823")
$si3085 = PAR(" -0.78183 14824 68030")
$si3342 = PAR(" -0.43388 37391 17558")
$si3600 = PAR(" 0.00000 00000 00000")

$co0257 = PAR(" 0.90096 88679 02419")
$co0514 = PAR(" 0.62348 98018 58734")
$co0771 = PAR(" 0.22252 09339 56314")
$co1028 = PAR(" -0.22252 09339 56314")
$co1285 = PAR(" -0.62348 98018 58733")
$co1542 = PAR(" -0.90096 88679 02419")
$co1800 = PAR(" -1.00000 00000 00000")
$co2057 = PAR(" -0.90096 88679 02419")
$co2314 = PAR(" -0.62348 98018 58734")
$co2571 = PAR(" -0.22252 09339 56315")
$co2828 = PAR(" 0.22252 09339 56315")
$co3085 = PAR(" 0.62348 98018 58733")
$co3342 = PAR(" 0.90096 88679 02419")
$co3600 = PAR(" 1.00000 00000 00000")

$si0129=PAR(" 0.22252 09339 56314")

```

```

$si0386=PAR(" 0.62348 98018 58733")
$si0643=PAR(" 0.90096 88679 02419")
$si0900=PAR(" 1.00000 00000 00000")
$si1157=PAR(" 0.90096 88679 02419")
$si1414=PAR(" 0.62348 98018 58733")
$si1671=PAR(" 0.22252 09339 56314")
$si1929=PAR("-0.22252 09339 56315")
$si2186=PAR("-0.62348 98018 58734")
$si2443=PAR("-0.90096 88679 02419")
$si2700=PAR("-1.00000 00000 00000")
$si2957=PAR("-0.90096 88679 02419")
$si3214=PAR("-0.62348 98018 58733")
$si3471=PAR("-0.22252 09339 56313")

$co0129=PAR(" 0.97492 79121 81824")
$co0386=PAR(" 0.78183 14824 68030")
$co0643=PAR(" 0.43388 37391 17558")
$co0900=PAR(" 0.00000 00000 00000")
$co1157=PAR("-0.43388 37391 17558")
$co1414=PAR("-0.78183 14824 68030")
$co1671=PAR("-0.97492 79121 81824")
$co1929=PAR("-0.97492 79121 81824")
$co2186=PAR("-0.78183 14824 68030")
$co2443=PAR("-0.43388 37391 17557")
$co2700=PAR(" 0.00000 00000 00000")
$co2957=PAR(" 0.43388 37391 17559")
$co3214=PAR(" 0.78183 14824 68030")
$co3471=PAR(" 0.97492 79121 81824")

$si3000 = PAR(" 0.50000 00000 00000")
$si6000 = PAR(" 0.86602 54037 84439")

$xdrum = PAR("$rdrum*$fl125")      ! Equiv polygon "r" for rdrum  !
$xtki  = PAR("$rtki*$fl125")      ! Equiv polygon "r" for inner tank !
$xtko  = PAR("$rtko*$fl125")      ! Equiv polygon "r" for outer tank !

!-----CCS for topBeR-----!
lgIhol = CCS($rlg1,$rlg2,$rlg3,$rlg4,$rlg5/4(3,5)/
           bcoo,lgIpl,lgIpl,lgIpl,lgIpl,lgIpl,
           lgIpl,lgIpl,lgIpl,lgIpl,
           bcoo, bcoo, bcoo, bcoo)  ! Large I hole  !

N16cir = CCS("0.6579/2","0.9525/2","1.16586/2",
             "1.5875/2",$rN16o//
             bcoo,tube,bcoo,tube,bcoo)  ! Round N16 hole  !

smIhol = CCS("0.635/2","3.25374/2","3.81/2"/4(3,3)/
             bcoo,smIpl, bcoo, bcoo, bcoo, bcoo)  ! Small I hole  !

mdIhol = CCS("1.11125/2","7.0993/2",$rmdIho/4(2,3)/
             bcoo,mdIpl,mdIpl,mdIpl,mdIpl,
             bcoo, bcoo, bcoo, bcoo)  ! Medium I hole  !

!bcoo tube smIpl mdIpl where are they see materials section --!

!---+---1---+---2---+---3---+---4---+---5---+---6---+---7---+---!
!-----topBeR materials-----!
!refl material!
!Be  = MAT(1.8538/4009,100)!  ! Be reflector material  !
Be   = MAT(/4009,1.2387E-1)  ! 1.2387E-1 atoms/barn-cm == 1.8538 g/cm3 !
BeWskt = MAT(/4009,1.2198E-1;  ! Be reflector with water socket  !
          8016,5.0792E-4;
          1001,1.0158E-3)

BePlug = MAT(/4009,1.2387E-1)
BePlugLI= MAT(/4009,1.2029E-1;  ! Be Plug for Large I-Holes  !
            8016,9.5940E-4;
            1001,1.9188E-3)
BePlugMI= MAT(/4009,1.1435E-1;  ! Be Plug for Medium I-Holes  !
            8016,2.5529E-3;

```

```

1001,5.1057E-3)
BeDrum = MAT(/4009,1.1492E-1; ! Be+Water in Outer Shim Control Cylinder !
8016,2.4002E-3;
1001,4.8003E-3)
alustr = MAT(/13027,5.8750E-2;
22000,6.7918E-6;
24000,5.9415E-5;
12000,6.0209E-4;
25055,2.3677E-5;
29063,4.42467E-5;
29065,1.97213E-5;
26000,1.1646E-4;
14000,3.7052E-4)
Hf = MAT(/72174,7.12946E-05;
72176,2.29111E-03;
72177,8.18831E-03;
72178,1.20131E-02;
72179,5.99799E-03;
72180,1.54472E-02;
40000,8.58980E-4)

coo = MAT(/ 1001,6.6394E-2; 8016,3.3197E-2) ! 0.9931 g/cm3, Table 37 !

!-----1-----2-----3-----4-----5-----6-----7-----!
$LoBeR = PAR( ! Right outer Beryllium reflector !
( 0 , $ydrum3) ! 1 !
("-$xdrum3+$xdrum ", "$ydrum3" ) ! 2 !
("-$xdrum3+$xdrum*$si7875", "$ydrum3+$xdrum*$si1125") ! 3 !
("-$xdrum3+$xdrum*$si6750", "$ydrum3+$xdrum*$si2250") ! 4 !
("-$xdrum3+$xdrum*$si5625", "$ydrum3+$xdrum*$si3375") ! 5 !
("-$xdrum3+$xdrum*$si4500", "$ydrum3+$xdrum*$si4500") ! 6 !
("-$xdrum3+$xdrum*$si3375", "$ydrum3+$xdrum*$si5625") ! 7 !
("-$xdrum3+$xdrum*$si2250", "$ydrum3+$xdrum*$si6750") ! 8 !
("-$xdrum3+$xdrum*$si1125", "$ydrum3+$xdrum*$si7875") ! 9 !
("-$xdrum3 ", "$ydrum3+$xdrum" ) ! 10 !
("-$xdrum3-$xdrum*$si1125", "$ydrum3+$xdrum*$si7875") ! 11 !
("-$xdrum3-$xdrum*$si2250", "$ydrum3+$xdrum*$si6750") ! 12 !
("-$xdrum3-$xdrum*$si3375", "$ydrum3+$xdrum*$si5625") ! 13 !
("-$xdrum3-$xdrum*$si4500", "$ydrum3+$xdrum*$si4500") ! 14 !
("-$xdrum3-$xdrum*$si5625", "$ydrum3+$xdrum*$si3375") ! 15 !
("-$xtki/2*( $si3375+$si2250)", "$xtki/2*( $si5625+$si6750)")! 16 !
("-$xtki*$si2250", "$xtki*$si6750") ! 17 !
("-$xtki*$si1125", "$xtki*$si7875") ! 18 !
( 0 , $xtki ) ! 19 !

( "0", "$yN16c-$rN16o" ) ! 20 !
( "-$rN16o", "$yN16c " ) ! 21 !
( "0", "$yN16c+$rN16o" ) ! 22 !

( "0", "$yllar-$rlg5" ) ! 23 !

( "-$rlg5*$si5625", "$yllar-$rlg5*$si3375" ) ! 24 !
( "-$rlg5*$si4500", "$yllar+$rlg5*$si4500" ) ! 25 !
( "0", "$yllar+$rlg5" ) ! 26 !

( "$RoBeRU1x", "$RoBeRU1y" ) ! 27 !
( "$RoBeRU2x", "$RoBeRU2y" ) ! 28 !
( "$RoBeRD1x", "$RoBeRD1y" ) ! 29 !
( "$RoBeRD2x", "$RoBeRD2y" ) ! 30 !
( "$N4LU1x", "$N4LU1y" ) ! 31 !
!----- 3 nodes on 27-29 -----!
("-(5*( $RoBeRU1x)+1*( $RoBeRD1x))/6", "(5*( $RoBeRU1y)+1*( $RoBeRD1y))/6" ) ! 32 !
("-(2.7*( $RoBeRU1x)+3.3*( $RoBeRD1x))/6",
(2.7*( $RoBeRU1y)+3.3*( $RoBeRD1y))/6" ) ! 33 !
("-(1*( $RoBeRU1x)+5*( $RoBeRD1x))/6", "(1*( $RoBeRU1y)+5*( $RoBeRD1y))/6" ) ! 34 !
!----- 3 nodes on 28-30 -----!
("-(5*( $RoBeRU2x)+1*( $RoBeRD2x))/6", "(5*( $RoBeRU2y)+1*( $RoBeRD2y))/6" ) ! 35 !
("-(2.8*( $RoBeRU2x)+3.2*( $RoBeRD2x))/6",
(2.8*( $RoBeRU2y)+3.2*( $RoBeRD2y))/6" ) ! 36 !
("-(1*( $RoBeRU2x)+5*( $RoBeRD2x))/6", "(1*( $RoBeRU2y)+5*( $RoBeRD2y))/6" ) ! 37 !

```

```

!----- 3 nodes on 5-31 ----- !
("-(5*(R0BeRNEEx)+1*(N4LU1x))/6","(5*(R0BeRNEy)+1*(N4LU1y))/6" )! 38 !
("-(3*(R0BeRNEEx)+3*(N4LU1x))/6","(3*(R0BeRNEy)+3*(N4LU1y))/6" )! 39 !
("-(1*(R0BeRNEEx)+5*(N4LU1x))/6","(1*(R0BeRNEy)+5*(N4LU1y))/6" )! 40 !
!----- !
("$xImed1+$rmdlho*$si2250","$yImed1+$rmdlho*$si6750" ) ! 41 !
("$xImed1+$rmdlho ", "$yImed1 ") ! 42 !
("$xImed1+$rmdlho*$si4500","$yImed1-$rmdlho*$si4500" ) ! 43 !

("$xImed1-$rmdlho*$si3375","$yImed1+$rmdlho*$si5625" ) ! 44 !
("$xImed1-$rmdlho*$si7875","$yImed1-$rmdlho*$si1125" ) ! 45 !
("$xImed1-$rmdlho*$si4500","$yImed1-$rmdlho*$si4500" ) ! 46 !

("$xImed2+$rmdlho*$si1125","$yImed2+$rmdlho*$si7875" ) ! 47 !
("$xImed2+$rmdlho*$si6750","$yImed2+$rmdlho*$si2250" ) ! 48 !
("$xImed2+$rmdlho*$si6750","$yImed2-$rmdlho*$si2250" ) ! 49 !

("$xImed2-$rmdlho*$si4500","$yImed2+$rmdlho*$si4500" ) ! 50 !
("$xImed2-$rmdlho*$si6750","$yImed2-$rmdlho*$si2250" ) ! 51 !
("$xImed2-$rmdlho*$si1125","$yImed2-$rmdlho*$si7875" ) ! 52 !

("$rlg5*$si7875 ", "$yllar+$rlg5*$si1125 ") ! 53 !

( 0 , "$ydrum3+$xdrum*$si1125 ") ! 54 !
! 69y = 18y !
( 0 , "$ydrum3+$xdrum*$si2250 ") ! 55 !
! 70y = 17y !

/19,refl
/N16cir(0,$yN16c)5 ,lgIhol(0,$yllar)8,
mdlhol("$xImed1",$yImed1),mdlhol("$xImed2",$yImed2)
/1,2,3,54, refl; ! Right !
3,4,55,54, refl;
4,5,21,20,55, refl;
5,6,7,8,29,21, refl;
21,29,24,23,22, refl;
24,29,33,53, refl;
53,33,27,25, refl;
25,27,19,26, refl;

28,18,27,32,41,44,35, refl; ! Middle !
41,32,33,42, refl;
43,42,33,34, refl;
34,29,30,37,46,43, refl;
37,36,45,46, refl;
36,35,44,45, refl;

9,10,11,12,30,29,8, refl; ! Middle Bottom !

16,17,28,35,47,50,38, refl; ! Left !
35,36,48,47, refl;
36,37,49,48, refl;
37,30,31,40,52,49, refl;
40,39,51,52, refl;
!39,38,50,51, refl;!

15,31,30,12,13,14, refl ! Left Bottom !
)

$RoBeRU1x=PAR("(4*(0 )+5*(Sxtki*$si1125))/9") ! 27x!
$RoBeRU1y=PAR("(4*(Sxtki)+5*(Sxtki*$si7875))/9") ! 27y!
! (4*(2)+5*(3))/9 = 27 !
! U = Up !

$RoBeRU2x=PAR("(5*(Sxtki*$si1125)+4*(Sxtki*$si2250))/9") ! 28x!
$RoBeRU2y=PAR("(5*(Sxtki*$si7875)+4*(Sxtki*$si6750))/9") ! 28y!
! (5*(3)+4*(4))/9 = 28 !
! U = Up !

$RoBeRD1x=PAR("(9*(Sxdrum3-$xdrum*$si2250)+1*(R0BeRU1x))/10") ! 29x!
$RoBeRD1y=PAR("(9*(Sxdrum3+$xdrum*$si6750)+1*(R0BeRU1y))/10") ! 29y!

```

```

! (9*(13)+1*(27))/10 = 29 !
! D = Down !

$RoBeRD2x=PAR("(6*( $xdrum3+$xdrum*$si2250)+1*( $RoBeRU2x))/7") ! 30x!
$RoBeRD2y=PAR("(6*( $ydrum3+$xdrum*$si6750)+1*( $RoBeRU2y))/7") ! 30y!
! (6*(9)+1*(28))/7 = 30 !
! D = Down !

$RoBeRNEx=PAR("$xtki/2*( $si3375+$si2250)") ! 5x !
$RoBeRNEy=PAR("$xtki/2*( $si5625+$si6750)") ! 5y !

!-----1-----2-----3-----4-----5-----6-----7-----!
$RoBeR = PAR( ! Right outer Beryllium reflector !
( 0 , $ydrum3)( 0 , $xtki ) ! 1-2 !
("$xtki*$si1125", "$xtki*$si7875") ! 3 !
("$xtki*$si2250", "$xtki*$si6750") ! 4 !
("$xtki/2*( $si3375+$si2250)", "$xtki/2*( $si5625+$si6750)") ! 5 !
("$xdrum3+$xdrum*$si5625", "$ydrum3+$xdrum*$si3375") ! 6 !
("$xdrum3+$xdrum*$si4500", "$ydrum3+$xdrum*$si4500") ! 7 !
("$xdrum3+$xdrum*$si3375", "$ydrum3+$xdrum*$si5625") ! 8 !
("$xdrum3+$xdrum*$si2250", "$ydrum3+$xdrum*$si6750") ! 9 !
("$xdrum3+$xdrum*$si1125", "$ydrum3+$xdrum*$si7875") ! 10 !
( "$xdrum3", "$ydrum3+$xdrum" ) ! 11 !
("$xdrum3-$xdrum*$si1125", "$ydrum3+$xdrum*$si7875") ! 12 !
("$xdrum3-$xdrum*$si2250", "$ydrum3+$xdrum*$si6750") ! 13 !
("$xdrum3-$xdrum*$si3375", "$ydrum3+$xdrum*$si5625") ! 14 !
("$xdrum3-$xdrum*$si4500", "$ydrum3+$xdrum*$si4500") ! 15 !
("$xdrum3-$xdrum*$si5625", "$ydrum3+$xdrum*$si3375") ! 16 !
("$xdrum3-$xdrum*$si6750", "$ydrum3+$xdrum*$si2250") ! 17 !
("$xdrum3-$xdrum*$si7875", "$ydrum3+$xdrum*$si1125") ! 18 !
( "$xdrum3-$xdrum", "$ydrum3" ) ! 19 !

( "0", "$yN16c-$rN16o" ) ! 20 !
( "$rN16o", "$yN16c " ) ! 21 !
( "0", "$yN16c+$rN16o" ) ! 22 !

( "0", "$yllar-$rlg5" ) ! 23 !

( "0+$rlg5*$si5625", "$yllar-$rlg5*$si3375" ) ! 24 !
( "0+$rlg5*$si4500", "$yllar+$rlg5*$si4500" ) ! 25 !
( "0", "$yllar+$rlg5" ) ! 26 !

( "$RoBeRU1x", "$RoBeRU1y" ) ! 27 !
( "$RoBeRU2x", "$RoBeRU2y" ) ! 28 !
( "$RoBeRD1x", "$RoBeRD1y" ) ! 29 !
( "$RoBeRD2x", "$RoBeRD2y" ) ! 30 !
( "$N4LU1x", "$N4LU1y" ) ! 31 !
!----- 3 nodes on 27-29 -----!
(" (5*( $RoBeRU1x)+1*( $RoBeRD1x))/6", " (5*( $RoBeRU1y)+1*( $RoBeRD1y))/6" ) ! 32 !
(" (2.7*( $RoBeRU1x)+3.3*( $RoBeRD1x))/6",
" (2.7*( $RoBeRU1y)+3.3*( $RoBeRD1y))/6" ) ! 33 !
(" (1*( $RoBeRU1x)+5*( $RoBeRD1x))/6", " (1*( $RoBeRU1y)+5*( $RoBeRD1y))/6" ) ! 34 !
!----- 3 nodes on 28-30 -----!
(" (5*( $RoBeRU2x)+1*( $RoBeRD2x))/6", " (5*( $RoBeRU2y)+1*( $RoBeRD2y))/6" ) ! 35 !
(" (2.8*( $RoBeRU2x)+3.2*( $RoBeRD2x))/6",
" (2.8*( $RoBeRU2y)+3.2*( $RoBeRD2y))/6" ) ! 36 !
(" (1*( $RoBeRU2x)+5*( $RoBeRD2x))/6", " (1*( $RoBeRU2y)+5*( $RoBeRD2y))/6" ) ! 37 !
!----- 3 nodes on 5-31 -----!
(" (5*( $RoBeRNEx)+1*( $N4LU1x))/6", " (5*( $RoBeRNEy)+1*( $N4LU1y))/6" ) ! 38 !
(" (3*( $RoBeRNEx)+3*( $N4LU1x))/6", " (3*( $RoBeRNEy)+3*( $N4LU1y))/6" ) ! 39 !
(" (1*( $RoBeRNEx)+5*( $N4LU1x))/6", " (1*( $RoBeRNEy)+5*( $N4LU1y))/6" ) ! 40 !
!-----!
(" $xImed1-$rmdlho*$si2250", "$yImed1+$rmdlho*$si6750") ! 41 !
(" $xImed1-$rmdlho ", "$yImed1 ") ! 42 !
(" $xImed1-$rmdlho*$si4500", "$yImed1-$rmdlho*$si4500") ! 43 !

(" $xImed1+$rmdlho*$si3375", "$yImed1+$rmdlho*$si5625") ! 44 !
(" $xImed1+$rmdlho*$si7875", "$yImed1-$rmdlho*$si1125") ! 45 !
(" $xImed1+$rmdlho*$si4500", "$yImed1-$rmdlho*$si4500") ! 46 !

(" $xImed2-$rmdlho*$si1125", "$yImed2+$rmdlho*$si7875") ! 47 !

```

```

(" $xImed2-$rmdlho*$si6750","$yImed2+$rmdlho*$si2250") ! 48 !
(" $xImed2-$rmdlho*$si6750","$yImed2-$rmdlho*$si2250") ! 49 !

(" $xImed2+$rmdlho*$si4500","$yImed2+$rmdlho*$si4500") ! 50 !
(" $xImed2+$rmdlho*$si6750","$yImed2-$rmdlho*$si2250") ! 51 !
(" $xImed2+$rmdlho*$si1125","$yImed2-$rmdlho*$si7875") ! 52 !

(" $rlg5*$si7875      ","$yllar+$rlg5*$si1125 ") ! 53 !

( 0      ,"$ydrum3+$xdrum*$si1125 ") ! 54 !
      ! 69y = 18y !
( 0      ,"$ydrum3+$xdrum*$si2250 ") ! 55 !
      ! 70y = 17y !

/19,refl
/N16cir(0,$yN16c)5      ,lgIhol(0,$yllar)8,
mdlhol($xImed1,$yImed1),mdlhol($xImed2,$yImed2)
/18,19, 1,54,      refl; ! Left      !
17,18,54,55,      refl;
16,17,55,20,21,      refl;

13,14,15,16,21,29,      refl;
21,22,23,24,29,      refl;
24,53,33,29,      refl;
33,53,25,27,      refl;
25,26, 2,27,      refl;

27,3,28,35,44,41,32,      refl; ! Middle      !
33,32,41,42,      refl;
34,33,42,43,      refl;
29,34,43,46,37,30,      refl;
37,46,45,36,      refl;
36,45,44,35,      refl;

9,10,11,12,13,29,30,      refl; ! Middle Bottom !

35,28,4,5,38,50,47,      refl; ! Right      !
36,35,47,48,      refl;
37,36,48,49,      refl;
30,37,49,52,40,31,      refl;
40,52,51,39,      refl;
39,51,50,38,      refl;

6,7,8,9,30,31,      refl ! Right Bottom !
)

```

```

!---+---1---+---2---+---3---+---4---+---5---+---6---+---7---+---!
!-----combine the two together RandLBeR-----!

```

```

$RLBeR = PAR(      ( 0 , $ydrum3 )      ! 1 !
("-$xdrum3+$xdrum      ","$ydrum3"      ) ! 2 !
("-$xdrum3+$xdrum*$si7875","$ydrum3+$xdrum*$si1125") ! 3 !
("-$xdrum3+$xdrum*$si6750","$ydrum3+$xdrum*$si2250") ! 4 !
("-$xdrum3+$xdrum*$si5625","$ydrum3+$xdrum*$si3375") ! 5 !
("-$xdrum3+$xdrum*$si4500","$ydrum3+$xdrum*$si4500") ! 6 !
("-$xdrum3+$xdrum*$si3375","$ydrum3+$xdrum*$si5625") ! 7 !
("-$xdrum3+$xdrum*$si2250","$ydrum3+$xdrum*$si6750") ! 8 !
("-$xdrum3+$xdrum*$si1125","$ydrum3+$xdrum*$si7875") ! 9 !
("-$xdrum3      ","$ydrum3+$xdrum"      ) ! 10 !
("-$xdrum3-$xdrum*$si1125","$ydrum3+$xdrum*$si7875") ! 11 !
("-$xdrum3-$xdrum*$si2250","$ydrum3+$xdrum*$si6750") ! 12 !
("-$xdrum3-$xdrum*$si3375","$ydrum3+$xdrum*$si5625") ! 13 !
("-$xdrum3-$xdrum*$si4500","$ydrum3+$xdrum*$si4500") ! 14 !
("-$xdrum3-$xdrum*$si5625","$ydrum3+$xdrum*$si3375") ! 15 !
("$xtki/2*(si3375+si2250),"$xtki/2*(si5625+si6750))! 16 !
("$xtki*$si2250", "$xtki*$si6750")      ! 17 !
("$xtki*$si1125", "$xtki*$si7875")      ! 18 !
( 0 , $xtki )      ! 19 !
      ! Nodes From RoBeR !
("$xtki*$si1125", "$xtki*$si7875")      ! 20=3!
("$xtki*$si2250", "$xtki*$si6750")      ! 21=4!

```

```

("xtki/2*(Ssi3375+Ssi2250),"xtki/2*(Ssi5625+Ssi6750)") ! 22=5!
("$xdrum3+$xdrum*Ssi5625","$ydrum3+$xdrum*Ssi3375") ! 23=6!
("$xdrum3+$xdrum*Ssi4500","$ydrum3+$xdrum*Ssi4500") ! 24=7!
("$xdrum3+$xdrum*Ssi3375","$ydrum3+$xdrum*Ssi5625") ! 25=8!
("$xdrum3+$xdrum*Ssi2250","$ydrum3+$xdrum*Ssi6750") ! 26=9!
("$xdrum3+$xdrum*Ssi1125","$ydrum3+$xdrum*Ssi7875") !27=10!
( "$xdrum3","$ydrum3+$xdrum" ) !28=11!
("$xdrum3-$xdrum*Ssi1125","$ydrum3+$xdrum*Ssi7875") !29=12!
("$xdrum3-$xdrum*Ssi2250","$ydrum3+$xdrum*Ssi6750") !30=13!
("$xdrum3-$xdrum*Ssi3375","$ydrum3+$xdrum*Ssi5625") !31=14!
("$xdrum3-$xdrum*Ssi4500","$ydrum3+$xdrum*Ssi4500") !32=15!
("$xdrum3-$xdrum*Ssi5625","$ydrum3+$xdrum*Ssi3375") !33=16!
("$xdrum3-$xdrum*Ssi6750","$ydrum3+$xdrum*Ssi2250") !34=17!
("$xdrum3-$xdrum*Ssi7875","$ydrum3+$xdrum*Ssi1125") !35=18!
( "$xdrum3-$xdrum","$ydrum3" ) !36=19!
! End of new outer nodes !
!nodes from LoBeR!
( "0","$yN16c-$rN16o" ) !37=20!
( "-$rN16o","$yN16c " ) !38=21!
( "0","$yN16c+$rN16o" ) !39=22!
( "0","$yIlar-$rlg5" ) !40=23!
( "-$rlg5*Ssi5625","$yIlar-$rlg5*Ssi3375" ) !41=24!
( "-$rlg5*Ssi4500","$yIlar+$rlg5*Ssi4500" ) !42=25!
( "0","$yIlar+$rlg5" ) !43=26!
( "-$RoBeRU1x","$RoBeRU1y" ) !44=27!
( "-$RoBeRU2x","$RoBeRU2y" ) !45=28!
( "-$RoBeRD1x","$RoBeRD1y" ) !46=29!
( "-$RoBeRD2x","$RoBeRD2y" ) !47=30!
( "-$N4LU1x","$N4LU1y" ) !48=31!
!----- 3 nodes on 27-29 ----- !
("-(5*(RoBeRU1x)+1*(RoBeRD1x))/6","(5*(RoBeRU1y)+1*(RoBeRD1y))/6") !49=32!
("-(2.7*(RoBeRU1x)+3.3*(RoBeRD1x))/6",
" (2.7*(RoBeRU1y)+3.3*(RoBeRD1y))/6") !50=33!
("-(1*(RoBeRU1x)+5*(RoBeRD1x))/6","(1*(RoBeRU1y)+5*(RoBeRD1y))/6") !51=34!
!----- 3 nodes on 28-30 ----- !
("-(5*(RoBeRU2x)+1*(RoBeRD2x))/6","(5*(RoBeRU2y)+1*(RoBeRD2y))/6") !52=35!
("-(2.8*(RoBeRU2x)+3.2*(RoBeRD2x))/6",
" (2.8*(RoBeRU2y)+3.2*(RoBeRD2y))/6") !53=36!
("-(1*(RoBeRU2x)+5*(RoBeRD2x))/6","(1*(RoBeRU2y)+5*(RoBeRD2y))/6") !54=37!
!----- 3 nodes on 5-31 ----- !
("-(5*(RoBeRNEEx)+1*(N4LU1x))/6","(5*(RoBeRNEEy)+1*(N4LU1y))/6" ) !55=38!
("-(3*(RoBeRNEEx)+3*(N4LU1x))/6","(3*(RoBeRNEEy)+3*(N4LU1y))/6" ) !56=39!
("-(1*(RoBeRNEEx)+5*(N4LU1x))/6","(1*(RoBeRNEEy)+5*(N4LU1y))/6" ) !57=40!
!----- 1-----2-----3-----4-----5-----6-----7-----!
("$xImed1+$rmdlho*Ssi2250","$yImed1+$rmdlho*Ssi6750") !58=41!
("$xImed1+$rmdlho ","$yImed1 ") !59=42!
("$xImed1+$rmdlho*Ssi4500","$yImed1-$rmdlho*Ssi4500") !60=43!
("$xImed1-$rmdlho*Ssi3375","$yImed1+$rmdlho*Ssi5625") !61=44!
("$xImed1-$rmdlho*Ssi7875","$yImed1-$rmdlho*Ssi1125") !62=45!
("$xImed1-$rmdlho*Ssi4500","$yImed1-$rmdlho*Ssi4500") !63=46!
("$xImed2+$rmdlho*Ssi1125","$yImed2+$rmdlho*Ssi7875") !64=47!
("$xImed2+$rmdlho*Ssi6750","$yImed2+$rmdlho*Ssi2250") !65=48!
("$xImed2+$rmdlho*Ssi6750","$yImed2-$rmdlho*Ssi2250") !66=49!
("$xImed2-$rmdlho*Ssi4500","$yImed2+$rmdlho*Ssi4500") !67=50!
("$xImed2-$rmdlho*Ssi6750","$yImed2-$rmdlho*Ssi2250") !68=51!
("$xImed2-$rmdlho*Ssi1125","$yImed2-$rmdlho*Ssi7875") !69=52!
("$-rlg5*Ssi7875 ","$yIlar+$rlg5*Ssi1125 ") !70=53!
( 0 ,"$ydrum3+$xdrum*Ssi1125 ") !71=54!
! 69y = 18y !
( 0 ,"$ydrum3+$xdrum*Ssi2250 ") !72=55!
! 70y = 17y !
!Nodes From RoBeR !
( "$rN16o","$yN16c " ) !73=21!
( "0+$rlg5*Ssi5625","$yIlar-$rlg5*Ssi3375" ) !74=24!
( "0+$rlg5*Ssi4500","$yIlar+$rlg5*Ssi4500" ) !75=25!
( "$RoBeRU1x","$RoBeRU1y" ) !76=27!
( "$RoBeRU2x","$RoBeRU2y" ) !77=28!
( "$RoBeRD1x","$RoBeRD1y" ) !78=29!
( "$RoBeRD2x","$RoBeRD2y" ) !79=30!
( "$N4LU1x","$N4LU1y" ) !80=31!

```

```

!----- 3 nodes on 27-29 ----- !
(" (5*(RoBeRU1x)+1*(RoBeRD1x))/6", " (5*(RoBeRU1y)+1*(RoBeRD1y))/6" ) !81=32!
(" (2.7*(RoBeRU1x)+3.3*(RoBeRD1x))/6",
   " (2.7*(RoBeRU1y)+3.3*(RoBeRD1y))/6" ) !82=33!
(" (1*(RoBeRU1x)+5*(RoBeRD1x))/6", " (1*(RoBeRU1y)+5*(RoBeRD1y))/6" ) !83=34!
!----- 3 nodes on 28-30 ----- !
(" (5*(RoBeRU2x)+1*(RoBeRD2x))/6", " (5*(RoBeRU2y)+1*(RoBeRD2y))/6" ) !84=35!
(" (2.8*(RoBeRU2x)+3.2*(RoBeRD2x))/6",
   " (2.8*(RoBeRU2y)+3.2*(RoBeRD2y))/6" ) !85=36!
(" (1*(RoBeRU2x)+5*(RoBeRD2x))/6", " (1*(RoBeRU2y)+5*(RoBeRD2y))/6" ) !86=37!
!----- 3 nodes on 5-31 ----- !
(" (5*(RoBeRNEEx)+1*(SN4LU1x))/6", " (5*(RoBeRNEYy)+1*(SN4LU1y))/6" ) !87=38!
(" (3*(RoBeRNEEx)+3*(SN4LU1x))/6", " (3*(RoBeRNEYy)+3*(SN4LU1y))/6" ) !88=39!
(" (1*(RoBeRNEEx)+5*(SN4LU1x))/6", " (1*(RoBeRNEYy)+5*(SN4LU1y))/6" ) !89=40!
!-----1-----2-----3-----4-----5-----6-----7-----!
(" $xImed1-$rmdlho*$si2250", "$yImed1+$rmdlho*$si6750" ) !90=41!
(" $xImed1-$rmdlho ", "$yImed1 ") !91=42!
(" $xImed1-$rmdlho*$si4500", "$yImed1-$rmdlho*$si4500" ) !92=43!
(" $xImed1+$rmdlho*$si3375", "$yImed1+$rmdlho*$si5625" ) !93=44!
(" $xImed1+$rmdlho*$si7875", "$yImed1-$rmdlho*$si1125" ) !94=45!
(" $xImed1+$rmdlho*$si4500", "$yImed1-$rmdlho*$si4500" ) !95=46!
(" $xImed2-$rmdlho*$si1125", "$yImed2+$rmdlho*$si7875" ) !96=47!
(" $xImed2-$rmdlho*$si6750", "$yImed2+$rmdlho*$si2250" ) !97=48!
(" $xImed2-$rmdlho*$si6750", "$yImed2-$rmdlho*$si2250" ) !98=49!
(" $xImed2+$rmdlho*$si4500", "$yImed2+$rmdlho*$si4500" ) !99=50!
(" $xImed2+$rmdlho*$si6750", "$yImed2-$rmdlho*$si2250" ) !100=51!
(" $xImed2+$rmdlho*$si1125", "$yImed2-$rmdlho*$si7875" ) !101=52!
(" $rlg5*$si7875 ", "$yllar+$rlg5*$si1125 ") !102=53!
/36.refl
/N16cir(0,$yN16c) ,!lgIhol(0,$yIlar),! !entire N16 & lgIhol CCS!
mdlhol($xImed1,$yImed1),mdlhol($xImed2,$yImed2),!CCS's RoBeR!
mdlhol("$-xImed1", $yImed1),mdlhol("$-xImed2", $yImed2)!frm LoBeR!

! combined LoBeR and RoBeR nodes !
/1,2,3,71,35,36, refl; ! Pan handle 1 !
3,4,72,34,35, refl; ! Pan handle 2 !
4,5,38,37,73,33,34,72, refl; ! N16 lower half !
5,6,7,8,46,38, refl; ! left edge close to N16 !
38,46,41,40,74,78,73,39, refl; !*under lrg Ihol top N16 !
41,46,50,70, refl; !*left of lrg Ihol !
70,50,44,42, refl; ! top left of lrg Ihol !
42,44,19,76,75,43, refl; ! top of lrg Ihol !
45,18,44,49,58,61,52, refl; ! top med Ihol/top edge !
58,49,50,59, refl; ! top right of med Ihol !
60,59,50,51, refl; ! right of med Ihol !
51,46,47,54,63,60, refl; ! bttm med Ihol !
54,53,62,63, refl; ! left med Ihol !
53,52,61,62, refl; ! top left of med Ihol !
9,10,11,12,47,46,8, refl; ! bttm left middle edge !
16,17,45,52,64,67,55, refl; ! top left edge !
52,53,65,64, refl; ! top left Ihol !
53,54,66,65, refl; ! betwn left Ihols !
54,47,48,57,69,66, refl; ! under left med Ihol !
57,56,68,69, refl; ! middle left edge !
15,48,47,12,13,14, refl; ! lower left edge !
! all of the nodes above came from LoBeR some cross over into RoBeR !
! Begin RoBeR nodes !
30,31,32,33,73,78, refl; !right edge under lrg I!
74,102,82,78, refl; !right of lrg I!
82,102,75,76, refl; !right uppr lrg I!
76,20,77,84,93,90,81, refl; ! Middle right edge !
82,81,90,91, refl; !right mddl btwn lrg-med!
83,82,91,92, refl; !right mddl btwn lrg-med!
78,83,92,95,86,79, refl; !rght undr mddl med-I!
86,95,94,85, refl; !rght btwn med-I!
85,94,93,84, refl; !rght uppr btwn med-I!
26,27,28,29,30,78,79, refl; !rght Mddl bttm edge !
84,77,21,22,87,99,96, refl; !rght top edge !
85,84,96,97, refl; !rght mddl med-I!
86,85,97,98, refl; !rght mddl med-I!

```

```

79,86,98,101,89,80,      refl; !rht undr rht med-I!
89,101,100,88,          refl !rht mddl edge !!
39,51,50,38,            refl! !39 51 50 38 not needed!
)

!-----1-----2-----3-----4-----5-----6-----7-----!
!-----system connection and structures-----!
$sk = PAR(4)              ! angle # of interface currents !
white = ALB(1/1/1)
RLBeR = STR($RLBeR)      ! combined LoBeR and RoBeR !
LoBeR = STR($LoBeR)     ! Left outer Be reflector !
RoBeR = STR($RoBeR)     ! Right outer Be reflector !
!N4 = STR($N4)          !control drum piece for outer rim!
!N1 = STR($N1)          !control drum piece for outer rim!

system = CNX( RLBeR,RoBeR,LoBeR / ! 1,2,3 !
( 1, 15,16)$k( 2, 6, 5)! RLBeR to RoBeR !
( 1,23,22)$k( 3, 15, 16))

system = BDRY((1,19,19)$k(white)) ! from node 19 to node 19 on 1=RLBeR !

!-----must have in the input file to work in helios/aurora-----!

! ?rename? all of the OVXX's fixed !
ovd = OVLD( 1 /*-**)
ovt = OVLT(310.93/*-**)          ! = 100 Fahrenheit !

ovm = OVLM( alustr/*-**!/
          coo/*-0-cool,*-*(shco,rgco,acoo,bcoo)!/
          !Hf/*-*-shab!/
          Be/*-0-refl!/
          BeWskt/*-0-refl!)
osm = OVSM(ovm)
osd = OVSD(ovd)
ost = OVST(ovt)

st = STAT(osm,osd,ost)
pa = PATH(/P,(st))
!-----!
!-----edit data -----!

all = AREA(<*-**>)

case = RUN() ! Leakage !

```

The Helios code listed below is the code that will be put into the ATR-Helios model to merge the two STRs with half a large-I position CCS into one subsystem to act as a single STR.

```

THEL
!-----1-----2-----3-----4-----5-----6-----7-----!
case = CASE('lib-47u'/LrgIpoly12.hrf/'ATR pieces')
!-----parameters from ATR.INP and ATR.SET to make LrgIpoly structure-----!
!-----1-----2-----3-----4-----5-----6-----7-----!
!-----1-start parameters DSC added for I-polygons-----6-----7-----!
$si1500 = PAR (" 0.25881 90451 02521")
$si3000 = PAR (" 0.50000 00000 00000")
!$si4500 = PAR (" 0.70710 67811 86548")!
$si6000 = PAR (" 0.86602 54037 84439")
$si7500 = PAR (" 0.96592 58262 89068")

$co1500 = PAR (" 0.96592 58262 89068")
$co3000 = PAR (" 0.86602 54037 84439")
$co4500 = PAR (" 0.70710 67811 86548")
$co6000 = PAR (" 0.50000 00000 00000")
$co7500 = PAR (" 0.25881 90451 02521")

!-----DSC added parameters for polygons-----!

```

$\$lrgIspc = PAR(" \$yIlar - \$lrg5 - \$yN16c - \$rN16o ")$
 $\$lrgIplyr = PAR(" \$lrg5 + \$lrgIspc / 4 ")$
 $\$N16polyr = PAR(" \$rN16o + \$lrgIspc / 4 ")$
 $\$mdIpolyr = PAR(" \$rmdIho + \$lrgIspc / 4 ")$

!---+----1--end parameters DSC added for I-polygons---+----6----+----7----+----!
 ! ----- Small water hole data ----- !

$\$rwhole = PAR(" 0.3155 * 2.54 / 2 ")$! Radius of water holes [cm] !
 $\$xwh1 = PAR(" 0.959 * 2.54 ")$! x-coordinate of hole 1 [cm] !
 $\$ywh1 = PAR(" \$yBhole - 0.499 * 2.54 ")$! y-coordinate of hole 1 [cm] !
 $\$xwh2 = PAR(" 1.015 * 2.54 ")$! x-coordinate of hole 2 [cm] !
 $\$ywh2 = PAR(" \$yBhole - 1.851 * 2.54 ")$! y-coordinate of hole 2 [cm] !
 $\$xwh3 = PAR(" 2.084 * 2.54 ")$! x-coordinate of hole 3 [cm] !
 $\$ywh3 = PAR(" \$yBhole - 1.631 * 2.54 ")$! y-coordinate of hole 3 [cm] !
 $\$xwh4 = PAR(" 3.109 * 2.54 ")$! x-coordinate of hole 4 [cm] !
 $\$ywh4 = PAR(" \$yBhole - 1.596 * 2.54 ")$! y-coordinate of hole 4 [cm] !

! ----- Small/medium/large I holes ----- !

$\$rmdIho = PAR(" 8.255 / 2 ")$! O.R. of Med. I hole [cm] !
 $\$xI sma = PAR(" 60.969 * \$si4500 ")$! x-coord small hole [cm] !
 $\$yI sma = PAR(" \$xI sma ")$! y-coord small hole [cm] !
 $\$xI med1 = PAR(" 4.5 * 2.54 ")$! x-coord medium hole 1 [cm] !
 $\$yI med1 = PAR(" (16.937 + 5.879) * 2.54 ")$! y-coord medium hole 1 [cm] !
 $\$xI med2 = PAR(" 8.0 * 2.54 ")$! x-coord medium hole 2 [cm] !
 $\$yI med2 = PAR(" (16.937 + 4.853) * 2.54 ")$! y-coord medium hole 2 [cm] !
 $\$yI lar = PAR(" (16.937 + 5.312) * 2.54 ")$! y-coord large hole [cm] !

! ----- N16 holes ----- !

$\$rN16o = PAR(" 1.905 / 2 ")$! O.R. of N16 hole [cm] !
 $\$yN16c = PAR(" (16.937 + 2.062) * 2.54 ")$! y-coord N16 round hole [cm] !
 $\$xN16s = PAR(" 46.925 * \$si4500 ")$! x-coord N16 aquar hole [cm] !
 $\$yN16s = PAR(" \$xN16s ")$! y-coord N16 aquar hole [cm] !

! ----- Core reflector tank ----- !

$\$rtki = PAR(" 25.25 * 2.54 ")$! Inner radius core reflector tank [cm] !
 $\$rtko = PAR(" \$rtki + 1.6875 * 2.54 ")$! Outer radius core reflector tank [cm] !

! ----- !
 $\$rdrum = PAR(" 7.50 * 2.54 / 2 ")$! Outer radius control drum hole [cm] !
 $\$rCHfo = PAR(" 3.62 * 2.54 ")$! Outer radius control Hf ring [cm] !
 $\$rCHfi = PAR(" 3.37 * 2.54 ")$! Inner radius control Hf ring [cm] !
 $\$xdrum3 = PAR(" 4.0 * 2.54 ")$! x-coordinate of centre of drum N3 [cm] !
 $\$ydrum3 = PAR(" 16.937 * 2.54 ")$! y-coordinate of centre of drum N3 [cm] !
 $\$xdrum4 = PAR(" 11.814 * 2.54 ")$! x-coordinate of centre of drum N4 [cm] !
 $\$ydrum4 = PAR(" (16.937 + 0.532) * 2.54 ")$! y-coordinate of centre of drum N4 [cm] !

$\$N4LU1x = PAR(" (6 * (\$xdrum3 + \$xdrum * \$si5625) + 1 * (\$xtki / 2 * (\$si3375 + \$si2250))) / 7 ") ! 52x!$
 $\$N4LU1y = PAR(" (6 * (\$ydrum3 + \$xdrum * \$si3375) + 1 * (\$xtki / 2 * (\$si5625 + \$si6750))) / 7 ") ! 52y!$

$\$N4LU2x = PAR(" (5 * (\$xdrum3 + \$xdrum * \$si5625) + 2 * (\$xtki / 2 * (\$si3375 + \$si2250))) / 7 ") ! 53x!$
 $\$N4LU2y = PAR(" (5 * (\$ydrum3 + \$xdrum * \$si3375) + 2 * (\$xtki / 2 * (\$si5625 + \$si6750))) / 7 ") ! 53y!$

$\$N4LU3x = PAR(" (4 * (\$xdrum3 + \$xdrum * \$si5625) + 3 * (\$xtki / 2 * (\$si3375 + \$si2250))) / 7 ") ! 54x!$
 $\$N4LU3y = PAR(" (4 * (\$ydrum3 + \$xdrum * \$si3375) + 3 * (\$xtki / 2 * (\$si5625 + \$si6750))) / 7 ") ! 54y!$

$\$N4LU4x = PAR(" (3 * (\$xdrum3 + \$xdrum * \$si5625) + 4 * (\$xtki / 2 * (\$si3375 + \$si2250))) / 7 ") ! 55x!$
 $\$N4LU4y = PAR(" (3 * (\$ydrum3 + \$xdrum * \$si3375) + 4 * (\$xtki / 2 * (\$si5625 + \$si6750))) / 7 ") ! 55y!$

$\$N4LU5x = PAR(" (2 * (\$xdrum3 + \$xdrum * \$si5625) + 5 * (\$xtki / 2 * (\$si3375 + \$si2250))) / 7 ") ! 56x!$
 $\$N4LU5y = PAR(" (2 * (\$ydrum3 + \$xdrum * \$si3375) + 5 * (\$xtki / 2 * (\$si5625 + \$si6750))) / 7 ") ! 56y!$

$\$N4LU6x = PAR(" (1 * (\$xdrum3 + \$xdrum * \$si5625) + 6 * (\$xtki / 2 * (\$si3375 + \$si2250))) / 7 ") ! 57x!$
 $\$N4LU6y = PAR(" (1 * (\$ydrum3 + \$xdrum * \$si3375) + 6 * (\$xtki / 2 * (\$si5625 + \$si6750))) / 7 ") ! 57y!$

$\$N4LV0x = PAR(" ((\$xlo + \$xhi) + (\$xlo + \$xhi * (1 - \$si1125))) / 2 ")$! 58x!
 $\$N4LV0y = PAR(" ((\$xlo + \$xhi * 2) + (\$xlo + \$xhi * (1 + \$si7875))) / 2 ")$! 58y!

$\$N4LV1x = PAR(" (5 * \$N4LV0x + 1 * \$N4LU1x) / 6 ")$! 59x!
 $\$N4LV1y = PAR(" (5 * \$N4LV0y + 1 * \$N4LU1y) / 6 ")$! 59y!

$\$N4LV2x = PAR(" (4 * \$N4LV0x + 2 * \$N4LU1x) / 6 ")$! 60x!
 $\$N4LV2y = PAR(" (4 * \$N4LV0y + 2 * \$N4LU1y) / 6 ")$! 60y!

```

$N4LV3x=PAR("(3*$N4LV0x+ 3*$N4LU1x)/6")           ! 61x!
$N4LV3y=PAR("(3*$N4LV0y+ 3*$N4LU1y)/6")           ! 61y!

$N4LV4x=PAR("(2*$N4LV0x+ 4*$N4LU1x)/6")           ! 62x!
$N4LV4y=PAR("(2*$N4LV0y+ 4*$N4LU1y)/6")           ! 62y!

$N4LV5x=PAR("(1*$N4LV0x+ 5*$N4LU1x)/6")           ! 63x!
$N4LV5y=PAR("(1*$N4LV0y+ 5*$N4LU1y)/6")           ! 63y!
$rlg1  = PAR(" 1.5875/2")
$rlg4  = PAR("11.5443/2")
$rlg5  = PAR("12.7000/2")
$rlg2  = PAR("(2*$rlg1+$rlg4)/3")
$rlg3  = PAR("($rlg1+2*$rlg4)/3")
!-----TRIG parameters used for the coordinates of the ATR-----!
$pi    = PAR("3.14159 26535 89793")
$fl125 = PAR("($pi/16/$si1125)**0.5")   ! Convert circle to polygon   !
$si1125 = PAR("0.19509 03220 16128")
$si2250 = PAR("0.38268 34323 65089")
$si3375 = PAR("0.55557 02330 19602")
$si4500 = PAR("0.70710 67811 86548")
$si5625 = PAR("0.83146 96123 02545")
$si6750 = PAR("0.92387 95325 11287")
$si7875 = PAR("0.98078 52804 03230")

$tg2250 = PAR("0.41421 35623 73095")
$tg6750 = PAR("2.41421 35623 73090")

$si0257 = PAR(" 0.43388 37391 17558")
$si0514 = PAR(" 0.78183 14824 68030")
$si0771 = PAR(" 0.97492 79121 81824")
$si1028 = PAR(" 0.97492 79121 81824")
$si1285 = PAR(" 0.78183 14824 68030")
$si1542 = PAR(" 0.43388 37391 17558")
$si1800 = PAR(" 0.00000 00000 00000")
$si2057 = PAR(" -0.43388 37391 17558")
$si2314 = PAR(" -0.78183 14824 68030")
$si2571 = PAR(" -0.97492 79121 81824")
$si2828 = PAR(" -0.97492 79121 81823")
$si3085 = PAR(" -0.78183 14824 68030")
$si3342 = PAR(" -0.43388 37391 17558")
$si3600 = PAR(" 0.00000 00000 00000")

$co0257 = PAR(" 0.90096 88679 02419")
$co0514 = PAR(" 0.62348 98018 58734")
$co0771 = PAR(" 0.22252 09339 56314")
$co1028 = PAR(" -0.22252 09339 56314")
$co1285 = PAR(" -0.62348 98018 58733")
$co1542 = PAR(" -0.90096 88679 02419")
$co1800 = PAR(" -1.00000 00000 00000")
$co2057 = PAR(" -0.90096 88679 02419")
$co2314 = PAR(" -0.62348 98018 58734")
$co2571 = PAR(" -0.22252 09339 56315")
$co2828 = PAR(" 0.22252 09339 56315")
$co3085 = PAR(" 0.62348 98018 58733")
$co3342 = PAR(" 0.90096 88679 02419")
$co3600 = PAR(" 1.00000 00000 00000")

$si0129=PAR(" 0.22252 09339 56314")
$si0386=PAR(" 0.62348 98018 58733")
$si0643=PAR(" 0.90096 88679 02419")
$si0900=PAR(" 1.00000 00000 00000")
$si1157=PAR(" 0.90096 88679 02419")
$si1414=PAR(" 0.62348 98018 58733")
$si1671=PAR(" 0.22252 09339 56314")
$si1929=PAR(" -0.22252 09339 56315")
$si2186=PAR(" -0.62348 98018 58734")
$si2443=PAR(" -0.90096 88679 02419")
$si2700=PAR(" -1.00000 00000 00000")
$si2957=PAR(" -0.90096 88679 02419")

```

\$si3214=PAR("-0.62348 98018 58733")
\$si3471=PAR("-0.22252 09339 56313")

\$co0129=PAR(" 0.97492 79121 81824")
\$co0386=PAR(" 0.78183 14824 68030")
\$co0643=PAR(" 0.43388 37391 17558")
\$co0900=PAR(" 0.00000 00000 00000")
\$co1157=PAR("-0.43388 37391 17558")
\$co1414=PAR("-0.78183 14824 68030")
\$co1671=PAR("-0.97492 79121 81824")
\$co1929=PAR("-0.97492 79121 81824")
\$co2186=PAR("-0.78183 14824 68030")
\$co2443=PAR("-0.43388 37391 17557")
\$co2700=PAR(" 0.00000 00000 00000")
\$co2957=PAR(" 0.43388 37391 17559")
\$co3214=PAR(" 0.78183 14824 68030")
\$co3471=PAR(" 0.97492 79121 81824")

\$xdrum = PAR("\$sdrum*\$fl125") ! Equiv polygon "r" for rdrum !
\$xtki = PAR("\$rtki*\$fl125") ! Equiv polygon "r" for inner tank !
\$xtko = PAR("\$rtko*\$fl125") ! Equiv polygon "r" for outer tank !
!---+---1---+---2---+---3---+---4---+---5---+---6---+---7---+---!
!---+---1---+---2---Be reflector parameters for STR---6---+---7---+---!
\$RoBeRU1x=PAR("(4*(0)+5*(\$xtki*\$si1125))/9") ! 27x!
\$RoBeRU1y=PAR("(4*(\$xtki)+5*(\$xtki*\$si7875))/9") ! 27y!
!(4*(2)+5*(3))/9 = 27 !
! U = Up !

\$RoBeRU2x=PAR("(5*(\$xtki*\$si1125)+4*(\$xtki*\$si2250))/9") ! 28x!
\$RoBeRU2y=PAR("(5*(\$xtki*\$si7875)+4*(\$xtki*\$si6750))/9") ! 28y!
!(5*(3)+4*(4))/9 = 28 !
! U = Up !

\$RoBeRD1x=PAR("(9*(\$sdrum3-\$sdrum*\$si2250)+1*(\$RoBeRU1x))/10") ! 29x!
\$RoBeRD1y=PAR("(9*(\$sdrum3+\$sdrum*\$si6750)+1*(\$RoBeRU1y))/10") ! 29y!
!(9*(13)+1*(27))/10 = 29 !
! D = Down !

\$RoBeRD2x=PAR("(6*(\$sdrum3+\$sdrum*\$si2250)+1*(\$RoBeRU2x))/7") ! 30x!
\$RoBeRD2y=PAR("(6*(\$sdrum3+\$sdrum*\$si6750)+1*(\$RoBeRU2y))/7") ! 30y!
!(6*(9)+1*(28))/7 = 30 !
! D = Down !

\$RoBeRNEx=PAR("\$xtki/2*(\$si3375+\$si2250)") ! 5x !
\$RoBeRNEy=PAR("\$xtki/2*(\$si5625+\$si6750)") ! 5y !
!-----topBeR materials-----!

!refl material!
!Be = MAT(1.8538/4009,100)! ! Be reflector material !
Be = MAT(4009,1.2387E-1) ! 1.2387E-1 atoms/barn-cm == 1.8538 g/cm3 !
BeWskt = MAT(/4009,1.2198E-1; ! Be reflector with water socket !
8016,5.0792E-4;
1001,1.0158E-3)

BePlug = MAT(/4009,1.2387E-1)
BePlugLI= MAT(/4009,1.2029E-1; ! Be Plug for Large I-Holes !
8016,9.5940E-4;
1001,1.9188E-3)
BePlugMI= MAT(/4009,1.1435E-1; ! Be Plug for Medium I-Holes !
8016,2.5529E-3;
1001,5.1057E-3)
BeDrum = MAT(/4009,1.1492E-1; ! Be+Water in Outer Shim Control Cylinder !
8016,2.4002E-3;
1001,4.8003E-3)
alustr = MAT(/13027,5.8750E-2;
22000,6.7918E-6;
24000,5.9415E-5;
12000,6.0209E-4;
25055,2.3677E-5;
29063,4.42467E-5;
29065,1.97213E-5;
26000,1.1646E-4;

14000,3.7052E-4)
Hf = MAT(/72174,7.12946E-05;
72176,2.29111E-03;
72177,8.18831E-03;
72178,1.20131E-02;
72179,5.99799E-03;
72180,1.54472E-02;
40000,8.58980E-4)

coo = MAT(/ 1001,6.6394E-2; 8016,3.3197E-2) ! 0.9931 g/cm3, Table 37 !

!----1----+----2----+----CCS's from ATR+----5----+----6----+----7----+----!

lgIhol = CCS(\$rlg1,\$rlg2,\$rlg3,\$rlg4,\$rlg5/4(3,5)/
bcOO,lgIpl, lgIpl,lgIpl,lgIpl,lgIpl,
lgIpl,lgIpl,lgIpl,lgIpl,
bcOO, bcOO, bcOO, bcOO) ! Large I hole !
mdlhol = CCS("1.11125/2","7.0993/2",\$rmdlho/4(2,3)/
bcOO,mdlpl,mdlpl,mdlpl,mdlpl,
bcOO, bcOO, bcOO, bcOO) ! Medium I hole !
N16cir = CCS("0.6579/2","0.9525/2","1.16586/2",
"1.5875/2",\$rN16o//
bcOO,tube,bcOO,tube,bcOO) ! Round N16 hole !

!----1----+----2----+DSC New STR = LrgIpoly--5----+----6----+----7----+----!

\$LrgIpoly = PAR((\$LrgIplyr , "Syllar") ! 1 !
("\$LrgIplyr*\$co1500" , "Syllar+\$LrgIplyr*\$si1500") ! 2 !
("\$LrgIplyr*\$co3000" , "Syllar+\$LrgIplyr*\$si3000") ! 3 !
("\$LrgIplyr*\$co4500" , "Syllar+\$LrgIplyr*\$si4500") ! 4 !
("\$LrgIplyr*\$co6000" , "Syllar+\$LrgIplyr*\$si6000") ! 5 !
("\$LrgIplyr*\$co7500" , "Syllar+\$LrgIplyr*\$si7500") ! 6 !
("\$LrgIplyr*\$co0900" , "Syllar+\$LrgIplyr*\$si0900") ! 7 !
("-\$LrgIplyr*\$co7500" , "Syllar+\$LrgIplyr*\$si7500") ! 8 !
("-\$LrgIplyr*\$co6000" , "Syllar+\$LrgIplyr*\$si6000") ! 9 !
("-\$LrgIplyr*\$co4500" , "Syllar+\$LrgIplyr*\$si4500") ! 10 !
("-\$LrgIplyr*\$co3000" , "Syllar+\$LrgIplyr*\$si3000") ! 11 !
("-\$LrgIplyr*\$co1500" , "Syllar+\$LrgIplyr*\$si1500") ! 12 !
("\$LrgIplyr" , "Syllar") ! 13 !
("-\$LrgIplyr*\$co1500" , "Syllar-\$LrgIplyr*\$si1500") ! 14 !
("-\$LrgIplyr*\$co3000" , "Syllar-\$LrgIplyr*\$si3000") ! 15 !
("-\$LrgIplyr*\$co4500" , "Syllar-\$LrgIplyr*\$si4500") ! 16 !
("-\$LrgIplyr*\$co6000" , "Syllar-\$LrgIplyr*\$si6000") ! 17 !
("-\$LrgIplyr*\$co7500" , "Syllar-\$LrgIplyr*\$si7500") ! 18 !
("-\$LrgIplyr*\$co0900" , "Syllar-\$LrgIplyr*\$si0900") ! 19 !
("\$LrgIplyr*\$co7500" , "Syllar-\$LrgIplyr*\$si7500") ! 20 !
("\$LrgIplyr*\$co6000" , "Syllar-\$LrgIplyr*\$si6000") ! 21 !
("\$LrgIplyr*\$co4500" , "Syllar-\$LrgIplyr*\$si4500") ! 22 !
("\$LrgIplyr*\$co3000" , "Syllar-\$LrgIplyr*\$si3000") ! 23 !
("\$LrgIplyr*\$co1500" , "Syllar-\$LrgIplyr*\$si1500") ! 24 !

!----1----+----2----+--node for the Large I-CCS+----6----+----7----+----!

(\$rlg5 , Syllar) ! 25 !
("\$rlg5*\$co1500" , "Syllar+\$rlg5*\$si1500") ! 26 !
("\$rlg5*\$co3000" , "Syllar+\$rlg5*\$si3000") ! 27 !
("\$rlg5*\$co4500" , "Syllar+\$rlg5*\$si4500") ! 28 !
("\$rlg5*\$co6000" , "Syllar+\$rlg5*\$si6000") ! 29 !
("\$rlg5*\$co7500" , "Syllar+\$rlg5*\$si7500") ! 30 !
("\$rlg5*\$co0900" , "Syllar+\$rlg5*\$si0900") ! 31 !
("-\$rlg5*\$co7500" , "Syllar+\$rlg5*\$si7500") ! 32 !
("-\$rlg5*\$co6000" , "Syllar+\$rlg5*\$si6000") ! 33 !
("-\$rlg5*\$co4500" , "Syllar+\$rlg5*\$si4500") ! 34 !
("-\$rlg5*\$co3000" , "Syllar+\$rlg5*\$si3000") ! 35 !
("-\$rlg5*\$co1500" , "Syllar+\$rlg5*\$si1500") ! 36 !
("\$Lrg5" , Syllar) ! 37 !
("-\$rlg5*\$co1500" , "Syllar-\$rlg5*\$si1500") ! 38 !
("-\$rlg5*\$co3000" , "Syllar-\$rlg5*\$si3000") ! 39 !
("-\$rlg5*\$co4500" , "Syllar-\$rlg5*\$si4500") ! 40 !
("-\$rlg5*\$co6000" , "Syllar-\$rlg5*\$si6000") ! 41 !
("-\$rlg5*\$co7500" , "Syllar-\$rlg5*\$si7500") ! 42 !
("-\$rlg5*\$co0900" , "Syllar-\$rlg5*\$si0900") ! 43 !
("\$rlg5*\$co7500" , "Syllar-\$rlg5*\$si7500") ! 44 !

("Srlg5*\$co6000" , "\$yllar-Srlg5*\$si6000") ! 45 !
 ("Srlg5*\$co4500" , "\$yllar-Srlg5*\$si4500") ! 46 !
 ("Srlg5*\$co3000" , "\$yllar-Srlg5*\$si3000") ! 47 !
 ("Srlg5*\$co1500" , "\$yllar-Srlg5*\$si1500") ! 48 !

/24,refl
 /lg!hol(0,\$yllar) !DSC GET ALL SEGMENTS!

/1,25,26,2, refl; ! Right !
 2,26,27,3, refl;
 3,27,28,4, refl;
 4,28,29,5, refl;
 5,29,30,6, refl;
 6,30,31,7, refl;
 7,31,32,8, refl;

8,32,33,9, refl; ! top !
 9,33,34,10, refl;
 10,34,35,11, refl;
 11,35,36,12, refl;
 12,36,37,13, refl;
 13,37,38,14, refl;

14,38,39,15, refl; ! left !
 15,39,40,16, refl;
 16,40,41,17, refl;
 17,41,42,18, refl;
 18,42,43,19, refl;

19,43,44,20, refl; ! bottom !
 20,44,45,21, refl;
 21,45,46,22, refl;
 22,46,47,23, refl;
 23,47,48,24, refl;
 24,48,25,1, refl

)
 !---+----1----+--Be between large I-pos and med I-pos on left---+----7----+----!
 \$BeLgMdL = PAR((0 , \$xtki) ! 19=1 !
 ("-\$RoBeRU1x", "\$RoBeRU1y") ! 44=2 !
 ("-\$xtki*\$si1125", "\$xtki*\$si7875") ! 18=3 !
 ("-\$xImed1-\$medIpolyr*\$co6000", "\$yImed1+\$medIpolyr*\$si6000") ! 9=4 !
 ("-\$xImed1-\$medIpolyr*\$co7500", "\$yImed1+\$medIpolyr*\$si7500") ! 8=5 !
 ("-\$xImed1+\$medIpolyr*\$co0900", "\$yImed1+\$medIpolyr*\$si0900") ! 7=6 !
 ("-\$xImed1+\$medIpolyr*\$co7500", "\$yImed1+\$medIpolyr*\$si7500") ! 6=7 !
 ("-\$xImed1+\$medIpolyr*\$co6000", "\$yImed1+\$medIpolyr*\$si6000") ! 5=8 !
 ("-\$xImed1+\$medIpolyr*\$co4500", "\$yImed1+\$medIpolyr*\$si4500") ! 4=9 !
 ("-\$xImed1+\$medIpolyr*\$co3000", "\$yImed1+\$medIpolyr*\$si3000") ! 3=10 !
 ("-\$xImed1+\$medIpolyr*\$co1500", "\$yImed1+\$medIpolyr*\$si1500") ! 2=11 !
 ("-\$xImed1+\$medIpolyr*\$co3600", "\$yImed1+\$medIpolyr*\$si3600") ! 1=12 !
 ("-\$xImed1+\$medIpolyr*\$co1500", "\$yImed1-\$medIpolyr*\$si1500") ! 24=13 !
 ("-\$xImed1+\$medIpolyr*\$co3000", "\$yImed1-\$medIpolyr*\$si3000") ! 23=14 !
 ("-\$xImed1+\$medIpolyr*\$co4500", "\$yImed1-\$medIpolyr*\$si4500") ! 22=15 !
 ("-\$xImed1+\$medIpolyr*\$co6000", "\$yImed1-\$medIpolyr*\$si6000") ! 21=16 !
 ("-\$xImed1+\$medIpolyr*\$co7500", "\$yImed1-\$medIpolyr*\$si7500") ! 20=17 !
 ("-\$xImed1-\$medIpolyr*\$co0900", "\$yImed1-\$medIpolyr*\$si0900") ! 19=18 !
 ("-\$xImed1-\$medIpolyr*\$co7500", "\$yImed1-\$medIpolyr*\$si7500") ! 18=19 !
 ("-\$xdrum3-\$xdrum*\$si1125", "\$ydrum3+\$xdrum*\$si7875") ! 11=20 !
 ("-\$xdrum3", "\$ydrum3+\$xdrum") ! 10=21 !
 ("-\$xdrum3+\$xdrum*\$si1125", "\$ydrum3+\$xdrum*\$si7875") ! 9=22 !
 ("-\$xdrum3+\$xdrum*\$si2250", "\$ydrum3+\$xdrum*\$si6750") ! 8=23 !
 ("-\$xdrum3+\$xdrum*\$si3375", "\$ydrum3+\$xdrum*\$si5625") ! 7=24 !
 ("-\$xdrum3+\$xdrum*\$si4500", "\$ydrum3+\$xdrum*\$si4500") ! 6=25 !
 ("-\$xdrum3+\$xdrum*\$si5625", "\$ydrum3+\$xdrum*\$si3375") ! 5=26 !
 ("-\$xdrum3+\$xdrum*\$si6750", "\$ydrum3+\$xdrum*\$si2250") ! 4=27 !
 ("-\$xdrum3+\$xdrum*\$si7875", "\$ydrum3+\$xdrum*\$si1125") ! 3=28 !
 ("-\$xdrum3+\$xdrum", "\$ydrum3") ! 2=29 !
 (0 , \$ydrum3) ! 1=30 !
 (0 , "\$ydrum3+\$xdrum*\$si1125") ! 71=31 !
 ("0" , "\$yN16c-\$N16polyr") ! 7=32 !
 ("-\$N16polyr*\$co6000", "\$yN16c-\$N16polyr*\$si6000") ! 6=33 !
 ("-\$N16polyr*\$co3000", "\$yN16c-\$N16polyr*\$si3000") ! 5=34 !

```

(" -N16polyr" , "$yN16c-$N16polyr*$si3600") ! 4=35 !
(" -N16polyr*$co3000" , "$yN16c+$N16polyr*$si3000") ! 3=36 !
(" -N16polyr*$co6000" , "$yN16c+$N16polyr*$si6000") ! 2=37 !
( "0" , "$yN16c+$N16polyr" ) !top of N16 poly! ! 1=38 !
! 19 bottom of Lrg I-poly !
! LrgIpoly 19 connects to 39 BeLgMdL1 !
(" -$lrgIplyr*$co0900" , "$yIlar-$lrgIplyr*$si0900") ! 19=39 !
(" -$lrgIplyr*$co7500" , "$yIlar-$lrgIplyr*$si7500") ! 18=40 !
(" -$lrgIplyr*$co6000" , "$yIlar-$lrgIplyr*$si6000") ! 17=41 !
(" -$lrgIplyr*$co4500" , "$yIlar-$lrgIplyr*$si4500") ! 16=42 !
(" -$lrgIplyr*$co3000" , "$yIlar-$lrgIplyr*$si3000") ! 15=43 !
(" -$lrgIplyr*$co1500" , "$yIlar-$lrgIplyr*$si1500") ! 14=44 !
(" -$lrgIplyr" , "$yIlar" ) ! 13=45 !
(" -$lrgIplyr*$co1500" , "$yIlar+$lrgIplyr*$si1500") ! 12=46 !
(" -$lrgIplyr*$co3000" , "$yIlar+$lrgIplyr*$si3000") ! 11=47 !
(" -$lrgIplyr*$co4500" , "$yIlar+$lrgIplyr*$si4500") ! 10=48 !
(" -$lrgIplyr*$co6000" , "$yIlar+$lrgIplyr*$si6000") ! 9=49 !
(" -$lrgIplyr*$co7500" , "$yIlar+$lrgIplyr*$si7500") ! 8=50 !
(" -$lrgIplyr*$co0900" , "$yIlar+$lrgIplyr*$si0900") ! 7=51 !
! node 51 connects to node 7 on LrgIpoly !
("-(5*(R0BeRU1x)+1*(R0BeRD1x))/6", "(5*(R0BeRU1y)+1*(R0BeRD1y))/6")!49=52 !
("-(2.7*(R0BeRU1x)+3.3*(R0BeRD1x))/6",
"(2.7*(R0BeRU1y)+3.3*(R0BeRD1y))/6")!50=53 !
("-(1*(R0BeRU1x)+5*(R0BeRD1x))/6", "(1*(R0BeRU1y)+5*(R0BeRD1y))/6")!51=54 !
("-$R0BeRD1x" , "$R0BeRD1y" ) !46=55 !
!---+---1---+---2---+---3---+---4---+---5---+---6---+---7---+---!
/51,refl/
/1,51,50,49,48,52,2, refl; ! top right!
2,52,8,7,6,5,4,3, refl; ! top left !
8,52,53,12,11,10,9, refl;
12,53,54,15,14,13, refl;
15,54,55,17,16, refl;
19,18,17,55,23,22,21,20, refl;
23,42,41,40,39,25,24, refl;
25,39,38,37,36,35,26, refl;
26,35,34,33,32,27, refl;
27,32,31,28, refl;
28,31,30,29, refl;
42,23,55,54,44,43, refl;
44,54,53,46,45, refl

```

```

)
!---+---DSC Medium I polygon left side Med I-CCS in polygon---+---7---+---!
$MedIpolyL1 = PAR(
("$xImed1+$medIpolyr*$co3600" , "$yImed1+$medIpolyr*$si3600")! 1 !
("$xImed1+$medIpolyr*$co1500" , "$yImed1+$medIpolyr*$si1500")! 2 !
("$xImed1+$medIpolyr*$co3000" , "$yImed1+$medIpolyr*$si3000")! 3 !
("$xImed1+$medIpolyr*$co4500" , "$yImed1+$medIpolyr*$si4500")! 4 !
("$xImed1+$medIpolyr*$co6000" , "$yImed1+$medIpolyr*$si6000")! 5 !
("$xImed1+$medIpolyr*$co7500" , "$yImed1+$medIpolyr*$si7500")! 6 !
("$xImed1+$medIpolyr*$co0900" , "$yImed1+$medIpolyr*$si0900")! 7 !
("$xImed1-$medIpolyr*$co7500" , "$yImed1+$medIpolyr*$si7500")! 8 !
("$xImed1-$medIpolyr*$co6000" , "$yImed1+$medIpolyr*$si6000")! 9 !
("$xImed1-$medIpolyr*$co4500" , "$yImed1+$medIpolyr*$si4500")! 10 !
("$xImed1-$medIpolyr*$co3000" , "$yImed1+$medIpolyr*$si3000")! 11 !
("$xImed1-$medIpolyr*$co1500" , "$yImed1+$medIpolyr*$si1500")! 12 !
("$xImed1-$medIpolyr*$co3600" , "$yImed1+$medIpolyr*$si3600")! 13 !
("$xImed1-$medIpolyr*$co1500" , "$yImed1-$medIpolyr*$si1500")! 14 !
("$xImed1-$medIpolyr*$co3000" , "$yImed1-$medIpolyr*$si3000")! 15 !
("$xImed1-$medIpolyr*$co4500" , "$yImed1-$medIpolyr*$si4500")! 16 !
("$xImed1-$medIpolyr*$co6000" , "$yImed1-$medIpolyr*$si6000")! 17 !
("$xImed1-$medIpolyr*$co7500" , "$yImed1-$medIpolyr*$si7500")! 18 !
("$xImed1-$medIpolyr*$co0900" , "$yImed1-$medIpolyr*$si0900")! 19 !
("$xImed1+$medIpolyr*$co7500" , "$yImed1-$medIpolyr*$si7500")! 20 !
("$xImed1+$medIpolyr*$co6000" , "$yImed1-$medIpolyr*$si6000")! 21 !
("$xImed1+$medIpolyr*$co4500" , "$yImed1-$medIpolyr*$si4500")! 22 !
("$xImed1+$medIpolyr*$co3000" , "$yImed1-$medIpolyr*$si3000")! 23 !
("$xImed1+$medIpolyr*$co1500" , "$yImed1-$medIpolyr*$si1500")! 24 !
!---+---1---+---2---+---node for the Medium I-CCS---+---6---+---7---+---!

```

```

("$xImed1+$rmdlho*$co3600", "$yImed1+$rmdlho*$si3600") ! 25 !
("$xImed1+$rmdlho*$co1500", "$yImed1+$rmdlho*$si1500") ! 26 !
("$xImed1+$rmdlho*$co3000", "$yImed1+$rmdlho*$si3000") ! 27 !
("$xImed1+$rmdlho*$co4500", "$yImed1+$rmdlho*$si4500") ! 28 !
("$xImed1+$rmdlho*$co6000", "$yImed1+$rmdlho*$si6000") ! 29 !
("$xImed1+$rmdlho*$co7500", "$yImed1+$rmdlho*$si7500") ! 30 !
("$xImed1+$rmdlho*$co0900", "$yImed1+$rmdlho*$si0900") ! 31 !
("$xImed1-$rmdlho*$co7500", "$yImed1+$rmdlho*$si7500") ! 32 !
("$xImed1-$rmdlho*$co6000", "$yImed1+$rmdlho*$si6000") ! 33 !
("$xImed1-$rmdlho*$co4500", "$yImed1+$rmdlho*$si4500") ! 34 !
("$xImed1-$rmdlho*$co3000", "$yImed1+$rmdlho*$si3000") ! 35 !
("$xImed1-$rmdlho*$co1500", "$yImed1+$rmdlho*$si1500") ! 36 !
("$xImed1-$rmdlho*$co3600", "$yImed1+$rmdlho*$si3600") ! 37 !
("$xImed1-$rmdlho*$co1500", "$yImed1-$rmdlho*$si1500") ! 38 !
("$xImed1-$rmdlho*$co3000", "$yImed1-$rmdlho*$si3000") ! 39 !
("$xImed1-$rmdlho*$co4500", "$yImed1-$rmdlho*$si4500") ! 40 !
("$xImed1-$rmdlho*$co6000", "$yImed1-$rmdlho*$si6000") ! 41 !
("$xImed1-$rmdlho*$co7500", "$yImed1-$rmdlho*$si7500") ! 42 !
("$xImed1-$rmdlho*$co0900", "$yImed1-$rmdlho*$si0900") ! 43 !
("$xImed1+$rmdlho*$co7500", "$yImed1-$rmdlho*$si7500") ! 44 !
("$xImed1+$rmdlho*$co6000", "$yImed1-$rmdlho*$si6000") ! 45 !
("$xImed1+$rmdlho*$co4500", "$yImed1-$rmdlho*$si4500") ! 46 !
("$xImed1+$rmdlho*$co3000", "$yImed1-$rmdlho*$si3000") ! 47 !
("$xImed1+$rmdlho*$co1500", "$yImed1-$rmdlho*$si1500") ! 48 !
!---+---1---+---2---+---3---+---4---+---5---+---6---+---7---+---!

```

/24,refl

```

/mdlhol("$xImed1", "$yImed1") !DSC GET ALL SEGMENTS!

```

```

/1,25,26,2,      refl; ! Right      !
2,26,27,3,      refl;
3,27,28,4,      refl;
4,28,29,5,      refl;
5,29,30,6,      refl;
6,30,31,7,      refl;
7,31,32,8,      refl;

```

```

8,32,33,9,      refl; ! top      !
9,33,34,10,     refl;
10,34,35,11,    refl;
11,35,36,12,    refl;
12,36,37,13,    refl;
13,37,38,14,    refl;

```

```

14,38,39,15,    refl; ! left !
15,39,40,16,    refl;
16,40,41,17,    refl;
17,41,42,18,    refl;
18,42,43,19,    refl;

```

```

19,43,44,20,    refl; ! bottom !
20,44,45,21,    refl;
21,45,46,22,    refl;
22,46,47,23,    refl;
23,47,48,24,    refl;
24,48,25,1,     refl;
)

```

```

!---+---1---+---Be between MedL1 I-poly and medL2 I-pos on left+---7---+---!
$BeMdMdL = PAR(("$xtki*$si1125", "$xtki*$si7875") ! 3=1 !
("$RoBeRU2x", "$RoBeRU2y") ! 45=2 !
("$xtki*$si2250", "$xtki*$si6750") ! 17=3 !
("$xImed2-$medlpolyr*$co4500", "$yImed2+$medlpolyr*$si4500") ! 10=4 !
("$xImed2-$medlpolyr*$co6000", "$yImed2+$medlpolyr*$si6000") ! 9=5 !
("$xImed2-$medlpolyr*$co7500", "$yImed2+$medlpolyr*$si7500") ! 8=6 !
("$xImed2+$medlpolyr*$co0900", "$yImed2+$medlpolyr*$si0900") ! 7=7 !
("$xImed2+$medlpolyr*$co7500", "$yImed2+$medlpolyr*$si7500") ! 6=8 !
("$xImed2+$medlpolyr*$co6000", "$yImed2+$medlpolyr*$si6000") ! 5=9 !
("$xImed2+$medlpolyr*$co4500", "$yImed2+$medlpolyr*$si4500") ! 4=10 !
("$xImed2+$medlpolyr*$co3000", "$yImed2+$medlpolyr*$si3000") ! 3=11 !
("$xImed2+$medlpolyr*$co1500", "$yImed2+$medlpolyr*$si1500") ! 2=12 !
("$xImed2+$medlpolyr*$co3600", "$yImed2+$medlpolyr*$si3600") ! 1=13 !

```

```

("$xImed2+$medIpolyr*$co1500", "$yImed2-$medIpolyr*$si1500") !24=14 !
("$xImed2+$medIpolyr*$co3000", "$yImed2-$medIpolyr*$si3000") !23=15 !
("$xImed2+$medIpolyr*$co4500", "$yImed2-$medIpolyr*$si4500") !22=16 !
("$xdrum3-$xdrum*$si4500", "$ydrum3+$xdrum*$si4500") !14=17 !
("$xdrum3-$xdrum*$si3375", "$ydrum3+$xdrum*$si5625") !13=18 !
("$xdrum3-$xdrum*$si2250", "$ydrum3+$xdrum*$si6750") !12=19 !
("$xdrum3-$xdrum*$si1125", "$ydrum3+$xdrum*$si7875") !11=20 !
("$xImed1-$medIpolyr*$co7500", "$yImed1-$medIpolyr*$si7500") !19=21 !
("$xImed1-$medIpolyr*$co6000", "$yImed1-$medIpolyr*$si6000") !17=22 !
("$xImed1-$medIpolyr*$co4500", "$yImed1-$medIpolyr*$si4500") !16=23 !
("$xImed1-$medIpolyr*$co3000", "$yImed1-$medIpolyr*$si3000") !15=24 !
("$xImed1-$medIpolyr*$co1500", "$yImed1-$medIpolyr*$si1500") !14=25 !
("$xImed1-$medIpolyr*$co3600", "$yImed1+$medIpolyr*$si3600") !13=26 !
("$xImed1-$medIpolyr*$co1500", "$yImed1+$medIpolyr*$si1500") !12=27 !
("$xImed1-$medIpolyr*$co3000", "$yImed1+$medIpolyr*$si3000") !11=28 !
("$xImed1-$medIpolyr*$co4500", "$yImed1+$medIpolyr*$si4500") !10=29 !
("$xImed1-$medIpolyr*$co6000", "$yImed1+$medIpolyr*$si6000") !9=30 !
("-(5*(R0BeRU2x)+1*(R0BeRD2x))/6", "(5*(R0BeRU2y)+1*(R0BeRD2y))/6") !52=31 !
("-(2.8*(R0BeRU2x)+3.2*(R0BeRD2x))/6",
"(2.8*(R0BeRU2y)+3.2*(R0BeRD2y))/6") !53=32 !
("$R0BeRD2x", "$R0BeRD2y") !47=33 !

```

```

!---+---1---+---2---+---3---+---4---+---5---+---6---+---7---+---!

```

```

/30,refl/

```

```

/1,30,29,28,31,2,      refl; ! top      !
2,31,8,7,6,5,4,3,     refl;
8,31,32,11,10,9,      refl;
11,32,33,16,15,14,13,12,  refl;
16,33,19,18,17,       refl;
19,33,21,20,          refl;
21,33,32,25,24,23,22,  refl
)

```

```

!---+---1---+---2---+---3---+---4---+---5---+---6---+---7---+---!

```

```

!---+Medium I polygon left side in position 2 left of med I-poly 1=$MedIpolyL1-!

```

```

$MedIpolyL2 = PAR(

```

```

("$xImed2+$medIpolyr*$co3600", "$yImed2+$medIpolyr*$si3600") ! 1 !
("$xImed2+$medIpolyr*$co1500", "$yImed2+$medIpolyr*$si1500") ! 2 !
("$xImed2+$medIpolyr*$co3000", "$yImed2+$medIpolyr*$si3000") ! 3 !
("$xImed2+$medIpolyr*$co4500", "$yImed2+$medIpolyr*$si4500") ! 4 !
("$xImed2+$medIpolyr*$co6000", "$yImed2+$medIpolyr*$si6000") ! 5 !
("$xImed2+$medIpolyr*$co7500", "$yImed2+$medIpolyr*$si7500") ! 6 !
("$xImed2+$medIpolyr*$co0900", "$yImed2+$medIpolyr*$si0900") ! 7 !
("$xImed2-$medIpolyr*$co7500", "$yImed2+$medIpolyr*$si7500") ! 8 !
("$xImed2-$medIpolyr*$co6000", "$yImed2+$medIpolyr*$si6000") ! 9 !
("$xImed2-$medIpolyr*$co4500", "$yImed2+$medIpolyr*$si4500") ! 10 !
("$xImed2-$medIpolyr*$co3000", "$yImed2+$medIpolyr*$si3000") ! 11 !
("$xImed2-$medIpolyr*$co1500", "$yImed2+$medIpolyr*$si1500") ! 12 !
("$xImed2-$medIpolyr*$co3600", "$yImed2+$medIpolyr*$si3600") ! 13 !
("$xImed2-$medIpolyr*$co1500", "$yImed2-$medIpolyr*$si1500") ! 14 !
("$xImed2-$medIpolyr*$co3000", "$yImed2-$medIpolyr*$si3000") ! 15 !
("$xImed2-$medIpolyr*$co4500", "$yImed2-$medIpolyr*$si4500") ! 16 !
("$xImed2-$medIpolyr*$co6000", "$yImed2-$medIpolyr*$si6000") ! 17 !
("$xImed2-$medIpolyr*$co7500", "$yImed2-$medIpolyr*$si7500") ! 18 !
("$xImed2-$medIpolyr*$co0900", "$yImed2-$medIpolyr*$si0900") ! 19 !
("$xImed2+$medIpolyr*$co7500", "$yImed2-$medIpolyr*$si7500") ! 20 !
("$xImed2+$medIpolyr*$co6000", "$yImed2-$medIpolyr*$si6000") ! 21 !
("$xImed2+$medIpolyr*$co4500", "$yImed2-$medIpolyr*$si4500") ! 22 !
("$xImed2+$medIpolyr*$co3000", "$yImed2-$medIpolyr*$si3000") ! 23 !
("$xImed2+$medIpolyr*$co1500", "$yImed2-$medIpolyr*$si1500") ! 24 !
!---+---1---+---2---+---node for the Medium I-CCS---+---6---+---7---+---!

```

```

("$xImed2+$rmdlho*$co3600", "$yImed2+$rmdlho*$si3600") ! 25 !
("$xImed2+$rmdlho*$co1500", "$yImed2+$rmdlho*$si1500") ! 26 !
("$xImed2+$rmdlho*$co3000", "$yImed2+$rmdlho*$si3000") ! 27 !
("$xImed2+$rmdlho*$co4500", "$yImed2+$rmdlho*$si4500") ! 28 !
("$xImed2+$rmdlho*$co6000", "$yImed2+$rmdlho*$si6000") ! 29 !
("$xImed2+$rmdlho*$co7500", "$yImed2+$rmdlho*$si7500") ! 30 !
("$xImed2+$rmdlho*$co0900", "$yImed2+$rmdlho*$si0900") ! 31 !
("$xImed2-$rmdlho*$co7500", "$yImed2+$rmdlho*$si7500") ! 32 !
("$xImed2-$rmdlho*$co6000", "$yImed2+$rmdlho*$si6000") ! 33 !
("$xImed2-$rmdlho*$co4500", "$yImed2+$rmdlho*$si4500") ! 34 !

```

```

("$xImed2-$rmdlho*$co3000", "$yImed2+$rmdlho*$si3000") ! 35 !
("$xImed2-$rmdlho*$co1500", "$yImed2+$rmdlho*$si1500") ! 36 !
("$xImed2-$rmdlho*$co3600", "$yImed2+$rmdlho*$si3600") ! 37 !
("$xImed2-$rmdlho*$co1500", "$yImed2-$rmdlho*$si1500") ! 38 !
("$xImed2-$rmdlho*$co3000", "$yImed2-$rmdlho*$si3000") ! 39 !
("$xImed2-$rmdlho*$co4500", "$yImed2-$rmdlho*$si4500") ! 40 !
("$xImed2-$rmdlho*$co6000", "$yImed2-$rmdlho*$si6000") ! 41 !
("$xImed2-$rmdlho*$co7500", "$yImed2-$rmdlho*$si7500") ! 42 !
("$xImed2-$rmdlho*$co0900", "$yImed2-$rmdlho*$si0900") ! 43 !
("$xImed2+$rmdlho*$co7500", "$yImed2-$rmdlho*$si7500") ! 44 !
("$xImed2+$rmdlho*$co6000", "$yImed2-$rmdlho*$si6000") ! 45 !
("$xImed2+$rmdlho*$co4500", "$yImed2-$rmdlho*$si4500") ! 46 !
("$xImed2+$rmdlho*$co3000", "$yImed2-$rmdlho*$si3000") ! 47 !
("$xImed2+$rmdlho*$co1500", "$yImed2-$rmdlho*$si1500") ! 48 !
!----1-----2-----3-----4-----5-----6-----7-----!
/24,refl
/mdlhol("$xImed2", "$yImed2") !DSC GET ALL SEGMENTS!
/1,25,26,2, refl; ! Right !
2,26,27,3, refl;
3,27,28,4, refl;
4,28,29,5, refl;
5,29,30,6, refl;
6,30,31,7, refl;
7,31,32,8, refl;

8,32,33,9, refl; ! top !
9,33,34,10, refl;
10,34,35,11, refl;
11,35,36,12, refl;
12,36,37,13, refl;
13,37,38,14, refl;

14,38,39,15, refl; ! left !
15,39,40,16, refl;
16,40,41,17, refl;
17,41,42,18, refl;
18,42,43,19, refl;

19,43,44,20, refl; ! bottom !
20,44,45,21, refl;
21,45,46,22, refl;
22,46,47,23, refl;
23,47,48,24, refl;
24,48,25,1, refl
)
!----1-----2-----3-----4-----5-----6-----7-----!
!----1-----+---Be between MedL1 I-poly and N1 str frm ATR left+----7-----+----!
$BeMdNIL = PAR((" $xtki*$si2250", "$xtki*$si6750") !17=1 !
("$xtki/2*($si3375+$si2250)", "$xtki/2*($si5625+$si6750)") !16=2 !
("$xdrum3-$xdrum*$si5625", "$ydrum3+$xdrum*$si3375") !15=3 !
("$xdrum3-$xdrum*$si4500", "$ydrum3+$xdrum*$si4500") !14=4 !
("$xImed2+$medlpolyr*$co4500", "$yImed2-$medlpolyr*$si4500")!22=5 !
("$xImed2+$medlpolyr*$co6000", "$yImed2-$medlpolyr*$si6000")!21=6 !
("$xImed2+$medlpolyr*$co7500", "$yImed2-$medlpolyr*$si7500")!20=7 !
("$xImed2-$medlpolyr*$co0900", "$yImed2-$medlpolyr*$si0900")!19=8 !
("$xImed2-$medlpolyr*$co7500", "$yImed2-$medlpolyr*$si7500")!18=9 !
("$xImed2-$medlpolyr*$co6000", "$yImed2-$medlpolyr*$si6000")!17=10!
("$xImed2-$medlpolyr*$co4500", "$yImed2-$medlpolyr*$si4500")!16=11!
("$xImed2-$medlpolyr*$co3000", "$yImed2-$medlpolyr*$si3000")!15=12!
("$xImed2-$medlpolyr*$co1500", "$yImed2-$medlpolyr*$si1500")!14=13!
("$xImed2-$medlpolyr*$co3600", "$yImed2+$medlpolyr*$si3600")!13=14!
("$xImed2-$medlpolyr*$co1500", "$yImed2+$medlpolyr*$si1500")!12=15!
("$xImed2-$medlpolyr*$co3000", "$yImed2+$medlpolyr*$si3000")!11=16!
("$xImed2-$medlpolyr*$co4500", "$yImed2+$medlpolyr*$si4500")!10=17!
("-(3*(R0BeRNEx)+3*(SN4LU1x))/6", "(3*(R0BeRNEy)+3*(SN4LU1y))/6")!56=18!
!----1-----2-----3-----4-----5-----6-----7-----!
/17,refl/
/1,17,16,15,2, refl; ! top !
2,16,15,14,13,12,18, refl;
18,12,11,10,9,8,7,3, refl

```

13,6,5,4 refl!
)

!---+---1---+---2---+---3---+---4---+---5---+---6---+---7---+---!
!---+---1---+---2---+Nodes for N16 polygon--5---+---6---+---7---+---!
\$N16poly = PAR(("0" , "\$yN16c+\$N16poly") !top of poly! ! 1 !
("\$N16poly*\$co6000" , "\$yN16c+\$N16poly*\$si6000") ! 2 !
("\$N16poly*\$co3000" , "\$yN16c+\$N16poly*\$si3000") ! 3 !
! Left of polygon !
("\$N16poly" , "\$yN16c-\$N16poly*\$si3600") ! 4 !
("\$N16poly*\$co3000" , "\$yN16c-\$N16poly*\$si3000") ! 5 !
("\$N16poly*\$co6000" , "\$yN16c-\$N16poly*\$si6000") ! 6 !
! bottom of polygon !
(("0" , "\$yN16c-\$N16poly") ! 7 !
("\$N16poly*\$co6000" , "\$yN16c-\$N16poly*\$si6000") ! 8 !
("\$N16poly*\$co3000" , "\$yN16c-\$N16poly*\$si3000") ! 9 !
! right of polygon !
("\$N16poly" , "\$yN16c+\$N16poly*\$si3600") ! 10 !
("\$N16poly*\$co3000" , "\$yN16c+\$N16poly*\$si3000") ! 11 !
("\$N16poly*\$co6000" , "\$yN16c+\$N16poly*\$si6000") ! 12 !
!---+---1---+---2---+---node for the N16 CCS---+---6---+---7---+---!
(("0" , "\$yN16c+\$rN16o") ! 13 !
("\$rN16o*\$co6000" , "\$yN16c+\$rN16o*\$si6000") ! 14 !
("\$rN16o*\$co3000" , "\$yN16c+\$rN16o*\$si3000") ! 15 !
! Left of polygon !
("\$rN16o" , "\$yN16c-\$rN16o*\$si3600") ! 16 !
("\$rN16o*\$co3000" , "\$yN16c-\$rN16o*\$si3000") ! 17 !
("\$rN16o*\$co6000" , "\$yN16c-\$rN16o*\$si6000") ! 18 !
! bottom of polygon !
(("0" , "\$yN16c-\$rN16o") ! 19 !
("\$rN16o*\$co6000" , "\$yN16c-\$rN16o*\$si6000") ! 20 !
("\$rN16o*\$co3000" , "\$yN16c-\$rN16o*\$si3000") ! 21 !
! right of polygon !
("\$rN16o" , "\$yN16c+\$rN16o*\$si3600") ! 22 !
("\$rN16o*\$co3000" , "\$yN16c+\$rN16o*\$si3000") ! 23 !
("\$rN16o*\$co6000" , "\$yN16c+\$rN16o*\$si6000") ! 24 !

/12,refl
/N16cir(0,\$yN16c)
!DSC GET ALL SEGMENTS!

!---+---1---+---2---+---3---+---4---+---5---+---6---+---7---+---!
/1,13,14,2, refl; ! top !
2,14,15,3, refl;
3,15,16,4, refl;
4,16,17,5, refl;
5,17,18,6, refl;
6,18,19,7, refl;
7,19,20,8, refl;
8,20,21,9, refl;
9,21,22,10, refl;
10,22,23,11, refl;
11,23,24,12, refl
)

!---+---1---+---Be between large I-pos and med I-pos on right---+---7---+---!
\$BeLgMdR = PAR((0 , \$xtki) ! 1 !
(("\$RoBeRU1x" , "\$RoBeRU1y") ! 2 !
("\$xtki*\$si1125" , "\$xtki*\$si7875") ! 3 !
("\$xImed1+\$medIpolyr*\$co7500" , "\$yImed1+\$medIpolyr*\$si7500") ! 4 !
("\$xImed1+\$medIpolyr*\$co0900" , "\$yImed1+\$medIpolyr*\$si0900") ! 5 !
("\$xImed1-\$medIpolyr*\$co7500" , "\$yImed1+\$medIpolyr*\$si7500") ! 6 !
("\$xImed1-\$medIpolyr*\$co6000" , "\$yImed1+\$medIpolyr*\$si6000") ! 7 !
("\$xImed1-\$medIpolyr*\$co4500" , "\$yImed1+\$medIpolyr*\$si4500") ! 8 !
("\$xImed1-\$medIpolyr*\$co3000" , "\$yImed1+\$medIpolyr*\$si3000") ! 9 !
("\$xImed1-\$medIpolyr*\$co1500" , "\$yImed1+\$medIpolyr*\$si1500") ! 10 !
("\$xImed1-\$medIpolyr*\$co3600" , "\$yImed1+\$medIpolyr*\$si3600") ! 11 !
("\$xImed1-\$medIpolyr*\$co1500" , "\$yImed1-\$medIpolyr*\$si1500") ! 12 !
("\$xImed1-\$medIpolyr*\$co3000" , "\$yImed1-\$medIpolyr*\$si3000") ! 13 !
("\$xImed1-\$medIpolyr*\$co4500" , "\$yImed1-\$medIpolyr*\$si4500") ! 14 !

```

("$Xlmed1-$medIpolyr*$co6000", "$Ylmed1-$medIpolyr*$si6000")! 15 !
("$Xlmed1-$medIpolyr*$co7500", "$Ylmed1-$medIpolyr*$si7500")! 16 !
("$Xlmed1-$medIpolyr*$co0900", "$Ylmed1-$medIpolyr*$si0900")! 17 !
("$xdrum3+$xdrum*$si1125", "$ydrum3+$xdrum*$si7875") ! 18 !
( "$xdrum3", "$ydrum3+$xdrum" ) ! 19 !
("$xdrum3-$xdrum*$si1125", "$ydrum3+$xdrum*$si7875") ! 20 !
("$xdrum3-$xdrum*$si2250", "$ydrum3+$xdrum*$si6750") ! 21 !
("$xdrum3-$xdrum*$si3375", "$ydrum3+$xdrum*$si5625") ! 22 !
("$xdrum3-$xdrum*$si4500", "$ydrum3+$xdrum*$si4500") ! 23 !
("$xdrum3-$xdrum*$si5625", "$ydrum3+$xdrum*$si3375") ! 24 !
("$xdrum3-$xdrum*$si6750", "$ydrum3+$xdrum*$si2250") ! 25 !
("$xdrum3-$xdrum*$si7875", "$ydrum3+$xdrum*$si1125") ! 26 !
( "$xdrum3-$xdrum", "$ydrum3" ) ! 27 !
( 0 , $ydrum3 ) ! 28 !
( 0 , "$ydrum3+$xdrum*$si1125" ) ! 29 !
( "0" , "$yN16c-$N16polyr" ) ! 30 !
("$N16polyr*$co6000" , "$yN16c-$N16polyr*$si6000") ! 31 !
("$N16polyr*$co3000" , "$yN16c-$N16polyr*$si3000") ! 32 !
("$N16polyr" , "$yN16c+$N16polyr*$si3600") ! 33 !

("$N16polyr*$co3000" , "$yN16c+$N16polyr*$si3000") ! 34 !
("$N16polyr*$co6000" , "$yN16c+$N16polyr*$si6000") ! 35 !
( "0" , "$yN16c+$N16polyr" ) ! top of N16 poly! ! 36 !
! Node 36 is the bottom of Large I poly !
("$lrgIplyr*$co0900" , "$yIlar-$lrgIplyr*$si0900") ! 37 !
("$lrgIplyr*$co7500" , "$yIlar-$lrgIplyr*$si7500") ! 38 !
("$lrgIplyr*$co6000" , "$yIlar-$lrgIplyr*$si6000") ! 39 !
("$lrgIplyr*$co4500" , "$yIlar-$lrgIplyr*$si4500") ! 40 !
("$lrgIplyr*$co3000" , "$yIlar-$lrgIplyr*$si3000") ! 41 !
("$lrgIplyr*$co1500" , "$yIlar-$lrgIplyr*$si1500") ! 42 !
($lrgIplyr , "$yIlar") ! 43 !
("$lrgIplyr*$co1500" , "$yIlar+$lrgIplyr*$si1500") ! 44 !
("$lrgIplyr*$co3000" , "$yIlar+$lrgIplyr*$si3000") ! 45 !
("$lrgIplyr*$co4500" , "$yIlar+$lrgIplyr*$si4500") ! 46 !
("$lrgIplyr*$co6000" , "$yIlar+$lrgIplyr*$si6000") ! 47 !
("$lrgIplyr*$co7500" , "$yIlar+$lrgIplyr*$si7500") ! 48 !
("$lrgIplyr*$co0900" , "$yIlar+$lrgIplyr*$si0900") ! 49 !
(" (5*($RoBeRU1x)+1*($RoBeRD1x))/6", " (5*($RoBeRU1y)+1*($RoBeRD1y))/6" ) ! 50 !
(" (2.7*($RoBeRU1x)+3.3*($RoBeRD1x))/6",
" (2.7*($RoBeRU1y)+3.3*($RoBeRD1y))/6" ) ! 51 !
(" (1*($RoBeRU1x)+5*($RoBeRD1x))/6", " (1*($RoBeRU1y)+5*($RoBeRD1y))/6" ) ! 52 !
( "$RoBeRD1x", "$RoBeRD1y" ) ! 53 !
!---+---1---+---2---+---3---+---4---+---5---+---6---+---7---+---!
/49.refl/
/1,2,50,46,47,48,49, refl;
2,3,4,5,6,7,50, refl;
7,8,9,10,11,51,50, refl;
51,11,12,13,14,52, refl;
52,14,15,16,53, refl;
53,16,17,18,19,20,21, refl;
22,39,40,21, refl;
21,40,41,42,52,53, refl;
52,42,43,44,51, refl;
51,44,45,46,50, refl;
24,33,34,35,36,37,23, refl;
23,37,38,39,22, refl;
24,33,34,35,36,37,23, refl;
25,30,31,32,33,24, refl;
26,29,30,25, refl
)

```

!---+---DSC Medium I polygon left side Med I-CCS in polygon----+---7----+---!

```

$MedIpolyR1 = PAR(
("$Xlmed1+$medIpolyr*$co3600", "$Ylmed1+$medIpolyr*$si3600")! 1 !
("$Xlmed1+$medIpolyr*$co1500", "$Ylmed1+$medIpolyr*$si1500")! 2 !
("$Xlmed1+$medIpolyr*$co3000", "$Ylmed1+$medIpolyr*$si3000")! 3 !
("$Xlmed1+$medIpolyr*$co4500", "$Ylmed1+$medIpolyr*$si4500")! 4 !
("$Xlmed1+$medIpolyr*$co6000", "$Ylmed1+$medIpolyr*$si6000")! 5 !
("$Xlmed1+$medIpolyr*$co7500", "$Ylmed1+$medIpolyr*$si7500")! 6 !

```

```

("$xImed1+$medIpolyr*$co0900", "$yImed1+$medIpolyr*$si0900")! 7 !
("$xImed1-$medIpolyr*$co7500", "$yImed1+$medIpolyr*$si7500")! 8 !
("$xImed1-$medIpolyr*$co6000", "$yImed1+$medIpolyr*$si6000")! 9 !
("$xImed1-$medIpolyr*$co4500", "$yImed1+$medIpolyr*$si4500")! 10 !
("$xImed1-$medIpolyr*$co3000", "$yImed1+$medIpolyr*$si3000")! 11 !
("$xImed1-$medIpolyr*$co1500", "$yImed1+$medIpolyr*$si1500")! 12 !
("$xImed1-$medIpolyr*$co3600", "$yImed1+$medIpolyr*$si3600")! 13 !
("$xImed1-$medIpolyr*$co1500", "$yImed1-$medIpolyr*$si1500")! 14 !
("$xImed1-$medIpolyr*$co3000", "$yImed1-$medIpolyr*$si3000")! 15 !
("$xImed1-$medIpolyr*$co4500", "$yImed1-$medIpolyr*$si4500")! 16 !
("$xImed1-$medIpolyr*$co6000", "$yImed1-$medIpolyr*$si6000")! 17 !
("$xImed1-$medIpolyr*$co7500", "$yImed1-$medIpolyr*$si7500")! 18 !
("$xImed1-$medIpolyr*$co0900", "$yImed1-$medIpolyr*$si0900")! 19 !
("$xImed1+$medIpolyr*$co7500", "$yImed1-$medIpolyr*$si7500")! 20 !
("$xImed1+$medIpolyr*$co6000", "$yImed1-$medIpolyr*$si6000")! 21 !
("$xImed1+$medIpolyr*$co4500", "$yImed1-$medIpolyr*$si4500")! 22 !
("$xImed1+$medIpolyr*$co3000", "$yImed1-$medIpolyr*$si3000")! 23 !
("$xImed1+$medIpolyr*$co1500", "$yImed1-$medIpolyr*$si1500")! 24 !
!-----1-----2-----node for the Medium I-CCS-----6-----7-----!
("$xImed1+$rmdlho*$co3600", "$yImed1+$rmdlho*$si3600") ! 25 !
("$xImed1+$rmdlho*$co1500", "$yImed1+$rmdlho*$si1500") ! 26 !
("$xImed1+$rmdlho*$co3000", "$yImed1+$rmdlho*$si3000") ! 27 !
("$xImed1+$rmdlho*$co4500", "$yImed1+$rmdlho*$si4500") ! 28 !
("$xImed1+$rmdlho*$co6000", "$yImed1+$rmdlho*$si6000") ! 29 !
("$xImed1+$rmdlho*$co7500", "$yImed1+$rmdlho*$si7500") ! 30 !
("$xImed1+$rmdlho*$co0900", "$yImed1+$rmdlho*$si0900") ! 31 !
("$xImed1-$rmdlho*$co7500", "$yImed1+$rmdlho*$si7500") ! 32 !
("$xImed1-$rmdlho*$co6000", "$yImed1+$rmdlho*$si6000") ! 33 !
("$xImed1-$rmdlho*$co4500", "$yImed1+$rmdlho*$si4500") ! 34 !
("$xImed1-$rmdlho*$co3000", "$yImed1+$rmdlho*$si3000") ! 35 !
("$xImed1-$rmdlho*$co1500", "$yImed1+$rmdlho*$si1500") ! 36 !
("$xImed1-$rmdlho*$co3600", "$yImed1+$rmdlho*$si3600") ! 37 !
("$xImed1-$rmdlho*$co1500", "$yImed1-$rmdlho*$si1500") ! 38 !
("$xImed1-$rmdlho*$co3000", "$yImed1-$rmdlho*$si3000") ! 39 !
("$xImed1-$rmdlho*$co4500", "$yImed1-$rmdlho*$si4500") ! 40 !
("$xImed1-$rmdlho*$co6000", "$yImed1-$rmdlho*$si6000") ! 41 !
("$xImed1-$rmdlho*$co7500", "$yImed1-$rmdlho*$si7500") ! 42 !
("$xImed1-$rmdlho*$co0900", "$yImed1-$rmdlho*$si0900") ! 43 !
("$xImed1+$rmdlho*$co7500", "$yImed1-$rmdlho*$si7500") ! 44 !
("$xImed1+$rmdlho*$co6000", "$yImed1-$rmdlho*$si6000") ! 45 !
("$xImed1+$rmdlho*$co4500", "$yImed1-$rmdlho*$si4500") ! 46 !
("$xImed1+$rmdlho*$co3000", "$yImed1-$rmdlho*$si3000") ! 47 !
("$xImed1+$rmdlho*$co1500", "$yImed1-$rmdlho*$si1500") ! 48 !
!-----1-----2-----3-----4-----5-----6-----7-----!
/24.refl
/mdlhol("$xImed1", "$yImed1") !DSC GET ALL SEGMENTS!
/1,25,26,2, refl; ! Right !
2,26,27,3, refl;
3,27,28,4, refl;
4,28,29,5, refl;
5,29,30,6, refl;
6,30,31,7, refl;
7,31,32,8, refl;

8,32,33,9, refl; ! top !
9,33,34,10, refl;
10,34,35,11, refl;
11,35,36,12, refl;
12,36,37,13, refl;
13,37,38,14, refl;

14,38,39,15, refl; ! left !
15,39,40,16, refl;
16,40,41,17, refl;
17,41,42,18, refl;
18,42,43,19, refl;

19,43,44,20, refl; ! bottom !
20,44,45,21, refl;
21,45,46,22, refl;

```

22,46,47,23, refl;
 23,47,48,24, refl;
 24,48,25,1, refl
)

!---+----1----+--Be between MedL1 I-poly and medL2 I-pos on left+----7----+----!
 \$BeMdMdr = PAR(("\$xtki*\$ssi1125", "\$xtki*\$ssi7875") ! 1!
 ("\$RoBeRU2x", "\$RoBeRU2y") ! 2!
 ("\$xtki*\$ssi2250", "\$xtki*\$ssi6750") ! 3!
 ("\$xImed2+\$medIpolyr*\$co4500", "\$yImed2+\$medIpolyr*\$ssi4500")! 4!
 ("\$xImed2+\$medIpolyr*\$co6000", "\$yImed2+\$medIpolyr*\$ssi6000")! 5!
 ("\$xImed2+\$medIpolyr*\$co7500", "\$yImed2+\$medIpolyr*\$ssi7500")! 6!
 ("\$xImed2+\$medIpolyr*\$co9000", "\$yImed2+\$medIpolyr*\$ssi9000")! 7!
 ("\$xImed2-\$medIpolyr*\$co7500", "\$yImed2+\$medIpolyr*\$ssi7500")! 8!
 ("\$xImed2-\$medIpolyr*\$co6000", "\$yImed2+\$medIpolyr*\$ssi6000")! 9!
 ("\$xImed2-\$medIpolyr*\$co4500", "\$yImed2+\$medIpolyr*\$ssi4500")! 10!
 ("\$xImed2-\$medIpolyr*\$co3000", "\$yImed2+\$medIpolyr*\$ssi3000")! 11!
 ("\$xImed2-\$medIpolyr*\$co1500", "\$yImed2+\$medIpolyr*\$ssi1500")! 12!
 ("\$xImed2-\$medIpolyr*\$co3600", "\$yImed2+\$medIpolyr*\$ssi3600")! 13!
 ("\$xImed2-\$medIpolyr*\$co1500", "\$yImed2-\$medIpolyr*\$ssi1500")! 14!
 ("\$xImed2-\$medIpolyr*\$co3000", "\$yImed2-\$medIpolyr*\$ssi3000")! 15!
 ("\$xImed2-\$medIpolyr*\$co4500", "\$yImed2-\$medIpolyr*\$ssi4500")! 16!
 ("\$xdrum3+\$xdrum*\$ssi4500", "\$ydrum3+\$xdrum*\$ssi4500") ! 17!
 ("\$xdrum3+\$xdrum*\$ssi3375", "\$ydrum3+\$xdrum*\$ssi5625") ! 18!
 ("\$xdrum3+\$xdrum*\$ssi2250", "\$ydrum3+\$xdrum*\$ssi6750") ! 19!
 ("\$xdrum3+\$xdrum*\$ssi1125", "\$ydrum3+\$xdrum*\$ssi7875") ! 20!
 ("\$xImed1-\$medIpolyr*\$co0900", "\$yImed1-\$medIpolyr*\$ssi0900")! 21!
 ("\$xImed1+\$medIpolyr*\$co7500", "\$yImed1-\$medIpolyr*\$ssi7500")! 20!
 ("\$xImed1+\$medIpolyr*\$co6000", "\$yImed1-\$medIpolyr*\$ssi6000")! 21!
 ("\$xImed1+\$medIpolyr*\$co4500", "\$yImed1-\$medIpolyr*\$ssi4500")! 22!
 ("\$xImed1+\$medIpolyr*\$co3000", "\$yImed1-\$medIpolyr*\$ssi3000")! 23!
 ("\$xImed1+\$medIpolyr*\$co1500", "\$yImed1-\$medIpolyr*\$ssi1500")! 24!
 ("\$xImed1+\$medIpolyr*\$co3600", "\$yImed1+\$medIpolyr*\$ssi3600")! 27!
 ("\$xImed1+\$medIpolyr*\$co1500", "\$yImed1+\$medIpolyr*\$ssi1500")! 28!
 ("\$xImed1+\$medIpolyr*\$co3000", "\$yImed1+\$medIpolyr*\$ssi3000")! 29!
 ("\$xImed1+\$medIpolyr*\$co4500", "\$yImed1+\$medIpolyr*\$ssi4500")! 30!
 ("\$xImed1+\$medIpolyr*\$co6000", "\$yImed1+\$medIpolyr*\$ssi6000")! 31!
 ("\$xImed1+\$medIpolyr*\$co7500", "\$yImed1+\$medIpolyr*\$ssi7500")! 32!
 ! begin the interior nodes !
 (" (5*(\$RoBeRU2x)+1*(\$RoBeRD2x))/6", "(5*(\$RoBeRU2y)+1*(\$RoBeRD2y))/6") ! 33!
 (" (2.8*(\$RoBeRU2x)+3.2*(\$RoBeRD2x))/6",
 "(2.8*(\$RoBeRU2y)+3.2*(\$RoBeRD2y))/6") ! 34!
 ("\$RoBeRD2x", "\$RoBeRD2y") ! 35!
)

!---+----1----+----2----+----3----+----4----+----5----+----6----+----7----+----!
 /32.refl/
 /1,2,33,29,30,31,32, refl; ! top !
 2,3,4,5,6,7,8,33, refl;
 33,8,9,10,11,34, refl;
 34,11,12,13,14,15,16,35, refl;
 35,16,17,18,19, refl;
 19,20,21,35, refl;
 35,21,22,23,24,25,26,34, refl
)

!---+----1----+----2----+----3----+----4----+----5----+----6----+----7----+----!
 !---+Medium I polygon left side in position 2 left of med I-poly 1=\$MedIpolyL1-!
 \$MedIpolyR2 = PAR(
 ("\$xImed2+\$medIpolyr*\$co3600", "\$yImed2+\$medIpolyr*\$ssi3600")! 1!
 ("\$xImed2+\$medIpolyr*\$co1500", "\$yImed2+\$medIpolyr*\$ssi1500")! 2!
 ("\$xImed2+\$medIpolyr*\$co3000", "\$yImed2+\$medIpolyr*\$ssi3000")! 3!
 ("\$xImed2+\$medIpolyr*\$co4500", "\$yImed2+\$medIpolyr*\$ssi4500")! 4!
 ("\$xImed2+\$medIpolyr*\$co6000", "\$yImed2+\$medIpolyr*\$ssi6000")! 5!
 ("\$xImed2+\$medIpolyr*\$co7500", "\$yImed2+\$medIpolyr*\$ssi7500")! 6!
 ("\$xImed2+\$medIpolyr*\$co9000", "\$yImed2+\$medIpolyr*\$ssi9000")! 7!
 ("\$xImed2-\$medIpolyr*\$co7500", "\$yImed2+\$medIpolyr*\$ssi7500")! 8!
 ("\$xImed2-\$medIpolyr*\$co6000", "\$yImed2+\$medIpolyr*\$ssi6000")! 9!
 ("\$xImed2-\$medIpolyr*\$co4500", "\$yImed2+\$medIpolyr*\$ssi4500")! 10!
 ("\$xImed2-\$medIpolyr*\$co3000", "\$yImed2+\$medIpolyr*\$ssi3000")! 11!
 ("\$xImed2-\$medIpolyr*\$co1500", "\$yImed2+\$medIpolyr*\$ssi1500")! 12!
 ("\$xImed2-\$medIpolyr*\$co3600", "\$yImed2+\$medIpolyr*\$ssi3600")! 13!
)

```

("$xImed2-$medIpolyr*$co1500", "$yImed2-$medIpolyr*$si1500")! 14 !
("$xImed2-$medIpolyr*$co3000", "$yImed2-$medIpolyr*$si3000")! 15 !
("$xImed2-$medIpolyr*$co4500", "$yImed2-$medIpolyr*$si4500")! 16 !
("$xImed2-$medIpolyr*$co6000", "$yImed2-$medIpolyr*$si6000")! 17 !
("$xImed2-$medIpolyr*$co7500", "$yImed2-$medIpolyr*$si7500")! 18 !
("$xImed2-$medIpolyr*$co0900", "$yImed2-$medIpolyr*$si0900")! 19 !
("$xImed2+$medIpolyr*$co7500", "$yImed2-$medIpolyr*$si7500")! 20 !
("$xImed2+$medIpolyr*$co6000", "$yImed2-$medIpolyr*$si6000")! 21 !
("$xImed2+$medIpolyr*$co4500", "$yImed2-$medIpolyr*$si4500")! 22 !
("$xImed2+$medIpolyr*$co3000", "$yImed2-$medIpolyr*$si3000")! 23 !
("$xImed2+$medIpolyr*$co1500", "$yImed2-$medIpolyr*$si1500")! 24 !
!----1----2----3----4----5----6----7----8----!
("$xImed2+$rmdlho*$co3600", "$yImed2+$rmdlho*$si3600") ! 25 !
("$xImed2+$rmdlho*$co1500", "$yImed2+$rmdlho*$si1500") ! 26 !
("$xImed2+$rmdlho*$co3000", "$yImed2+$rmdlho*$si3000") ! 27 !
("$xImed2+$rmdlho*$co4500", "$yImed2+$rmdlho*$si4500") ! 28 !
("$xImed2+$rmdlho*$co6000", "$yImed2+$rmdlho*$si6000") ! 29 !
("$xImed2+$rmdlho*$co7500", "$yImed2+$rmdlho*$si7500") ! 30 !
("$xImed2+$rmdlho*$co0900", "$yImed2+$rmdlho*$si0900") ! 31 !
("$xImed2-$rmdlho*$co7500", "$yImed2-$rmdlho*$si7500") ! 32 !
("$xImed2-$rmdlho*$co6000", "$yImed2-$rmdlho*$si6000") ! 33 !
("$xImed2-$rmdlho*$co4500", "$yImed2-$rmdlho*$si4500") ! 34 !
("$xImed2-$rmdlho*$co3000", "$yImed2-$rmdlho*$si3000") ! 35 !
("$xImed2-$rmdlho*$co1500", "$yImed2-$rmdlho*$si1500") ! 36 !
("$xImed2-$rmdlho*$co3600", "$yImed2-$rmdlho*$si3600") ! 37 !
("$xImed2-$rmdlho*$co1500", "$yImed2-$rmdlho*$si1500") ! 38 !
("$xImed2-$rmdlho*$co3000", "$yImed2-$rmdlho*$si3000") ! 39 !
("$xImed2-$rmdlho*$co4500", "$yImed2-$rmdlho*$si4500") ! 40 !
("$xImed2-$rmdlho*$co6000", "$yImed2-$rmdlho*$si6000") ! 41 !
("$xImed2-$rmdlho*$co7500", "$yImed2-$rmdlho*$si7500") ! 42 !
("$xImed2-$rmdlho*$co0900", "$yImed2-$rmdlho*$si0900") ! 43 !
("$xImed2+$rmdlho*$co7500", "$yImed2-$rmdlho*$si7500") ! 44 !
("$xImed2+$rmdlho*$co6000", "$yImed2-$rmdlho*$si6000") ! 45 !
("$xImed2+$rmdlho*$co4500", "$yImed2-$rmdlho*$si4500") ! 46 !
("$xImed2+$rmdlho*$co3000", "$yImed2-$rmdlho*$si3000") ! 47 !
("$xImed2+$rmdlho*$co1500", "$yImed2-$rmdlho*$si1500") ! 48 !
!----1----2----3----4----5----6----7----8----!
/24.refl
/mdlhol("$xImed2", "$yImed2") !DSC GET ALL SEGMENTS!
/1,25,26,2, refl; ! Right !
2,26,27,3, refl;
3,27,28,4, refl;
4,28,29,5, refl;
5,29,30,6, refl;
6,30,31,7, refl;
7,31,32,8, refl;

8,32,33,9, refl; ! top !
9,33,34,10, refl;
10,34,35,11, refl;
11,35,36,12, refl;
12,36,37,13, refl;
13,37,38,14, refl;

14,38,39,15, refl; ! left !
15,39,40,16, refl;
16,40,41,17, refl;
17,41,42,18, refl;
18,42,43,19, refl;

19,43,44,20, refl; ! bottom !
20,44,45,21, refl;
21,45,46,22, refl;
22,46,47,23, refl;
23,47,48,24, refl;
24,48,25,1, refl
)
!----1----2----3----4----5----6----7----8----!
!----1----2----3----4----5----6----7----8----!
$BeMdN1R = PAR(

```

```

("$xtki*$si2250", "$xtki*$si6750")          ! 1 !
("$xtki/2*($si3375+$si2250)", "$xtki/2*($si5625+$si6750)") ! 2 !
("$xdrum3+$xdrum*$si5625", "$ydrum3+$xdrum*$si3375") ! 3 !
("$xdrum3+$xdrum*$si4500", "$ydrum3+$xdrum*$si4500") ! 4 !
("$xImed2-$medIpolyr*$co4500", "$yImed2-$medIpolyr*$si4500") ! 5 !
("$xImed2-$medIpolyr*$co6000", "$yImed2-$medIpolyr*$si6000") ! 6 !
("$xImed2-$medIpolyr*$co7500", "$yImed2-$medIpolyr*$si7500") ! 7 !
("$xImed2-$medIpolyr*$co9000", "$yImed2-$medIpolyr*$si9000") ! 8 !
("$xImed2+$medIpolyr*$co7500", "$yImed2-$medIpolyr*$si7500") ! 9 !
("$xImed2+$medIpolyr*$co6000", "$yImed2-$medIpolyr*$si6000") ! 10 !
("$xImed2+$medIpolyr*$co4500", "$yImed2-$medIpolyr*$si4500") ! 11 !
("$xImed2+$medIpolyr*$co3000", "$yImed2-$medIpolyr*$si3000") ! 12 !
("$xImed2+$medIpolyr*$co1500", "$yImed2-$medIpolyr*$si1500") ! 13 !
("$xImed2+$medIpolyr*$co3600", "$yImed2+$medIpolyr*$si3600") ! 14 !
("$xImed2+$medIpolyr*$co1500", "$yImed2+$medIpolyr*$si1500") ! 15 !
("$xImed2+$medIpolyr*$co3000", "$yImed2+$medIpolyr*$si3000") ! 16 !
("$xImed2+$medIpolyr*$co4500", "$yImed2+$medIpolyr*$si4500") ! 17 !
("(3*($RoBeRNEx)+3*(N4LU1x))/6", "(3*($RoBeRNEy)+3*(N4LU1y))/6") ! 18 !
!-----1-----2-----3-----4-----5-----6-----7-----!
/17,refl/
/1,2,16,17,          refl; ! top      !
2,16,15,14,13,12,18,      refl;
18,12,11,10,9,8,7,3,      refl
13,6,5,4          refl!
)
!-----1-----2-----3-----4-----5-----6-----7-----!
!-----system connection and structures-----!
Sk = PAR(4)          ! angle # of interface currents !
white = ALB(1/1/1)
LrgIpoly = STR($LrgIpoly) ! Be reflector around Large I-pos. !
BeLgMdL = STR($BeLgMdL)
MedIpolyL1 = STR($MedIpolyL1)
BeMdMdL = STR($BeMdMdL)
MedIpolyL2 = STR($MedIpolyL2)
BeMdN1L = STR($BeMdN1L)
N16poly = STR($N16poly)
BeLgMdR = STR($BeLgMdR)
MedIpolyR1 = STR($MedIpolyR1)
BeMdMdR = STR($BeMdMdR)
MedIpolyR2 = STR($MedIpolyR2)
BeMdN1R = STR($BeMdN1R)
!-----1-----2-----3-----4-----5-----6-----7-----!
system = CNX( LrgIpoly,BeLgMdL,MedIpolyL1,BeMdMdL,MedIpolyL2,BeMdN1L,N16poly,
BeLgMdR,MedIpolyR1,BeMdMdR,MedIpolyR2,BeMdN1R/
! 1,2,3,4,5,6,7,
8,9,10,11,12 !
( 1, 7,19)$k( 2, 51, 39)/! LrgIpoly to BeLgMdL !
(2,6,18)$k(3,7,19)/ ! BeLgMdL to MedIpolyL1 !
(2,3,20)$k(4,1,20)/ ! BeLgMdL to BeMdMdL !
(4,4,16)$k(5,4,16)/ ! BeMdMdL to MedIpolyL2 !
(4,3,17)$k(6,1,4)/ ! BeMdMdL to BeMdN1L !
(2,38,32)$k(7,1,7)/ ! N16 to BeLgMdL !
(2,1,30)$k(8,1,28)/ ! BeLgMdL to BeLgMdR !
(8,5,17)$k(9,7,19)/ ! BeLgMdR to MedIpolyR2 !
(8,3,18)$k(10,1,20)/ ! BeLgMdR to BeMdMdR !
(10,4,16)$k(11,4,16)/ ! BeMdMdR to MedIpolyR2 !
(10,3,17)$k(12,1,4) ! BeMdMdR to BeMdN1R !
)
system = BDRY((2,1,1)$k(white)) ! from node 1 to node 1 on BeLgMdL struct!

!-----must have in the input file to work in helios/aurora-----!

! ?rename? all of the OVXX's fixed !
ovd = OVLD( 1 /*_**)
ovt = OVLT(310.93/*_**)          ! = 100 Fahrenheit !

ovm = OVLM( alustr/*_**!/
coo/*-0-cool,*-*(shco,rgco,acoo,bcoo)!/
!Hf/*_*-shab!/

```

```
Be/*-0-refl!  
BeWskt/*-0-refl!  
osm = OVSM(ovm)  
osd = OVSD(ovd)  
ost = OVST(ovt)  
  
st = STAT(osm,osd,ost)  
pa = PATH(/P,(st))  
!-----!  
!----- edit data -----!  
  
all = AREA(<*.***>)  
case = RUN() ! Leakage !
```

APPENDIX B - METHOD FOR LEAST-SQUARES ADJUSTMENT OF NEUTRON SPECTRA USING ACTIVATION DATA

David W. Nigg (INL) and Yale D. Harker (INL)

The volume-average neutron activation rate per atom for a foil or wire dosimeter placed in a neutron flux field may be calculated as:

$$R = \int_0^{\infty} \sigma_f(E) \Psi_f(E) dE \quad (1)$$

where $\sigma_f(E)$ is the microscopic activation cross section of interest for the foil or wire material, as a function of neutron energy and $\Psi_f(E)$ is the volume-average scalar neutron flux within the foil or wire, again as a function of energy. Equation (1) can also be expressed as:

$$R = \int_0^{\infty} \sigma_f(E) \left(\frac{\Psi_f(E)}{\Psi(E)} \right) \Psi(E) dE = \int_0^{\infty} \sigma_f(E) P_f(E) \Psi(E) dE \quad (2)$$

where $\Psi(E)$ is the unperturbed neutron flux that would exist at the measurement location in the absence of the foil. Equation (2) may also be expressed in standard multigroup form as:

$$R = \sum_{j=1}^{NG} a_j \phi_j \quad (3)$$

where NG is the total number of groups,

$$a_j = \frac{\int_{EL_j}^{EH_j} \sigma_f(E) P_f(E) \Psi(E) dE}{\int_{EL_j}^{EH_j} \Psi(E) dE} \quad (4)$$

and

$$\phi_j = \int_{EL_j}^{EH_j} \Psi(E) dE. \quad (5)$$

If additional dosimeters are placed in the beam, or if a particular foil or wire exhibits more than one activation response, then Equation (3) may be written as a system of equations:

$$R_i = \sum_{j=1}^{NG} a_{ij} \phi_j \quad (6)$$

where R_i is the total activation rate for interaction i and a_{ij} is the activation constant from Equation (4) for reaction i due to neutrons in energy group j .

There will be a total of NF equations, where NF is the total number of activation responses available. The activation constants a_{ij} may be obtained using any standard computational method that yields a valid *a-priori* estimate for the perturbed and unperturbed neutron spectrum at the measurement location within each energy group for the given foil or wire geometry and composition.

The system of activation equations, Equation (6), may be written out in matrix form as:

$$\begin{bmatrix} a_{11} & a_{12} & a_{13} & \cdots & a_{1NG} \\ a_{21} & a_{22} & a_{23} & \cdots & a_{2NG} \\ a_{31} & a_{32} & a_{33} & \cdots & a_{3NG} \\ \vdots & \vdots & \vdots & & \vdots \\ \vdots & \vdots & \vdots & & \vdots \\ a_{NF1} & a_{NF2} & a_{NF3} & \cdots & a_{NFNG} \end{bmatrix} \begin{bmatrix} \phi_1 \\ \phi_2 \\ \phi_3 \\ \vdots \\ \phi_{NG} \end{bmatrix} = \begin{bmatrix} R_1 \\ R_2 \\ R_3 \\ \vdots \\ R_{NF} \end{bmatrix} \quad (7)$$

or, more compactly:

$$[A][\Phi] = [R]. \quad (8)$$

Equation (7) is exact, provided that the reaction rates R_i , the activation constants a_{ij} and the group fluxes, ϕ_j all correspond to the same self-consistent *a-priori* model. If measured reaction rates for each interaction R_i are substituted into Equation (7), a solution of the resulting new system of equations for adjusted fluxes corresponding to the measured reaction rates may also be obtained under certain conditions.

In particular, if $NF = NG$, then the matrix $[A]$ is square, its inverse will ordinarily exist, and the unknown adjusted flux vector may be obtained by any standard solution method that converges, provided that the rows of $[A]$ are linearly-independent. In physical terms this implies that the response functions (cross sections) for the activation interactions used in the measurement must be selected such that they have different shapes as functions of energy. It may be noted that positive fluxes are not guaranteed to result from this procedure, but if the elements of $[A]$ are computed in a sufficiently valid, physically-realistic manner for the specific measurement configuration, and if the measured reaction rates are accurately determined, a positive solution can generally be obtained.

There are two possibilities for the situation where NF , the number of available activation response functions, is not equal to NG , the number of energy groups for which it is desired to obtain adjusted fluxes. If $NF < NG$ the problem is underdetermined and additional information must be introduced in some manner to permit a solution. If $NF > NG$ the problem is overdetermined and the “extra” information that is thereby available can be incorporated into the solution for the adjusted group fluxes by a linear least-squares fitting procedure as follows:

$$\begin{aligned}
2 \sum_{i=1}^{NF} -(R_i - (a_{i1} \phi_1 + a_{i2} \phi_2 \cdots + a_{iNG} \phi_{NG})) a_{i1} &= 0 \\
2 \sum_{i=1}^{NF} -(R_i - (a_{i1} \phi_1 + a_{i2} \phi_2 \cdots + a_{iNG} \phi_{NG})) a_{i2} &= 0 \\
&\vdots \\
2 \sum_{i=1}^{NF} -(R_i - (a_{i1} \phi_1 + a_{i2} \phi_2 \cdots + a_{iNG} \phi_{NG})) a_{iNG} &= 0
\end{aligned} \tag{13}$$

or, upon rearrangement:

$$\begin{aligned}
\sum_{i=1}^{NF} (a_{i1} \phi_1 + a_{i2} \phi_2 \cdots + a_{iNG} \phi_{NG}) a_{i1} &= \sum_{i=1}^{NF} a_{i1} R_i \\
\sum_{i=1}^{NF} (a_{i1} \phi_1 + a_{i2} \phi_2 \cdots + a_{iNG} \phi_{NG}) a_{i2} &= \sum_{i=1}^{NF} a_{i2} R_i \\
&\vdots \\
\sum_{i=1}^{NF} (a_{i1} \phi_1 + a_{i2} \phi_2 \cdots + a_{iNG} \phi_{NG}) a_{iNG} &= \sum_{i=1}^{NF} a_{iNG} R_i.
\end{aligned} \tag{14}$$

If it is noted that:

$$[A]^T = \begin{bmatrix} a_{11} & a_{21} & a_{31} & \cdots & a_{NF1} \\ a_{12} & a_{22} & a_{32} & \cdots & a_{NF2} \\ \vdots & \vdots & \vdots & \vdots & \vdots \\ a_{1NG} & a_{2NG} & a_{3NG} & \cdots & a_{NFNG} \end{bmatrix}. \tag{15}$$

It is seen by referring to Equations (7) and (9) that the system of equations, (14) can be written compactly as:

$$[A]^T [A] [\Phi] = [A]^T [R] \tag{16}$$

or

$$[B][\Phi] = [S] \quad (17)$$

where the new matrix $[B] = [A]^T [A]$ will be of dimensions $NG \times NG$ and the new vector $[S]$ will be of length NG .

Equation (17) is solved by any appropriate method to yield the desired “best estimate” flux vector that is consistent with the measured reaction rates. If $NF = NG$, the solution of Equation (17) will be the same as would be obtained by simply solving Equation (8) without multiplying through first by $[A]^T$.

It should also be noted that insertion of the adjusted fluxes back into the basic balance equation [Equation (7)] will not ordinarily produce adjusted reaction rates that are the same as the measured reaction rates, unless $NF = NG$, in which case the adjusted fluxes are forced by definition to produce the measured reaction rates exactly.

It is also necessary to consider the propagation of uncertainties in the adjustment process described here. In general the measured reaction rates in Equation (16) will each have an associated experimental uncertainty. In addition there will be a component of variance in the adjusted fluxes associated with the nature of the least-squares process itself.

If the measured reaction rates R_i are assumed to be statistically independent, and the fractional uncertainty associated with the activation constants a_{ij} is negligible compared to the uncertainties of the measured reaction rates then an estimate for the total variance of the adjusted flux in group j may be expressed as:

$$s_j^2 = \sum_{i=1}^{NF} \left(\frac{\partial \phi_j}{\partial R_i} \right)^2 [\delta_i^2 + u_i^2] \quad (18)$$

where δ_i is computed from Equation (11) and u_i is the experimental uncertainty associated with reaction rate i . Thus it is necessary to compute a matrix of derivatives of the group fluxes with respect to each reaction rate in order to evaluate the uncertainties in the adjusted fluxes from Equation (18).

To obtain the required matrix of derivatives, first rearrange and partially expand Equation (16) to yield:

$$\begin{bmatrix} \phi_1 \\ \phi_2 \\ \phi_3 \\ \vdots \\ \phi_N \end{bmatrix} = [C] \begin{bmatrix} a_{11}R_1 + a_{21}R_2 \cdots + a_{NF1}R_{NF} \\ a_{12}R_1 + a_{22}R_2 \cdots + a_{NF2}R_{NF} \\ a_{13}R_1 + a_{23}R_2 \cdots + a_{NF3}R_{NF} \\ \vdots \\ a_{1NG}R_1 + a_{2NG}R_2 \cdots + a_{NFNG}R_{NF} \end{bmatrix} = [C][A]^T [R] \quad (19)$$

where $[C] = [B]^{-1} = [[A]^T [A]]^{-1}$.

Or, expanding further:

$$\begin{bmatrix} \phi_1 \\ \phi_2 \\ \phi_3 \\ \vdots \\ \phi_{NG} \end{bmatrix} = \begin{bmatrix} c_{11} & c_{12} & c_{13} & \cdots & c_{1NG} \\ c_{21} & c_{22} & c_{23} & \cdots & c_{2NG} \\ c_{31} & c_{32} & c_{33} & \cdots & c_{3NG} \\ \vdots & \vdots & \vdots & \ddots & \vdots \\ c_{NG1} & c_{NG2} & c_{NG3} & \cdots & c_{NGNG} \end{bmatrix} \begin{bmatrix} a_{11}R_1 + a_{21}R_2 \cdots + a_{NF1}R_{NF} \\ a_{12}R_1 + a_{22}R_2 \cdots + a_{NF2}R_{NF} \\ a_{13}R_1 + a_{23}R_2 \cdots + a_{NF3}R_{NF} \\ \vdots \\ a_{1NG}R_1 + a_{2NG}R_2 \cdots + a_{NFNG}R_{NF} \end{bmatrix}. \quad (20)$$

Differentiating the elements of the flux vector will respect to R_1 , for example, yields:

$$\begin{aligned} \frac{\partial \phi_1}{\partial R_1} &= c_{11}a_{11} + c_{12}a_{12} + c_{13}a_{13} \cdots c_{1NG} a_{1NG} \\ \frac{\partial \phi_2}{\partial R_1} &= c_{21}a_{11} + c_{22}a_{12} + c_{23}a_{13} \cdots c_{2NG} a_{1NG} \\ &\vdots \\ \frac{\partial \phi_{NG}}{\partial R_1} &= c_{NG1}a_{11} + c_{NG2}a_{12} + c_{NG3}a_{13} \cdots c_{NGNG} a_{1NG} \end{aligned} \quad (21)$$

or:

$$\frac{\partial [\Phi]}{\partial R_1} = [C] \begin{bmatrix} a_{11} \\ a_{12} \\ a_{13} \\ \vdots \\ a_{1NG} \end{bmatrix} = [C] [\text{column 1 of } [A]^T] \quad (22)$$

and thus:

$$[B] \frac{\partial[\Phi]}{\partial R_1} = [\text{column 1 of } [A]^T]. \quad (23)$$

In general:

$$[B] \frac{\partial[\Phi]}{\partial R_i} = [\text{column } i \text{ of } [A]^T]. \quad (24)$$

Equation (24) thus describes NF systems of NG simultaneous equations that can be solved to obtain all of the derivatives necessary to evaluate Equation (18) for the uncertainties associated with the group fluxes.

If the matrix [A] is square, i.e., if NF = NG, the evaluation of the derivatives can be simplified by beginning with Equation (8):

$$[\Phi] = [C][R] \quad (25)$$

where [C] is now defined to be the inverse of [A] rather than the inverse of [B]. In this case expansion of Equation (25) yields:

$$\begin{bmatrix} \phi_1 \\ \phi_2 \\ \vdots \\ \phi_{NG} \end{bmatrix} = \begin{bmatrix} c_{11}R_1 + c_{12}R_2 \cdots c_{1NG} R_{NF} \\ c_{21}R_1 + c_{22}R_2 \cdots c_{2NG} R_{NF} \\ \vdots \\ c_{NG1}R_1 + c_{NG2}R_2 \cdots c_{NGNG} R_{NF} \end{bmatrix} \quad (26)$$

where NF = NG. Differentiating with respect to R_1 now yields

$$\frac{\partial \phi_1}{\partial R_1} = c_{11}, \quad \frac{\partial \phi_2}{\partial R_1} = c_{21}, \quad \frac{\partial \phi_1}{\partial R_2} = c_{12}, \quad \frac{\partial \phi_2}{\partial R_2} = c_{22}, \text{ etc.}$$

Thus:

$$\frac{\partial[\Phi]}{\partial R_1} = [C] \begin{bmatrix} 1 \\ 0 \\ 0 \\ \vdots \\ 0 \end{bmatrix} = [C] [\text{column 1 of an } NG \times NG \text{ identity matrix}] \quad (27)$$

and in general

$$[A] \frac{\partial[\Phi]}{\partial R_i} = [\text{column } i \text{ of an } NG \times NG \text{ identity matrix}] \quad (28)$$

since $[C] = [A]^{-1}$.

Equation (28) then describes NF (now equal to NG) systems of simultaneous equations for the necessary derivatives. These are used to evaluate Equation (18) where, in this case, the “fit variances” δ_i^2 , assumed to result largely from the (necessarily) approximate values of the reaction rate constants a_{ij} , are zero by definition, and only the experimental reaction rate variances, u_i^2 , propagate through to the adjusted fluxes. The fact that the δ_i^2 values are zero in this case does not necessarily mean that the adjusted fluxes are somehow more accurate, or more physically realistic. It simply means that the fluxes were forced to match the measured reaction rates when premultiplied by the given activation matrix $[A]$, and that no information is available to estimate the fit variance in each group.

The methods outlined here have been implemented in a FORTRAN program SPECTRE, which inputs the activation cross section functions $\sigma_f(E)$ and the *a-priori* volume-average flux functions $\Psi_f(E)$ in a user-specified fine-group form for each activation foil or wire interaction of interest. These, along with a user-input *a-priori* fine-group unperturbed spectrum, $\Psi(E)$, are used to compute the elements of the matrix $[A]$ for NG broad groups, each of which spans one or more specified fine groups. The number of broad groups, NG for which adjusted fluxes are determined may be equal to or less than the number of activation interactions, NF. Solution of the various systems of equations to produce the adjusted fluxes and associated uncertainties corresponding to a user-input set of NF measured activation rates (and associated experimental uncertainties) is accomplished using standard Gauss-Seidel iterations, with linear extrapolation to accelerate convergence (which can be rather slow in some cases).

A more rigorous approach is also available to compute adjusted fluxes using a least-squares objective function whose components are weighted by the individual experimental variances associated with the measured reaction rates. In this case, Equation (10) becomes:

$$\Delta = \sum_{i=1}^{NF} \frac{\delta_i^2}{u_i^2} \quad (29)$$

where u_i is the previously-defined experimental uncertainty associated with reaction rate i . In this case it is straightforward to show that Equation (16) becomes:

$$[A]^T [V] [A] [\Phi] = [A]^T [V] [R] \quad (30)$$

where [V] is an NF x NF matrix, given by:

$$[V] = \begin{bmatrix} \frac{1}{u_1^2} & & & 0 \\ & \frac{1}{u_2^2} & & \\ & & \frac{1}{u_3^2} & \\ 0 & & & \dots & \frac{1}{u_{NF}^2} \end{bmatrix} \quad (31)$$

Thus, the matrix [B] in Equations(17) and (24), and the vector [S] in Equation (17) are redefined according to Equation (30). In addition, $[A]^T$ in Equation (24) is postmultiplied by [V]. Equations (30) are generally referred to in the literature as the “normal equations”. They are applicable to many different types of least-square based data adjustment and fitting procedures.

It is useful to note that in the formulation represented by Equation 30, the inverse of the matrix [B] is now a covariance matrix for the adjusted fluxes, based on propagation of the measurement uncertainties u_i . Accordingly, the diagonal elements of $[B]^{-1}$ correspond to the components of the total flux variance that are attributable to propagation of the measurement uncertainties.

It is also possible to construct a weighted objective function using the measured reaction rates as weights. In this case, Equation (10) becomes:

$$\Delta = \frac{\delta_i^2}{R_i^2} \quad (32)$$

In this case the sum of the squares of the fractional differences between the measured and fitted reaction rates is minimized. This is accomplished by substituting R_i^2 for u_i^2 in each diagonal term of Equation (31). This generally produces results that are very similar to what is obtained using Equation (29), and it produces identical results if all of the measured reaction rates have the same fractional uncertainty.

Finally it may be noted that although the term “foil or wire” is used here for the dosimeters used to make activation measurements, the method is equally-applicable to any other type of dosimeter, with or without an associated spectral modification shield, for which the neutron response parameters needed to compute the associated elements of the matrix [A] can be accurately determined in some manner.